THE ELECTROCHEMICAL AND ELECTROCATALYTIC BEHAVIOUR OF GLASSY ALLOYS

by

CHRISTINE MARY CROSBY
BSc (Hons) (Natal)

Submitted in fulfilment of
the academic requirements for the degree of
Master of Science
in the Department of Chemistry
University of Natal
Durban.

May 1999

ABSTRACT

The aim of this study was to investigate the electrochemical and electrocatalytic properties of a selection of glassy alloys for the hydrogen evolution reaction in base. The glassy alloy compositions tested included the known alloys $Fe_{67}Co_{18}B_{14}Si_1$, $Co_{66}Fe_4Si_{16}B_{12}Mo_2$, $Fe_{40}Ni_{40}B_{20}$ and $Fe_{40}Ni_{40}P_{14}B_6$ and an entirely new alloy $Zr_{74}Ti_{19}Cu_2Fe_5$. The electrochemical techniques employed were cyclic voltammetry and slow sweep polarisation. Electrochemical techniques were used in conjunction with the surface analysis techniques of scanning electron microscopy (SEM) and energy dispersive x-ray spectrometry (EDS) to gain insight into the morphology and chemical compositions of the electrode surfaces after various treatments. The aims included:

1) To obtain an understanding of the field of electrochemistry of glassy alloys.
2) To develop systems, techniques and procedures to enable the testing of a new alloy to be performed with confidence.
3) To this end, techniques were firstly developed and then compared with published data on the known alloys. Once the handling techniques were satisfactory the new and previously untested $Zr_{74}Ti_{19}Cu_2Fe_5$ glassy alloy was characterised, in particular its catalytic properties and its corrosion resistant properties were investigated. The physical properties of the $Zr_{74}Ti_{19}Cu_2Fe_5$ alloy are under investigation by another group in the School of Physics. My findings are presented here.

The corrosion resistance of the alloys was determined in their as-polished state and after surface pretreatment from slow sweep anodic polarisation studies and cyclic voltammetry. Glassy $Fe_{67}Co_{18}B_{14}Si_1$ and $Co_{66}Fe_4Si_{16}B_{12}Mo_2$ displayed the poorest corrosion resistance of the alloy compositions tested. The anodic polarisation curve of the $Zr_{74}Ti_{19}Cu_2Fe_5$ alloy produced no active region and displayed potentially excellent anticorrosive properties in the basic media which was attributed to highly passivating Zr oxide and Ti oxide surface films.

The electrocatalytic activity of the glassy alloys for hydrogen evolution was evaluated in 1M KOH. Cathodic polarisation curves were used to construct Tafel plots from which the kinetic Tafel parameters, i_o and b, were calculated. The least corrosion resistant glassy alloy compositions, $Fe_{67}Co_{18}B_{14}Si_1$ and $Co_{66}Fe_4Si_{16}B_{12}Mo_2$, displayed the highest catalytic activity for hydrogen evolution in the as-polished state. The most corrosion resistant alloy, $Zr_{74}Ti_{19}Cu_2Fe_5$, showed the poorest catalytic activity for the reaction in the as-polished state and only a slight improvement was obtained by increasing the electrolyte temperature in comparison to the other alloys tested. This was again attributed to passivating Zr oxide and Ti oxide surface layers that inhibited the HER. It was found that the Zr-based alloy displayed no substantial advantages over the other glassy alloys or more expensive noble metal surfaces in basic media, unless pre-treated as described in this thesis.

The influence of *ex situ* chemical pretreatment on the electrocataytic activity of the glassy alloys for the HER was determined using pure HF and HF/HNO_3 mixtures. Acid pretreatment of glassy $Co_{66}Fe_4Si_{16}B_{12}Mo_2$ and $Fe_{40}Ni_{40}P_{14}B_6$ with 1M HF/1M HNO_3 (10 minutes) and $Zr_{74}Ti_{19}Cu_2Fe_5$ with 1M HF (10 seconds) resulted in a significant improvement in the activity of the alloys in comparison to their as-polished state. SEM/EDS analysis indicated that preferential dissolution of a P-enriched surface region on the $Fe_{40}Ni_{40}P_{14}B_6$ electrode created a porous structure with a greatly enlarged surface area at which the HER could occur. In comparison, the P-free, $Fe_{40}Ni_{40}B_{20}$, composition displayed a much lower improvement in activity after acid pretreatment with only slight surface roughening observed. The Zr component of glassy $Zr_{74}Ti_{19}Cu_2Fe_5$ was selectively leached by acid pretreatment to produce a porous surface, however, the corrosion resistance of the alloy was also reduced, as indicated from anodic polarisation curve that showed an active and passive region of greater current density than the as-polished electrode. Hence the beneficial effect of acid pretreatment in activating the alloy surface for the HER was countered by a reduction in the general corrosion resistance of the alloy.

In view of the dramatic effect on the HER shown by prior *ex situ* (acidic) oxidation of the glassy alloy surface, the influence of *in situ* (anodic) oxidation in the basic medium was investigated for comparison. For all the glassy alloy compositions tested, anodic activation was found to be less effective than acidic activation. Anodic pretreatment of glassy $Zr_{74}Ti_{19}Cu_2Fe_5$ ($3000\mu A.cm^{-2}$) resulted in the greatest improvement in activity in comparison to the as-polished state out of the alloy compositions tested. In addition, the corrosion resistance of the alloy was not reduced by anodic pretreatment and consequently formed a less destructive activation procedure than acidic pretreatment. In this regard, anodic pretreatment would produce a more durable electrocatalyst and is the preferred technique for activating the glassy alloy surfaces for the HER. Initial characterisation of the surface deposits formed by anodic oxidation, using SEM and EDS techniques, indicates that the composition of these deposits and the mechanism by which anodic activation activates the glassy alloy surfaces requires further investigation.

PREFACE

The experimental work described in this thesis was carried out in the Department of Chemistry, University of Natal, Durban, under the supervision of Professor H.C. Brookes.

These studies represent original work by the author and have not otherwise been submitted in part or in whole, to any other tertiary institution. Where use has been made of the work of others it has been duly acknowledged in the text.

DECLARATION

I hereby certify that this research is the result of my own investigation, which has not been accepted in any substance for any other degree, and is not concurrently submitted in candidature for any other degree.

Signed:

C.M. Crosby
BSc (Hons) (Natal)

I hereby certify that the above statement is correct.

Signed:

Professor H.C. Brookes
PhD (Cape Town)
Professor of Inorganic Chemistry
University of Natal
Durban

Department of Chemistry
University of Natal
Durban
1999

ACKNOWLEDGEMENTS

My sincere thanks go to Professor H.C. Brookes for all the support, guidance and encouragement he has provided throughout this project.

I would also like to thank:

- Professor T. Doyle for supplying the glassy alloy samples.
- Dr F. Graham for her patient instruction in the use of the SEM.
- V. Carruthers for his help with computer related problems and in writing the macro.
- FRD for the bursary in 1996 and 1997.
- UND for graduate assistance.
- URF for providing running expenses for the project.
- Mum and Dad for financial support and all the interest and encouragement they have shown in the work.

TABLE OF CONTENTS

LIST OF SYMBOLS AND ABREVIATIONS

ELECTROCHEMICAL CONVENTIONS

- Potentials more oxidising than the saturated sulphate electrode (SSE) are positive.
  $E_{SSE,\,mV} = E_{SHE,mV} - 642mV$ at 25°C.
- Currents at an electrode corresponding to a net oxidation are positive.

Some of the symbols which are used only once are not defined here, but are adequately defined in the text.

Symbol	**Description**	**Units**
APC	Anodic polarisation curve	
CV	Cyclic voltammetry	
SSE	Saturated sulphate electrode	
SHE	Standard hydrogen electrode	
WE	Working electrode	
RE	Reference electrode	
CE	Counter electrode	
HER	Hydrogen evolution reaction	
SEM	Scanning electron microscopy	
EDS	Energy dispersive x-ray analysis	
AES	Auger electron spectroscopy	
RDE	Rotating disk electrode	
Rds	Rate determining step	
XPS	X-ray photoelectron spectroscopy	
I	Current	mA
i	Current density	mA/cm^2
i_o	Exchange current density	mA/cm^2
i_{pp}	Primary passive current density	mA/cm^2
i_p	Passive current density	mA/cm^2
i_{pa}	Current density of anodic CV peak	mA/cm^2
i_{pc}	Current density of cathodic CV peak	mA/cm^2
i_L	Limiting current density	mA/cm^2

i_a	Anodic current density	mA/cm^2
i_c	Cathodic current density	mA/cm^2
E_a	Activation energy	kJ/mol
E_{pa}	Potential of anodic CV peak	V or mV
E_{pc}	Potential of cathodic CV peak	V or mV
E_{corr}	Corrosion potential	V or mV
E_{Flade}	Flade potential	V or mV
E_{tr}	Transpassive potential	V or mV
E_{pp}	Primary passivation potential	V or mV
$J_l(x)$	Flux of species 1 at distance x (cm) from the electrode surface	mol/s/cm
n	Number of electrons in electron transfer reaction	
R	Gas constant	8.314 J/K/mol
T	Temperature	K or °C
A	Area of electrode	cm^2
C_l	Concentration of species 1	mol/cm^3
C_o	Concentration of species O	mol/cm^3
D_l	Diffusion coefficient of species 1	cm^2/s
D_o	Diffusion coefficient of species O	cm^2/s
F	Faraday constant	96485 C/mol
β	Anodic transfer coefficient	
α	Cathodic transfer coefficient	
η	Overpotential	V or mV
b	Tafel slope	mV
v	Scan rate	mV/s
$V_o(x)$	Velocity of species O along x-axis	cm/s
Z_o	Charge of species O	C
$C_{o(x=0)}$	Concentration of species O at electrode surface	mol/cm^3
C_o^*	Bulk solution concentration of species O	mol/cm^3
δ	Nernst diffusion layer thickness	cm

CHAPTER 1: INTRODUCTION

Metallic glasses represent a novel class of alloy that combines a metallic electronic structure with an amorphous (non-crystalline) molecular structure that lacks the long-range order present in conventional crystalline alloys. They are prepared by rapid solidification of alloy melts, in which cooling rates of 10^6 K/s prevent the nucleation and growth of metallic crystals. Rapid quenching produces a solid ribbon of about a 20-60μm thickness and 1-25mm width. Two broad categories of metallic glass alloys are recognised, metal-metalloid glasses and binary metal-metal glasses (usually 1:1 in composition). Metal-metalloid glasses are the most widely studied group, with a metal to metalloid ratio of 4:1 being typical. The consistent glassy forming ratio suggests that a specific type of chemical bonding is present and it is found that alloy compositions that form "deep eutectics" in the phase diagram generally display the greatest ease of amorphization. The metalloid elements are believed to stabilise the amorphous structure by providing an appropriate atomic volume. Glassy alloys are metastable and practical applications are limited to those requiring thin layers at low operating temperatures since temperatures approaching the glass transition temperature cause the alloys to rapidly devitrify into their crystalline phases. To date, most research has focused on the physical properties of glassy alloys and relatively little work has been conducted on their surface properties. In the light of their unique amorphous surface structure and the ability to form a wide variety of different glassy alloy compositions, further research into the surface properties of these alloys is important for developing potentially new corrosion resistant and catalytically active materials as well as for gaining a greater understanding of the nature of the surface processes involved in these characteristics which are clearly of fundamental importance in understanding the behaviour of glassy metal alloys.

Some previous research at this University has focused on the physical properties of glassy alloys. The amorphous structure of the alloys has been investigated using Mossbauer Spectroscopy and X-ray Diffraction techniques and research into their electrical and magnetic properties conducted. The influence of structural relaxation by controlled heat treatment on the metastable amorphous structure and its effect on the electrical and magnetic properties of the alloys has also been investigated. In an attempt to chemically characterise these unique alloy structures and compositions, this study focuses on the surface chemical properties of the glassy alloys also selected for physical investigation, thereby enabling a more complete picture of their behaviour to be obtained.

In this work the corrosion behaviour and electrocatalytic activity of a selection of five different glassy alloys was investigated in base. Four commercially available glassy alloys of composition $Fe_{67}Co_{18}B_{14}Si_1$, $Co_{66}Fe_4Si_{16}B_{12}Mo_2$, $Fe_{40}Ni_{40}B_{20}$ and $Fe_{40}Ni_{40}P_{14}B_6$ and one specially produced glassy alloy, $Zr_{74}Ti_{19}Cu_2Fe_5$, were tested. The influence of the alloy metal and metalloid components, the amorphous structure and different surface activation pretreatments on the activity of the alloys was investigated. Experiments were initially conducted on the four commercially available glassy alloys for which a limited amount of electrochemical research had already been conducted so that comparisons could be made with literature data where available. The electrochemical properties of the unique and previously untested $Zr_{74}Ti_{19}Cu_2Fe_5$ composition were then investigated.

Initially, a technique for mounting the thin glassy alloy specimens was developed so that an evenly polished and reproducible electrode surface could be prepared for each experiment. Since handling of thin films of this nature was new to our laboratory the development of satisfactory procedures to solve these problems involved a considerable amount of research and development.

The general corrosion resistance of the glassy alloys was evaluated in base using the electrochemical techniques of anodic polarisation and cyclic voltammetry. The electrocatalytic activity of the alloys for the hydrogen evolution reaction (HER) was initially determined in their as-polished state, at different electrolyte temperatures and after surface activation. Cathodic polarisation curves were obtained in the hydrogen evolution region from which Tafel plots were constructed and the kinetic parameters, i_o and b, calculated. Surface analysis by scanning electron microscopy (SEM) and energy dispersive x-ray spectrometry (EDS) were used to monitor changes in the alloy surface morphology and chemical composition after the different surface pretreatments. Anodic polarisation curves of the pretreated surfaces were also obtained to determine the influence of surface activation on the corrosion resistance of the alloys.

The HER can occur by an electrocatalytic mechanism at electrode surfaces by the formation of adsorbed hydrogen intermediates. The reaction has been widely investigated at a range of different electrode surfaces, in particular at polycrystalline metal and alloy surfaces and forms a good prototype reaction for investigating the electrocatalytic activity of the relatively new and unstudied group of glassy alloys. The HER is also of technological importance because the development of efficient and cost effective electrodes for hydrogen generation from water electrolysis and for hydrogen oxidation in power generation from fuel cells is of importance in developing the future hydrogen economy.

An increase in the electrocatalytic activity of a metal or alloy can be accomplished by using either an electrode material with a high intrinsic activity for hydrogen evolution (for example, single metals such as Pt, Au, Ni, Rh or Ni based alloys which are expensive) or by increasing the effective surface area of the electrode. The latter method is the most successful way of overcoming intrinsically low reaction rates and can be accomplished by different pretreatment procedures of the electrode surface. Pretreatment that produces an electrode with a roughened or porous surface increases the reaction rate as it provides a greater surface area at which adsorption of the reaction intermediates can occur. In general, amorphous alloys display a poorer electrocatalytic activity for the HER in their as-quenched and as-polished states than their pure metal components or equivalent crystalline compositions. This is attributed to their homogeneous amorphous surface that lacks the defect sites inherent on crystalline surfaces, such as screw or step dislocations that act as adsorption sites for hydrogen. Pretreatment of glassy alloys has been found to activate the alloy surfaces in comparison to their as-quenched state and in this study the influence of surface activation by *ex situ* chemical (acid etching) as well as *in situ* electrochemical (anodic oxidation) pretreatment was also investigated.

CHAPTER 2: THEORETICAL BACKGROUND

The background theory and relevant equations used in this study are presented. The derivations are omitted but may be found in the cited references.

2.1 MASS TRANSFER

2.1.1 Types of mass transfer

For a simple electrode reaction where species O is reduced at a cathode:

$$O + ne^- \leftrightarrow R \qquad (2.1)$$

species O and R may be in solution, adsorbed on the electrode surface, or form the electrode material and n represents the number of electrons transferred in the reaction. If the rate of electron transfer is fast compared with the movement of electroactive species to the electrode surface, then the reaction is mass transfer controlled.

Mass transfer may occur in three different modes:

- Diffusion, involving the movement of species down a concentration gradient. Diffusion occurs whenever a chemical change at the electrode surface alters the concentration of reactants and products with respect to the bulk solution.
- Migration, which results from electrostatic forces and causes charged species to pass through the electrolyte due to a potential gradient. The effects of migration of electroactive species may be largely overcome by adding a greater than ten-fold excess of inert background electrolyte to carry most of the charge.
- Convection, involves the movement of the bulk solution by forces that may be natural or imposed.

The three modes of mass transfer result a the flux of electroactive species to the electrode surface and may be represented quantitatively by the Nernst-Planck equation [1]:

$$J_o(x) = -D_o \frac{\partial C_o(x)}{\partial x} - \frac{Z_o F}{RT} D_o C_o(x) \frac{\partial E(x)}{\partial x} + C_o(x) V_o(x) \qquad (2.2)$$

The equation is applicable for one-dimensional mass transfer to a planar electrode surface along the x-axis,

where, $J_o(x)$ = flux of species O (mol s^{-1} cm^{-2}) at distance x (cm) from the electrode surface
D_o = diffusion coefficient of species O (cm^2 s^{-1})
$\partial C_o(x)/\partial x$ = concentration gradient at distance x
$\partial E(x)/\partial x$ = potential gradient
Z_o = charge (Coulombs) on species O
C_o = concentration of species O (mol cm^{-3})
$V_o(x)$ = velocity of movement of the electroactive species to the electrode surface along the x-axis (cm s^{-1})
F, R and T represent the Faraday constant, gas constant and temperature (K) respectively

The three terms on the right hand side of the equation represent the contributions of diffusion, migration and convection respectively. Electrochemical systems are usually designed so that one or more of the contributions to mass transfer are negligible.

2.1.2 Diffusion to a linear planar electrode

In an unstirred solution and in the presence of a supporting electrolyte, diffusion is the only form of mass transport that needs to be considered. The simplest model describing diffusion assumes that the electrode surface is flat, planar and of infinite dimensions, so that concentration variation arises in a direction perpendicular to the electrode surface. Diffusion is described quantitatively by Fick's laws [2]. Fick's first law describes concentration variation with distance from the electrode surface, by the equation:

$$J_1(x) = -D_1 \frac{dC_1}{dx} \qquad (2.3)$$

where, $J_1(x)$ (mol m^{-2} s^{-1}) represents the flux and dC_1/dx the concentration gradient of species 1 along the x-axis. By equating the flux of species O and R in equation (2.1) with the flux of electrons at the electrode surface (x = 0), current is related to chemical change (Fig. 1) by:

$$\frac{i}{nFA} = -D_o\left(\frac{\partial C_o}{\partial x}\right)_{x=0} \quad \text{or} \quad \frac{i}{nFA} = -D_R\left(\frac{\partial C_R}{\partial x}\right)_{x=0} \tag{2.4}$$

where, A is the electrode area (cm^2).

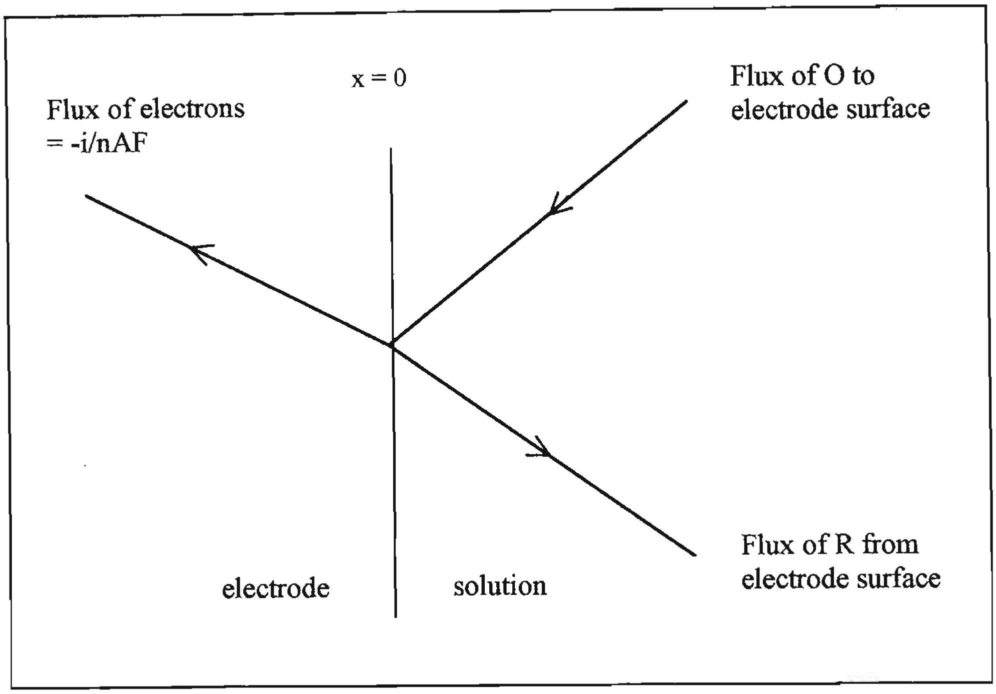

Fig. 1: Flux of electroactive species and electrons at the electrode surface (x = 0) for the reaction, O + ne → R.

Fick's second law describes how the concentration of electroactive species changes with time by the development of concentration profiles. It is expressed by the equation:

$$\frac{\partial C_o}{\partial t} = D_o\frac{\partial^2 C_o}{\partial x^2} \tag{2.5}$$

As the reaction $O + ne^- \rightarrow R$ proceeds, the electrode surface concentration of O decreases until it becomes effectively zero. At this point, the reaction becomes diffusion controlled, and concentration profiles develop (Fig. 2). At short times, the concentration profile is steep, but with increasing time, diffusion causes the profile to relax towards its steady state by extending into the solution and becoming less steep. Since current is a function of the flux of O at the electrode surface, the current will also decrease with time.

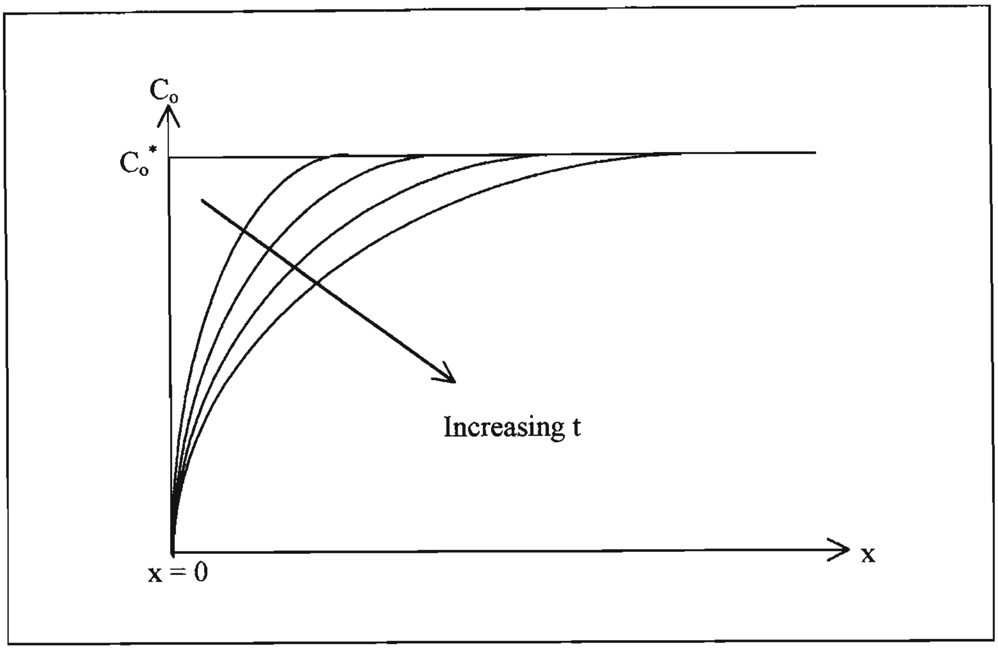

Fig. 2: Concentration profiles at an electrode surface for the reaction, O + ne → R, at a potential where the process is diffusion controlled, for t > 0 and $C_o = 0$ at x = 0.

2.1.3 Rotating electrodes

Controlled hydrodynamic transport using a rotating disc electrode (RDE) increases the flux of electroactive species to the electrode surface so that steady state conditions may be achieved more rapidly. The Nernst diffusion layer model describes two distinct layers within the electrolyte. Close to the electrode surface a diffusion layer of thickness, δ (cm), forms in which diffusion constitutes the only significant mode of mass transport. Beyond this layer convection is strong enough to maintain a uniform concentration of electroactive species. The Nernst diffusion layer approximation assumes that $\partial C_o/\partial x$ is a constant from x = 0 to $x = \delta_o$, where $C_o = C_o^*$, i.e.

$$\frac{\partial C_0}{\partial x} = \frac{C_{0(x=0)} - C_0^*}{\delta_o} \qquad (2.6)$$

The steady state current density, i, is proportional to the concentration gradient of O at the electrode surface. The concentration of O is determined by potential, while the rate of diffusion depends on the thickness of the diffusion layer and hence on the rotation rate of the RDE. As rotation rate is increased the Nernst diffusion layer thickness decreases [2]. These factors are expresses by the equation:

$$i = nFAm_o[C_o^* - C_{o(x=0)}] \qquad (2.7)$$

where m_o = mass transfer coefficient (cm/s)

$m_o = D_o/\delta_o$

At a sufficiently high potential $C_{o(x=0)} = 0$ and i must become independent of further increases in potential. A limiting current density, i_L , will then result and is given by the equation:

$$i_L = nFAm_oC_o^* \tag{2.8}$$

Convective-diffusion and hydrodynamic equations have been solved for steady state conditions at the RDE. For totally mass transfer limited conditions, the Levich equation [1] predicts that i_L is proportional to the bulk concentration, C_o^*, and the square root of the rotation rate ω (rad s^{-1}):

$$i_L = 0.62FAnD^{2/3}v_k^{-1/6}C_o^*\omega^{1/2} \tag{2.9}$$

where v_k is the kinematic viscosity ($cm^2\ s^{-1}$).

Combining equations (2.8) and (2.9) gives:

$$\delta = 1.61D_o^{1/3}\omega^{-1/2}v_k^{1/6} \tag{2.10}$$

The Nernst diffusion layer thickness is proportional to $\omega^{-1/2}$ for a diffusion limited case. For an irreversible reaction the current-potential relationship is given by:

$$i = \frac{Fk_fAnC_o^*}{1 + k_f\dfrac{\delta}{D_o}} \tag{2.11}$$

where k_f is the heterogeneous rate constant (cm s^{-1}) for the forward reaction. Equation (2.11) is useful in defining the conditions for kinetic or mass transfer control at the RDE.
If $k_f\delta/D_o << 1$ then the current is kinetically controlled and i_L is independent of $\omega^{-1/2}$.
If $k_f\delta/D_o >> 1$ then the reaction is mass transfer controlled and equation (2.10) results.

The useful rotation rate range of a RDE system (and therefore the range for which the Nernst diffusion layer approximation is valid) in water at 25°C is given by:

$$10\,\frac{\nu_k}{r_l^2} < \omega < 2 \times 10^{-5}\,\frac{\nu_k}{r_l^2} \qquad (2.12)$$

where r_l is the radius of the disc (cm). At ω less than the lower theoretical limit, the hydrodynamic boundary thickness becomes too large. At ω greater than the larger theoretical limit, turbulent flow commences.

2.2 ELECTRON TRANSFER

2.2.1 Butler-Volmer equation

The rate of a reaction controlled by electrode kinetics is dependent on the rate of electron transfer at the electrode-solution interface. Consider the electrode reaction (2.1) in which species O is reduced to species R in a reversible reaction. When the rate of electron transfer is slow compared to the processes of mass transfer, both O and R will be present in solution so that both the forward (k_f) and reverse (k_b) reaction rates must be considered. Under such conditions, the Butler-Volmer equation may be derived [3]. The equation is fundamental to electrode kinetics and shows the way in which current density (i) varies with the exchange current density (i_o), overpotential (η) and the transfer coefficients (α and β). The equation used here applies to a one electron processes ($n = 1$) taking place in a single step. More complex relations must be written for multielectron and multistep processes.

$$i = i_o\left[\exp\left(\frac{\beta nF\eta}{RT}\right) - \exp\left(\frac{-\alpha nF\eta}{RT}\right)\right] \qquad (2.13)$$

The first exponential term in the equation refers to the anodic current (i_a) contribution and the second term refers to the cathodic current (i_c) contribution to the overall current density (i).

$$i = i_a + i_c \qquad (2.14)$$

The exchange current density (i_o), is a measure of the amount of electron transfer activity at equilibrium potential ($\eta = 0$). It is the current density obtained when the rate of reduction of species O equals the rate of oxidation of species R. The anodic current density is of equal magnitude but opposite direction to the cathodic current density (negative by convention).

$$i_o = i_{a\,(\eta=0)} = -i_{c\,(\eta=0)} \qquad (2.15)$$

The transfer coefficients α and $\beta = (1 - \alpha)$ refer to the reductive and oxidative transfer coefficients respectively. They determine the symmetry of the net current versus the applied overpotential response resulting from the anodic and cathodic current contributions. Consider the following reductive process, in which α and $(1 - \alpha)$ appear as stochiometric coefficients:

$$O + \alpha e \equiv R - (1 - \alpha)e \qquad (2.16)$$

Increasing the electrochemical activity of electrons will accelerate the rate of the reductive process by a fraction α and retard the rate of the oxidative process by a fraction $(1 - \alpha)$. In a perfectly symmetrical reaction, the two contributions are equal, then $\alpha = \beta = 0.5$. Simple reactions often have a symmetry factor close to 0.5 [4].

The overpotential is defined as the deviation of the applied potential from the equilibrium, E_e, potential of the O/R couple, i.e.

$$\eta = E - E_e \qquad (2.17)$$

2.2.2 Limiting forms of the Butler-Volmer equation

The Butler-Volmer equation may be written in three different limiting forms which are used to obtain electrode kinetic data.

When the overpotential is small ($\eta < 10$ mV), i.e. close to E_e, the Taylor expansion approximation ($\exp(x) \approx 1 + x$, $x << 1$) can be applied to the Butler-Volmer equation to give:

$$i = i_o \frac{nF\eta}{RT} \qquad (2.18)$$

This equation indicates that close to equilibrium the current density varies in a linear manner with overpotential.

If the positive (anodic) overpotential is sufficiently large ($\eta > \sim 50$ mV), the cathodic exponential term in equation (2.10) becomes negligible and the equation simplifies to:

$$\log i = \log i_o + \frac{\beta nF}{2.3RT}\eta \qquad (2.19)$$

in which only the anodic current density contributes to the total current density.

Conversely, when a large negative overpotential is applied, the first term of the equation can be neglected and equation (2.10) simplifies to:

$$\log|-i| = \log i_o - \frac{\alpha nF}{2.3RT}\eta \tag{2.20}$$

Equations (2.19) and (2.20) are known as the Tafel equations and are used to calculate the kinetic parameters i_o, α and β [3]. If the current is measured as a function of overpotential and plotted as log i vs. η, a linear region extending over approximately 0.3 V should result (Fig. 3).

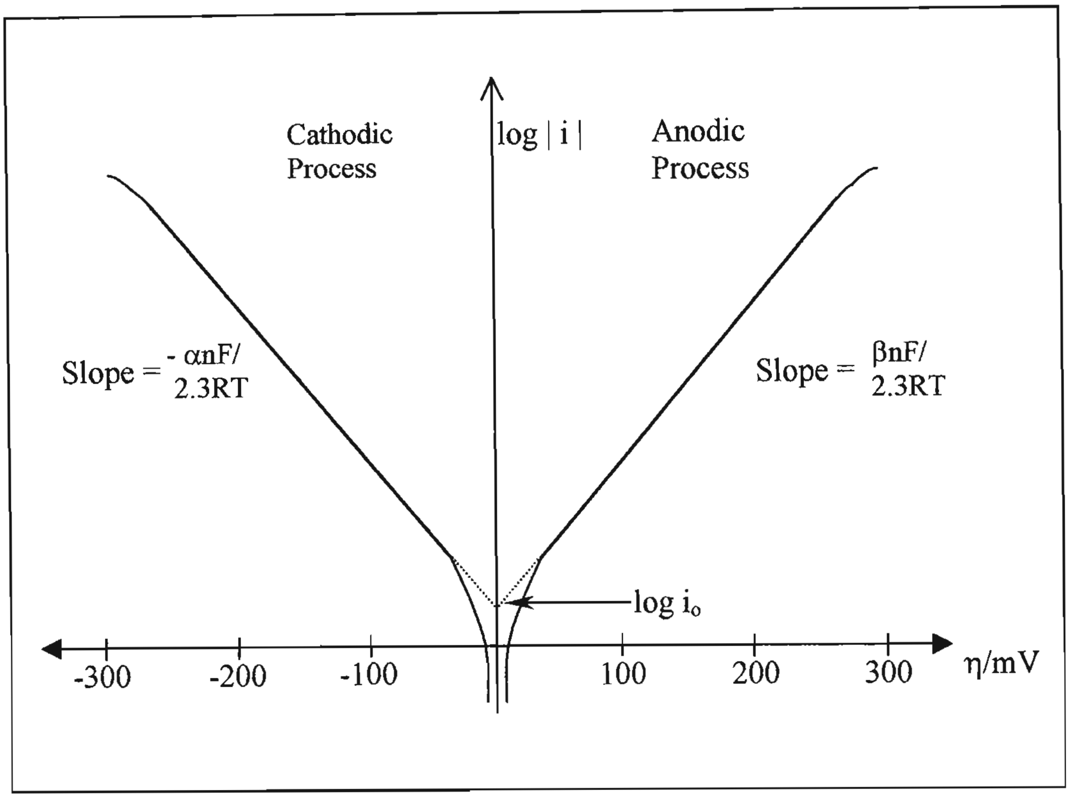

Fig. 3: Tafel plots for the determination of kinetic parameters i_o, α and β for the O/R redox couple.

The Tafel plot indicates that i increases exponentially with increasing η, until a point is reached at which i becomes limited by the rate of mass transport, causing the log i vs. η relation to flatten out. The point at which this occurs is determined by the efficiency of stirring, the diffusion coefficients and rates of electron transfer of the electroactive species. For very fast electron transfer processes mass transport limitation may set in before there is time for a linear Tafel region to be established. At low overpotentials deviation from linearity also occurs because the limiting Tafel form of the Butler-Volmer equation does not apply in this region. Extrapolation of the linear region to the intercept at zero overpotential yields log i_o. The anodic and cathodic Tafel slopes may be used to calculate β and α respectively.

2.3 CYCLIC VOLTAMMETRY

2.3.1 Reaction systems

Linear sweep voltammetry involves sweeping the electrode potential between limits E_1 and E_2 at a known sweep rate, v (mV/s). In cyclic voltammetry, the forward potential scan is followed by a reverse scan (normally at the same sweep rate), to produce a saw-tooth versus time signal (Fig. 4).

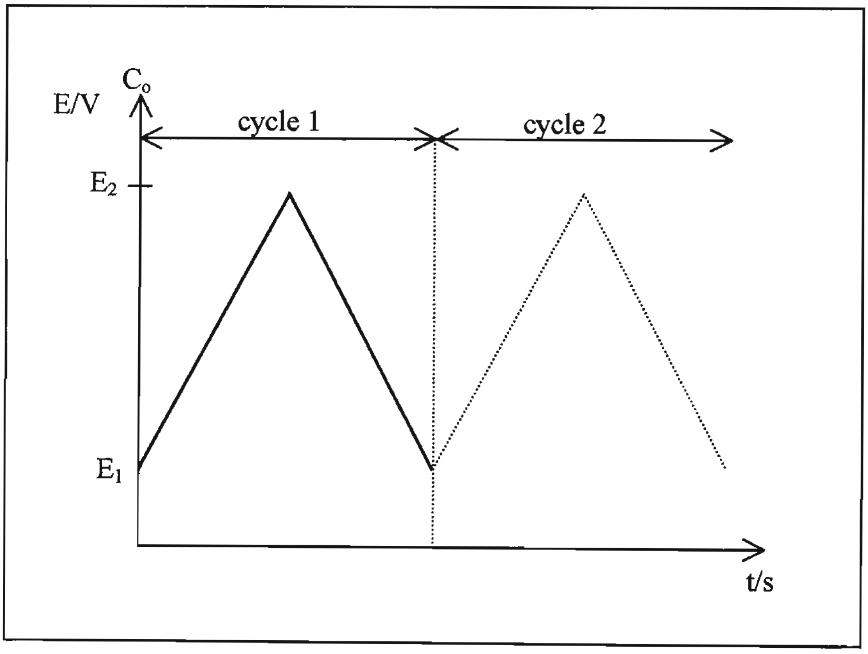

Fig. 4: An applied potential-time waveform.

The resulting current response plotted against this applied potential yields a voltammogram. If the system is reversible or quasi-reversible, e.g. $R \leftrightarrow O + ne^-$, an anodic peak current i_{pa}, at potential E_{pa}, on the forward sweep, will be followed by a cathodic peak current i_{pc}, at potential E_{pc}, on the reverse sweep. For an irreversible process, e.g. $R \rightarrow O + ne^-$, no cathodic current will be observed on the reverse sweep (Fig. 5).

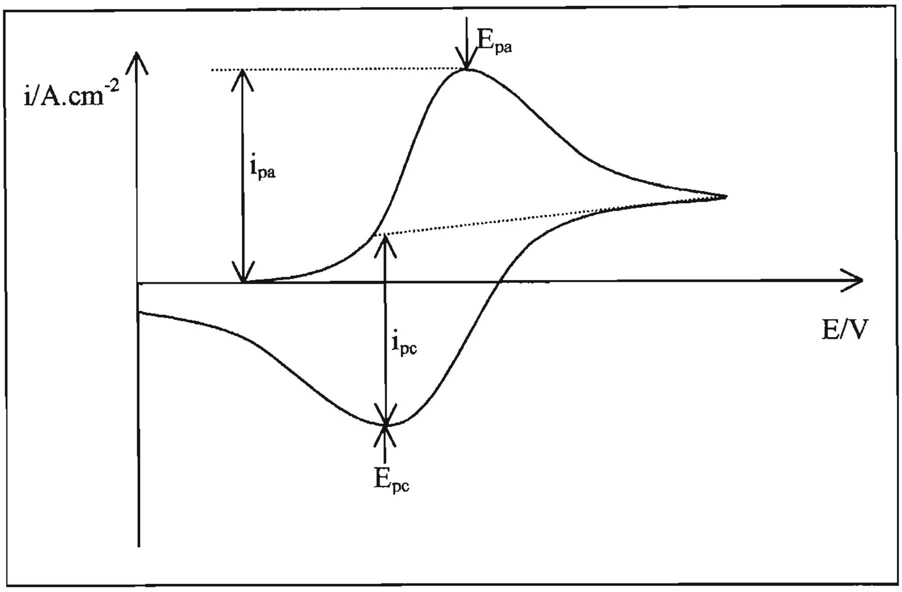

Fig. 5: Cyclic voltammogram for a reversible process, R ↔ O + ne, where initially only R is present in solution.

For a reversible electrochemical system, the rate of electron transfer is greater than the rate of mass transfer of electroactive species to the electrode surface, so that Nernstian equilibrium is always maintained at the electrode surface. For an irreversible system, the electron transfer rate is significantly lower than that of mass transport and Nernstian equilibrium is not maintained. Clearly certain reactions that are reversible at low sweep rates may become irreversible at higher ones, passing through some quasi-reversible region at the interchange. This results when the rate of mass transport becomes insufficient for maintaining equilibrium at the electrode surface [5].

Diagnostic tests for cyclic voltammograms and relevant equations have been formulated that can be used to identify the reaction type, based on the anodic and cathodic potentials (E_{pa}, E_{pc}), and current densities (i_{pa}, i_{pc}). The main equations and criteria relevant to reversible, irreversible and quasi-reversible systems are listed in Table 1.

Table 1: Cyclic voltammetric equations and diagnostic tests for the charge transfer process, O + ne ↔ R, where both reactants and products are soluble at 25°C.

Reversible process [2]

$$i_{pa} = (2.69x10^5)An^{3/2}D_o^{1/2}C_o^{*}v^{1/2}$$ (Randles – Sevcik equation)

$$\Delta E_p = E_{pa} - E_{pc} = \tfrac{59}{n}\,\mathrm{mV}$$

$$\left|E_p - \frac{E_p}{2}\right| = \tfrac{59}{n}\,\mathrm{mV}$$

$$\frac{i_{pa}}{i_{pc}} = 1$$

$$i_p \propto v^{1/2}$$

E_p is independent of v

At potentials beyond E_p, $i^{-2} \propto t$

Irreversible process [2]

$$i_{pc} \propto v^{1/2}$$

$$i_{pa} = (2.99x10^5)An(\alpha_c n_\alpha)^{1/2}D_o^{1/2}C_o^{*}v^{1/2}$$

E_{pc} shifts $-\dfrac{30}{\alpha_c n_\alpha}\,\mathrm{mV}$ for each 10-fold increase in v

$$\left|E_p - \frac{E_p}{2}\right| = \frac{48}{\alpha_c n_c}\,\mathrm{mV}$$

Quasi-reversible process [2]

$|i_p|$ increases with $v^{1/2}$ but not in a linearly proportional manner

$\dfrac{|i_{pa}|}{|i_{pc}|} = 1$ provided $\alpha_c = \alpha_a = 0.5$

$\Delta E_p > \dfrac{59}{n}\,\mathrm{mV}$ and increases with increasing v

E_{pc} shifts negatively with increasing v

where, n_α = number of electrons involved in the rate determining step

Cyclic voltammetry is also a useful technique for investigating reactions involving adsorption processes [2]. For such systems mass transfer effects can be ignored. If electron transfer is reversible then sharp and symmetrical oxidation and reduction peaks are obtained. Cyclic voltammograms of the Pt electrode in 1M H_2SO_4 show the oxidation and reduction peaks associated with adsorbed hydrogen atoms. Two pairs of hydrogen adsorption and desorption peaks are clearly visible at potentials positive to hydrogen evolution on a polycrystalline Pt electrode. These peaks are associated with different adsorption sites which result in different metal-hydrogen adsorption bond strengths [2].

The simplest case to consider is that in which only the adsorbed forms of reactive intermediates O and R are electroactive. The charges associated with the anodic and cathodic processes are equal due to the fixed amount of adsorbed reactant, O, available on the electrode surface for reduction. The actual values of i_p and E_p, and the peak width depend on the type of adsorption isotherm involved and the relative strengths of adsorption of adsorbed O and R. For cases in which adsorption can be described by a Langmuir isotherm, $E_{pa} = E_{pc}$ and the peak current density is given by the equation:

$$\left|i_{pc}\right| = \frac{n^2F^2\Gamma_o}{4RT}v \qquad (2.21)$$

where, Γ_o is the surface excess of species O before the start of the sweep.

$$\Gamma_o = \left|\frac{Q}{nF}\right| \qquad (2.22)$$

For adsorption reactions, equation (2.21) shows that the peak current is proportional to the sweep rate, v, not its square root.

2.3.2 Anodic polarisation curves

Slow linear sweep positive going voltammograms, or anodic polarisation curves (APC) provide an indication of the corrosion properties of metals and alloys. The curves are obtained at slow potential sweep rates of 0.1 – 2.0 mV/s and the current density is usually recorded on a logarithmic scale. The different potential regions i.e. the passive and non-passive regions, may then be determined. Fig. 6 shows a schematic APC, representative of the response observed for many systems.

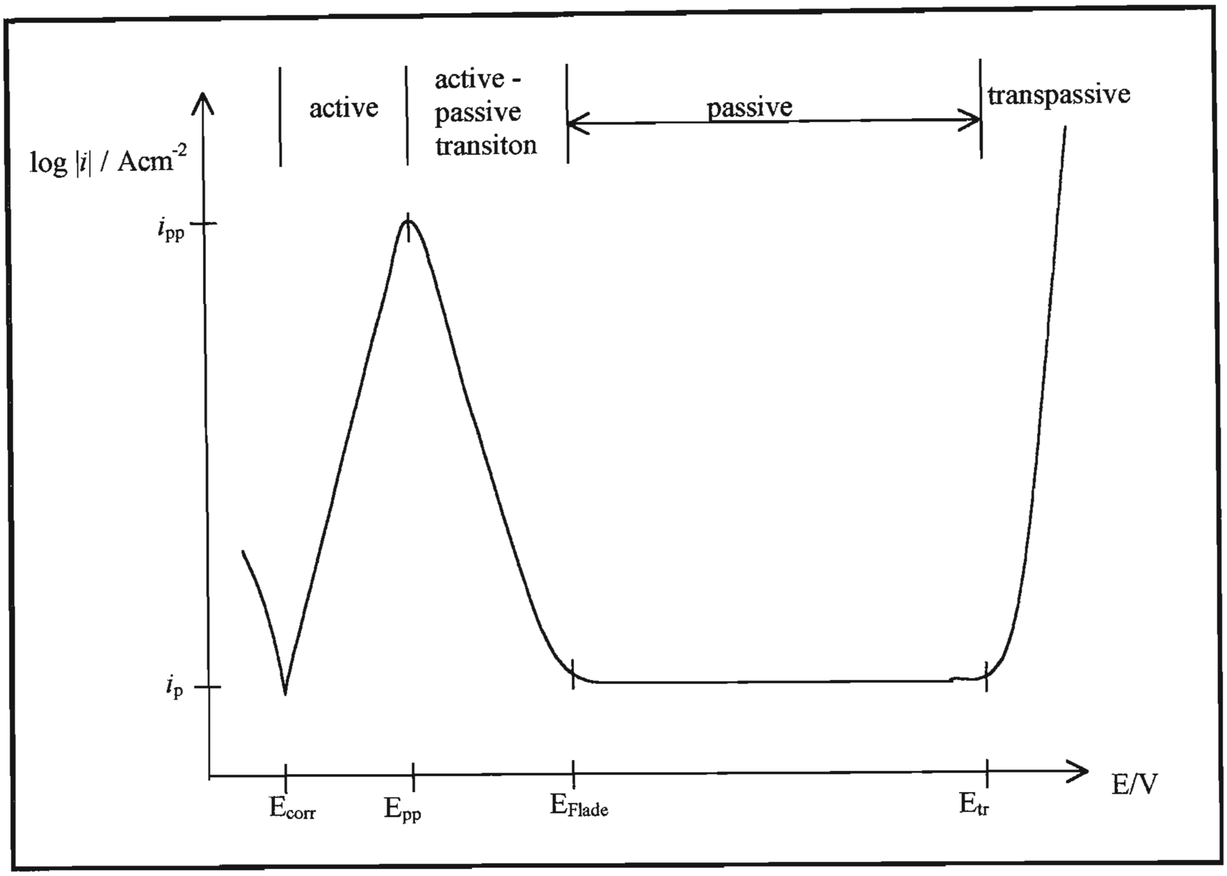

Fig. 6: Schematic anodic polarisation curve for iron in an acid electrolyte.

The potential sweep is usually initiated at the corrosion potential (E_{corr}), at which the rate of oxidation is equal to the rate of reduction. As the potential is increased, the current density increases to a maximum critical current density (i_{pp}) at the primary passivation potential (E_{pp}). The potential region over which the current density increases is known as the active region and is the region in which dissolution of the metal occurs. Beyond E_{pp}, the electrode undergoes an active-passive transition and the current decreases until the passive current density (i_p) is reached. The passive region extends from the Flade potential (E_{Flade}), at which the passive current is first attained, to the transpassive potential (E_{tr}). Beyond E_{tr}, the passive film begins to breakdown. Certain metals and alloys such as stainless steel, may undergo secondary passivation at higher potentials, where the current may level out or decrease before total passivity breakdown and oxygen evolution occurs. In this work the corrosion resistance of an alloy in a given solution will be called "better" the more extensive the passive region and the lower the critical current density. Depending on the chemical stability of the system, the passivating layer may or may not be removed when the potential sweep direction is reversed. Non-passivating materials produce a current response which increases monotonically with increasing potential [12].

2.4 ELECTROCATALYSIS AND THE HER

2.4.1 Hydrogen evolution and the "hydrogen economy"

The hydrogen evolution reaction (HER) may proceed by an electrocatalytic mechanism at a cathode material. The reaction has been extensively investigated for a wide range of different electrolytes and electrode materials and has been central to the development of modern concepts in electrochemistry. Tafel's work on hydrogen evolution at mercury cathodes led to the experimental establishment of the Tafel equation and electrode kinetics (section 2.2.2) [6]. The HER forms a prototype electrodic reaction involving charge transfer, a number of reaction steps, adsorbed intermediates, ionic reactants in acidic solution or neutral reactants in basic solution and a gaseous product. The reaction was initially believed to proceed by a simple reaction mechanism, however it has been found to be a substantially more complex reaction than initially thought and is still a subject of research.

The rate of hydrogen evolution is strongly dependent on the electrode material. Wide variations in Tafel slopes (b) and exchange current densities (i_o) are obtained according to the cathode material used. For mercury and other soft metals such as Pb or Tl, values of i_o range between $1x10^{-12}$ and $1x10^{-14}$ A.cm^{-2} (in 1M acid solution). These metals form good cathode materials when hydrogen evolution is an unwanted competing reaction. Noble metals such as Pt, Pd and Ir produce i_o values ranging between $1x10^{-2}$ and $1x10^{-4}$ A.cm^{-2}, making these metals suitable as reversible standard hydrogen electrodes (SHE). Metals such as Fe, Cu, Ag and Au produce intermediate i_o values ranging between $1x10^{-6}$ to $1x10^{-8}$ A.cm^{-2} [7]. The exact i_o value is determined by the electrolyte composition.

The HER is of technological importance, since in some cases hydrogen production is desirable (e.g. as the cathode reaction in water electrolysis, in diaphragm and membrane cells for the manufacture of Cl_2 or in hydrogen-oxygen fuel cells) while for other reactions it is essential to suppress hydrogen evolution (e.g. as a competing reaction in metal winning, electroplating processes and cathodic syntheses and to prevent the hydrogen embrittlement of metals).

Hydrogen has attracted considerable attention as a possible fuel for the future. The development of efficient and cost effective electrodes for hydrogen generation from water electrolysis and for hydrogen oxidation for power generation from fuel cells is important in developing the hydrogen economy. The Hydrogen Economy involves the development of a synthetic fuel system that can supplement or ultimately replace conventional fossil-fuels (which supply about 85% of the energy consumed by thermal combustion of carbon-based fuels including coal, oil and natural gases) [7]. The demand for an alternative fuel source will increase as the shortage in fossil-fuels increases. It is hoped that with abundant nuclear power, water could be decomposed to provide hydrogen as a portable fuel.

The production of usable energy by the combustion of fuels is an extremely inefficient process. Modern electric power plants are able to harness only about 35-40% of the energy theoretically available from fossil-fuels. The gasoline or diesel engine has an efficiency of only about 25-30% and the remaining energy is lost to the surroundings as heat. Alternative non-fossil energy sources include nuclear and solar energy amongst those used to generate electric power. The problem associated with electric power is that it cannot be stored or economically transmitted over long distances.

The simplest synthetic chemical fuel with which to generate is hydrogen. The standard method of preparation is by electrolysis of water at moderate temperatures and electric power could be used to generate hydrogen, providing an alternative energy source to an all-electric economy. It could provide an economical means of delivering and storing nuclear or solar energy. Hydrogen transport is efficient on an energy-to-weight basis and it can be transported over long distances in underground pipes and stored under pressure or as a cryogenic liquid until required for use. Hydrogen can be burned as a heating fuel, used in internal combustion engines or as the fuel in fuel cells to generate electrical energy. On the negative side, hydrogen has a low ignition energy and is potentially hazardous. The implementation of hydrogen as a fuel for wide scale use would be expensive due to the need to develop new engineering technology. Hydrogen production by electrolysis is not yet an economically viable fuel production process.

The cost of electrolytic hydrogen production is directly related to the overpotential necessary to drive the reaction at a given current density. In general, the overpotentials required are too high to generate hydrogen at a competitive cost and this has slowed the development and commercial utilization of hydrogen as a fuel. Improvements in electrode design are required. A decrease in overpotential is obtained by using electrode materials with a high intrinsic activity for hydrogen evolution such as Pt, Ni, Rh, Au or Ni-based alloys, however these materials tend to be expensive. Alternatively, greater current densities can be obtained by increasing the effective surface area of the electrode without increasing the electrode size. Porous electrodes, such as Raney-type Ni catalysts, have a large surface area at which the reaction can occur.

Fuel cells are devices in which chemical free energy is converted into electrical energy in an electrochemical reaction. The cell electrodes act as catalysts for the oxidation and reduction reactions. Fuel cells can be classified according to the fuel used (hydrogen, hydrazine, hydrocarbons), the temperature (low, medium, high) or the type of electrolyte (aqueous, molten, solid-electrolyte). Examples of fuel cells include the hydrogen/oxygen, hydrazine/air and methanol/air but in all cases the ultimate fuel is the hydrogen released via a range of reactions. Fuel cells operate under conditions that are more thermodynamically reversible than simple combustion and therefore achieve greater efficiencies (~75%). The simplest fuel cell (Bacon cell) to construct runs on hydrogen and oxygen gas which is fed into a cell containing hot concentrated KOH (~28%) under pressure in the temperature range of 150-200°C. The reaction involves the oxidation and reduction of hydrogen and oxygen respectively to form water and electricity. Hydrogen and oxygen are separated in the anode and cathode compartments and do not meet so that combustion and high temperatures are not created. The commercial success of fuel cells, e.g. as the source of energy in electric cars, hinges on the development of more efficient, stable and inexpensive electrocatalysts. At present fuel cells have only been regularly used for very specialized purposes (e.g. space flight) in which minimum weight has been of great importance. Hydrogen-Oxygen fuel cells were developed for both the Gemini and Apollo space missions providing the only source of electric power for maintaining communications and drinking water. The cells are also extremely reliable [8].

2.4.2 HER mechanisms

The overall reaction involved in hydrogen evolution is:

$2H_3O^+ + 2e \rightarrow H_2 + 2H_2O$ (in acid solution)

or

$2H_2O + 2e \rightarrow H_2 + 2OH^-$ (in neutral or basic solution) (2.23)

At an electrocatalyst, the reaction proceeds by a multistep reaction pathway, involving chemisorbed hydrogen atoms and may occur by two different mechanisms with different rate determining steps in both acidic and alkaline electrolytes, as described below.

The reaction has been most extensively studied in acid solution in which the generally accepted steps include:

1) discharge of hydrogen ions onto free sites on the electrode to form adsorbed hydrogen atoms,

$M + H_3O^+ + e \rightarrow M\text{-}H_{ads} + H_2O$ (Electrochemical)

where, "ads" refers to adsorption of the reactive intermediate on the electrode surface and

M refers to an adsorption site on the electrode surface (a metal atom or possibly an interstitial site).

2) the formation of molecular hydrogen may occur by either of two mechanisms:
a) by a chemical-desorption step in which two adsorbed hydrogens collide to form a hydrogen molecule.

$M\text{-}H_{ads} + M\text{-}H_{ads} \rightarrow 2M + H_2$ (Chemical)

b) by an electrochemical desorption step or ion-atom recombination in which a second hydrogen ion arrives at the site of an adsorbed hydrogen atom and the two combine to form a hydrogen molecule.

$M\text{-}H_{ads} + H_3O^+ + e \rightarrow H_2 + H_2O + M$ (Electrochemical)

Steps 1) and 2b) are seen as electrochemical steps while step 2a) is chemical, forming a possible ECE mechanism. The overall reaction may proceed by either chemical-desorption or electrochemical desorption in a two-step mechanism in which either step 1) or 2) is rate determining.

In basic solution, a possible reaction sequence could be:

1) $M + H_2O + e \rightarrow M\text{-}H_{ads} + OH^-$

2a) $M\text{-}H_{ads} + M\text{-}H_{ads} \rightarrow 2M + H_2$

2b) $M\text{-}H_{ads} + H_2O + e \rightarrow H_2 + OH^-$

The different reaction mechanisms and rate determining steps (rds) result in different reaction orders and Tafel slopes whose values can be compared with the values obtained experimentally from Tafel plots [2]. The adsorbed H-atom plays a key role in the mechanism and kinetics of hydrogen evolution. Certain mechanistic possibilities for the HER in acidic media are used to predict Tafel slopes. It is assumed that the fractional surface coverage, θ, of active sites by hydrogen atoms can be estimated from Langmuir isotherms. Similar derivations are also possible for the Frumkin or other isotherms. The results obtained are not totally diagnostic because different mechanisms can lead to the same Tafel slope and other mechanisms not considered here may also be possible.

Consider reaction 1) as the rds:

When reaction 1) is rate determining the reaction mechanism cannot be determined because the adsorption of hydrogen is common to both mechanisms. The surface coverage of adsorption sites is low because as the hydrogen adsorbs it is rapidly consumed in reaction 2). The current density for a rate determining reaction 1) is expressed by the equation [2]:

$$i = Fk_1C_{H^+}\exp\left(\frac{-\alpha_1 F}{RT}\eta\right) \tag{2.24}$$

where, k_1 = rate constant for reaction 1) in the forward direction

C_{H+} = concentration of electroactive species

α_1 = cathodic transfer coefficient for reaction 1)

If it is assumed that $\alpha_1 = 0.5$, then the Tafel slope (b) = 118mV.

Reaction 1) is generally accepted as the rate determining step for high overpotential metals such as Hg, Pb or Cd.

Consider reaction 2a) as the rds:

Protons are readily discharged in reaction 1) and a relatively high surface coverage of adsorbed hydrogen atoms will build up on the electrode surface until a steady state value is reached at which the number of atoms arriving is balanced by the sum of the number combining to form molecules. This occurs when i_o is high and reaction 1) is at equilibrium. Hydrogen evolution at low overpotential metals such as Pt and Rh generally proceeds by this 2a) reaction mechanism.

The surface coverage of the adsorption sites is approximated by the equation [2]:

$$\theta = \frac{k_1^{'}}{k_1}C_{H^+}\exp\left(\frac{-F}{RT}\eta\right) \tag{2.25}$$

where, $k_1^{'}$ = rate constant for reaction 1) in the reverse direction.

The current density for a rate determining reaction 2a) is given by the equation [2]:

$$i = 2Fk_{2a}\left(\frac{k_1^{'}}{k_1}\right)^2 (C_{H^+})^2 \exp\left(\frac{-2F}{RT}\eta\right) \tag{2.26}$$

where, k_{2a} = chemical rate constant for reaction 2a) and is potential independent.

From this equation a Tafel slope of 30mV is obtained and the current density varies with the square root of the proton concentration.

Consider reaction 2b) as the rds:

When reaction 2b) is rate determining, both high and low overpotential cases must to be considered.

For low overpotentials: the surface coverage is found in the same manner as used for the reaction 2a) rds and is expressed by equation (2.25). The current density is given by the equation [2]:

$$i = 2Fk_{2b}\left(\frac{k_1'}{k_1}\right)\left(C_{H^+}\right)^2 \exp\left(\frac{-(1+\alpha_{2b})F}{RT}\eta\right) \qquad (2.27)$$

where, k_{2b} = the potential dependent rate constant for reaction 2b)

α_{2b} = cathodic transfer coefficient for reaction 2b).

If it is assumed that α_{2b} = 0.5, then b = 40mV and the current density will depend on the square of the proton concentration.

For high overpotentials: θ is independent of potential and the current density is given by the equation [2]:

$$i = 2Fk_{2b}\left(\frac{k_1'}{k_1}\right)C_{H^+} \exp\left(\frac{-\alpha_{2b}F}{RT}\eta\right) \qquad (2.28)$$

The Tafel slope is calculated to be 120mV.

Hydrogen evolution at intermediate overpotential metals such as Ni or Au often proceeds by a 2b) reaction mechanism.

2.4.3 Volcano plots

The following factors are important for elucidating the role of the electrode material as an electrocatalyst for the HER:

- the stages of hydrogen evolution and ionization
- the strength of the metal-hydrogen bond

- the dependence of surface coverage on the hydrogen overpotential
- the double-layer structure

The metal-hydrogen bond strength is the key factor in determining the coverage of active sites by hydrogen atoms, the reaction mechanism and the electrocatalytic activity of the electrode material. Adsorbed hydrogen atoms change the free energy of the electron transfer step by an amount equal to the free energy of the metal-hydrogen adsorption bond. Hydrogen evolution will occur at a potential that is $-\Delta G^{o}_{ads}$ cathodic of the equilibrium potential. The stronger the M-H bond, the larger the shift in the reversible potential. Balandin [9] developed the "volcano-shaped curve" that predicated that an optimum adsorption energy for the adsorbed reactive intermediates existed at which a maximum reaction rate was obtained. Volcano plots were then developed for the HER consisting of a plot of the M-H_{ads} bond enthalpy against the exchange current density for different electrode materials (Fig. 7).

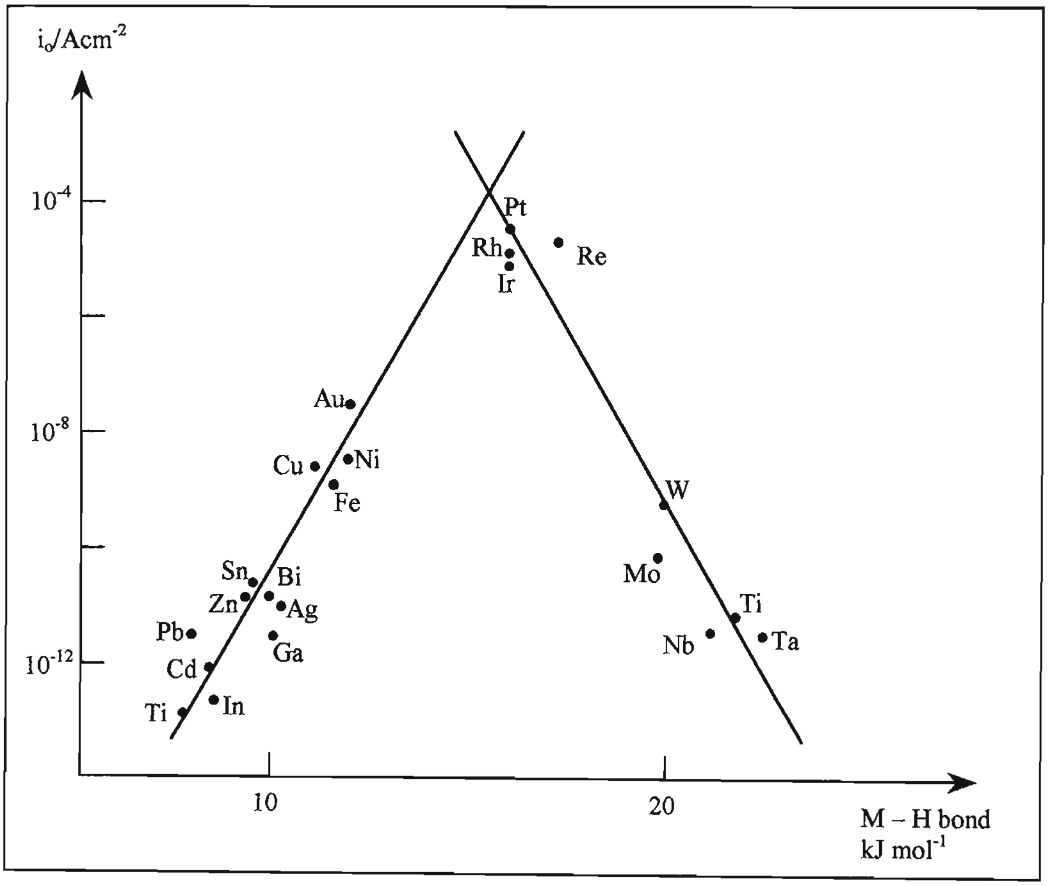

Fig. 7: The variation of exchange current density with the metal-hydrogen bond strength for polycrystalline elements in acid solution [2].

The graph indicates that both low and high M-H_{ads} bond strengths tend to inhibit the HER while materials that form intermediate bond strengths with adsorbed hydrogen atoms form the best electrocatalysts. If the strength of chemisorption of the adsorbate is very weak the electrode materials acts as a poor electrocatalyst. The electrode surface has a low affinity for hydrogen atoms and reaction 1) is then rate determining in both acidic and basic media. If the strength of chemisorption is high the activity for hydrogen evolution also declines because the adsorbate is immobilized and reaction 2a) or 2b) become rate determining. The curve predicts that a maximum electrocatalytic activity is obtained for intermediate bond strengths which leads to a significant but not monolayer coverage of the surface sites by hydrogen. No similar curve has been constructed for amorphous alloys.

CHAPTER 3: LITERATURE REVIEW

3.1 BACKGROUND ON GLASSY ALLOYS

Glassy metals represent a novel class of alloy that combines a metallic electronic structure with a rigid, liquid-like molecular structure that lacks the long-range order and periodic symmetry of crystalline alloys [10]. The amorphous (non-crystalline) structure is confirmed by x-ray, electron and neutron spectroscopy, in which diffraction patterns consisting of diffuse rings are obtained, rather than the sharply defined Bragg rings characteristic of polycrystalline solids.

3.1.1 Preparation of glassy alloys

The first glassy alloy, consisting of gold and silicon atoms ($Au_{81}Si_{19}$), was produced by Pol Duwez in 1959 by "spat quenching" of the alloy melt [11]. This led to the subsequent development of a wide range of metallic glasses with diverse compositions and properties. The technique has now progressed to the extent that certain glassy alloys are produced commercially by numerous laboratories and industrial plants, including Allied Corporation, New Jersey, U.S.A (Metglas alloys) and Vacuumschmelze GmbH, Hanau, Germany (Vitrovac alloys) [12].

Glassy alloys are prepared by rapid solidification of alloy melts in which cooling rates greater than 10^6 K/s prevent the nucleation and growth of metallic crystals. The usual method of fabrication involves melt spinning in an inert gas environment in which a jet of molten alloy is projected through a hole or slit onto a cold, rotating copper wheel. Amorphous layers can also be formed on a cold substrate by laser melting or sputter deposition. In the latter case the glass is quenched from the vapour phase instead of the liquid phase. Amorphous deposits can also be formed by electrolytic deposition from salt solutions, or thin amorphous films and powders can be obtained by solid state reactions involving the constituent elements [13]. A common feature of all these techniques is that the resulting amorphous material has one small dimension, usually less than a few tens of microns. The melt spinning technique produces alloy ribbons of 20-60μm thickness and 1-25mm width. Wider ribbons (up to 75mm) may be produced by planar-flow-casting in which the alloy melt is projected through a wider slit in close proximity to the revolving wheel. Amorphous wires can be produced by projecting the alloy melt into a stream of cold liquid such as brine, flowing concurrently with the alloy [14].

Glassy alloy ribbons contain certain physical and chemical inhomogeneities [15]. Melt spinning results in the formation of gas entrainment furrows on the wheel surface of the ribbon due to the entrapment of inert gas bubbles between the incipient ribbon and the rotating wheel [12]. The wheel surface of the ribbon has a dull appearance, while the upper surface is smooth, undulant and shiny (Fig. 8). It has been reported that the upper surface of certain glassy metals is more heavily oxidised, particularly at the ribbon edges [15]. Variations in chemical composition have also been detected on the two surfaces of glassy alloy ribbons [16,17]. For example, the glassy $Ni_{35}Fe_{30}Cr_{15}P_{14}B_6$ [18] wheel surface was found to be Fe enriched and that the shiny surface Cr enriched. Asami et al. [19] found that the corrosion behaviour, shown by anodic polarisation curves, of the wheel surface and upper surface of the glassy $Zr_{40}Cu_{60}$ alloy were different. A light mechanical polishing removed such differences and identical polarisation curves were obtained, highlighting the importance of surface preparation on the electrochemical results. In this study substantial effort went into the development of a mounting and surface preparation technique for the thin film glassy alloy ribbons so that reproducible electrochemical results could be obtained.

The speed of cooling is a crucial factor in ensuring that an amorphous alloy is produced. Due to the high viscosity of liquid metals, the atomic rearrangements necessary to yield a crystalline structure take time. A metal or alloy melt cooled slowly will solidify into the conventional crystalline state at the freezing temperature (T_m). If cooling rates more rapid than the atomic rearrangement time are applied the melt will solidify into a liquid structure at the glass transition temperature (T_g) in which the atoms occupy irregular positions [20]. Time-temperature-curves measured during the crystallisation process show that crystals can form very rapidly (within a few microseconds) in the case of metals due to their simple atomic structures [14]. However certain alloy compositions have crystallisation times of few milliseconds making cooling rates of 10^6 K/s adequate for glass formation.

The production of glassy alloy ribbons has certain advantages over the conventional metallurgical processing of alloys. The production of glassy alloys consists of only two main steps, melting and casting, and is very rapid (up to 2 kilometers per minute). Preparation of conventional steel strips requires several more steps including forging, rolling, annealing, and drawing, making the production of crystalline alloys more energy intensive and costly. Glassy alloys also display a wider alloying capacity than crystalline alloys so that novel alloy compositions can be produced and tested that have not previously been available in crystalline form [20].

There are a number of limitations associated with the glassy state. Heat must be extracted from the alloy very rapidly so that at least one dimension of the solid is small. This limits the feasible shapes to powders, wires, ribbons and thin shells. Under some conditions, shock compression can be used to produce solid objects from amorphous powders. The glassy state is thermodynamically metastable with respect to bulk crystallisation at room temperature due to kinetic barriers restricting atomic translation. If the alloys are heated to temperatures approaching T_g they devitrify rapidly into their crystalline phase(s), however, even mild heat treatment at temperatures well below T_g can lead to partial relaxation of the amorphous structure, resulting in the formation of small crystallites that are undetectable by X-ray diffraction [12]. The glass transition temperature is generally higher for metal-metal type glasses than for metal-metalloid glasses. This places an upper limit on the temperature range and environment in which glassy alloys can be used and is a major practical limitation. Suzuki et al. [21] reported that even a mild heat treatment (400K) caused the small and relatively mobile metalloid atoms, P and S, to accumulate on the surface of certain Fe-based glasses. Thermal embrittlement resulting from heat treatment has been linked with diffusion and segregation of phosphorus within several P-containing glasses. Heat treatment of glassy $Fe_{40}Ni_{40}P_{14}B_6$ (353 K) resulted in formation of P-clusters (diameter < 6 nm) on the ribbon surface. These clusters were thought to be precursors to the crystalline Fe_3P phase (among other phases) which form at higher temperatures [16,22]. XPS analysis of glassy $Fe_{81}B_{13.5}Si_{3.5}C_2$ showed that heat treatment (450°C) resulted in enrichment of the metalloids B, Si and C on the alloy surface and the growth of Fe particles ($d \approx 25$nm) [23].

3.1.2 Compositions of glassy metals

The compositional range from which glassy alloy can be formed is extremely diverse and generally broader than that available to crystalline alloys. The crystalline equivalents of many glassy alloy compositions are brittle and display poor mechanical properties [12]. Glassy alloys are broadly classified as metal-metalloid and metal-metal systems. Metal-metalloid glasses are the most widely studied group and typically contain around 80 at.% transition metal(s) and 20 at.% metalloid(s) such as Si, B, P or C. A small percentage of passivating element(s) such as Cr, Mo, Ti, Zr may also be added to increase the corrosion resistance of the alloys. Binary metal-metal glasses are subdivided into several categories according to the metal types they contain and include early-late transition metals (Zr-Ni, Ti-Cu), group A-transition metals (Al-Zr, Mg-Cu), group A-group A metals (Al-Ca, Ca-Mg), group A-rare earth metals (Al-Sm), actinide-transition metals (U-Fe) [24].

Metal-metalloid mixtures with a metal to metalloid ratio of 4:1 respectively generally form “deep eutectics” in the phase diagram and display the greatest ease of amorphization [20,25,26]. At a eutectic composition the alloy melting temperature is a minimum and the molten alloy phase solidifies into a mixture of crystalline phases that are characterised by having markedly different structures. Therefore, large structural changes occur during solidification and the atomic movements of the atoms to their correct atomic positions takes time and must often occur in a specific sequence. This has the effect of delaying the crystallisation "start time", obtained from the time-temperature-crystallisation diagrams, thereby decreasing the quench rate required to produce the amorphous alloy [14]. It has not yet been possible to amorphize pure metals by rapid quenching from the molten or vapour phases as the quench rates applied have not been sufficiently rapid to prevent crystallisation.

The search for multicomponent alloys that readily form glassy alloys has been guided by the fact that eutectic compositions display the greatest ease of glass formation. It has recently been found that alloys containing Zr, Cu, Ni, Ti and Be or Al can be amorphized into bulk forms and plates that are several millimetres thick by rapid quenching of the alloy melt in copper moulds [27]. It is possible to cast different shapes with these compositions while maintaining the glassy structure of the alloy. Careful control of the purity of the alloy is necessary, specifically with respect to the oxygen content of Zr. Excess oxygen results in the development of the nucleation seeds that lead to crystal formation and a decreased glass-forming tendency. Electrochemical and electrocatalytic properties of a unique and previously untested glassy alloy, $Zr_{74}Ti_{19}Cu_2Fe_5$, were investigated in this study. This alloy composition was prepared by rapid quenching and was also in ribbon form but had a greater thickness (~ 1mm) than the other commercially produced Fe-Ni and Co-Fe-containing glasses (~0.03mm thickness) that were also tested.

3.1.3 Structure of glassy alloys

Glassy alloys consist of a single-phase structure that lacks the long-range periodic order characteristic of crystalline alloys. They are also homogeneous and lack defect sites such as steps, kinks, dislocations and grain boundaries that are present in crystalline materials. However, glassy alloys are not truly amorphous on the atomic scale and the existence of short-range atomic order over a few atomic distances has been identified by anelastic relaxation studies, magnetic textures and annealing phenomena and Mossbauer spectroscopy [14]. Short-range order does not generally extend beyond the nearest neighbours but the degree of amorphousness (or, the degree of short-range order) is determined by the severity of the quench rate.

Various models have been postulated that describe the atomic arrangement of glassy alloys [20,26,28,29]. Bernal [30] first proposed a model for simple liquids based upon a dense random packing of hard spheres in which atomic packing was predicted to be homogeneous and irregular. Turnbull and Cohen [31] extended the model to predict a structure for glassy alloys. Finney and Wallace [32] proposed that the structure could be considered to consist of an irregular arrangement of distorted tetrahedra and octahedra. Polk [33] suggested that the metalloid atoms occupied the larger holes created by dense random packing of the metal atoms and that interaction between the metal and metalloid atoms produced a short-range order that stabilised the amorphous structure. The models predict an upper and lower limit for the metal-metalloid ratio. Too little metalloid (< 15 at%) does not fill sufficient holes to stabilise the glassy structure and produce the correct atomic volume, while too much forces the excess metalloid atoms to occupy energetically unfavourable sites e.g. if metalloid atoms become nearest neighbours. The various models predicting the structure of glassy metals have been extended and refined, though no single model has been proposed to date that is able to fully describe the atomic structure of glassy metals as can be done for crystalline materials. Generally, either the model is not sufficiently well characterised to be tested adequately or the agreement with experimental observations is not satisfactory. The structures of amorphous alloys are currently being investigated by the School of Physics at this University using the techniques of Mossbauer Spectroscopy and X-ray Diffraction. The influence of structural relaxation by controlled heat treatment on the metastable amorphous structure is also being investigated.

3.1.4 Properties and applications of glassy metals

The wide composition range available to glassy alloys and their unique amorphous structure has been found to produce physical, chemical and mechanical properties that are often very different to those displayed by crystalline materials. Certain glassy alloy compositions possess important properties such as ease of magnetisation, superconductivity, high mechanical strength, ductility, corrosion resistance and enhanced catalytic activity for specific reactions [14]. Combined with low manufacturing costs, these properties make glassy alloys attractive alternatives for many applications. Possible applications include the manufacture of protective coatings in chemical plants or machine parts, alternate materials for surgical implants, razor blades, scalpels, electrodes, reinforcement materials in tyres, concrete or cables [14]. A combination of favourable properties such as high mechanical strength combined with high corrosion resistance are necessary in order for glassy alloys to find commercial application. Therefore, characterisation of the properties of glassy alloys is an interdisciplinary field and requires close collaboration between the disciplines of chemistry, physics, metallurgy and engineering. A large amount of research remains to be conducted in the characterising these unique alloys.

Much of the research activity has focussed on the magnetic properties of glassy alloys. Certain ferromagnetic glasses require a small applied magnetic field to control their magnetisation compared with crystalline ferromagnetic materials that are often relatively difficult to magnetise [34]. Conventionally easily magnetised materials become mechanically soft when annealed whereas glassy alloys remain mechanically hard, helping to minimise wear [14]. They are also easier and cheaper to manufacture than conventional magnets. For example glassy $Fe_{60}Cr_{10}Ni_{10}P_{10}C_7$ possess favourable properties including ease of magnetisation, high mechanical strength and corrosion resistance. The ease of magnetisation make many Fe-based glassy alloy compositions viable energy saving alternatives for carrying flux in magnetic devices such as transformers, motors, generators or amplifiers. In particular, glassy ferromagnets such as $Fe_{82}B_{12}Si_6$ and $Fe_{80}B_{20}$ have been used to replace crystalline iron-silicon alloys in transformer cores [14].

Glassy alloys display unique electrical properties [35]. They are poorer electrical conductors than crystalline alloys due to their amorphous structure, however, the electrical resistance of glassy alloys varies less with temperature due to the absence of lattice vibrations. The electrical resistance of glassy alloys such as $Pd_{80}Si_{20}$ and $Fe_{32}Ni_{36}Cr_{14}P_{12}B_6$ remain constant over a wide temperature range (below T_g) and can be used as resistance standards. Modification of the glassy alloy composition can be used to alter the resistance.

Certain glassy alloy compositions display high mechanical strength and ductility. The first metallic glass produced commercially in 1978 was a glassy Ni-based brazing foil (Ni-Cr-Sn-P). The crystalline Ni-based brazing alloys used prior to this were brittle and were applied in a powdered form, making them less convenient to use than the glassy alloy ribbons. A unique feature of glassy alloys is their biaxial strength in both longitudinal and transverse directions, making them attractive reinforcement materials in compliant materials such as rubber. Fe-Mo-B-containing glasses have been suggested as cheap and strong materials for reinforcing concrete [14,36].

Chromium-containing glassy alloys, such as Cr-Ni-P-B, display a high corrosion resistance that is superior to equivalent crystalline alloys, particularly to pitting corrosion in chloride and sulphate environments [37]. Corrosion resistant glassy alloys could find application as cladding materials in chemical reaction vessels, pipes, valves and fittings, particularly in harsh marine or biomedical environments [12]. Glassy alloys could also be useful as prosthetic materials for implants in the human body. The high catalytic activity of some glassy alloys coupled with high corrosion resistance could lead to their application as electrodes in fuel cells and electrolytic cells [12]. The general corrosion resistance and electrocatalytic activity of five different glassy alloy compositions for the HER were tested in this study in base.

3.2 ELECTROCHEMISTRY OF GLASSY ALLOYS

Most of the research conducted on glassy alloys has focused on their physical properties and a relatively small amount of work has been conducted on their chemical properties. Electrochemical research into the surface properties of glassy alloys is sparse and not comprehensive, making generalisations about the role the metal and metal components and the amorphous structure difficult. Detailed systematic investigations of different glassy alloy compositions over a wide pH range in different electrolytes is still required. There remains a great deal of work to be done in the development of detailed mechanistic studies so that a greater understanding of the complex processes occurring at the glassy alloy surfaces can be obtained. Electrochemical research conducted on glassy alloys can be divided into four main categories including general and localised corrosion, anodic dissolution, passivation and catalysis. Most electrochemical studies have concentrated on the corrosion properties of glassy alloys and in particular those compositions which possess a high corrosion resistance [38,39,40,41,42,43]. The electrochemical properties of glassy metals can vary greatly from those of the base metal components, equivalent crystalline structures and crystalline alloys produced by devitrification of the glassy phase. A far wider range of alloy compositions is accessible to the amorphous state than in the crystalline state, enabling unique alloy compositions to be prepared and characterised.

3.2.1 General Corrosion

Interest in the corrosion properties of glassy alloys was initiated by the work of Naka et al. [44], in 1974, when Fe-based glasses containing Cr and P were reported to exhibit extremely high corrosion resistance in comparison to crystalline stainless steels, particularly in acidic chloride solutions.

Several experimental techniques are used to study the corrosion properties of glassy alloys. Immersion tests and weight loss measurements provide an indication of the rate of general corrosion of the alloy in aqueous media [45]. Electrochemical potentiostatic and potentiodynamic [46] measurements provide an indication of the passivating ability of the alloy and its susceptibility to localised corrosion such as pitting. Scratching techniques have been used to evaluate the repassivation rate of the alloy substrate [40] and the mechanism of corrosion has been investigated by a.c. impedance spectroscopy [47]. In this study the general corrosion resistance of the glassy alloy samples was investigated by obtaining anodic polarisation curves in base.

3.2.1.1 Surface analysis techniques

Since both corrosion and heterogeneous catalysis are surface chemical phenomena, extensive characterisation of the alloy surface for comparison with the electrochemical data is required. Surface compositions and structures can be investigated using the complementary techniques of electron microscopy and high energy ion scattering. Surface analysis techniques frequently used include scanning electron microscopy (SEM), energy dispersive x-ray analysis (EDS), transmission electron microscopy (TEM), scanning tunnelling microscopy (STM), ultraviolet photoelectron spectroscopy (UPS), x-ray photoelectron spectroscopy (XPS), Auger electron spectroscopy (AES), soft x-ray appearance potential spectroscopy (SXAPS), secondary ion mass spectrometry (SIMS), ion scattering spectrometry (ISS), high resolution transmission electron microscopy (STEM), Rutherford backscattering (RBS), infrared spectroscopy (IRS), x-ray diffraction (XRD), electron stimulated desorption (ESD) and Mossbauer spectroscopy. Yoon and Cocke [48,49,88] have reviewed the application of surface analysis techniques to amorphous materials. AES is used for depth profiling, determination of the alloy surface composition and also the nature of bonding among the surface film elements by providing information on oxidation states and the local density of states of the surface atoms. The UPS technique is used to identify the valence electrons involved in bonding and the electronic states present at the alloy surface. The shifts in binding energies or chemical shifts of the photoelectron lines, measured by XPS, are correlated with valence states and chemical interactions providing information on surface chemical composition and oxidation states. No single technique can supply sufficient information to fully characterise alloy surface as there are physical as well as interpretative difficulties inherent in the different techniques. Most of the techniques are *ex-situ* and involve removal of the sample from the electrolyte, disconnection of the applied potential and in many cases require a high vacuum environment with bombardment of the sample surface with an electron or x-ray beam. Such treatments may result in a substantial modification of the structure and composition of the sample surface. Ideally, samples should be analysed *in situ* to avoid surface changes that may arise from removal of the sample from the electrolyte. Post electrolyte changes that may occur are not fully known, but it has been recognised by comparison of *in situ* and *ex situ* analysis results that definite changes in the electrode surface do occur when the electrode is removed form the electrolyte. SEM and EDS surface analysis techniques were used in this study to identify changes in the glassy alloy surface morphology and chemical composition produced from different surface pretreatments.

3.2.1.2 Glassy alloy metallic components

The general corrosion behaviour of glassy metals have been studied most widely in acid media, H_2SO_4 and HCl [39,40,41,42,43] and to a more limited extent in alkaline solutions [50]. Fe, Ni and Co-based metal-metalloid glasses passivate in alkaline solutions, as do the crystalline metals and alloys, and show a general decrease in corrosion resistance with decreasing pH which is not unexpected.

The corrosion resistance of glassy alloys varies greatly according to the metal-metalloid composition and can display either an enhanced or reduced corrosion resistance in comparison to equivalent crystalline materials. Glassy alloys are thermodynamically metastable and contain a high proportion of metalloid(s), such as P, C, B and Si, and on this basis it is predicted that glassy alloys should show a lower corrosion resistance than crystalline alloys. Indeed, glassy Fe, Ni and Co-based alloys containing only a single metal component are found to be chemically unstable and display a lower corrosion resistance than their pure polycrystalline metal components [12]. The anodic polarisation curve of glassy $Fe_{80}P_{13}C_7$ showed no active-passive transition in 1M H_2SO_4 whereas Fe does [51].

The corrosion resistance of Fe, Ni and Co-based glassy alloys is improved by the addition of a second metallic element, in particular a more noble metal (Cu, Pd, Pt, Rh) or a passivating metal (Cr, Ti, Zr, Mo, W, V, Ta, Ru, Al) [12]. Chromium additions are particularly effective in improving the corrosion resistnace of glassy alloys and in general, smaller Cr additions are reported to produce good passivating ability in glassy alloys than in crystalline stainless steels. Both the active and passive current densities of glassy $Fe_{75}Cr_5P_{13}C_7$ were lower than crystalline 18Cr-8Ni stainless steel in 1M H_2SO_4 [52]. Cr-containing glassy alloys (Fe-Cr-P-C and Fe-Ni-Cr-P-C) were found to be corrosion resistant in 6% $FeCl_3$ (40 and 60°C) while crystalline 18Cr-8Ni and 17Cr-14Ni-2.5Mo alloys underwent severe pitting corrosion. No weight losses were detected for glassy alloys containing 8 at% or more Cr after 168 hours exposure in 0.01-1N HCl, 1N NaCl and 6% $FeCl_3$ at 30°C [45]. Diegle [53] reported that Cr additions of only 2% to Fe-Ni-Cr-P-B glasses significantly improved their crevice corrosion resistance, particularly in NaCl. This is often attributed to a synergistic interaction between the metal and metalloid components of the glassy alloy combined with the chemically homogeneous nature of the alloy surface, which produces a uniform passive layer [12,45]. The protective surface film on glassy Cr-containing alloys has been shown to consist primarily of hydrated chromium oxyhydroxides, $CrO_x(OH)_{3-2x}.nH_2O$, where n and x depend on the composition of the underlying alloy and the electrolyte, and are similar to those formed on high-Cr crystalline stainless steels [12]. Additions of Cu, Ti and Zr also improve the corrosion resistance of glassy alloys, however, the addition of significant quantities of these elements has been found to result in problems regarding the melting and production of the amorphous alloy structure [12]. Ti forms a passive layer that, unlike Cr, does not undergo transpassive dissolution to form a soluble species, at any pH. However, a comparison of the anodic polarisation curves of glassy $Ni_{65}Ti_{15}P_{20}$ and $Ni_{65}Cr_{15}P_{20}$ alloys showed that the passive Cr-containing film was more effective than the Ti-containing film in improving the general corrosion resistance of the alloy [12]. The corrosion resistance of the glassy Fe-$Mo_xP_{13}C_7$ and Fe-$W_xP_{13}C_7$ alloys improved with increasing Mo and W content in 1M HCl. Additions of 10 at.% Mo or W resulted in a higher resistance to general and pitting corrosion than equivalent binary crystalline alloys which did not passivate in 1M HCl [54].

The effects of additive elements in improving the corrosion resistance of Fe-Cr-P-C type glasses are greatest when Cr is present together with a third metallic element. The corrosion rates of glassy Fe-$Cr_3P_{13}C_7$-X (X = Ti, Mn, Nb, V, W, Mo, Ni) alloys, in 1M HCl at 30°C, were found to decrease rapidly with the addition of the extra metallic element, X [46]. Additions of Mo, W, Ti and V were particularly effective [55]. The passivating capability of glassy alloys in which both Cr and Mo are present together with P is reported to be very high [55], however, these alloy compositions also shows a tendency towards hydrogen embrittlement and transpassive dissolution [55,56]. The chemical mechanism by which these effects take place has yet to be elucidated. Passivity models, such as the point defect model of Macdonald [57], which has been applied to polycrystalline alloys, may lead to an understanding of the complex processes which are involved in glassy alloys, after suitable modification.

Amorphous alloy compositions displaying an extremely high corrosion resistance that have been extensively studied include FeNiCrPC(orB) [39,45,58,59,60,61,62,63,64,65] and FeCrYX (X and Y = B, C, Si, P) [40,41,66]. Cr additions of 2% to glassy $FeNi_{30}Cr_xP_{15}B_6$ improved the general and localised corrosion resistance of the alloy in 1M NaCl and 1M HCl [53,65], reducing both the active and passive current densities of the APC. The glassy alloys displayed a greater corrosion resistance than the crystalline Fe-Cr and Fe-Ni-Cr alloys of equivalent Cr content. The active region of glassy Fe-xCr-13P-7C in 1M H_2SO_4 and 1N NaCl was almost non-existent for $x > 8$ [45] and followed directly into a passive region, indicating that a highly uniform passive film was formed. No weight change was detected after 168 hour immersion in the electrolyte and no pitting was observed after subsequent SEM analysis of the alloy surface. The corrosion behaviour of several Fe-Ni-P-containing glasses was investigated by anodic polarisation in 2M H_2SO_4, SEM and XPS analysis [67] and compared with the Cr-containing $Fe_{60}Cr_{10}Ni_{10}P_{13}C_7$ glassy alloy. Glassy $Fe_{60}Cr_{10}Ni_{10}P_{13}C_7$ alloys displayed a higher corrosion resistance than the Ni-free composition, $Fe_{70}Cr_{10}P_{13}C_7$, indicating that Ni functioned in promoting passive film formation and stability. XPS analysis of the film revealed that Ni itself was not incorporated into the passive film, however, Ni was believed to interact with Cr in a synergistic manner in promoting passive film formation.

Very limited research has been conducted on the corrosion properties of binary metal-metal glasses without the metalloid. The corrosion behaviour of the glassy $Cu_{50}Ti_{50}$ and $Cu_{50}Zr_{50}$ alloys have been examined in various acidic, neutral and alkaline solutions [50]. The corrosion resistance of glassy $Cu_{50}Zr_{50}$ was higher than the crystalline alloy as well as its polycrystalline components in 1N H_2SO_4, 1N HNO_3 and 1N NaOH and particularly in the aggressive chloride solutions 1N HCl and 3% NaCl [50]. In 1M H_2SO_4 the current densities of glassy $Cu_{50}Zr_{50}$ were two orders of magnitude lower than the equivalent crystalline alloy. It was suggested that the homogeneous structure contributed to a greater corrosion resistance of the glassy alloy due to the formation of a uniform passive film that lacked defect sites such as grain boundaries that could act as preferential sites for corrosion [64]. The corrosion resistance of the glassy $Cu_{50}Ti_{50}$ and $Cu_{30}Ti_{70}$ alloys in 1M HCl were lower than polycrystalline Ti due to, it seems, the detrimental effect of Cu, producing higher current densities in all regions of the anodic polarisation curve. The corrosion resistance of glassy $Cu_{50}Ti_{50}$ was greatly improved by small additions of P (2-5%) [50]. Glassy $Cu_{45}Ti_{50}P_5$ passivated spontaneously in 1N HCl and the passive current density was two orders of magnitude lower than the glassy $Cu_{50}Ti_{50}$ P-free composition. This was interpreted in terms of the rapid formation of a Ti-concentrated passive film owing to the accelerated dissolution of P. Other metal-metal glasses that benefit from metalloid P additions include Ti-(Ni, Cu, or Pd) in 1M HCl and 1M HNO_3 and $Cu_{60}Zr_{40}$ in 0.5M H_2SO_4, 1M HCl and 3.5% NaCl [50].

In this study the general corrosion resistance of Fe, Co, Ni and Zr-based glassy alloys was determined by anodic polarisation in 1M KOH and comparisons were made with literature data, where available. Most of the research interest has focused on Cr-containing glassy alloys because these compositions display an extremely high corrosion resistance. For this reason there is very little information available in the literature pertaining to the corrosion properties of the Cr-free compositions tested in this study. No results on the corrosion resistance of the glassy $Fe_{67}Co_{18}B_{14}Si_1$ and $Co_{66}Fe_4Si_{16}B_{12}Mo_2$ compositions were available in the literature for direct comparisons, however, comparisons were made with the anodic polarisation curves and cyclic voltammograms of the similar glassy alloy compositions, $Fe_{60}Co_{20}Si_{10}B_{10}$ and $Fe_{78}B_{11}Si_{11}$ [68,69,70,71]. Anodic polarisation curves of the glassy $Fe_{40}Ni_{40}P_{14}B_6$ and $Fe_{40}Ni_{40}B_{20}$ alloys are available in the literature [72,73,76] and were compared directly with the curves obtained in this study. All experiments conducted at the glassy $Zr_{74}Ti_{19}Cu_2Fe_5$ alloy were exclusively new.

Sorenson et al. [72] and Chaudhary et al. [73] investigated the electrochemical behaviour of the glassy $Fe_{40}Ni_{40}P_{14}B_6$ and $Fe_{40}Ni_{40}B_{20}$ alloys. The anodic polarisation curve of $Fe_{40}Ni_{40}P_{14}B_6$ showed an active-passive transition with similar current densities obtained in both 1M H_2SO_4 and 1M KOH indicating that pH had little effect on the corrosion properties of the alloy. AES investigation indicated that the active and passive regions corresponded to a Ni-rich film and a relatively more protective Fe-rich film respectively [72,73]. In 3.5% at 303K the $Fe_{40}Ni_{40}B_{20}$ alloy did not passivate while the $Fe_{40}Ni_{40}P_{14}B_6$ composition displayed an active-passive transition. In this electrolyte the replacement of B by 14% P increased the corrosion resistance of the alloy. The addition of 14% Cr to FeNiPB reduced the corrosion rate of the alloy in 1M H_2SO_4, 1M KOH and 3.5% NaCl, causing the alloy to passivate spontaneously with no active region obtained. AES analysis indicated that the passive film of glassy $Fe_{32}Ni_{36}Cr_{14}P_{12}B_6$ was enriched with chromium oxyhydroxide [73]. In the transpassive region the concentration of chromium was further increased indicating that dissolution of the Cr layer, possibly as Cr^{6+}, resulting in an accumulation of Cr at the electrode surface. A similar explanation was provided by Sorenson et al. [72] for the glassy $Fe_{32}Ni_{36}Cr_{14}P_{12}B_6$ alloy in H_2SO_4.

3.2.1.3 Glassy alloy metalloid components

Metal-metalloid glasses contain up to 20 at.% metalloids, such as B, C, Si and P, which are believed to stabilise the amorphous structure by providing an appropriate atomic volume. Metalloid additions play an important role in the corrosion behaviour of amorphous alloys. Interaction between the passivating element and the metalloid component can result in the formation of a highly stable passive film, although the role of the metalloid elements in film formation and stability is not clearly understood and is a subject of debate. Particular attention has been paid to the role of phosphorus in Fe-Cr-based glasses in this regard [45]. The effect of a given metalloid depends on the other constituents of the glassy alloy as well as the solution composition and to date experimental investigations are limited, making generalisations about their role difficult [12]. Clearly more work is needed and a preliminary investigation into the influence of the metalloids, Si, P and B components on corrosion and electrocatalytic properties of the glassy alloys, $Fe_{67}Co_{18}B_{14}Si_1$, $Co_{66}Fe_4Si_{16}B_{12}Mo_2$, $Fe_{40}Ni_{40}B_{20}$ and $Fe_{40}Ni_{40}P_{14}B_6$, was undertaken in this study. Metalloid addition may shift E_{corr} to more positive values due to the low exchange current density of the H^+/H_2 couple of metalloids [64].

Glassy $FeCr_{10}X_{7\text{-}13}Y_{7\text{-}13}$ alloys (X and Y = B, C, Si and P) have been investigated in 0.1M H_2SO_4 with 3% NaCl at 30°C [40,41]. P addition produced the greatest increase in corrosion resistance, particularly in NaCl, and resulted in passive current densities two orders of magnitude lower than for alloy systems containing B as the major metalloid. The corrosion resistance of the Fe-Cr-based glasses was greatest in the order P > C > B > Si. A high corrosion resistance was also reported for glassy $Fe_{32}Ni_{36}Cr_{14}P_{12}B_6$ in 0.5M Na_2SO_4

compositions in which both P and Cr were present due to a synergistic interaction between the Cr and P components [38].

The beneficial effect of P and Cr on the corrosion behaviour of glassy alloys is widely recognised but a detailed understanding of the role of P in the passive film is still unclear. Masumoto and Hashimoto [46] reported that P addition accelerated the initial dissolution rate of the unfilmed surface, resulting in surface Cr-enrichment and the rapid formation of a Cr-enriched passive film into which P itself was not incorporated. In similar studies, XPS analysis indicated that anodic polarisation produced a porous nickel phosphate and iron phosphate pre-passive film which dissolved anodically and was replaced by a chromium-enriched passive film consisting of hydrated chromium oxyhydroxide, $CrO_x(OH)_{3-2x}.nH_2O$, into which very little P was incorporated [38,40]. Only chromium oxy hydroxide was detected in the surface film of glassy $Fe_{70}Cr_{10}P_{13}C_7$ in 1M HCl [74] while Chaudhary et al. [73] found that significant amounts of both P and Cr were present in the passive film of glassy $Fe_{32}Ni_{36}Cr_{14}P_{12}B_6$ in 3.5% NaCl solution (303K). In chronoamperometric experiments repassivation transients of glassy $Fe_{70}Cr_{10}B_{13}X_7$ (X=P, Si, C) alloys in 0.05M H_2SO_4 [75], subsequent to *in situ* abrasion of the electrode surface, showed that the P-containing alloys repassivated more quickly than Si or C-containing alloys. However, the passive films were found to contain 7% PO_4^{3-} as well as chromium oxy hydroxide and were not greatly different in composition to the passive film on glassy $Fe_{70}Cr_{10}B_{13}Si_7$ alloy which contained 8% SiO_4^{4-}. Diegle and Lineman [43] obtained current decay transients for glassy $Fe_{32}Ni_{36}Cr_{14}B_{12}Si_6$ and $Fe_{32}Ni_{36}Cr_{14}P_{12}B_6$ in 0.5M H_2SO_4 and 0.5M H_2SO_4 plus 1M NaCl. In 0.5M H_2SO_4, the alloy containing the Si/B metalloids was found to repassivate faster while in the presence of chloride ions the P/B composition repassiveated faster. Moffat et al. [76] found that P addition decreased the corrosion rate of glassy $Fe_{40}Ni_{40}P_{14}B_6$ in comparison to the P-free $Fe_{40}Ni_{40}B_{20}$ composition. The passive film on $Fe_{32}Ni_{36}Cr_{14}P_{12}B_6$ showed a pronounced variation in composition with depth [59]. The outermost part of the film was P-depleted and a P-enriched layer was present under the main chromium oxy hydroxide layer, in a layer associated with Cr depletion. Thus, while it is clear that there exists a synergism between Cr and P in promoting the passivity of glassy alloys, the mechanism of the interaction is not understood. These discrepancies reported in the literature indicate that even an elementary understanding of the precise chemical role of the metalloid remains to be developed as do detailed mechanistic studies of the chemistry involved.

In contrast, the addition of P to the Cr-free glasses, $Fe_{80}P_{20}$ [47] and NiP [42] in H_2SO_4 and HCl, lowered their passivity in comparison to polycrystalline Fe and Ni. Electrodeposited amorphous $Ni_{80}P_{20}$ and $Fe_{80}P_{20}$ alloys also displayed a poorer corrosion resistance than both polycrystalline Fe and Ni in sulphate solutions at all pH values. $Fe_{80}P_{20}$ displayed an active-passive transition with higher current densities than pure Fe obtained at all potentials while

$Ni_{80}P_{20}$ showed no sign of passivation in sulphate solution at any pH, although pure Ni is typically more passive than Fe. This was attributed to anodic dissolution of phosphorus as P^{+5} in a non-protective nickel phosphate and iron phosphate film that was subject to severe pitting and general corrosion [12,47].

3.2.1.4 Amorphous structure and passive film formation

The passive film that forms at the surface of metals or alloys is a corrosion product in which chemically stable species are concentrated. This requires the accumulation of beneficial metallic and hydroxyl ions at the alloy/solution interface prior to the formation of the passive film, and the dissolution of those alloy components useless to barrier film formation. This passive film enriched with certain elements, with respect to the bulk alloy composition, influences the electrochemistry and corrosion properties of the metal.

The high corrosion resistance of Fe-Cr-P-based glassy metals has been attributed to the rapid formation of a thick and corrosion resistant passive film consisting of chromium oxy hydroxide. The homogeneous and single-phase structure of glassy alloys is believed to facilitate the formation of a uniform passive film in which passivating elements such are Cr, Al, Ti or Zr are concentrated [12,45].

As already mentioned, the addition of a third metallic element such as Ni or Mo to Fe-Cr-containing glasses enhances passive film formation. Glassy Fe-Mo-13P-7C showed a high pitting resistance in 1M HCl, while crystalline $Fe\text{-}Mo_{4\text{-}40}$ alloys were susceptible to pitting corrosion [54]. XPS analysis of the surface film on glassy Fe-Mo-13P-7C indicated that it contained only trace amounts of Mo in the hydrated iron oxy-hydroxide film and was compositionally similar to the passive film formed on polycrystalline Fe and Fe-based alloys of low Cr content. This indicated that the high corrosion resistance of the glassy alloys was determined not only by the composition of the passive film but also by its structure. Asami et al. [77] proposed that Mo in glassy Fe-Cr-Mo-B alloys resulted in the formation of an Fe/Cr oxyhydroxide film into which Mo^{5+} ions were incorporated in HCl. The Mo-containing film acted as a diffusion barrier, preventing further dissolution of the alloy, and assisted the accumulation of the passivating species (Fe and Cr) under film. At higher potentials the Mo^{5+} ions were dissolved transpassively as soluble Mo^{6+} ions and a corrosion resistant hydrated Cr oxyhydroxide film formed. The addition of further Mo to the glassy alloy reduced its corrosion resistance due to the formation of the less stable Mo oxyhydroxide surface film [78].

Detailed investigation into the anodic oxidation of stainless steel alloys and their constituent elements in acidic electrolytes have been conducted in this laboratory [79]. Chronoamperometric experiments indicate that metal dissolution followed by nucleation and growth of anodic surface films occurs at transpassive potentials. A model describing the nucleation and growth of the passive film on stainless steel alloys has been proposed. A minimum of about 12 at.% Cr is required to passivate crystalline Fe-Cr alloys. XPS analysis of a series of crystalline Fe-Cr alloys revealed that the film composition depended on the Cr content of the alloy. The passive film on low-Cr alloys in H_2SO_4 consists mainly of iron oxy-hydroxide $FeO_x(OH)_y.nH_2O$ while for higher chromium concentrations (Cr > 12 at.%) the passive film consists of a highly corrosion resistant hydrated chromium oxy-hydroxide, $CrO_x(OH)_{3-2x}.nH_2O$, layer. In general, the corrosion resistance of alloys depends upon the concentration of trivalent Cr in the surface film, increasing as the Cr content increases. Analysis of the passive films formed on austenitic and ferritic steels in neutral and acidic aqueous solutions showed that they consisted of an inner Cr-rich oxide, CrO_3, and an outer hydroxide layer. A continuous transition from the oxide to the hydroxide region of the film resulted in its characterisation as an oxyhydroxide. Passive film formation is enhanced with increasing pH due to the greater ease of formation of chromic hydroxide $Cr(OH)_3$ or chromic oxide $Cr_2O_3.nH_2O$. The presence of bound oxygen, OH^- and H_2O, in the passive film is now well established and is believed to play a crucial role in the passivating ability of the glassy alloy although there is controversy as to its exact role [80]. OH^- and H_2O may enhance the rate of passive film formation by capturing the dissolving metal ions for incorporation into the passive film. In addition, OH^- and H_2O are reported to form a cross-linked monolithic amorphous passive film via hydrogen bonding that increases the ductility of the film and reduces its susceptibility to mechanical breakdown. Hashimoto et al. [40] reported that surface films on Fe-based glasses containing Cr and P were compositionally similar to the passive films that formed on stainless steels. XPS analysis of the surface film of glassy Fe-10Cr-13P-7C, after immersion in 1M HCl for 168 hours, indicated that it consisted exclusively of hydrated chromium oxy-hydroxide [81], however, the thickness of the hydrated chromium oxy-hydroxide layer was found to be greater than that of high-Cr steels (30%) and the concentration of OH^- and H_2O higher [80].

Rapid film formation is believed to contribute to the high passivity of Cr-containing glasses [53]. Being thermodynamically metastable, glassy alloys are highly reactive and scratching electrode studies have been used to confirm this [40,54]. Scratching electrode experiments in 1M H_2SO_4 revealed that the current density on glassy $Fe_{70}Cr_{13}P_7C_{10}$ was initially higher than crystalline 18Cr-8Ni steel but that the repair rate of the surface film on the amorphous alloy was higher [40] and the final passive current density lower than that of the crystalline alloy. The high reactivity of glassy alloys facilitates the enrichment to trivalent Cr at the alloy/solution interface and hence increases the rate of passive film formation. Metalloid P is believed to enhance the rate of initial dissolution of glassy alloys so that passivating species can concentrate at the alloy surface, enabling a corrosion resistant layer to form more rapidly [47,53].

3.2.1.5 Influence of heat treatment

There is evidence that glassy alloys display a superior corrosion resistance to crystalline alloys. This is generally attributed to the homogeneous structure of glassy alloys and their lack of defect sites that may act as preferential sites for corrosion. The influence of the amorphous structure on the corrosion properties of glassy alloys has been investigated by heat treatment which causes the alloy to devitrify into its more stable crystalline phase(s). In certain cases the structural changes induced by heat treatment have been found to reduce the corrosion resistance of the alloys by several orders of magnitude [15,63,82]. Anodic polarisation curves of the heat treated glassy $Fe_{32}Ni_{36}Cr_{14}P_{12}B_6$ alloy in H_2SO_4 (380°C for 1000 minutes) showed that greater current densities were obtained in all regions of the curve in comparison to the as-quenched alloy, indicating that corrosion resistance was reduced by heat treatment. A similar reduction in corrosion resistance was observed for glassy $Fe_{70}Cr_{10}P_{13}C_7$ and $Fe_{80}B_{20}$ in 1M H_2SO_4 after heat treatement at 350°C [40]. The anodic current density of the crystallised $Fe_{70}Cr_{10}P_{13}C_7$ alloy was two orders of magnitude higher than the glassy alloy in the passive region. After immersion in 1M H_2SO_4 for 15 minutes SEM analysis indicated that severe general corrosion of the crystallised alloy surface had occurred. The dissolution current of glassy $Co_{75}B_{25}$ was found to increase when heat-treated at temperatures greater than 600K. This temperature corresponded to the formation of a crystalline Co_3B phase that became more abundant as the temperature and treatment time was increased, reflecting the increased activity of the emerging crystalline surface. Metal-metalloid glasses commonly consist of eutectic compositions that crystallise into two or more different phases when heat-treated [39]. The different crystalline phases may increase the defect nature of the alloy by introducing phase boundaries or other surface defects. The surface defects provide preferential sites for localised attack and hence decrease the corrosion resistance of the alloy in comparison to its amorphous structure.

Glassy $Cu_{60}Zr_{40}$ [83] devitrifies into a single-phase crystalline structure when heat treated, avoiding the problem of phase boundary formation with crystallisation. No significant differences in the dissolution rates of the glassy and heat-induced crystalline structure were detected for this composition, in contrast to metal-metalloid glasses, suggesting that the chemically homogeneous structure is responsible for the high corrosion resistance of the glassy alloy. Further research is, however, required to determine whether the amorphous structure or the homogeneous chemical composition is responsible for the corrosion resistant properties. This study investigates the corrosion behaviour of the Zr-based glassy alloy, $Zr_{74}Ti_{19}Cu_2Fe_5$, in 1M KOH.

3.2.2 Localised corrosion studies

Little work on localised forms of corrosion such as pitting, crevicing, hydrogen embrittlement or stress cracking corrosion have been reported and the mechanisms of attack and breakdown are poorly understood. Localised corrosion may occur due to breakdown of the passive film or by active dissolution of regions of the alloy.

Certain physical and chemical inhomogeneities resulting from the rapid solidification process have been found to influence the electrochemical results [12]. Preferential pitting was observed along the edges and the bottom of gas entrainment furrows on the wheel surface of the "as-quenched" glassy $Fe_{40}Ni_{40}P_{14}B_6$ ribbon in $FeCl_3$ [84]. Differences were observed in the shapes of the anodic polarisation curves on the wheel (Fe-rich) and shiny upper (Cr-rich) surfaces of the "as-quenched" ribbon [12,61,63] of glassy $Fe_{30}Ni_{35}Cr_{15}P_{14}B_6$ in 3% NaCl [63]. A light mechanical polishing removed these differences. Kovacs et al. [85] found that processing parameters had a perceptible influence on the corrosion behaviour of glassy $Fe_{83.4}B_{16.6}$. Anodic polarisation curves indicated that the current density of the glassy alloy increased slightly as the quench rate of the molten alloy was decreased until a threshold level connected with crystallisation was reached. Low quench rates were found to permit some topological relaxation without causing crystallisation. Clearly further investigation is needed in order to understand the mechanisms involved.

Pitting corrosion of metals and stainless steels in aqueous environments involves a localised attack in which most of the metal surface does not corrode but is stable and passive. In most of the published work on pitting of metals Cl^- has been used as the aggressive anion. Pitting corrosion is unpredictable as regards times of initiation and place of attack and the mechanism of processes leading to pit formation and nucleation is still a subject of controversy. At inhomogeneities and defect sites within a metal and/or passive film it is reasonable to expect that preferential adsorption of halides at these sites will occur. This is in accord with the observations that pits form at grain boundaries, nonmetallic inclusions and at some dislocations. Even in the absence of aggressive ions accelerated dissolution of a metal has been observed at certain inhomogeneities such as nonmetallic inclusions [86]. Little research has been conducted into the pitting corrosion resistance of glassy alloys and a great deal of work remains to be done in this area. The glassy $Fe_{67}Co_{18}B_{14}Si_1$ alloy tested in this study has been reported to display superior magnetic properties, however, it is susceptible to pitting corrosion in the presence of chloride ions [87]. In general Fe, Ni and Co-based glassy alloys containing Cr display a high resistance to pitting corrosion [45]. No pitting was observed in glassy Ni-Co-Cr or Fe-Ni-Cr-P-C alloys during polarisation in 1M H_2SO_4 plus 1M NaCl [45]. The influence of Cr in preventing pitting is dependent upon the chemical composition of the glassy alloy. Naka et al. [45] showed that 8% Cr in glassy Fe-xCr-P-C and Fe-Ni-xCr-P-C alloys in 1M NaCl prevented pitting on anodic polarisation and that Cr dissolved as a Cr^{6+} species in the transpassive region. Alloys with Cr < 8% were found to contain many tiny pits when viewed under an SEM after anodic polarisation in the transpassive potential region. Diegle and Slater [82] found that glassy Fe-xCr-13B-7C and Fe-xCr-13B-7Si that contained 2-5% Cr in 3% NaCl pitted close to open circuit potential, while alloys that contained 8% Cr only pitted in the transpassive region. Glassy Ni-xCr-15P-5B alloys required a Cr content of 7% to prevent pitting in 10% $FeCl_3$ at 30°C. In the case of ferritic stainless steels, a Cr content of at least 28% was required to avoid pitting corrosion up to the transpassive potential [86].

Archer and McKim [84] investigated the stress corrosion behaviour of glassy $Fe_{40}Ni_{40}B_{20}$ in aqueous acid media (ferric chloride, polythionic acid and hydrochloric acid). Corrosion behaviour was found to be potential dependent with hydrogen embrittlement occurring at cathodic potentials in the HER, general corrosion at E_{corr} and stress corrosion cracking and/or crevice attack at anodic potentials.

3.3 ELECTROCATALYSIS OF GLASSY ALLOYS

A catalyst enhances a reaction rate by providing an alternative lower activation energy pathway and is not consumed in the overall reaction sequence. Electrocatalysis is the study of heterogeneous multi-step reactions in which reactants, intermediates or products chemisorb with the electrode surface. Electrocatalytic activity is greatly influenced by the nature of the electrode-adsorbate interaction. Electrocatalytic reactions are generally more specific than catalytic reactions due to constraints imposed by the electrolyte and the electrode material. The distinction between electrocatalysis and chemical catalysis is that the former displays a potential dependent reaction rate while the latter does not. Potential dependence offers a far greater degree of freedom for the reaction rate as a change in electrode potential over a narrow range can change the reaction rate by up to 10 orders of magnitude. In the case of a chemical reaction, variation in the reaction rate is achieved by changing the temperature within the operational temperature range of the catalyst (generally <500°C) which offers a far lower degree of freedom.

A practical electrocatalyst needs to satisfy of number of different criteria for a specific reaction. The electrode material must produce a high current density (i.e. a high reaction rate) close to equilibrium potential (i.e. at a low overpotential). A high activity results in a high exchange current density (i_o) and a low Tafel slope (b). Exchange current densities provide an indication of the reaction rate at equilibrium potential and are used to compare the reaction rates of different electrode materials. Comparisons between amorphous and crystalline materials are often based on exchange current densities. Tafel slopes provide an indication of the reaction mechanism at an electrode surface and the nature of the active sites. Similar Tafel slopes for different electrode materials indicate that reaction mechanisms are possibly the same and that the active sites are similar in nature. For a material to form a good electrocatalyst a number of conditions must be satisfied:

- The catalyst must display a high activity and selectivity for the required reaction, i.e. it must inhibit competing reactions as well as catalyzing the desired reaction. For example, in the chlor-alkali cell the anode must catalyze Cl_2 production and have a high overpotential for O_2 production so as to prevent oxygen contamination.
- The catalyst surface must show good stability, e.g. corrosion resistance when the cell is working and when it is at open circuit potential, and be resistant to poisoning.
- The catalyst should have a large surface area at which the reaction can occur. Surface area can often be deliberately enhanced by chemical or electrochemical treatments of the electrode.
- Often electrocatalyst materials with a high inherent activity for reactions are expensive (e.g. Pt, Au). A low loading of these materials by dispersion on a cheaper matrix is important for cost reduction, e.g. Pt coated on C or Ti coated on C or Ni. Preparation of such electrodes can be achieved by techniques such as electroplating or vacuum sputtering.

Electrocatalysts are playing an increasingly important role in electrochemical technology as they may provide alternative and lower activation energy pathways for certain reactions. They are important in industrial reforming processes, hydrogenation, ammonia synthesis chlorine evolution and polymerisaton reactions [88]. Gas evolution reactions can occur by an electrocatalytic mechanism and hydrogen evolution, oxygen evolution and reduction and methane oxidation are important reactions in the development of fuel cells. Many multi-step electroorganic reactions proceed by electrocatalytic mechanisms such as the hydrogenation of unsaturated organic molecules. The development of DSA electrodes (dimensionally stable anodes) composed of RuO_2/Ti composites for chlorine manufacture was a major advance in electrocatalysis. On the other hand, the failure to develop efficient electrocatalysts for the oxidation of primary fuels (e.g. hydrocarbons, alcohols and carbon monoxide) and the oxidation and reduction of oxygen and hydrogen has slowed the development of fuel cells and is an active area of research interest.

A large amount of research is required for the further development of electrocatalysts and it is not fully known why certain reactions are specific to particular materials. Electrocatalysts generally consist of transition metals in the form of alloys, oxides or complexes. Catalyst design appears to require the placement of transition metal atoms or ions in a matrix which optimises electronic configuration and geometry and enables unfilled d-orbitals with the correct energy to form bonds of appropriate strength. Gennero de Chialvo and Chialvo [89] found that the electrocatalytic activity of crystalline $Ni_{1-x}Mo_x$ (x = 0 to 25) for the HER, in 2M NaOH at 30°C, increased with increasing Mo concentration. The results were interpreted on the basis of the synergistic nature of the electronic effects between the Mo and Ni components. Referring to the volcano curve for crystalline metals, the metals of early and late transition metals occur on opposite sides of the curve and display low activities for hydrogen evolution in comparison to noble metals such as Pt and Pd (Fig. 7). In contrast, alloys composed of early-late transition metals display a high activity for hydrogen evolution, possibly due to maximum utilisation of all d-orbitals and electrons. Investigation into the electronic and geometric structure of the active sites on crystalline alloys is complicated by the heterogeneous nature of the alloy surfaces and could be simplified at homogeneous amorphous alloy surfaces [88]. A greater understanding of the activity, selectivity and stability of electrocatalysts will be obtained from investigation into the electronic and geometric structure of the active sites and their density on the alloy surface, and part of this study involves the first steps in such a process.

Conventional metal-based heterogeneous catalysts are complex. The catalyst centres consist of clusters of metal atoms that are either pure or supported on a carrier. Electronic promotors may be added, such as alkali metals to fine-tune electronic parameters, or textural promotors to stabilise the high dispersion of the metal particles. An iron oxide catalyst for the industrial synthesis of ammonia is a typical example of such a complex catalyst [90]. The ability to control electronic properties is limited by the feasible compositions of crystalline alloys and by the addition of promotors. The catalyst surfaces are easily poisoned and the preparation of reproducible surfaces is difficult. Amorphous materials posses a number of unique properties which make them of interest as catalysts and electrocatalysts [88]. Their homogeneous atomic arrangement and the presence of a high concentration of coordinatively unsaturated sites may, in many cases, lead to a high catalytic activity. The high mechanical strength and excellent corrosion resistance of certain amorphous alloys also make them of interest as durable catalysts relative to crystalline materials. Their preparation is rapid and reproducible as well as being relatively cheap. The active sites are self-supported by the bulk alloy substrate and no promotors are required to improve catalyst efficiency. Amorphous materials could be useful in small-scale applications where reproducible performance is important [90], however, only a limited amount of work has been conducted on the catalytic activity of amorphous metals. Amorphous alloys display a diverse alloying capacity and the composition ratios can be gradually changed in contrast to crystalline alloys that generally have fixed compositions.

Properties which make amorphous materials of interest as catalysts and electrocatalysts include:

- A different surface topology in comparison to crystalline counterparts that may influence catalyst activity, selectivity and lifetime. Amorphous surfaces are believed to be rough at the atomic level and support a high number of protuberances with a wide range of coordination numbers that are analogous to kink and ledge sites on crystalline alloys [10].
- Amorphous materials are homogeneous and single phase, simplifying the characterisation of the active sites on the alloy surface. Investigation of crystalline surfaces is complicated by multiple phases of the alloy and structural defects which have been found to display different catalytic properties to the bulk alloy that are difficult to isolate and characterise.
- Amorphous materials are isotropic and can be used to contrast orientation effects known to be important in catalysis. Studies of amorphous surfaces can be used to compliment the studies of single crystals [91], where catalytic behaviour is known to vary depending on the particular crystal face exposed. It is well known that the catalytic activity of the single crystal faces of Pt for H_2 adsorption are quite different and the activity of polycrystalline Pt is a weighed average of these [91,92].

The amorphous state is present in several commercially important heterogeneous catalysts and is believed to influence the catalytic activity of these materials. Amorphous metal oxides have been widely used as cracking catalysts. Examples include alumina, silica, titania, silica-alumina, silica-magnesia, silica-zirconia-titania and hopcalite (amorphous $CaMn_2O_4$). The active phase in supported catalysts such as WO_3 on γ-Al_2O_3 and MoO_3 on γ-Al_2O_3 is amorphous in character [88]. Certain amorphous materials show potential as catalysts in cracking, oxidation and hydrogenation reactions. There is interest in the suitability of glassy alloys as electrodes in fuel cells and for water electrolysis [12] especially for those compositions with high mechanical, chemical and electrochemical stability. Certain glassy alloys, of the general composition Fe-Ni-Co-P-Si-B, display a superior catalytic activity for hydrogen evolution to equivalent crystalline alloys of similar composition and could potentially be used as cathode materials in water electrolysis [68,69,93,96]. They are particularly effective, in alkaline media, in lowering the hydrogen evolution overvoltage.

A point of interest concerning the literature published on glassy alloys and their characterisation is that little work has been conducted after 1992, indicating that research interests have been diverted elsewhere. The most intensive research investigations into the electrochemical and electrocatalytic properties of glassy alloys were conducted during the 1980's.

3.3.1 Hydrogen evolution

Electrode activity is determined by the intrinsic activity of the alloy components and by the surface nature of the electrode. In general, the electrocatalytic activity of glassy alloys for the HER can be substantially improved by some form of chemical or electrochemical surface pretreatment in comparison to the as-quenched state [88,94]. The influence of chemical (acid) and electrochemical (anodic oxidation) pretreatment on the electrocatalytic activity of five different glassy alloy compositions was investigated in this study.

The electrocatalytic activity of glassy alloys as cathodes for the HER have been tested under both mild conditions, i.e. 1M KOH [95], 1M NaOH [96] and 0.5-1M H_2SO_4 [97,98] at 25-30°C and under the more severe conditions used in the industrial electrolysers, such as 30 wt% KOH at 70°C [99].

3.3.1.1 Glassy alloy metallic components

The HER has been most extensively researched on metal-metalloid Fe and Ni-based glassy alloys. The activity of glassy alloys for the HER has been compared to crystalline alloys of similar composition and to the pure metal components. A number of glassy alloys display a higher activity and selectivity to crystalline materials of similar composition [10,90,100], however, it is not known whether this results from the unique surface structure of glassy alloys or their ability to support a higher concentration of active sites. Schloegl [101] believes that glassy and crystalline structures have been insufficiently characterised to make conclusions. In fact there is not even general agreement that the amorphous state is really the origin of enhanced catalytic activity [71]. Clearly a greater knowledge of the electronic and geometric structures of the catalytically active sites and their concentration on both amorphous and crystalline surfaces is required [88].

Certain amorphous alloys possess a high inherent electrocatalytic activity for the HER that is superior to equivalent crystalline alloys. Kreysa and Hakansson [68] reported that the glassy $Co_{58}Ni_{10}Fe_5Si_{11}B_{16}$, $Co_{66}Fe_4Si_{16}B_{12}Mo_2$ and $Fe_{60}Co_{20}Si_{10}B_{10}$ compositions displayed a higher activity for hydrogen evolution in 1M KOH than polycrystalline Fe, Co or glassy $Fe_{78}Si_{11}B_{11}$. The glassy $Fe_{60}Co_{20}Si_{10}B_{10}$ alloy produced lower overvoltages for hydrogen evolution in the as-quenched than polycrystalline Pt and Ni [68]. Similar results were obtained by Alemu and Juttner [69] who found that glassy $Fe_{78}Si_{11}B_{11}$ and $Fe_{60}Co_{20}Si_{10}B_{10}$ were better electrocatalysts for hydrogen evolution in 1M KOH than polycrystalline Fe. At constant current density, the overpotentials of $Fe_{78}Si_{11}B_{11}$ and $Fe_{60}Co_{20}Si_{10}B_{10}$ were 80 and 110mV lower than polycrystalline Fe respectively, indicating that the glassy Fe-based alloys possessed a substantially higher activity for hydrogen evolution than pure polycrystalline Fe. The exchange current density of glassy $Fe_{60}Co_{20}Si_{10}B_{10}$ was 4-5 times greater than polycrystalline Fe, while similar Tafel slopes indicated that the mechanism of hydrogen evolution was possibly the same on both the amorphous and crystalline surfaces. Diegle [102] reported that the structure and composition of the active sites on the amorphous and crystalline materials were similar. Differences in activity were attributed to the homogeneous nature of the amorphous surface which, for certain alloy compositions, was able to support a greater surface density of more evenly distributed active sites than the crystalline material, resulting in the greater activity of the amorphous material. Investigation into the mechanism by which these effects takes place is required.

Endoh et al. [103] reported that glassy Ni-Co-based alloys displayed low overpotentials for hydrogen evolution and good stability in KOH, hence forming potentially good electrocatalyst materials. This was attributed to a synergistic interaction between the Ni and Co components of the alloy. However, in a separate study by Kirk et al. [104], $Ni_{72}Co_8$-metalloid glasses were found to display a poorer activity for hydrogen evolution than polycrystalline Ni on the basis of the geometric electrode area, although good corrosion resistance was also reported for the glassy alloys in an alkaline electrolyte. Clearly a great deal of further investigation is required for clarification of the results.

Glassy metal-metal alloys have been reported to show a definite relationship between electrocatalytic activity and alloy composition. Naka et al. [98] studied the HER on glassy Fe-Zr, Ni-Zr, Co-Zr, Ni-Nb, Co-Nb, and Cu-Ti alloys of different composition ratio in 1N H_2SO_4 at 25°C and compared the results with the polycrystalline metal components. The glassy Fe-Zr, Ni-Zr and Co-Zr alloys produced Tafel slopes and hydrogen overpotentials similar to ideal mixtures of the pure metals, whereas the kinetic parameters of the Nb and Cu-based glasses, Ni-Nb, Co-Nb and Cu-Ti, did not. Increasing the Zr content improved the corrosion resistance of the alloys but simultaneously raised the overpotential for hydrogen evolution, since Zr is comparatively inactive for hydrogen evolution. The hydrogen overpotentials of glassy Ni-Nb and Co-Nb were greater than their crystalline components while the Cu-Ti alloy displayed lower overpotentials, indicating that a synergistic interaction between the Cu and Ti components occurred in acid solution. A transfer of electrons from Cu to Ti in the Cu-Ti alloy was believed to create a d-electron deficiency in the Cu atoms, resulting in increased electrocatalytic activity. The synergistic interaction was destroyed in alkaline solution, however the chemical reasons for the loss of activity at higher pH remain unknown.

Kinetic parameters for the HER were obtained for glassy Co-based alloys in 0.5M Na_2SO_4 (pH 1.8) at 25°C and compared with equivalent crystalline alloys and the pure metal components. Cathodic Tafel slopes of 120 mV/dec were reported for both glassy and crystalline $Co_{75}B_{25}$ in acid sulphate solution but i_o values several orders of magnitude higher were obtained for the amorphous structure [105]. Similar Tafel slopes indicate that the mechanism of hydrogen evolution was the same on both the crystalline and amorphous alloys and that structure had little influence on the reaction. The amorphous surface supported a greater number of active sites which resulted in the greater i_o value.

Turn and Latanision [83] investigated hydrogen evolution on glassy and crystalline $Cu_{60}Zr_{40}$ alloys. Exchange current densities were similar while Tafel slopes differed with values of 100 and 120 mV/dec obtained for the amorphous and crystalline structures respectively. It was proposed that the glassy state supported metal clusters with unique structures and catalytic properties.

The electrocatalytic activity of the five glassy alloys tested in this study for the HER was determined in base. The kinetic parameters, i_o and b, were calculated from Tafel plots and the values obtained for the glassy $Fe_{67}Co_{18}B_{14}Si_1$ and $Co_{66}Fe_4Si_{16}B_{12}Mo_2$ alloys compared with the values obtained by Kreysa and Hakansson [68] and Alemu and Juttner [69] for the similar glassy compositions, $Fe_{78}Si_{11}B_{11}$ and $Fe_{60}Co_{20}Si_{10}B_{10}$. Direct comparisons were made with the results obtained by Kreysa and Hakansson and Crousier et al. [71] for hydrogen evolution at the $Fe_{40}Ni_{40}P_{14}B_6$ and $Fe_{40}Ni_{40}B_{20}$ alloys. For comparison, the kinetic values of the glassy alloys were also compared with the polycrystalline metal components, Fe, Co, Pt and Ni.

3.3.1.2 Glassy alloy metalloid components

Glassy alloys contain significant concentrations of metalloid elements such as to be capable of exerting a strong influence on the kinetics of cathodic reactions [64]. Exchange current densities for hydrogen evolution on metalloids are several orders of magnitude lower than those of most transition metals so that it can be concluded that the metal-metalloid interaction leads to a significantly different electrochemistry from that of the metalloid element alone [94]. The exchange current density for the hydrogen reaction is orders of magnitude higher on noble metal (typically 10^{-3} $A.cm^{-2}$) or transition metal surfaces (10^{-6} $A.cm^{-2}$) than on metalloid surfaces (typically 10^{-13} $A.cm^{-2}$). Metalloid elements are believed to "poison" the recombination reaction for adsorbed hydrogen on the electrode surface, inhibiting the formation of molecular hydrogen [64]. This also increases the population of adsorbed hydrogen on the electrode and increases the probability that atomic hydrogen will be absorbed by the metal. It is predicted that metal-metalloid glasses should show a greater tendency to absorb hydrogen due to the metalloid component of the alloy. Certain glassy alloy compositions have been reported to absorb significant amounts of hydrogen and also to show susceptibility to hydrogen embrittlement [56,64,106], not unlike many crystalline materials.

The influence of the metalloid on the electrocatalytic activity of glassy alloys is poorly understood and in a number of cases apparently conflicting results are reported. In a comparison between polycrystalline Ni and glassy $Ni_{78}Si_8B_{14}$ it was found that at both 30 and 90°C the Ni electrode exhibited lower overvoltages for hydrogen evolution than the alloy, indicating that the B and Si components of the glassy alloy inhibited the HER. This was in agreement with Linker and Plieth [107] who reported hydrogen evolution was inhibited by boron-containing glasses ($Ni_{78}Si_8B_{14}$). In contrast to this finding a synergistic interaction was reported for the glassy $Fe_{40}Ni_{40}B_{20}$ alloy which displayed a higher electrocatalytic activity for hydrogen evolution in 1M KOH than either of the polycrystalline Ni or Fe components. For this alloy composition B addition improved the activity of the material for the HER [68]. The Tafel slope for hydrogen evolution on glassy $Ni_{67}B_{33}$ in 1M H_2SO_4 was found to be sensitive to structure. The slope changed from 97 mV/dec to 71 mV/dec after heat treatment of the alloy to its more stable crystalline phase at 770 K for 5 hours. Therefore, the alloy showed improved electrocatalytic activity in its crystalline state.

Gonzalez et al. [108] reported that glassy $Ni_{70}P_{30}$ had a low activity for hydrogen evolution, however, P could be leached from the Ni-P electrode by electrochemical oxidation to produce a porous surface with an improved activity. Glassy $Pd_{20}Ni_{60}P_{20}$ was reported to have a lower activity for hydrogen evolution in its as-quenched state than the polycrystalline Pd and Ni components in 1M KOH [68]. The influence of the P in glassy $Fe_{40}Ni_{40}P_{14}B_6$ on its corrosion resistance and electrocatalytic activity for hydrogen evolution in 1M KOH was investigated in this study for the alloy in its as-polished state and after chemical and electrochemical pretreatment and compared with the P-free glassy $Fe_{40}Ni_{40}B_{20}$ composition.

Conflicting reports have been published concerning the influence of metalloid P on the activity of amorphous alloys. Lian et al. [109] reported that the P-containing glassy alloy, $Ni_{50}Co_{25}P_{15}B_{10}$, displayed a higher activity for hydrogen evolution than the Si-containing $Ni_{50}Co_{25}Si_{15}B_{10}$ alloy in 1M KOH at 25°C. Similar findings were obtained by Podesta et al. [110] who reported that Ni-Co-P alloys (prepared by electroless deposition) containing 25.9 at.% P displayed a high activity for hydrogen evolution in 1M KOH after heating in air than alloys containing 12.5 at.% P. The high activity of the electrodes was attributed to their ability to adsorb and absorb large amounts of hydrogen, which altered the electron structure of the base metals [111]. However, Paseka [112] found that amorphous Ni-P electrodes (prepared electrodeposition) of lower P content prepared at low temperatures and low current densities displayed a higher activity for hydrogen evolution in 1M NaOH at 25°C. These studies show that the influence of the metalloid P on the electrocatalytic response of glassy alloys has not been resolved and much remains to be clarified.

3.3.1.3 Hydrogen absorption and embrittlement

The rate of hydrogen evolution often determines the extent of corrosion of a metal and therefore the stability of the metal surface. Hydrogen is well known to permeate into the crystalline metal/alloy structure and accumulate, particularly at defect sites within the lattice. Absorbed hydrogen affects the inner strength of the material and may result in hydrogen embrittlement or stress corrosion cracking. Hydrogen embrittlement occurs when a metal loses its strength and ductility and becomes brittle. It no longer yields when strained but fractures. Stress corrosion cracking occurs at the metal surface when high corrosion rates combined with an external stress cause a crack to form and advance into the material. The stress may be mechanically applied or result from internal pressure in the material due to hydrogen absorption. The propogation of the crack is sustained by dissolution of the metal [7].

Hydrogen embrittlement of glassy alloys is well documented [56,64], occurring on the entry of 50-150ppm of diffusible hydrogen into the material. Hydrogen absorption and hydrogen embrittlement has been reported for glassy Ni-Mo [113] and several glassy Ni-based alloys [114] during cathodic polarisation in the hydrogen evolution region in alkaline solutions. The glassy $Fe_{40}Ni_{40}P_{14}B_6$ alloy, tested in this study, has been reported to absorb hydrogen [64]. Cathodic polarisation at a constant current density caused hydrogen embrittlement to occur in glassy $Fe_{32}Ni_{36}Cr_{14}P_{12}B_6$ in 1N H_2SO_4 [115], as determined using the constant extension rate technique, and significantly decreased the fracture stress of the hydrogenized specimen. This was believed to result from the high affinity of the alloys for hydrogen combined with their extreme thinness. Tong and Macur [115] found that glassy $Fe_{32}Ni_{36}Cr_{14}P_{12}B_6$ recovered its fracture stress on ageing in air at room temperature. The reversibility of embrittlement suggests that hydrogen atoms are relatively mobile, even at ambient temperatures, and diffuse within the alloy. Hydrogen absorption is believed to modify the electronic and structural properties of the substrate over the near-surface region of the alloy and influence the electrocatalytic properties of the alloy. The formation of a three-dimensional hydride in the near-surface region of Ni-containing glasses during hydrogen evolution has been reported to improve the electrocatalytic activity of the alloy [114].

A decrease in the electrocatalytic activity of the glassy $Ni_{65}Nb_{35}$, $Ni_{65}Al_{10}B_{25}$ and $Ni_{70}Mo_{20}Si_5B_5$ alloys [99] and the glassy $Zr_{67}Ni_{33}$ [93] alloy for the HER in 30 wt% KOH at $70^{\circ}C$ was observed with an increasing time of cathodic polarisation. Initially the alloys displayed a higher activity for hydrogen evolution than polycrystalline Ni, however, significant deactivation occurred during cathodic polarisation in the hydrogen evolution region until a steady current was attained with a lower activity than Ni. This was attributed to hydrogen absorption into the amorphous matrix and hydride formation, the latter phenomenon contributing to hydrogen embrittlement. Zr hydride formation at the alloy surface was believed to inhibit the HER by removing the active sites at which hydrogen discharge could occur. A similar result was reported to occur at Ni-Ti surfaces when cathodically polarised in alkali [116].

Corrosion resistant glassy compositions generally display a high resistance towards hydrogen embrittlement [45] while single metal iron-metalloid glasses are susceptible to hydrogen embrittlement. For example, Nagumo and Takahashi [106] found that glassy $Fe_{80}P_{13}C_7$ and $Fe_{78}B_{13}Si_9$ alloys displayed poor corrosion resistance and were susceptible to hydrogen embrittlement in 1M HCl. Kawashima et al. [56] suggested that the susceptibility of a glassy metal to hydrogen embrittlement strongly depends on the Cr content and metalloid additives of the alloy. Metalloids are believed to poison the hydrogen recombination reaction and thus promote the absorption and permeation of atomic hydrogen into the alloy structure [12]. The effects of metalloid additions on the susceptibility for glassy Fe-5Cr-12Mo-X and Fe-10Cr-X (X = 18C, 20B and 13P-7C) to hydrogen embrittlement were tested in 1M HCl, 0.5M NaCl and 0.5M H_2SO_4. The time to failure in a bending test was shortest for the C-containing alloys. The P-C-containing combination was less susceptible to hydrogen embrittlement due to its higher corrosion resistance and rapid passivating rate, especially when Cr was present in the alloy. No differences in the stress-elongation behaviour were observed for glassy $Fe_{32}Ni_{36}Cr_{14}P_{16}B_2$ and $Fe_{40}Ni_{40}P_{14}B_6$, indicating that Cr-addition had little influence on the susceptibility of these alloy compositions to hydrogen embrittlement [115]. Here too it is clear that much remains to be done before a comprehensive understanding of the behaviour of glassy alloys is achieved.

No widely accepted mechanism has been developed to adequately describe the nature of hydrogen embrittlement nor is the location of embrittling hydrogen in crystalline or glassy alloys well established. The interstitial sites within the glassy structure may form traps for hydrogen accumulation. The atomic hydrogen may then combine to form molecular hydrogen with a pressure build up resulting in ultimate failure of the material [115]. Gilman [117] found that fractured portions of the glassy $Fe_{40}Ni_{40}P_{14}B_6$ and $Fe_{40}Ni_{40}B_{20}$ alloys contained numerous micron-sized voids when viewed under an electron microscope. The voids were believed to form during rapid quenching of the alloy melt. It was suggested that the voids acted as traps for atomic hydrogen as it diffused into the alloy in much the same way that hydrogen is trapped in the interstices in crystalline metals. When atomic hydrogen combined to form molecular hydrogen, pressure buildup within the voids contributed to hydrogen embrittlement and reduced the fracture stress of the alloy. The fact that hydrogen is absorbed and permeates through the material does not, however, necessarily establish that the material will be embrittled. Metalloids have also been found to play a role in the intergranular embrittlement of crystalline metals and alloys. Metalloid segregation has been detected at grain boundaries that have undergone hydrogen embrittlement and it is believed that the metalloid stimulates the absorption of atomic hydrogen into the solid.

3.3.1.4 Surface activation

In many cases, glassy alloys display a poor electrocatalytic activity in the as-quenched state but the activity can be substantially improved by surface treatment that may be chemical, thermal or electrochemical [109]. Treatment modifies the alloy surface area, surface structure and chemical composition and changes may be monitored using surface analysis techniques [70]. The manner in which surface treatment activates the electrode surface has not yet been clarified. Treatment often produces surface products and increases the active surface area of the electrode in comparison with the smooth as-quenched surface, producing a roughened or porous surface [96,97]. In some cases the improved activity is attributed to the removal of an inhibiting oxide film that is formed during the manufacture of the alloy [95]. Alloys that contain leachable elements, such as Zr, Al, Zn, Sn, S or P, are particularly effective in forming high surface area electrodes after suitable surface pretreatment. The influence of both chemical and electrochemical surface pretreatment on the electrocatalytic activity of the five glassy alloy compositions tested for the HER and on their corrosion resistance was investigated in this study.

When Zr-based amorphous alloys are leached with dilute HF, selective dissolution of Zr occurs, giving rise to an increase in the concentration of the alloying metallic species as well as an increase in surface porosity. Immersion of the alloys in 1M HF (10 seconds) resulted in a substantial improvement in the electrocatalytic activity of the alloys for the HER and i_o increased by several orders of magnitude in comparison to their as-quenched state. The as-quenched glassy $Zr_{67}Ni_{33}$ alloy displayed a poorer activity for hydrogen evolution than polycrystalline Ni, in 30% KOH at 70°C, but a greater activity was obtained after HF treatment [93,99]. Similar results were obtained in independent studies for hydrogen evolution on HF-treated glassy Ni-Zr and Ni-Ti alloys in 1M NaOH at 30°C [96], glassy $Zr_{65}Pd_{35}$ in 0.5M H_2SO_4 at 30°C [97] and the glassy $Zr_{64}Ni_{36}$ and $Zr_{48}Ni_{27}Al_{25}$ alloys in 1M KOH at 25°C [95]. XPS analysis indicated that acid treatment produced a porous and electrocatalytically active Ni-rich electrode surface, possibly by removing thin passivating Ti oxide and Zr oxide films from the as-quenched alloy surface and by selective dissolution of the Zr and Ti components [95,96,97,118]. Acid treatment of crystalline alloys did not alter the activity of the alloys for hydrogen evolution because removal of the oxide layer and formation of the porous Ni layer was not effectively achieved. The electrocatalytic activity of Zr-based glassy alloys for the HER was found to decrease with increasing time of cathodic polarisation in the hydrogen evolution region, possibly due to hydrogen absorption and the formation of zirconium hydride in the alloy surface layers that inhibited the reaction. The hydride layer was assumed to remove active sites from the alloy surface at which hydrogen discharge could occur [93,99]. A similar effect has been reported to occur at glassy Ni-Ti surfaces [116]. Zr-based glassy alloys are reported to be susceptible to hydrogen absorption and embrittlement after acid treatment and exposure to extended hydrogen evolution [90,93]. The electrocatalytic activities of the glassy $Zr_{67}Ni_{33}$ [93], $Zr_{64}Ni_{36}$ and $Zr_{48}Ni_{27}Al_{25}$ [95] alloys for the HER in their as-quenched state and after HF treatment were compared with the results obtained for the $Zr_{74}Ti_{19}Cu_2Fe_5$ alloy in this study.

In similar findings, XPS analysis indicated that a porous Cu-enriched surface layer was produced by HF-treatment of the glassy $Ti_{50}Cu_{50}$, $Ti_{65}Cu_{35}$ and $Zr_{67}Cu_{33}$ alloys due to preferential leaching of the Ti and Zr components [119]. The acid treated surfaces displayed higher activities for hydrogen evolution than the as-polished surfaces in 1M NaOH at 30°C. The i_o values of the as-quenched alloys were lower than polycrystalline Cu while higher values were obtained after acid treatment of the glassy alloys. In a 0.5M H_2SO_4 electrolyte surface activation was destroyed and electrocatalytic activity of the acid treated glassy alloy surface was very low. It was suggested that the porous copper layer on the amorphous surface was oxidized in air and it was this oxide layer that produced the high catalytic activity in NaOH rather than Cu itself. Dissolution of this oxide layer occurred in an acid medium destroying the catalytic activity of the alloy. Cadet et al. [47] reported that a synergistic interaction between the Cu and Ti components in the as-quenched glassy $Cu_{70}Ti_{30}$ alloy produced a higher activity for hydrogen evolution in 1M KOH than either polycrystalline Cu or Ti. In a contrary finding, Kreysa and Hakansson [68] reported that the alloy was a poorer catalyst for hydrogen evolution in the as-quenched state than either polycrystalline Cu or Ti. Clearly these contradictions require independent resolution.

Glassy Pd-Zr alloys have been investigated as electrode materials for hydrogen evolution in acid solutions (0.5M H_2SO_4) [97,120]. Glassy $Pd_{35}Zr_{65}$ was found to have a low activity for hydrogen evolution in the as-quenched state and the i_o value obtained was 10^2 times lower than polycrystalline Pd foil. The activity of the glassy alloy was substantially improved by acid pretreatment with 1M HF and the exchange current density increased to a value one order of magnitude greater than the Pd foil. SEM and XPS analysis indicated that the improved activity resulted from a porous Pd-enriched surface layer that was created by selective dissolution of the Zr component from the alloy.

Lian et al. [109] compared the electrocatalytic activity of glassy $Co_{50}Ni_{25}Si_{15}B_{10}$, $Ni_{50}Co_{25}Si_{15}B_{10}$ and $Ni_{50}Co_{25}P_{15}B_{10}$ alloys for the HER with the crystalline equivalent alloys Co_2Ni and Ni_2Co in 1M KOH at 25°C. The glassy alloys exhibited lower activities for hydrogen evolution than the crystalline alloys in the as-polished state but after chemical treatment with HF and HF/HNO_3 mixtures the amorphous alloys displayed a greater activity than their crystalline equivalents. Chemical treatment selectively leached the Si, B and P metalloid elements from the electrode to produce a Co and Ni enriched porous surface. It was proposed that the surface metalloid elements inhibited the recombination of adsorbed hydrogen to form molecular hydrogen. After acid treatment the electrode surface was enriched with Ni and Co hydrogen adsorption sites that displayed a higher activity for the HER. In comparison, acid treatment did not increase the activity of the crystalline alloys, indeed chemical pretreatment was reported to deactivate or "poison" the crystalline surface. These findings were supported by Kumagai et al. [120] who reported that crystalline alloys could not be activated by HF treatment. Hout et al. [99] also used HF and $HF\text{-}HNO_3$ mixtures to activate some amorphous Ni-based alloys and obtained similar results. The influence of pretreatment with pure HF and HF/HNO_3 mixtures on the activity of the glassy alloys for the HER was investigated in this study.

The influence of *in situ* electrochemical treatment on the activity of glassy alloys for the HER has also been investigated. Electrochemical treatments including anodic oxidation at constant current density [70,71] and potential cycling [121,122] have been employed. Enhanced electrocataytic activity was generally attributed to the formation of a catalytically active oxide layer supported on the base amorphous substrate. The influence of *in situ* anodic oxidation at different constant current densities on the electrocatalytic activity of the five glassy alloys tested in this work was investigated and compared with the results reported for similar glassy alloy compositions in the literature [70,71].

Huot et al. [70] and Crousier et al. [71] investigated the influence of *in situ* anodic oxidation on the electrocatalytic activity of Fe-Co and Fe-Ni-based glassy alloys in base. Glassy $Fe_{60}Co_{20}Si_{10}B_{10}$ was found to display a high electrocatalytic activity for the HER in 30 wt% KOH at 70°C after *in situ* anodic oxidation at constant current density [70] in comparison to the as-quenched state. In the as-quenched state a Tafel slope of 138mV and an exchange current density of 0.4 $mA.cm^{-2}$ was obtained. After an anodic treatment of 1$mA.cm^{-2}$ the Tafel slope was 77mV and the exchange current density 2.3 $mA.cm^{-2}$ indicating that a substantial improvement in the electrode activity had occurred. SEM, EDS, AES and x-ray diffraction studies revealed that the treatment resulted in the formation of a thick porous film of Fe_3O_4 that was proposed to form by a dissolution-precipitation mechanism involving Fe(II) species. Subsequent cathodic polarisation prior to the onset of hydrogen evolution caused the oxide layer to be reduced to form a fine layer of Fe particles supported on the amorphous matrix. SEM micrographs taken after different periods of cathodic polarisation showed that the Fe particles grew and coalesced during the first thousand seconds of hydrogen evolution producing a highly porous surface structure. Similar results were obtained by Crousier et al. [71] for *in situ* anodic oxidation of the glassy $Fe_{60}Co_{20}Si_{10}B_{10}$, $Fe_{40}Ni_{40}P_{14}B_6$, $Fe_{67}Ni_{20}Cr_5Zr_3B_5$ and $Fe_{60}Ni_{10}Cr_{10}Zr_8B_{12}$ compositions in 1M KOH at 25°C. The glassy $Fe_{40}Ni_{40}P_{14}B_6$, $Fe_{67}Ni_{20}Cr_5Zr_3B_5$ and $Fe_{60}Ni_{10}Cr_{10}Zr_8B_{12}$ alloys displayed a low activity for hydrogen evolution in the as-quenched state, however a substantial improvement in activity was obtained after *in situ* anodic oxidation. Catalytic activity was found to increase with increasing oxidation current and a porous surface layer was also observed on the alloy surface by SEM. The glassy $Fe_{60}Co_{20}Si_{10}B_{10}$ composition displayed the highest activity for hydrogen evolution of the alloys tested after anodic treatment with a charging current of 0.5 $mAcm^{-2}$ for 2 minutes. Further increases in the oxidation current led to a reduction in the activity of the alloy [70,71], possibly due to the formation of a new oxide or a restructuring of the passive layer, leading to the formation of a compact layer rather than a porous layer. The influence of identical anodic treatments on the electrocatalytic activity of the similar glassy $Fe_{67}Co_{18}B_{14}Si_1$ composition was tested in this study and the results compared with the $Fe_{60}Co_{20}Si_{10}B_{10}$ alloy.

3.3.2 Other catalytic reactions

Only a small number of catalytically important reactions have been examined using glassy alloy catalysts and an extremely wide range of alloy compositions and different reactions remain to be investigated. Table 2 lists reactions that have been investigated on glassy alloy surfaces. There is evidence that certain glassy metal compositions form stable and efficient catalysts for the reactions.

Table 2: Catalytic reactions investigated using glassy metal catalysts.

Reaction	Glassy Metal Compositions	References
Chlorine evolution	Pd-M-P (M = Rh, Pt, Ir, Ru, Ti) Ni-Pt-M (M = Ti, Zr, Nb, Ta)	[123,124] [125]
Oxygen evolution	Ni-Co-based alloys Ni-Ta-X, Ni-Nb-X (X = Ru, Rh, Ir, Pt)	[68,69,109,121,122, 136] [120]
Methanol oxidation	Cu-Ti, Cu-Zr Fe-P, Fe-B, Ni-P, Ni-B, Co-B, Pd-Si, Pd-P, Pd-M-P (M=Ni, Sn, Ru, Rh, Ir, Pt)	[126] [127]
Formaldehyde oxidation	Cu-Ti, Cu-Zr Cu-Pd-Zr	[128] [129]
Alkene reduction	Ni-P, Ni-B	[130,131]
CO hydrogenation	Fe-Ni-M (M = B, P) Fe-Zr, Ni-Zr, Pd-Zr, Pd-Zr-Si Pd-Si, Pd-Ge Fe-P, Fe-B, Ni-P, Ni-B	[100,118,132] [133,134] [10] [135]

Methanol oxidation

A great deal of interest has focussed on the development of small-scale transportable fuel cells which employ organic fuels which are subsequently converted to release hydrogen. Methanol is an important organic fuel that is cheaper to produce and easier to store and handle than hydrogen and much effort has gone into the development of electrodes with a high electrocatalytic activity for methanol oxidation.

Pd-based metallic glasses containing Fe, Co, Ni, Zr, Pt or Ti have been investigated as potential electrodes for methanol oxidation in 1M KOH [127]. In all cases the as-quenched alloys had a low activity for alkaline methanol oxidation. Surface activation of the Pd-based glassy alloys improved the activity to a level comparable with that of platinized Pt. Surface treatment involved electrodeposition of Zn metal onto the alloy surface followed by heat treatment (473-573K for 30 minutes) and then dissolution of the Zn in 6M KOH [127]. The heat treatment resulted in uniform diffusion of the Zn into the bulk alloy and the subsequent dissolution produced a porous alloy surface. Heat-treatment of the Zn coated glassy alloy resulted in uniform diffusion of the Zn into the alloy, which was attributed to the homogeneous nature of the alloy surface. A similar treatment of Zn coated crystalline alloys resulted in preferential diffusion of the Zn along grain boundaries and produced no improvement in catalyst activity. The activity of Pd-based metallic glasses was improved by alloying with P, Ni, Pt, Rh and Ru. A high corrosion resistance and catalytic activity was obtained using the glassy $Pd_{76}Ni_5P_{19}$ alloy after heat treatment at 573K. The glassy $Cu_{35}Ti_{65}$ and $Cu_{38}Zr_{62}$ alloys displayed a similar increase in activity for methanol oxidation after surface activation with HF in comparison with their as-polished state [126].

Chlorine evolution

Amorphous Pd-based alloys have a high activity for chlorine production in comparison with the conventional dimensionally stable anodes (DSA) of RuO_2/Ti composite structures. A problem associated with DSA is that RuO_2 has a relatively low overpotential for oxygen evolution and so oxygen is present as an impurity in the chlorine produced. Pd metal has very low electrocatalytic activity for oxygen evolution but it is not usable in the chlor-alkali electrolysis cell due to its high corrosion rate. Improvement in the chemical stability of Pd was obtained by alloying Pd-P with different concentrations of Ru, Rh, Ir, Pt and Ti in the amorphous state. These anodes have been tested by potentiostatic polarization in 4M NaCl and 1M Na_2SO_4 under typical industrial conditions (buffered to pH 4 with 4M HCl at 353K) [123,124]. The Pd-Ir-P containing alloys showed a greater activity for chlorine evolution and a higher overpotential for oxygen evolution than conventional DSA electrodes and a good stability (i.e. high corrosion resistance) in hot concentrated NaCl. The most favourable compositions included $Pd_{46}Ir_{30}Ti_5P_{19}$, $Pd_{41}Ir_{30}Ru_{10}P_{19}$ and $Pd_{50}Ir_{30}Rh_1P_{19}$. Hara et al. [124] stated that glassy $Pd_{30}Ir_{30}Ti_5P_{19}$ and $Pd_{41}Ir_{30}Ru_{10}P_{19}$ alloys exhibited a higher electrocatalytic activity for chlorine evolution than an activated Ti anode in 4M NaCl.

Amorphous Ni-based alloys containing a few at% Ti, Zr, Nb, Ta or Pt-group elements were also found to display a high electrocatalytic activity for chlorine evolution [125]. The surfaces were prepared by laser and electron beam processing of the alloy onto a corrosion-resistant bulk metal such as niobium. The current required to produce 1kg of chlorine by the amorphous electrodes was one-third of the current used for the most active Pt-Ir/Ti electrodes.

CO hydrogenation

Fe and Ni-based glassy alloys containing P and B metalloid stabilizers were investigated as catalysts for the Fischer-Tropsch hydrogenation of CO [100,118]. The glassy alloys displayed a superior activity and selectivity for CO hydrogenation than their crystalline counterparts [100]. Glassy $Fe_{20}Ni_{60}P_{20}$ [118] displayed a higher activity for CO production than its crystalline analogue. The glassy and crystalline alloys had the same activation energy and it was suggested that the glassy alloy was able to support a greater number of active sites that were similar in nature to those on the crystalline alloy. Similar results were obtained by

Yokoyama et al. [100] who studied CO hydrogenation on glassy FeP, FeB, NiP and FeNiP alloys. Studies of the metal-metal glassy $Fe_{90}Zr_{10}$, $Ni_{63}Zr_{37}$ and $Pd_{35}Zr_{65}$ alloys as possible Fischer-Tropsch catalysts have also been conducted [134]. The activity of glassy Pd-Zr alloys was found to be orders of magnitude higher than that of conventional Raney-Ni and supported Pd catalysts. The catalytically active species was reported to be an oxide of Pd and Zr. Addition of Si reduced the activity as the active oxide species was not formed.

Brower et al. [10] investigated hydrogenation and isomerisation reactions on the Pd-based glasses $Pd_{80}Si_{20}$ and $Pd_{77}Ge_{23}$ and compared their activity with crystalline counterparts and with pure Pd. In all cases higher activities and better selectivities were obtained for the alloys in the glassy phase. In conjunction with UPS and AES surface analysis it was found that the glassy alloys had a different surface topography to the crystalline alloy. As before (p. 21) the glassy alloys were believed to support a high number of protuberances analogous to the kink and ledge sites on crystalline surfaces with a wide range of available coordination numbers. Therefore, the nature of the active sites was different on the glassy and crystalline surfaces. A further increase in the activity of the glassy alloys was obtained by partial crystallization of the amorphous structure by heat treatment. Kisfaludi et al. [135] also found that the activity of glassy $Fe_{82.2}B_{17.8}$ for CO hydrogenation was increased after heat treatment at 560K. Partial crystallisation of the alloy surface was detected using conversion electron Mossbauer spectroscopy.

Oxygen evolution

Investigation of oxygen evolution at alloy surfaces is more complex than hydrogen evolution due to oxide formation or the possibility of competitive dissolution on certain metals prior to oxygen evolution. Amorphous Ni-Co-based alloys display a high electrocatalytic activity for oxygen evolution in alkaline solution [68,69,109,121,122,136]. The effect of potential cycling and steady state polarisation on the electrocatalytic activity of glassy Ni-Co alloys was determined in 1M KOH [121,122]. Potential cycling between the oxygen and hydrogen evolution limits of the electrolyte produced a greater increase in the activity of the glassy Ni-Co alloys for the OER than anodic polarisation at a constant current density. Surface analysis indicated that potential cycling produced a hydrous oxide film with a micro-porous structure filled with solvent and hydroxyl ions. Glassy $Co_{50}Ni_{25}Si_{15}B_{10}$ and $Fe_{60}Co_{20}Si_{10}B_{10}$ alloys were identified as good electrocatalysts for the OER in the as-quenched state and after *in situ* anodic oxidation at a constant current density [68]. Anodic oxidation produced mixed oxide/hydroxide layers similar to a spinel oxide consisting mainly of $NiCo_2O_4$ and $CoFe_2O_4$ oxides for the $Co_{50}Ni_{25}Si_{15}B_{10}$ and $Fe_{60}Co_{20}Si_{10}B_{10}$ alloys respectively.

Kumagai et al. [120] investigated oxygen evolution at glassy Ni-Ta-X and Ni-Nb-X electrodes (X = Ru, Rh, Ir and Pt) in 1.5 M H_2SO_4 at 40 °C. Pretreatment by immersion of the alloy in HF resulted in an enhanced activity for oxygen evolution that was higher than the activity of conventional Pb-Ag electrodes. Glassy $Ni_{57}Ta_{40}Ir_3$ was found to be the most effective catalyst out of the compositions tested. The pretreatment process increased the surface roughness of the alloy and resulted in surface enrichment of iridium. The inclusion of the metals tantalum or niobium increased the passivating ability of these alloys and improved the durability of the catalysts in these environments. Clearly a veritable mine of mechanistic information at the molecular level awaits elucidation in order to understand these facts.

CHAPTER 4: EXPERIMENTAL

4.1 GLASSY ALLOY SAMPLES

Five different glassy metal alloy samples were tested in this investigation. Four of the samples are commercially available and one was specially prepared. The alloys and their chemical compositions are listed in Table 3. The compositions were measured accurately using a JY 24 Sequential ICP/AES Spectrometer.

Table 3: Chemical compositions of the glassy metal alloys (weight %).

Trade name with nominal chemical composition	ICP analysis of chemical composition (weight %)
Allied Chemicals 2605: $Fe_{67}Co_{18}B_{14}Si_1$	$Fe_{68.0}\,Co_{18.2}\,Si_{1.5}\,B_{12.3}$
Vitrovac 0040: $Fe_{40}Ni_{40}B_{20}$	$Fe_{43.2}\,Ni_{41.4}\,B_{15.4}$
Vitrovac 6025: $Co_{66}Fe_4Si_{16}B_{12}Mo_2$	$Co_{66.3}\,Fe_{4.6}\,Si_{14.8}\,B_{11.4}\,Mo_{2.9}$
Allied Chemicals 2826: $Fe_{40}Ni_{40}P_{14}B_6$	$Fe_{42.1}\,Ni_{37.7}\,P_{14.4}\,B_{5.8}$
Kirchartov Institute, Moscow	$Zr_{74.4}\,Ti_{19.3}\,Cu_{1.5}\,Fe_{4.8}$

Vitrovac is the trade name of Vakuumschmelze GmbH, Hanau.

All alloy samples were supplied via Professor T. Doyle, Physics Department, University of Natal, Durban. The alloy compositions chosen where, in part, determined by the parallel studies of their physical properties currently being investigated by the School of Physics. The alloy compositions investigated are referred to as glassy $Fe_{67}Co_{18}B_{14}Si_1$, $Co_{66}Fe_4Si_{16}B_{12}Mo_2$, $Fe_{40}Ni_{40}B_{20}$, $Fe_{40}Ni_{40}P_{14}B_6$ and $Zr_{74}Ti_{19}Cu_2Fe_5$ in this study.

The $Fe_{40}Ni_{40}B_{20}$ and $Co_{66}Fe_4Si_{16}B_{12}Mo_2$ samples were manufactured by Vitrovac, and the $Fe_{67}Co_{18}B_{14}Si_1$ and $Fe_{40}Ni_{40}P_{14}B_6$ samples by Allied Chemicals. The alloys were in the form of continuous ribbons, of widths of 25, 2, 3 and 25mm for the $Fe_{67}Co_{18}B_{14}Si_1$, $Fe_{40}Ni_{40}B_{20}$, $Co_{66}Fe_4Si_{16}B_{12}Mo_2$ and $Fe_{40}Ni_{40}P_{14}B_6$ samples respectively. Ribbon thicknesses were approximately 30-60μm. The $Zr_{74}Ti_{19}Cu_2Fe_5$ sample was specially produced by Kirchartov Institute, Moscow, with a ribbon width of 10mm and a thickness 0.5mm. All samples were prepared by the melt spinning technique. This method of fabrication gives rise to two surfaces, *viz* the one in contact with the roller, which has a duller finish and the other in contact with the inert gas atmosphere, which has a shiny surface (Fig. 8). In these experiments, the shiny sides of the specimens were studied. Gas entrainment furrows were visible on the wheel surface of the alloy that were formed by the entrapment of gas bubbles between the incipient ribbon and the rotating wheel during the manufacture of the alloy.

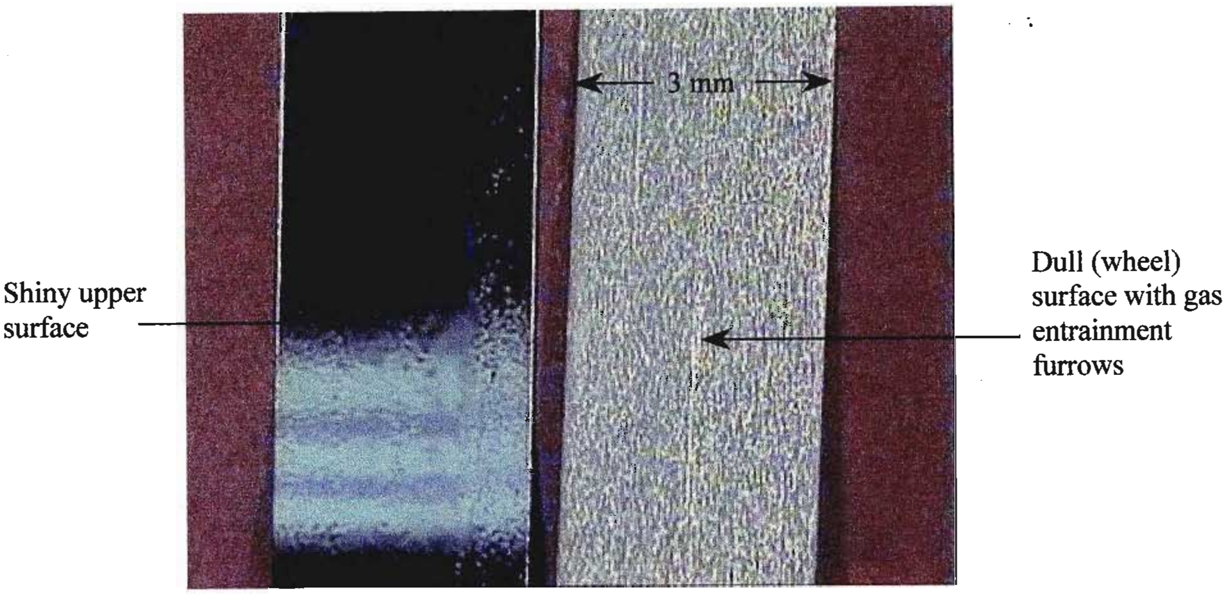

Fig. 8: The shiny (upper) surface and dull (wheel) surface of the $Co_{66}Fe_4Si_{16}B_{12}Mo_2$ alloy (Vitrovac 6025).

4.2 CHEMICALS

Experiments were performed in an alkaline electrolyte consisting of 1M KOH. Most of the research conducted into the electrocatalytic properties of glassy alloys has been preformed in basic media and so 1M KOH was chosen for this study so that direct comparisons could be made with the literature data, where available, in order that confirmation of experimental and handling techniques could be obtained. Solutions were prepared from analytical reagent KOH pellets (AnalaR, A.C.E. Chemicals) and Millipore water (resistivity 18MΩ cm). The water was obtained from a Milli-Q system, where tap water was passed through a reverse osmosis membrane, an activated carbon cartridge to remove organic impurities, two iron exchange cartridges to remove dissolved inorganic impurities and finally through a polymeric membrane filter which removed all particles larger than 0.2μm.

The acid solutions for acid protreatment of the alloy samples was prepared from 40% HF (AnalaR) and HNO_3 (BDH AnalaR).

4.3 THE CELL

A standard three electrode, water-jacketed glass cell was used in all experiments (Fig. 9). The cell was connected to a thermostatted water bath by means of the two horizontal arms on the jacket. This enabled the temperature of the electrolyte to be controlled to within ±0.5°C ot 25, 30, 40, 50 and 70°C. Cotton wool was wrapped around the cell and water inlet and outlet pipes at 40, 50 and 70°C to reduce heat loss and temperature fluctuations in the electrolyte. The temperature of the laboratory was maintained at approximately 22°C by efficient air conditioning.

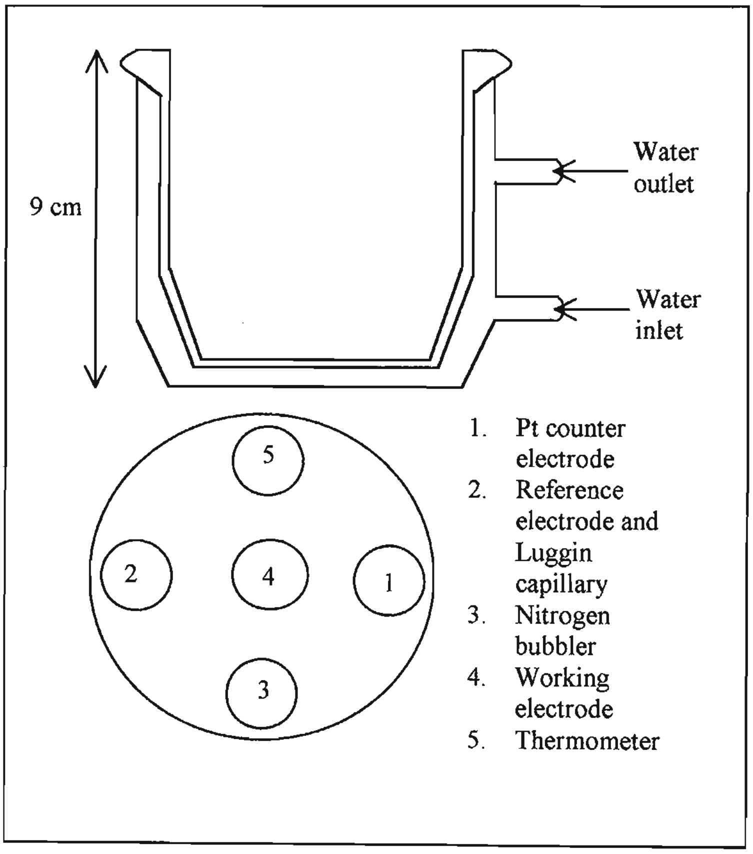

Fig. 9: Water-jacketed glass cell with its cover showing the cell inlets.

The cell inlets (Fig. 9) were for:

1. A spiral Pt wire counter electrode (CE). The CE had a significantly greater surface area than the working electrode surface area and was placed parallel to the latter to ensure correct cell geometry.
2. A Luggin capillary and reference electrode assembly. A mercurous sulphate reference electrode (SSE) was placed in the reservoir above the Luggin capillary and separated from the electrolyte by an ungreased and wetted Teflon stopcock (Fig. 10). All potentials were recorded with respect to the SSE (having a potential of +642 mV against the standard

hydrogen electrode). A water vacuum pump was used to draw a saturated K_2SO_4 solution through the capillary tip into the Luggin reservoir to avoid the formation of air bubbles in the capillary. The capillary tip was positioned directly under the WE at a distance equivalent to twice the diameter of the Luggin capillary tip, to minimise resistance error between the WE and RE [2].

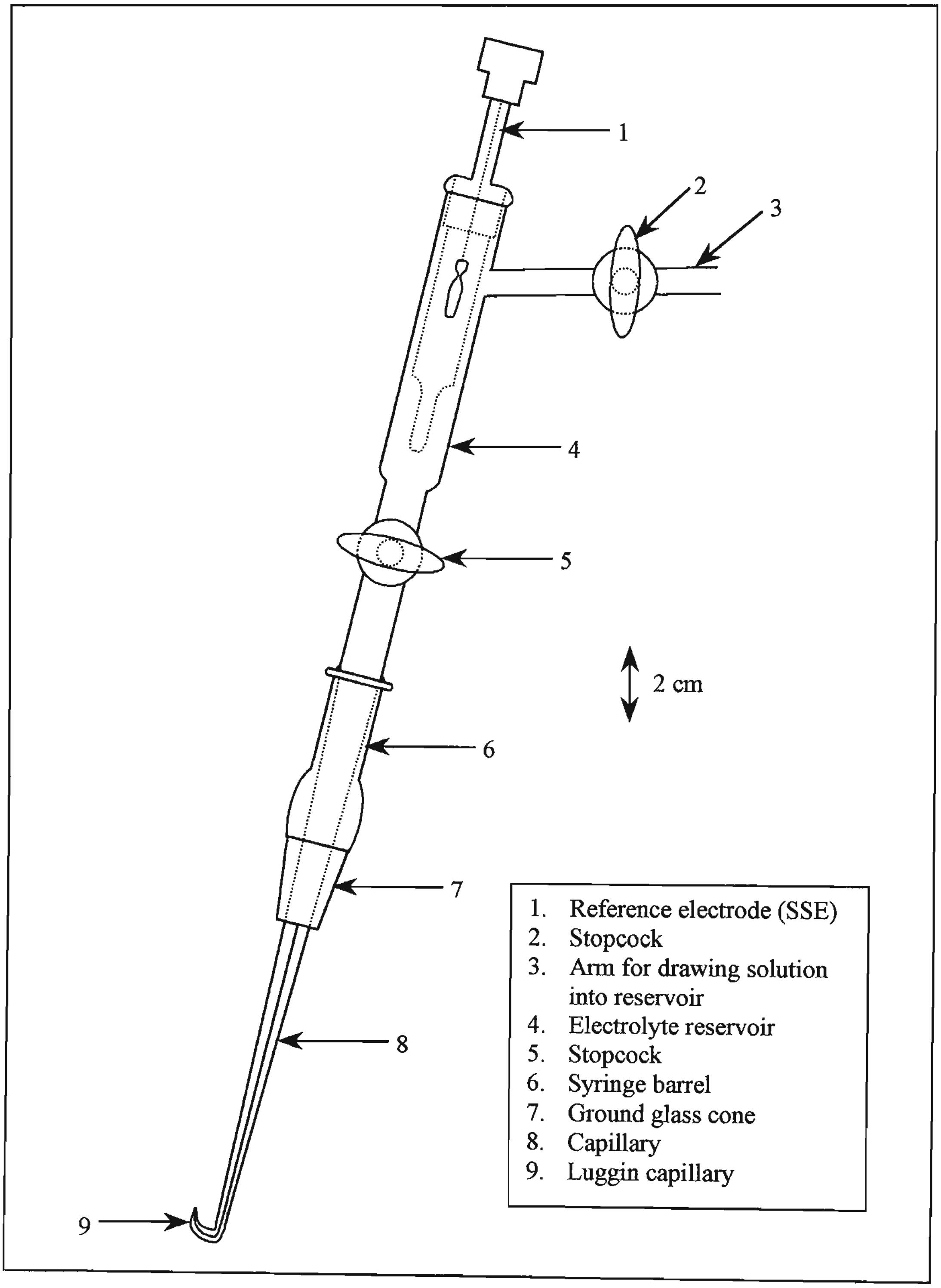

Fig. 10: Reference electrode assembly.

3. A nitrogen bubbler, attached to an oil trap (Fig. 11) that was used to deaerate the electrolyte with high purity nitrogen (99.998%, < 3 ppm O_2) prior to experimentation and to maintain a nitrogen blanket over the electrolyte during experimentation.

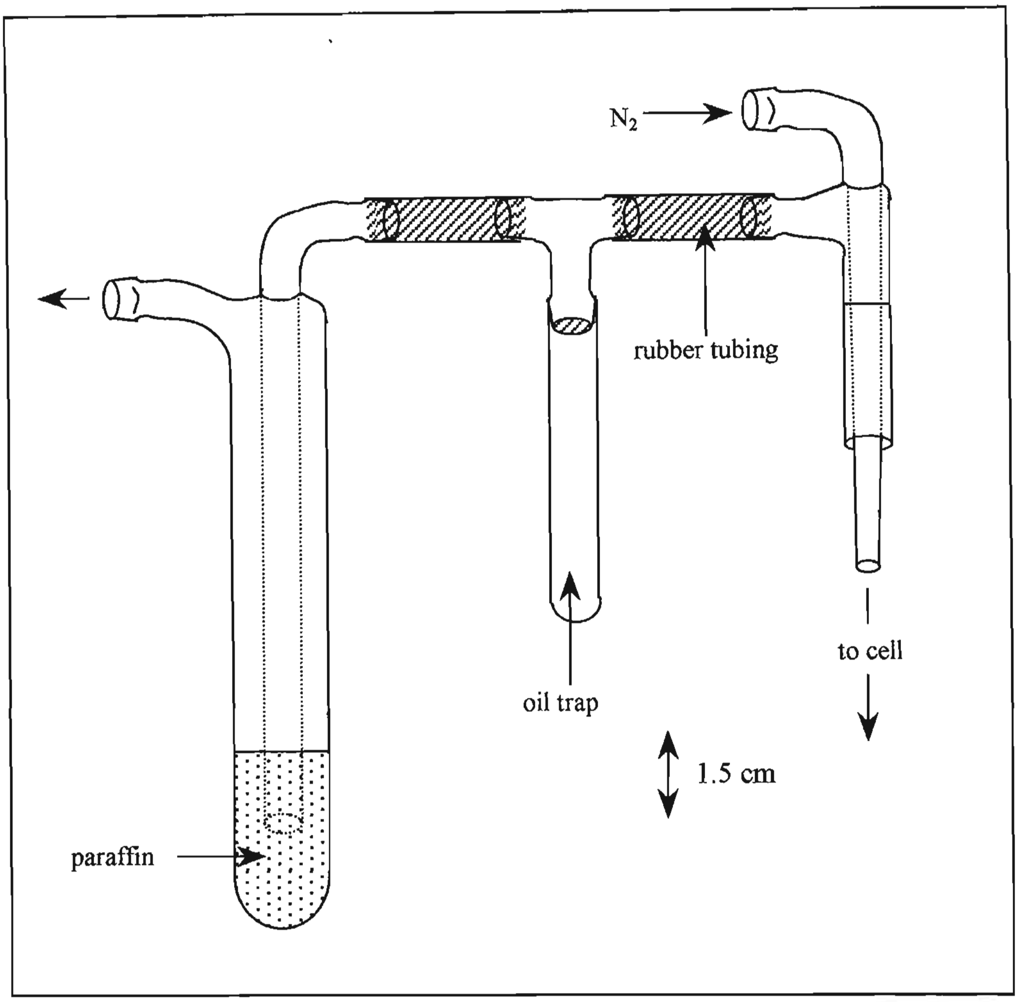

Fig. 11: Nitrogen bubbler with oil trap.

4.4 INSTRUMENTATION AND SOFTWARE

A schematic diagram of the experimental set-up is given in Fig. 12. The potential between the RE and WE was controlled using a BAS CV-27 potentiostat. Voltammograms were first monitored as current-time and potential-time waveforms on a Nicolet 3091, twin-channel digital storage oscilloscope. A hard copy of the voltammogram could simultaneously be obtained on a LLOYD PL-3 X-Y recorder via the pen function of the oscilloscope for slower scan rates (<500 mV/s).

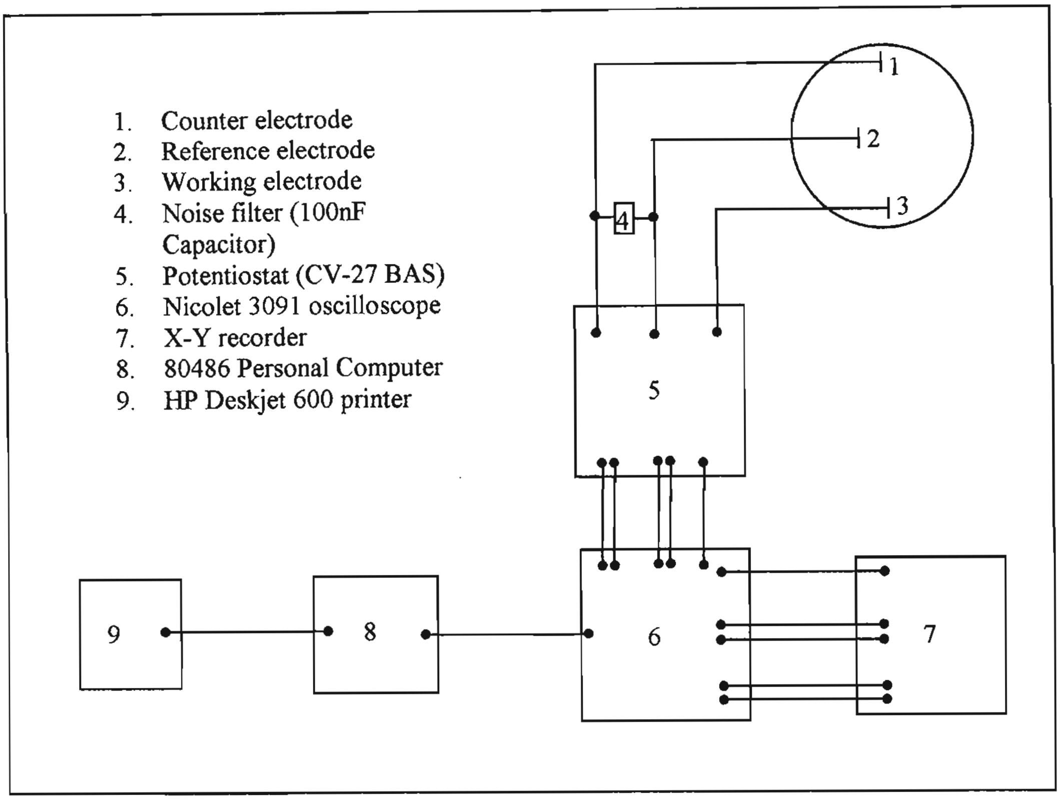

Fig. 12: Schematic diagram of the experimental setup.

The oscilloscope converted the waveforms into 4000 data points. Each point represented an I-V position on the waveform. The oscilloscope passed each of the points via an RS-232 (serial) interface to a 80-486 personal computer. A program written in basic for msdos (Collver8.Bas [137]) copied the incoming data points from the RS-232 interface to an ASCII format text file. The text file stored space delimited points with one point per line.

The text file was copied into a excel–97 spreadsheet running on a Windows-95 machine. The x and y points where copied into separate columns that represented the potential and current respectively, forming a 2 by 4000 matrix. Each of the x and y points were rounded to 2 decimal places with the logarithm of the current taken. For each unique x point, the y points associated with that x point were averaged and the new x and averaged y points moved to a new series of data cells. The new series of data represented a far smoother version of the original data obtained from the oscilloscope, consisting of approximately 30 data points. An excel macro was written to automate the above process (Appendix).

4.5 CONSTRUCTION OF THE WORKING ELECTRODE

The glassy alloy samples were extremely thin and much time was spent in developing a mounting technique that produced flat and evenly polished specimens with clean, polished and reproducible working surfaces. Fig. 13 shows a diagram of an assembled working electrode.

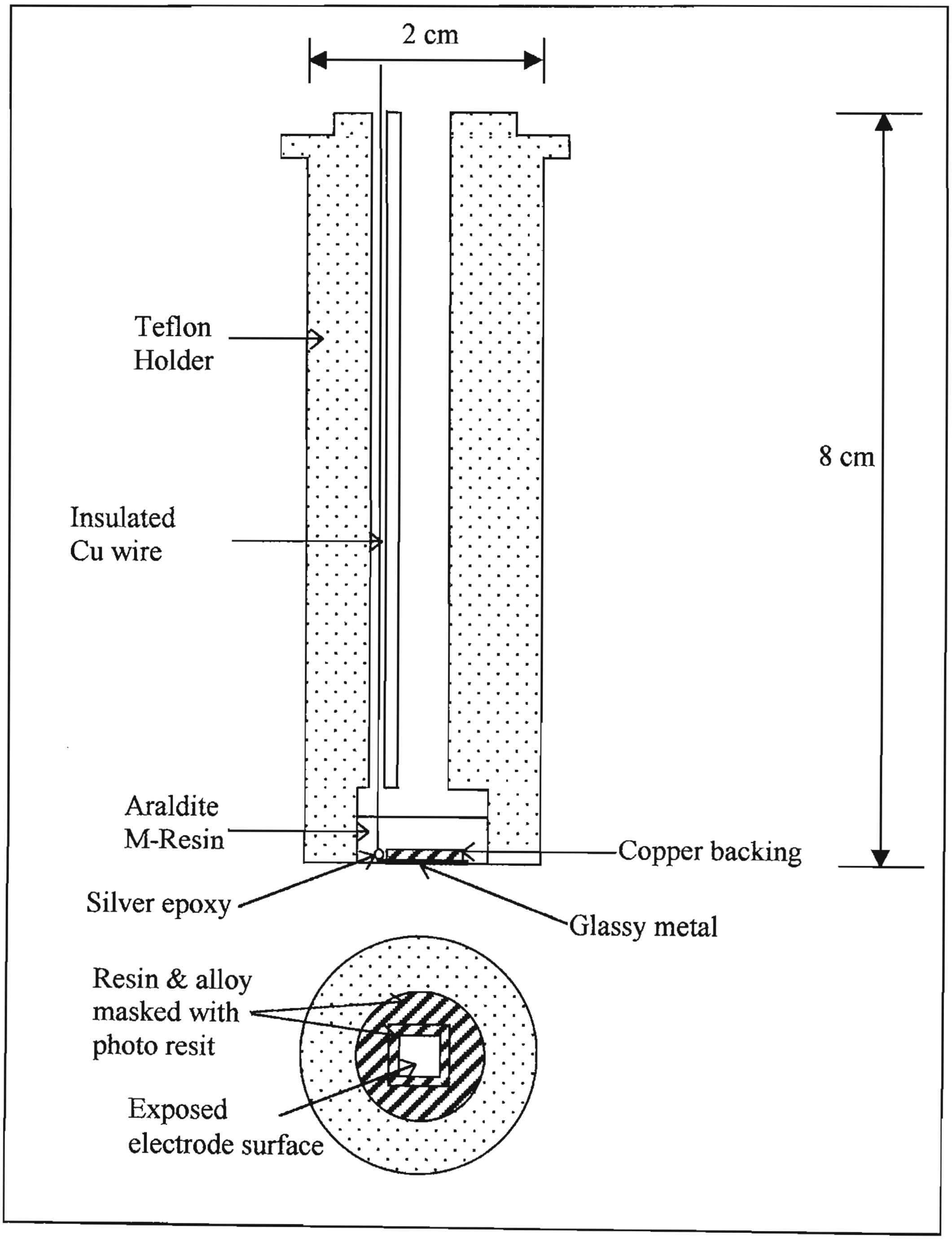

Fig. 13: An assembled working electrode.

The mounting technique involved cutting a section of alloy ribbon (1cm^2), which was ultrasonically degreased in ethanol and secured to a flat copper backing surface (0.9cm^2), using an epoxy based adhesive (Patex Epoxy Steel, Henkel). The copper backing was a disc of about 2mm thickness that was polished with SiC adhesive discs (Leco Corporation, Grit 400) on a Struers Planopol-2/PdM-Force polishing wheel until a smooth and flat surface was obtained. The copper surface was also cleaned ultrasonically prior to mounting to remove grease and dirt from the metal surface. The dull face of the ribbon surface (Fig. 1) and the polished copper surface were pressed firmly together in a clamp as the epoxy cured (40°C for 2 hours). The copper backing supported the alloy sample and added strength to the final electrode. Without the backing, the alloy-resin contact was weak and the electrode lifted when it was polished and placed in the electrolyte. An insulated wire was joined to the back of the alloy sample using a silver epoxy cement (Emerson and Cuming, Belgium). The working surface of the alloy was firmly pressed onto a double-sided adhesive tape on a flat surface and a hollow cylindrical Teflon mould centred around the sample. The mould was filled with an epoxy resin (Araldite M-Resin with HY-Hardener in a 5:1 ratio) that had been degassed under vacuum (40°C for 5 minutes) and was then oven cured (100°C for 60 minutes). The glassy ribbon was cut so that it was larger than the copper backing and overlapped the backing at all edges. Therefore, when the glassy ribbon and backing were mounted in epoxy, the copper backing was totally insulated within the whole electrode and did not get exposed to the electrolyte. After curing, the electrode was removed from the mould and press fitted into a heated Teflon holder. Electrical contact between the electrode surface and the wire tip was checked with a multitester.

4.5.1 Electrode polishing

Electrochemical results have been shown to vary significantly with the surface pretreatment procedure used [138] and so a standard pretreatment method was adopted to ensure that a reproducible electrode surface prepared for each experiment. Pretreatment involved two stages, *viz* mechanical polishing of the alloy surface followed by electrochemical pretreatment of after immersion of the electrode into the electrolyte.

Mechanical polishing was performed using the Struers Planopol-2/PdM-Force polishing wheel with Lecloth B PSA polishing cloths, onto which an aluminium oxide powder suspension was spread. The electrode surfaces were polished with powders of progressively smaller particle diameter sizes (5, 1 and 0.3μm) and ultrasonically cleaned in deionised water between each change in powder grade. Due to the extreme thinness of the alloys, only light polishing was possible as vigorous polishing was found to rapidly erode through the entire ribbon thickness and destroy the sample. The polished electrode surfaces were examined under an optical microscope (Zeiss-Stemi 2000 (x10)) after polishing to ensure that they were free of scratches. Final ultrasonic cleaning was conducted in ethanol for one minute to remove any residual grease.

4.5.2 Photo resist coatings

A major problem encountered with the smooth glassy alloy samples was a poor mechanical adhesion at the electrode-resin interface. Once placed in the electrolyte, the electrode edges lifted, creating an undefined working electrode surface area. To overcome this problem, the electrode-resin interface was masked, leaving only a limited area of the mounted alloy specimen exposed to the electrolyte (Fig. 14).

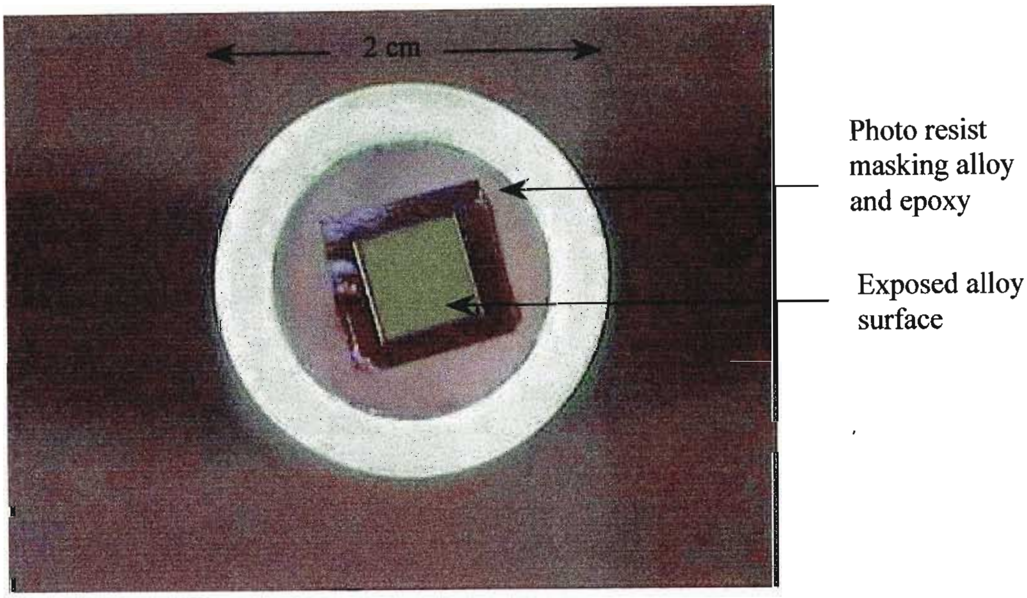

Fig. 14: Prepared electrode surface after application of the Dynachem Photo resist coating.

A number of different coating materials have been used to mask thin metal sheets and foils [139], but after testing different alternatives, a photo-resist coating was found to give the best performance for the glassy alloy samples. Two different types of photo resist coatings were used that were easy and convenient to apply, a base resistant photo resist (Kodac photo resist (KPR) and Kodac photo resist developer (KPR developer)) and an acid resistant photo resist (Dynachem Dry Film Photopolymer, Morton Electronic Materials). Application involved warming the electrode surface and evenly spreading the photo resist emulsion over the entire surface. The emulsion was heat dried with a hair dryer. A photographic negative of the required electrode dimensions was placed onto the emulsion over the area of alloy chosen to form the working surface and held firmly in place with a piece of glass. The electrode was placed under a UV lamp (RWYUV-GS) and the emulsion exposed to UV light for exposure times of 7 and 3 minutes for the Kodac and Dynachem photo resists respectively. After exposure, the unexposed portion of the emulsion was removed with a developing agent, which involved soaking the electrode in Kodac developing agent (1minute) or 1M Na_2CO_3 (2 minutes) for the Kodac and Dynachem photo resists respectively. The photo resist masked the alloy-epoxy interface and produced a sharp alloy-photo resist interface. It also had the advantage of creating a consistent and well-defined electrode area. The geometrical electrode areas chosen were 0.09 and 0.36 cm^2, according to the original dimensions of the alloy ribbon. When dry, both photo resists formed a strong and electrically insulating contact with the alloy and epoxy surfaces. The photo resist was lifted on completion of an experiment using ethylacetate or 1M NaOH for the Kodac and Dynachem photo resists respectively. Other coating materials were found to be less effective than the photo resists. Coating materials tested included a phenolic resin (FSC-115, Schenectady (Pty) Ltd) and three different types of epoxy phenolic resins (MD-5286, MD-5714, and Pro-struct 802 Base and 1833 Activator, Plascon ICP). Two different airdrying resins (JJ56 and CHL8, Plascon ICP) were also tested. These coatings adhered weakly to the smooth glassy alloy surfaces and were prone to lifting, especially at the alloy-coating interface, allowing the electrolyte to penetrate under the coating. The coatings had to be applied with a paintbrush around a template that masked the required working electrode dimensions and this method of application also resulted in less precise control over the electrode surface area.

A third photo resist (Elpemer SD 2461 SM-G Solder Resist) was also found to be effective and was used to test the reproducibility of results obtained with the Kodac and Dynachem photo resists. The Elpemer photo resist was more versatile as it was inert in both acidic and basic media, however, its application was more time consuming and hence it was not the photo resist of choice used for the bulk of the experiments. The Elpemer photo resist consisted of two components, a resin and a hardner combined (4:1 ratio by weight). Butylcarbitol solvent was added to thin the mixture and a thin layer was painted over the entire electrode surface. The solvent was removed by pre-drying the photo resist in an oven (15 minutes at 80°C). A photographic negative was then placed over the required alloy electrode surface and the emulsion exposed to UV light for 9 seconds. The unexposed portion was removed with a 1% Na_2CO_3 developing solution. Final thermal curing of the photo resist (45 minutes at 150°C) produced a very strong bond between the photo resist and alloy. No chemical solvent was found that could lift the cured photo resist and it was removed by mechanical polishing with 5μ Al_2O_3. Electrochemical results, anodic polarisation curves and cyclic voltammorgams, obtained with the Elpemer photo resist were the same as those obtained using the Kodac and Dynachem coatings. It was concluded that the photo resists were inert under the experimental conditions used and did not introduce any detectable electroactive species into the system. Each photo resists formed an effective coating materials that produced reproducible electrode surfaces and results in the electrolyte media used in this study.

When viewed under an electron microscope, the working electrode surface was found to be scratch free and clean (Fig. 15). Good edge retention was also observed at the alloy-photo resist interface. Other techniques for mounting thin-film specimens and glassy metals have been developed and are reported in the literature [140,141], however the above procedure was found to be the most convenient and entirely effective for the glassy alloy samples.

4.6 ELECTROCHEMICAL EXPERIMENTS

4.6.1 Electrochemical pretreatment

The prepared working electrode was immersed directly into the cell electrolyte after application of the photo resist. Prior to this, all glassware had been soaked in a cleaning solution (Extran MA 02 neutral) and rinsed thoroughly with deionised water, millipore water and finally the solution to be used. The electroylte was also deaerated with high purity nitrogen for 30 minutes. Electrical connections were then made to the electrodes and care was taken to ensure that the Luggin capillary was free from air bubbles and was not leaking, and that no bubbles were adhering to the working electrode surface. A nitrogen blanket was maintained over a quiescent electrolyte throughout the experiment to prevent oxygen entering the system. Between experiments, the solution was stirred using a magnetic stirrer and nitrogen bubbled for at least one minute to ensure a homogeneous solution. As an electrochemical cleaning procedure the working electrode was held at a potential 10mV cathodic of its corrosion potential, E_{corr}, for 10 minutes in order to reduce any air formed oxide film on the electrode surface. This pretreatment was found to produce reproducible cyclic voltammograms and was used consistently for all electrochemical experiments.

4.6.2 Cyclic voltammetric experiments

Following the electrode pretreatment (section 4.6.1), the electrode was stepped to the required initial potential and swept to a positive potential limit. The scan direction was automatically reversed and the electrode potential was swept to the negative limit to complete the voltammogram. Cycling was continued until the required number of voltammograms had been obtained. Cyclic voltammograms were recorded at different sweep rates and between different potential limits, although the limits chosen did not extend into the hydrogen or oxygen evolution regions of the electrolyte.

4.6.3 Polarisation experiments

The elementary corrosion behaviour of the glassy alloys were investigated by anodic polarisation. Anodic polarisation curves were obtained by sweeping the electrode potential in an anodic direction at 1mV/s subsequent to the electrochemical pretreatment from an initial potential that was 10mV cathodic of the corrosion potential.

The electrocatalytic activity of the glassy alloys for the HER was also determined by sweeping the potential from E_{corr} in a cathodic direction into the hydrogen evolution region at 1mV/s until the reaction became diffusion limited and a limiting current was reached. Tafel plots were constructed from the cathodic polarisation curves and the kinetic characteristics, i_o and b, calculated. Each experiment was repeated six times to ensure that reproducible results were obtained.

4.6.4 *In situ* anodic pretreatment

The electrocatalytic activity of the glassy alloy samples for the HER was determined after anodic oxidation *in situ* at constant current density. Anodic galvanostatic currents of magnitudes 10, 50, 100, 300, 500, 750, 1000, 2000 and 3000 $\mu A.cm^{-2}$ were applied to the working electrodes using an EG and G 363 Galvanostat/Potentiostat. The electrodes were then held at a potential 10mV cathodic of the open-circuit potential for 10 minutes and the cathodic polarization curves were obtained in the same manner as outlined in section 4.6.3.

4.6.5 *Ex situ* acid pretreatment

The effect of acid pretreatment on the electrocatalytic activity of the glassy alloy samples for the HER was investigated. The electrodes were immersed in HF and HF/HNO_3 (1:4 ratio respectively) acid solutions of different concentration for different treatment periods prior to immersion into the cell electrolyte after rinsing with millipore water followed by the 1M KOH. The treatment time and acid concentration used varied according to the glassy alloy sample tested. Table 4 lists the different acid concentrations and treatment times tested for the different glassy alloy samples. The cathodic polarisation curves were obtained in the 1M KOH and the influence of acid pretreatment on the Tafel parameters thereby determined.

Table 4: The different acid treatments conducted on the glassy alloy electrodes prior to cathodic polarisation in 1M KOH.

$Fe_{67}Co_{18}B_{14}Si_1$	$Co_{66}Fe_4Si_{16}B_{12}Mo_2$	$Fe_{40}Ni_{40}P_{14}B_6$ / $Fe_{40}Ni_{40}B_{20}$	$Zr_{74}Ti_{19}Cu_2Fe_5$
0.5M HF (1min)			0.1M HF (10 seconds)
1.0M HF (0.5,1,10min)	1.0M HF (1,5,10min)	1.0M HF (1,10min)	0.5M HF (10 seconds)
2.0M HF (1min)			1.0M HF (10 seconds)
4.0M HF (1min)		4.0M HF (1min)	
8.0M HF (1min)	8.0M HF (1min)	8.0M HF (1min)	
0.1M HF/0.1M HNO_3 (1min)			
0.5M HF/0.5M HNO_3 (15,30,60 seconds)			
1.0M HF/1.0M HNO_3 (1min)	1.0M HF/1.0M HNO_3 (1,5,10min)	1.0 M HF/1.0M HNO_3 (1,10min)	1.0M HF/1.0M HNO_3 (10,60 seconds)
		2.0 M HF/2.0M HNO_3 (1min)	

4.7 SURFACE ANALYSIS

The aim of SEM/EDS surface analysis was to detect changes in the surface topography and composition of the glassy alloy samples after acid and anodic pretreatment. A Hitachi S520 scanning electron microscope was used for qualitative examination of the electrode surface. Quantitative analysis was obtained using a LINK ISIS energy dispersive x-ray spectrometer (EDS) that measured the energy and intensity distribution of the x-ray signal generated by the focused electron beam.

On completion of each experiment, the electrode was removed from its Teflon holder, rinsed in reagent grade water and dried using high purity nitrogen. It was then stored in a dry, oxygen free, high purity nitrogen atmosphere prior to surface analysis. The sample was screwed into a specimen stub holder designed to make provision for the contact wires, so that they did not need to be cut off each time an electrode was examined in the SEM. The electrode surface was held flush with the holder surface, which was necessary for accurate determination of the distance from the electrode to the final lens for EDS analysis.

All EDS analyses of surface features were obtained at an accelerating voltage of 20keV for a period of 100s, resulting in a penetration depth of approximately 0.5 μm into the sample. The magnification, and hence the probe size, depended on the area or feature under investigation. General analyses were obtained at a low magnification (x 1000), while analyses of specific surface features were obtained at a higher magnification using the spot probe. Quantitative elemental compositions for each spectra were determined using the APP internal standard method, and the ZAF routine on the Kevex QUANTEX – RAY programme disc [86]. Net peak intensities were converted to concentration via the MAGIC V column quantitative programme. EDS results were reported as weight percentages with a reproducibility of 0.1 wt % obtained at 20keV. The EDS system is unable to detect elements of low atomic number and it was found that boron, which was present in four of the glassy alloy samples tested, could not be detected. This is because the EDS detector has a thin beryllium window through which the x-rays generated from a specimen pass and this window absorbs lighter x-rays.

For qualitative analysis the electrodes were gold sputter coated using a POLARON SEM coating unit E5100. Sputter coating was found to be necessary to prevent surface charging and to improve resolution. The gold coating was applied after EDS analysis to avoid changes in surfaces compositions resulting from the coating. SEM micrographs were obtained at constant magnifications for comparison purposes. The general electrode surface was photographed at a x500 magnification and specific surface features were photographed at x4000. Photographic negatives and digital images of the electrode features were obtained and digital images are incorporated into this thesis in a suitable format.

CHAPTER 5: RESULTS AND DISCUSSION

5.1 AS-POLISHED ELECTRODE SURFACES

5.1.1 SEM analysis

The electrode surfaces were polished prior to immersion in the electrolyte using Al_2O_3 powder of increasingly fine grades (as described in section 4.5.1) to give reproducible working electrode surfaces for each experiment. The polished surfaces were found to be smooth and scratch free (x40 magnification). Current densities were measured using the geometric surface areas of the electrodes which were similar to the true surface areas due to the low roughness factor of the polished surfaces. SEM analysis revealed slight differences in the polished surfaces of the different alloy samples and selected micrographs are shown in Fig. 15. The polished $Fe_{40}Ni_{40}P_{14}B_6$, $Fe_{40}Ni_{40}B_{20}$ and $Co_{66}Fe_4Si_{16}B_{12}Mo_2$ alloys all had shiny and mirror-like surfaces and were free from a visible surface layer. A surface layer rapidly formed on the $Fe_{67}Co_{18}B_{14}Si_1$ surface after mechanical polishing and ultrasonic cleaning with water and ethanol resulted in a dull and mottled appearance. The $Zr_{74}Ti_{19}Cu_2Fe_5$ surface was shiny after polishing, however SEM analysis revealed that the surface was inhomogeneous and supported small nodules ranging in size between 5 and 20μm. The nodules were firmly embedded in the alloy and were present throughout the entire ribbon thickness as extended polishing just uncovered further nodules. EDS analysis indicated that the nodule composition was 95% Zr and 5% Ti indicating that the nodules had a crystalline structure. The quench rates employed in the melt spinning technique are not sufficiently rapid to prepare amorphous structures consisting almost exclusively of a single metal component. The $Zr_{74}Ti_{19}Cu_2Fe_5$ electrode therefore consisted of two discrete surfaces with different compositions as well as different structures (both crystalline and amorphous). The two surfaces would be predicted to produce different electrochemical and electrocatalytic responses, however it would be difficult to separate the two surfaces and analyse their responses separately. This observation indicates that it is difficult to prepare homogeneous alloys that are completely amorphous throughout the entire sample thickness using the technique of rapid quenching. Due to the greater thickness of the $Zr_{74}Ti_{19}Cu_2Fe_5$ alloy sample (~0.5mm) in comparison to the other four samples (~30-50μm), it appears that the lower quench rate resulted in partial crystallisation of the alloy. The nodules were more abundant on the shiny undulant surface.

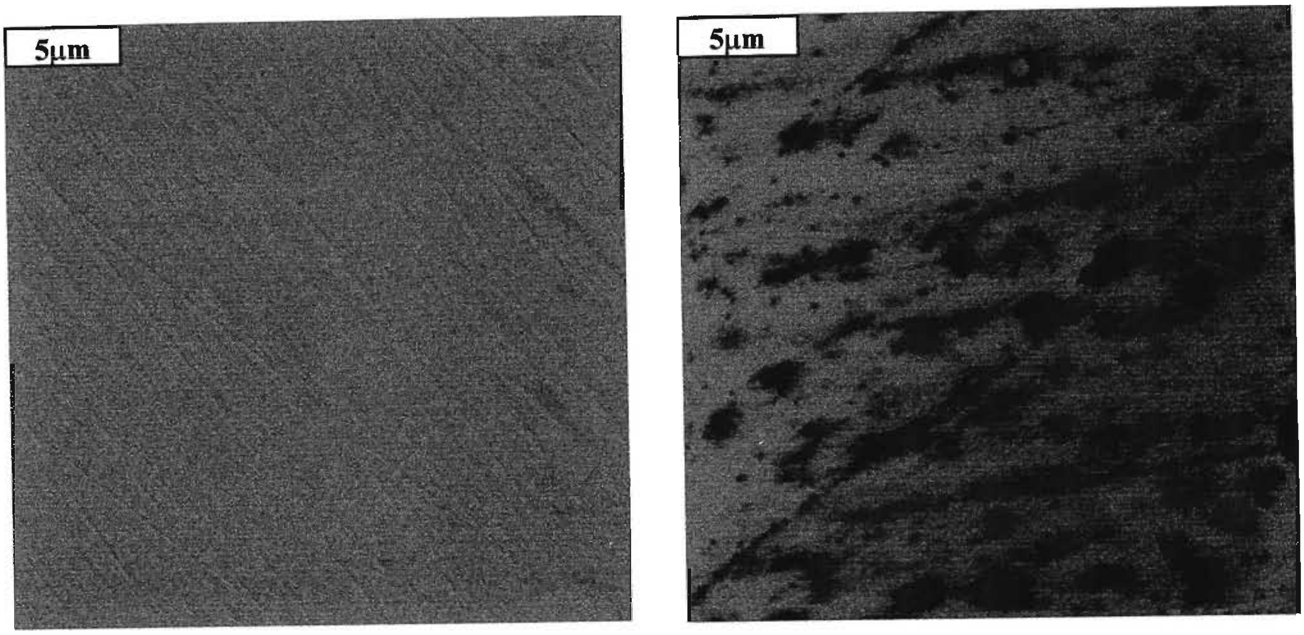

(a) $Fe_{40}Ni_{40}P_{14}B_6$ (mag. x4000) (b) $Fe_{67}Co_{18}B_{14}Si_1$ (mag. x4000)

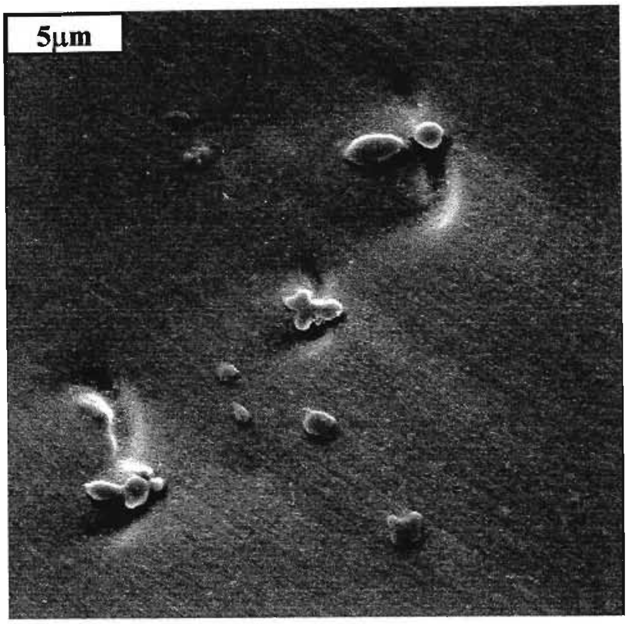

(c) $Zr_{74}Ti_{19}Cu_2Fe_5$ (mag. x4000)

Fig. 15: Polished glassy metal electrode surfaces.

This was interpreted by the fact that the upper alloy surface cooled at a lower rate than the wheel surface, resulting in a longer crystallisation time for the upper surface. Although the $Zr_{74}Ti_{19}Cu_2Fe_5$ alloy was visibly inhomogeneous the $Fe_{40}Ni_{40}P_{14}B_6$, $Fe_{40}Ni_{40}B_{20}$, $Fe_{67}Co_{18}B_{14}Si_1$ and $Co_{66}Fe_4Si_{16}B_{12}Mo_2$ alloys could also contain similar inhomogeneities that were too small to distinguish by SEM microscopy but could possibly be detected by X-ray diffraction. It has been reported that certain low-temperature anneals and slowly quenched glasses contain small crystallites and patches of compositional inhomogeneity [12]. Small crystallites have been detected in Co-Cr and Fe-Cr containing glasses [17]. An increase in the corrosion current was reported [85] for metallic Fe-B glasses that were prepared at low cooling rates and this was attributed to the nucleation of crystalline embryos that were detectable by Mossbauer spectroscopy.

5.1.2 EDS analysis

EDS analyses of the as-quenched upper (shiny) and wheel (dull) ribbon surfaces were made to determine if there were detectable differences in the alloy component concentrations between the two surfaces (Table 5). These results were also compared with analyses of the mechanically polished shiny ribbon surface. The reproducibility of the results was 0.1 wt% (20keV) and the average value was recorded from three separate analyses. The analyses were performed at fairly low magnification (1000x) and thus represent a general surface composition.

Table 5: EDS analysis of the $Fe_{67}Co_{18}B_{14}Si_1$, $Zr_{74}Ti_{19}Cu_2Fe_5$ and $Fe_{40}Ni_{40}P_{14}B_6$ ribbon surfaces.

Glassy $Fe_{67}Co_{18}B_{14}Si_1$	**Fe**	**Co**	**Si**	
as-quenched dull (wheel) surface of ribbon	78.20	20.65	1.15	
as-quenched shiny (upper) surface of ribbon	77.56	21.30	1.14	
Polished electrode surface	77.80	21.22	0.98	
Glassy $Zr_{74}Ti_{19}Cu_2Fe_5$	**Zr**	**Ti**	**Cu**	**Fe**
as-quenched dull (wheel) surface of ribbon	71.92	19.64	1.78	6.66
as-quenched shiny (upper) surface of ribbon	74.70	19.14	1.09	5.07
polished electrode surface	73.22	19.71	1.24	5.83
Glassy $Fe_{40}Ni_{40}P_{14}B_6$	**Fe**	**Ni**	**P**	
as-quenched dull (wheel) surface of ribbon	40.14	42.23	17.63	
as-quenched shiny (upper) surface of ribbon	39.09	41.97	18.94	
Polished electrode surface	41.05	42.15	16.80	

Note: Data presented as weight %.

Elements with a molar mass of < 6 cannot be detected by EDS because the lighter x-rays generated from low atomic number elements are absorbed on passing through a thin beryllium window. As a result no values are available for the B component of $Fe_{67}Co_{18}B_{14}Si_1$ and $Fe_{40}Ni_{40}P_{14}B_6$ alloys.

The glassy $Fe_{67}Co_{18}B_{14}Si_1$ alloy showed a 0.65 wt% enrichment of Co on the upper ribbon surface and a 0.64 wt% enrichment of Fe on the roller surface. The Si concentration was constant on both surfaces. A light mechanical polishing of the shiny alloy surface resulted in a decrease in the Si concentration while the Co and Fe concentrations did not change significantly. For the $Zr_{74}Ti_{19}Cu_2Fe_5$ alloy, a significant 2.78 wt% enrichment of Zr was detected on the shiny ribbon surface (probably due to the higher concentration of Zr-based nodules) and a 0.50, 0.69 and 1.59 wt% enrichment of the Ti, Cu and Fe components on the wheel surface respectively. The polished alloy surface concentrations were found to be intermediate between these values. The glassy $Fe_{40}Ni_{40}P_{14}B_6$ alloy showed a 1.05 wt% enrichment of Fe on the as-quenched wheel surface, a 1.31 wt% enrichment of P on the upper shiny ribbon surface. After polishing a decrease in the P concentration on the upper ribbon surface resulted. P-enrichment in the near-surface region of amorphous $Co_{80}P_{20}$ and $Ni_{80}P_{20}$ has also been reported in the literature [142]. No differences in Ni concentration were detected between the two surfaces. EDS analysis did not detect significant variations in component concentrations between the wheel and upper surfaces of the as-quenched glassy $Co_{66}Fe_4Si_{16}B_{12}Mo_2$ and $Fe_{40}Ni_{40}B_{20}$ ribbons.

It should be noted that the EDS surface analysis technique provides only an indication of the alloy surface composition due to an electron beam-specimen interaction volume. Using this technique the analysis of specific surface features also results in the inclusion of bulk alloy analysis and only deposits of substantial thickness produce detectable concentration variations in comparison to the bulk alloy composition. As the accelerating voltage of the electron beam is increased the sampling volume from which x-rays are generated and received by the detector (the sampling volume) increases. Fig. 16 shows the sampling volume of the electron beam at an accelerating voltage of 20keV. In this study EDS spot analyses of specific surface features, such as pits or surface deposits, did not produce results that were significantly different from the general surface analyses. The surface features were generally very small and only substantially thickening of deposits produced concentration variations that were detectable by EDS.

A number of empirical equations exist for determining the interaction volume of the electron beam e.g. the Kanaya-Okayama range [143]. Graham [86] attempted to obtain quantitative information of only the alloy surface composition by placing a leaf of gold foil over the alloy surface to act as a "beam absorber" and progressively increasing the electron accelerating voltage. From the results obtained it was not possible to make a definite differentiation between the surface passive film composition and the bulk alloy composition. Accurate analyses of surface compositions and depth profiles would need to be obtained by different surface analysis techniques such as AES or XPS.

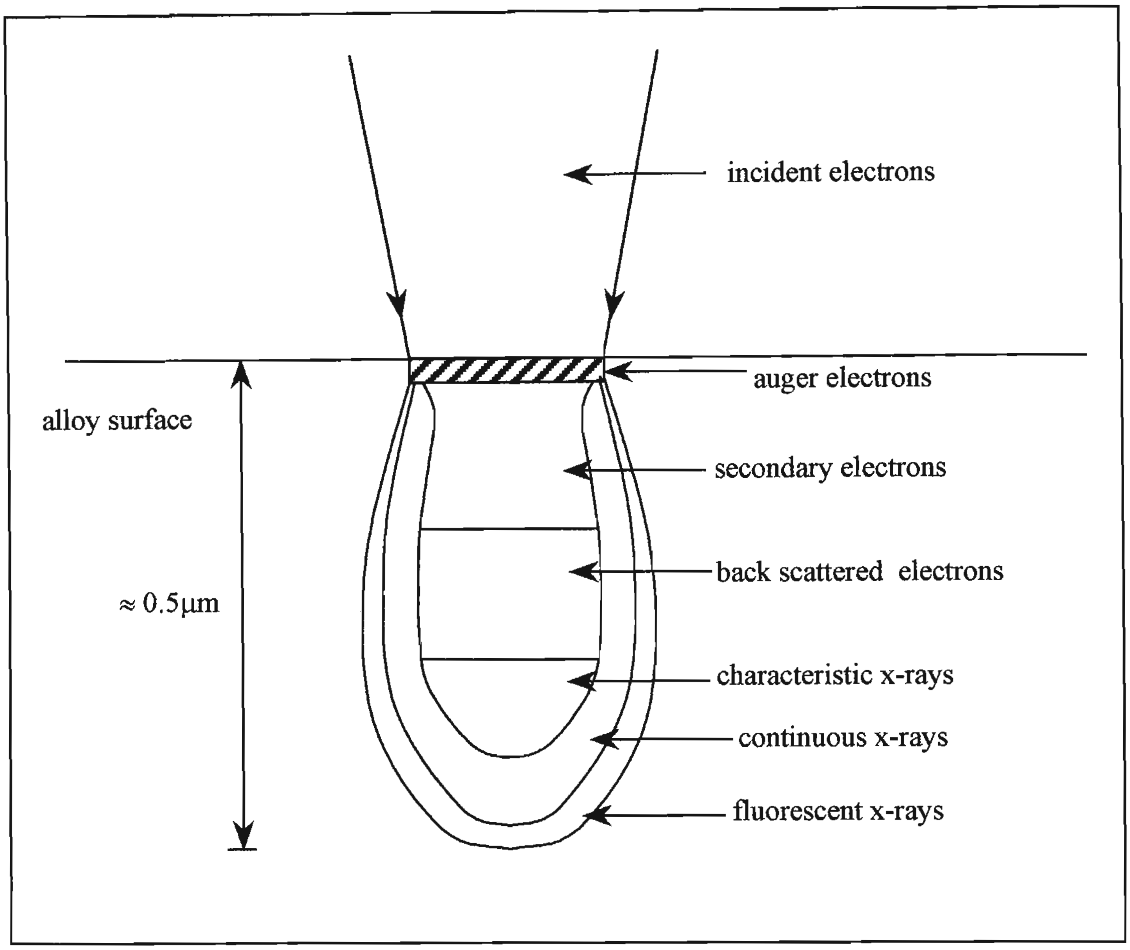

Fig. 16: The EDS electron beam interaction volume at an accelerating voltage of 20keV.

5.2 ANODIC POLARISATION IN 1M KOH

Anodic polarisation curves of the five different glassy alloys were obtained to provide an indication of their corrosion resistance in the as-polished state in 1M KOH (Fig. 17). The corrosion parameters obtained from the curves are listed in Table 6.

Table 6: Corrosion parameters obtained from the anodic polarisation curves of the glassy metal alloys in 1M KOH at a sweep rate of 1mV/s.

	Potentials / V (vs. SSE)			Current densities / mA.cm^{-2}		
Alloy sample	$\mathbf{E_{corr}}$	$\mathbf{E_{pp}}$	$\mathbf{E_{Flade}}$	$\mathbf{E_{tr}}$	$\mathbf{i_{pp}}$	$\mathbf{i_p}$
$Fe_{67}Co_{18}B_{14}Si_1$	-1.53	-1.16	-0.36	0.04	0.251	2.09×10^{-2}
$Co_{66}Fe_4Si_{16}B_{12}Mo_2$	-1.55	-1.23	-0.21	0.03	0.223	4.73×10^{-2}
$Fe_{40}Ni_{40}P_{14}B_6$	-1.16	-1.03	-0.90	-0.04	7.93×10^{-3}	4.91×10^{-3}
$Fe_{40}Ni_{40}B_{20}$	-1.14	-1.02	-0.96	-0.01	8.65×10^{-3}	6.32×10^{-3}
$Zr_{74}Ti_{19}Cu_2Fe_5$	-1.07	-	-	0.13	-	4.93×10^{-3}

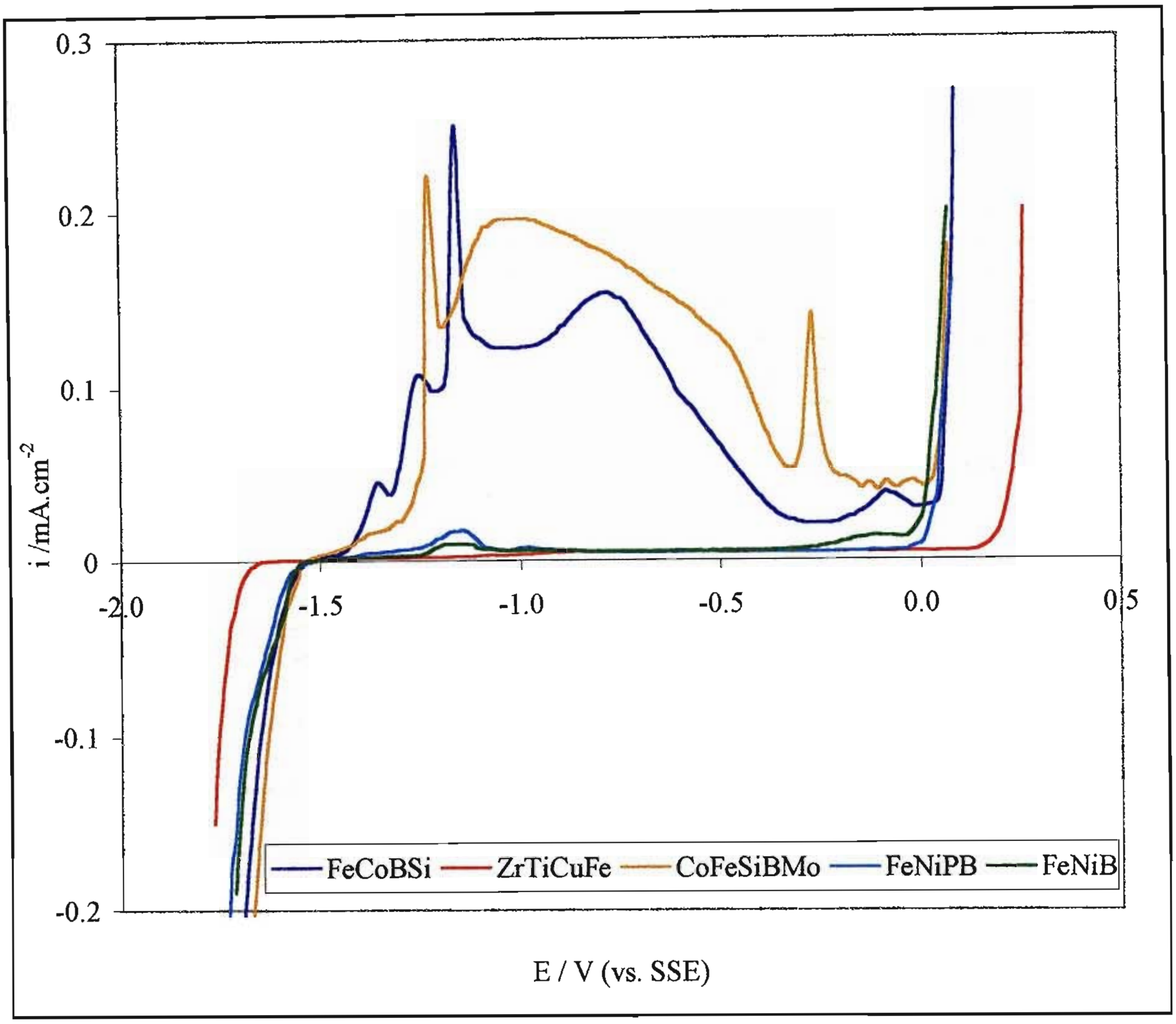

Fig. 17: Anodic polarisation curves of the glassy metal alloys in 1M KOH at 25°C and 1mV/s (first potential sweep).

The corrosion resistance of an alloy is characterised as being better the more extensive the passive region and the lower the critical current density. On this basis, the $Fe_{67}Co_{18}B_{14}Si_1$ and $Co_{66}Fe_4Si_{16}B_{12}Mo_2$ alloys displayed the poorest corrosion resistance and the $Zr_{74}Ti_{19}Cu_2Fe_5$ alloy the greatest resistance. The E_{corr} values became more noble in the order $Co_{66}Fe_4Si_{16}B_{12}Mo_2$, $Fe_{67}Co_{18}B_{14}Si_1$, $Fe_{40}Ni_{40}P_{14}B_6$, $Fe_{40}Ni_{40}B_{20}$ and $Zr_{74}Ti_{19}Cu_2Fe_5$. The $Fe_{67}Co_{18}B_{14}Si_1$, $Co_{66}Fe_4Si_{16}B_{12}Mo_2$, $Fe_{40}Ni_{40}P_{14}B_6$ and $Fe_{40}Ni_{40}B_{20}$ alloys exhibited an active to passive transition and the shapes of the polarisation curves varied greatly according to the alloy composition. The $Zr_{74}Ti_{19}Cu_2Fe_5$ alloy did not display an active region and passivated spontaneously in this medium.

The $Fe_{67}Co_{18}B_{14}Si_1$ and $Co_{66}Fe_4Si_{16}B_{12}Mo_2$ alloys displayed poor passivating ability in 1M KOH. Both alloys produced several anodic peaks and a current density that did not remain constant, suggesting that the structure and properties of the anodic film varied with the applied potential. Active regions of high current density were obtained in comparison to the FeNi and ZrTi-based alloys. The $Fe_{67}Co_{18}B_{14}Si_1$ alloy produced three anodic peaks in the active region at potentials of -1.35, -1.25 and -1.16V. The curve showed an active to passive transition at -0.80V, however the magnitude of the nominally passive current in the potential region -1.11 to -0.50V was almost as high as that of the active region. At potentials greater than -0.80V a decrease in the passive current density was observed. The current decrease may be associated with a restructuring of the passive layer or the formation of a new phase or oxide. A small anodic at -0.09V occurred just prior to transpassivity (0.04V). The shape of the curve and the magnitude of the current density were the same as that obtained by Crousier et al. [71] for the glassy alloy $Fe_{60}Co_{20}B_{10}Si_{10}$ (G14) of similar composition. The $Co_{66}Fe_4Si_{16}B_{12}Mo_2$ alloy produced a single anodic peak at -1.23V in the active region. Between potentials of -1.20 to -0.48V a broad peak with a current density of similar magnitude to the anodic peak was obtained, indicating that the alloy displayed a poor passivity in this potential region. A second anodic peak occurred at -0.29V was followed by a passive region that spanned a small potential range (-0.20 to -0.03V).

The $Fe_{40}Ni_{40}B_{20}$ and $Fe_{40}Ni_{40}P_{14}B_6$ alloys produced almost identical anodic polarisation curves suggesting that P is not important as regards redox properties of these glassy alloys. Single anodic peaks occurred at potentials of -1.03 and -1.02V for the $Fe_{40}Ni_{40}P_{14}B_6$ and $Fe_{40}Ni_{40}B_{20}$ alloys respectively, followed by a passive region of constant current density. The E_{corr} and E_{tr} values were very similar for both alloys. The shape and magnitude of the potential-current response obtained for the $Fe_{40}Ni_{40}P_{14}B_6$ alloy was the same as that obtained by Crousier et al. [71] for the same alloy, suggesting that our procedures produced results agreeing with published work, where available.

Sorensen et al. [72] investigated the anodic polarisation behaviour of glassy $Fe_{40}Ni_{40}P_{14}B_6$ in H_2SO_4. The polarisation curve in the acid medium was identical to the curve obtained in 1M KOH indicating that electrolyte pH did not influence the corrosion properties of the alloy. The active and passive regions were attributed to the formation of two separate regions of film growth. The current peak (200mV vs. SCE) was attributed to the formation of a thin black Ni-rich film and the passive region to the formation of a transparent Fe-rich film that was relatively more protective. AES analysis indicated that at active potentials the dissolution rate of Fe exceeded that of Ni, producing a Ni-rich surface that was also deficient in P and B. As the potential became more anodic the dissolution rate of Ni became higher than that of Fe and the Ni-rich film was replaced by an Fe-rich rich film until the transpassive potential was reached with the onset of oxygen evolution. The thickness of the passive film was around 80Å and the P content of the passive film was the same as the bulk alloy. Electrolyte pH did not influence the magnitude of the active or passive current densities indicating that the transition from a region of high current density to one of lower current density was not a true active-passive transition. This conclusion is based on the Pourbaix diagrams of Fe and Ni which indicate that the equilibrium between dissolved species and the oxide varies as a function of pH. The transition between the two types of film was potential dependent and was found to occur reversibly, which again refutes active-passive behaviour. Chaudhary et al. [73] obtained the same polarisation curve for $Fe_{40}Ni_{40}P_{14}B_6$ in 3.5% NaCl and attributed the active and passive regions to the same Fe and Ni-rich surface films. The glassy $Fe_{40}Ni_{40}B_{20}$ alloy did not passivate in 3.5% NaCl at 303K. In this electrolyte replacement of B by 14% P increased the corrosion resistance of the alloy. The polarisation curves of glassy $Fe_{40}Ni_{40}B_{20}$, $Fe_{80}B_{20}$, $Fe_{60}Ni_{20}B_{20}$ and $Fe_{20}Ni_{60}B_{20}$ in 1M H_2SO_4 all exhibited an active-passive transition. The current density in the passive region increased in the order $Fe_{20}Ni_{60}B_{20} < Fe_{40}Ni_{40}B_{20} < Fe_{60}Ni_{20}B_{20} < Fe_{80}B_{20}$. These results combined with EDS analysis indicate that the passive oxide layer that formed on the FeNiB alloys in H_2SO_4 was mainly iron oxide and not a nickel oxide [84].

The hitherto unstudied new $Zr_{74}Ti_{19}Cu_2Fe_5$ alloy displayed the highest passivity of the alloys tested and no active peak was identified indicating that passivation occurred spontaneously. The current density was very low throughout the passive region and transpassivity occurred at potentials greater than 0.16V, which was substantially higher than that of the other glassy alloys tested. E_{corr} also occurred at more noble potentials than the other glassy alloy compositions. The electrode surface was also shiny and polished on completion of the polarisation curve. Clearly this alloy has potentially excellent anticorrosive properties in basic media. The high corrosion resistance of Zr and Ti-based alloys is attributed to the formation of a highly protective oxide film [12]. Naka et al. [50] found that glassy $Zr_{50}Cu_{50}$ passivated spontaneously in 1N H_2SO_4, 1N HNO_3 and 1N NaOH but showed a poor corrosion resistance in aggressive chloride solutions such as 1N HCl and 3% NaCl. The corrosion resistance of glassy $Zr_{50}Cu_{50}$ was greater than that of the equivalent crystalline alloy, particularly in chloride-containing solutions. The high corrosion resistance of the glassy alloy was attributed to the Zr component and the homogeneous nature of the alloy structure which resulted in the formation of a uniform passive film that was resistant to attack.

5.3 CYCLIC VOLTAMMETRY OF GLASSY $Fe_{67}Co_{18}B_{14}Si_1$ IN 1M KOH

A typical voltammogram of glassy $Fe_{67}Co_{18}B_{14}Si_1$ in 1M KOH at 25°C is shown in Fig. 18. A sweep rate of 50mV/s was used since all of the peaks are clearly defined at this sweep rate and show the potential ranges associated with the different reaction processes. The voltammogram was initiated at -0.2V where no electrochemical reaction takes place and scanned in the negative direction to a potential of -1.72V at which hydrogen evolution begins

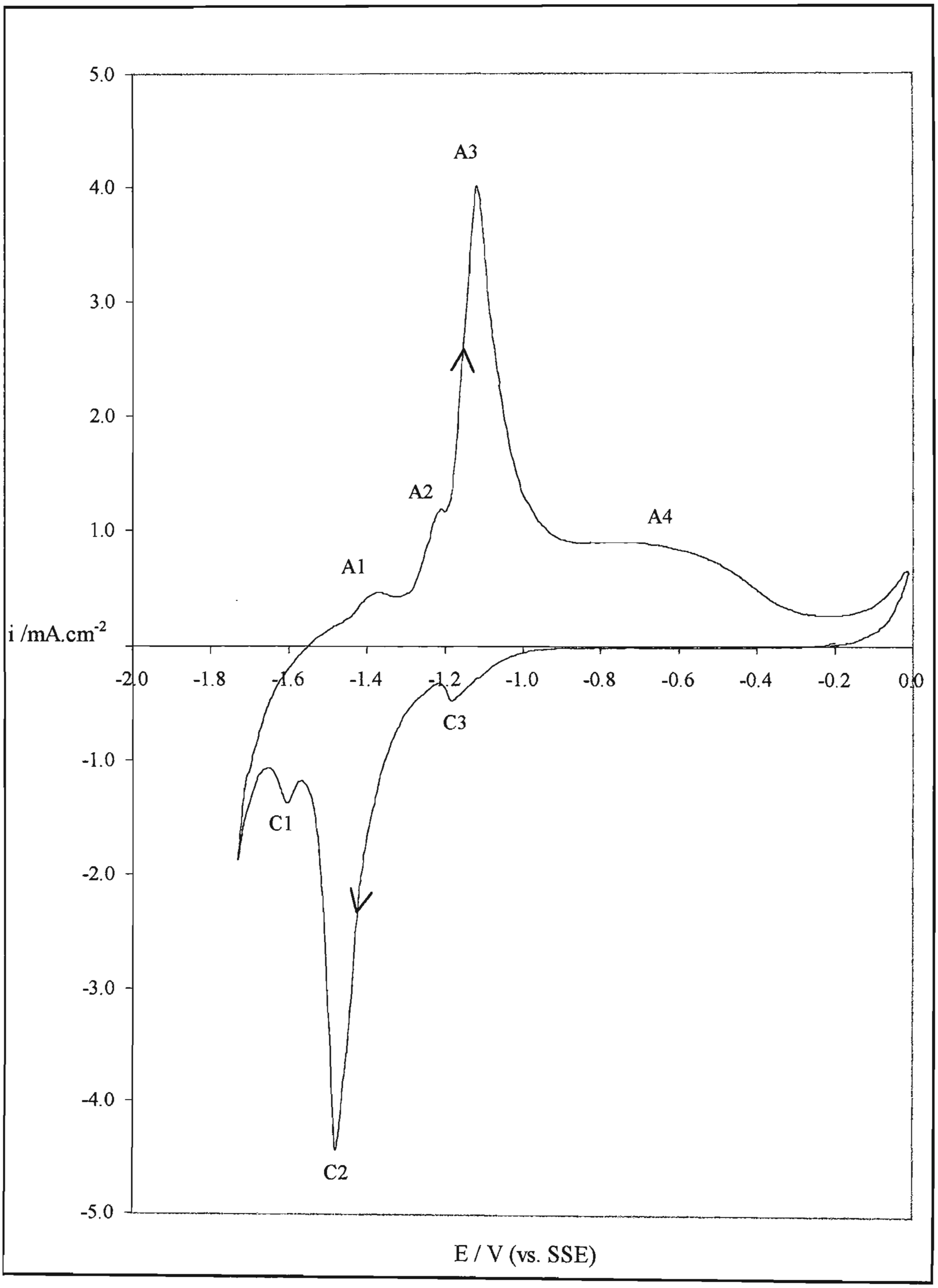

Fig. 18: Cyclic voltammogram of a $Fe_{67}Co_{18}B_{14}Si_1$ electrode in 1.0M KOH at 25°C, swept between –1.72 and –0.05V at 50mV/s, showing the four oxidation peaks and three reduction peaks.

and then in the opposite direction to the oxygen evolution potential at -0.05V. Four anodic peaks and three cathodic peaks were identified. Anodic peaks labeled A1 (-1.37V) and A2 (-1.20V) occurred at the most negative potentials with A2 forming a shoulder on the larger peak A3 (-1.12V). At the most positive potentials a broad peak A4 (-0.66V) was identified. The three cathodic peaks were labelled peak C1 (-1.61V), C2 (-1.48V) and C3 (-1.18V). The voltammogram of glassy $Fe_{67}Co_{18}B_{14}Si_1$ was similar to that obtained by Kreysa and Hakansson [68] at a glassy $Fe_{78}Si_{11}B_{11}$ electrode under the same experimental conditions, while glassy $Fe_{60}Co_{20}B_{10}Si_{10}$ [68] showed a complex peak multiplicity and did not show a close similarity to the former two alloys. However, the cyclic voltammograms of the glassy $Fe_{60}Co_{20}Si_{10}B_{10}$ alloy obtained by Alemu and Juttner [69] and Huot et al. [70] in 1M KOH corresponded closely to that of $Fe_{67}Co_{18}B_{14}Si_1$ alloy. Clearly Kreysa and Alemu do not agree indicating that the experiments need to be repeated independently for this alloy for confirmation of the results.

The CV responses were studied as a function of sweep rate and the potential range scanned. As the scan rate was increased, the current densities of peaks A3, A4 and C2 increased and masked the smaller peaks A1, A2, C1 and C3. At scan rates of 10, 20 and 50mV/s all peaks could be distinguished. At 100mV/s, peak C3 was masked and peaks A1, A2, and C1 formed shoulders in the dominant peaks A3 and C2. At sweep rates of 150mV/s and greater only peaks A3, A4 and C2 were visible indicating that these peaks represent diffusion processes. As the scan rate was increased less time was spent in the potential range in which the reaction occurred, causing the diffusion layer to become thinner and the flux of reactant to the electrode surface higher. The current densities of peaks A3 and C2 were measured at different sweep rates and are listed in Table 7. With increasing sweep rate peak A3 shifted towards more positive potentials and peak C2 towards more negative potentials resulting in an increase in peak separation. A linear i_p against $v^{1/2}$ relationship existed for both A3 and C2, indicating these peaks represented diffusion controlled processes i.e. electron transfer was fast with respect to diffusion. When peak A4 was omitted from the potential range scanned peak C3 was absent from the CV and the other peaks remained unaffected indicating that C3 and A4 were conjugated. Similar findings were obtained by Hout et al. [70] who measured the anodic/cathodic charge ratio Q_a/Q_c of the peaks A3 and C2 of the similar glassy $Fe_{60}Co_{20}B_{10}Si_{10}$ alloy. The ratio was greater than one indicating that the processes associated with these peaks were influenced by mass transport effects. It was suggested that peak A3 involved the diffusion of dissolved species in solution, possibly FeO_2^{2-}, and that a dissolution process accompanied the oxide film formation rather than a simple oxide film formation/reduction process involving only one species.

Table 7: Sweep rate dependence of the major anodic and cathodic peak currents of the glassy $Fe_{67}Co_{18}B_{14}Si_1$ electrode in 1M KOH at 25°C.

v / mV.s^{-1}	Anodic Peak (A3) i_p / mA.cm^{-2} (E_p / V)	Cathodic Peak (C2) i_p / mA.cm^{-2} (E_p / V)
10	0.587 (-1.156)	-0.676 (-1.464)
20	2.308 (-1.141)	-2.581 (-1.469)
50	4.350 (-1.120)	-4.420 (-1.475)
75	7.748 (-1.102)	-9.994 (-1.503)
100	10.000 (-1.081)	-12.500 (-1.517)
150	11.917 (-1.058)	-14.330 (-1.520)
200	15.015 (-1.021)	-18.260 (-1.530)
250	17.500 (-0.986)	-21.000 (-1.540)

5.3.1 Comparison with pure Fe

The shape of the cyclic voltammogram of glassy $Fe_{67}Co_{18}B_{14}Si_1$ was very similar to the voltammogram obtained by Graham [144] for polycrystalline Fe in work previously conducted in this laboratory. A CV of polycrystalline Fe in a 1M NaOH electrolyte is provided in Fig. 5 for comparison with the CV of $Fe_{67}Co_{18}B_{14}Si_1$ in Fig. 19. Four anodic peaks labelled a1, a2, a3 and a4 were obtained for the Fe electrode that were analogous to the peaks formed at the $Fe_{67}Co_{18}B_{14}Si_1$ electrode. Slight variations noted were that peak a2 of Fe formed a distinct and separate peak while peak A2 on $Fe_{67}Co_{18}B_{14}Si_1$ formed a shoulder on the main peak A3. Peak a4 on Fe was small and current densities at potentials more positive than this peak decayed to a passive potential region that extended to the onset of the oxygen evolution region. Peak A4 of glassy $Fe_{67}Co_{18}B_{14}Si_1$ was larger and broader so that the passive potential region of the alloy was reduced and also displayed a greater current density than the pure Fe electrode. Only two cathodic peaks, labelled c1 and c2, were identified on Fe that corresponded to peaks C1 and C2 on $Fe_{67}Co_{18}B_{14}Si_1$. Peak C3 was absent from pure Fe. By varying the potential window scanned, Graham found that the anodic peaks a1, a2 and a4 were conjugated to c1 and that peak a3 was conjugated to c2. It was proposed that the conjugated sets of peaks represented the formation of a duplex surface film in the alkaline electrolyte. Peaks a1, a2 and a4 were attributed to the formation of a passivating barrier layer adjacent to the Fe substrate consisting of FeO. Peak a3 was believed to result from the formation of an upper non-protective Fe_2O_3 and FeOOH layer [145]. Potential cycling resulted in a progressive increase in the current density of peaks a3 and c2 while a1, a2, and a4 remained constant. SEM analysis indicated that the base layer that formed maintained a uniform thickness with potential cycling while the upper layer became progressively thicker and eventually cracked and flaked [144].

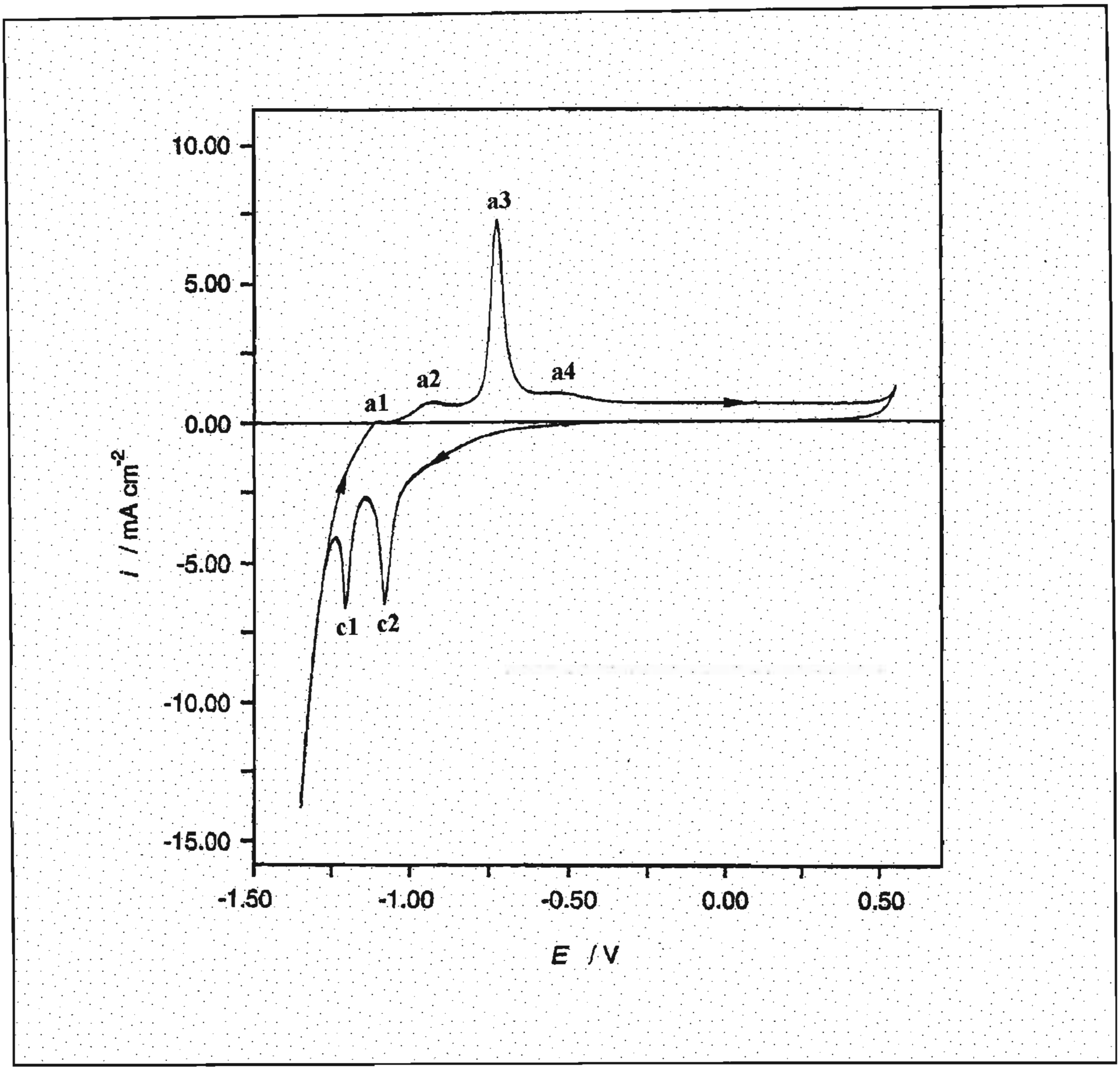

Fig. 19: A CV of polycrystalline Fe in 1M NaOH swept at 100mV/s between -1.35 and 0.55V (vs. SCE), showing the four oxidation and two reduction peaks [144].

Graham proposed a mechanism for dissolution of Fe in weakly alkaline electrolytes at ambient temperatures [144]. Since the close similarity between the cyclic voltammograms of polycrystalline Fe and glassy $Fe_{67}Co_{18}B_{14}Si_1$ indicate that the voltammetric response of the glassy alloy is predominantly that of pure Fe, the main species attributed to the Fe peaks have been outlined. Although the responses of Fe and $Fe_{67}Co_{18}B_{14}Si_1$ are qualitatively similar, they clearly will not be identical due to the extra metal and metalloid components of the glassy alloy and the possible influence of the amorphous structure. The suggested Fe responses are:

Peak a1: oxidation of Fe to form adsorbed hydroxy species, resulting in the growth of the inner surface layer:

$Fe + OH^- \rightarrow FeOH_{ads} + e^-$

Peak a2: Fe(II) oxide/hydroxide formation on the inner layer:

$FeOH_{ads} \rightarrow FeOH_{ads}^+ + e^-$

$FeOH_{ads}^+ + OH^- \rightarrow Fe(OH)_2$

$Fe(OH)_2 \rightarrow FeO + H_2O$

Peak a3: the a3 process proceeds in parallel to a1 and a2 and corresponds to the formation of an upper layer on the base layer consisting of Fe(III) oxide.

$FeO + 2OH^- \rightarrow FeO_2^{2-} + H_2O$

$FeO_2^{2-} + 2H_2O \rightarrow Fe(OH)_4^- + e$

$2Fe(OH)_4^- \rightarrow Fe_2O_3 + 4H_2O + O^{2-}$

Peak a4: oxidation of the FeO to Fe_2O_3.

$FeO \rightarrow Fe_2O_3 \rightarrow FeOOH$ (at higher potentials)

Peak c2: formation of soluble Fe(II) species:

$2FeOOH + 2e \rightarrow FeO_2^{2-} + FeO + H_2O$

Peak c1:

$FeO + 2OH^- \rightarrow FeO_2^{2-}$

$FeO_2^{2-} + 2H_2O + 2e \rightarrow 4Fe + 4OH^-$

5.3.2 Potential cycling of $Fe_{67}Co_{18}B_{14}Si_1$

The cyclic voltammogram of glassy $Fe_{67}Co_{18}B_{14}Si_1$ obtained after 18 cycles between the oxygen and hydrogen evolution limits is shown in Fig. 20. Again, the voltammogram of the glassy alloy is very similar to that obtained by Graham [144] after potential cycling of Fe under similar conditions. As observed for Fe, potential cycling resulted in only a small increase in the current densities of peaks A1, A2 and C1 while peaks A3 and C2 showed a much larger and progressive increase in magnitude. A steady state voltammogram was obtained at the Fe electrode after 50 cycles while the $Fe_{67}Co_{18}B_{14}Si_1$ alloy did not attain a steady state. Similarly, Alemu and Juttner [69] reported that steady state voltammograms were not obtained for the glassy $Fe_{78}Si_{11}B_{11}$ and $Fe_{60}Co_{20}B_{10}Si_{10}$ alloys. A visible orange/brown layer was observed to cover the $Fe_{67}Co_{18}B_{14}Si_1$ electrode that increased in

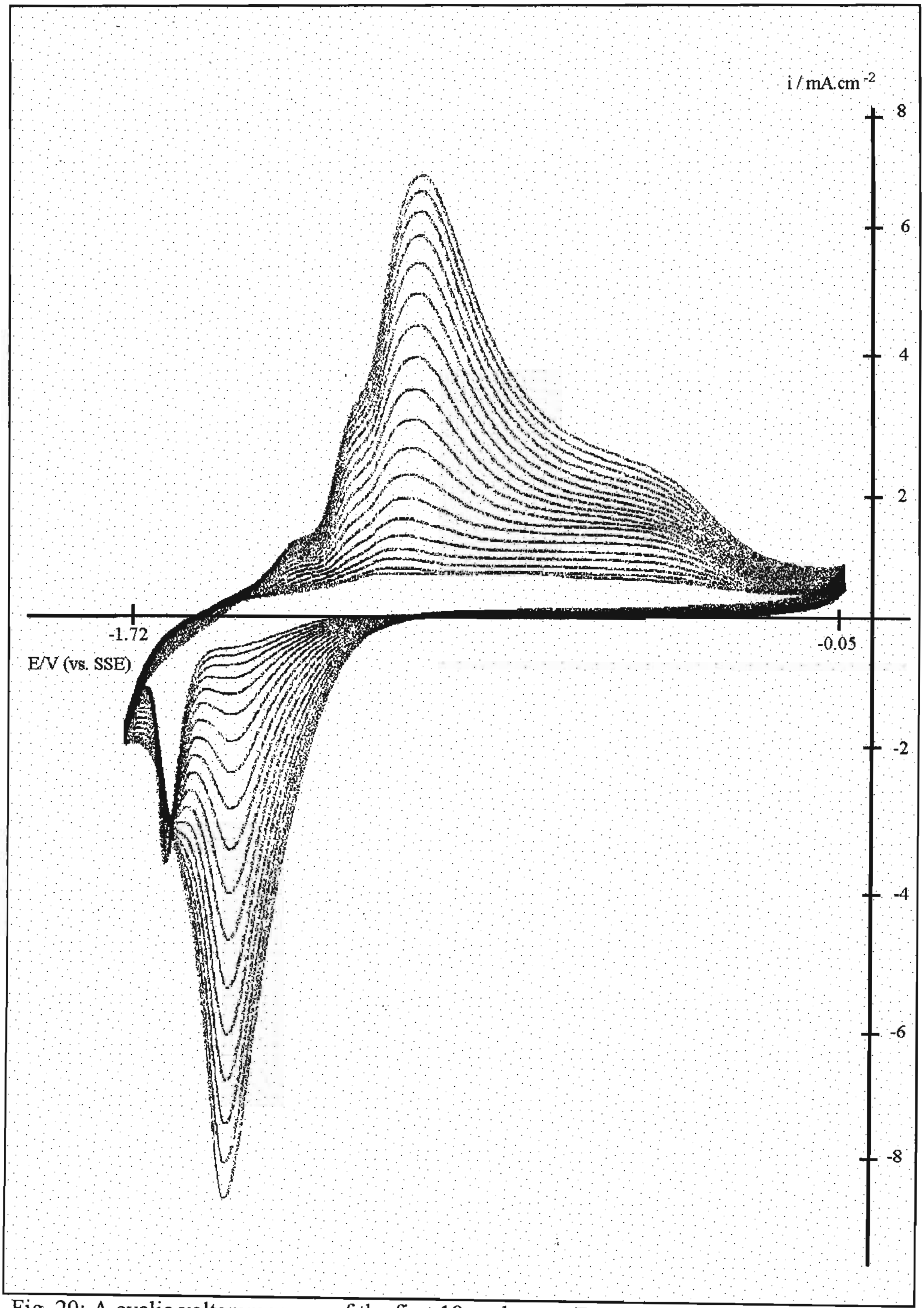

Fig. 20: A cyclic voltammogram of the first 18 cycles at a $Fe_{67}Co_{18}B_{14}Si_1$ electrode in 1.0 M KOH (25°C), swept at 100mV/s between -1.72 and -0.05V, showing the progressive buildup of the surface film.

thickness as the number of cycles increased and eventually cracked and flaked into the electrolyte as a discrete layer. A further difference noted between the glassy alloy and polycrystalline Fe was that cycling resulted in an increase in the current density of peak A4 while peak a4 of Fe was unaffected and was eventually masked by peak a3 as it increased in magnitude.

The increase in the peak current densities (A3, A4 and C2) of glassy $Fe_{67}Co_{18}B_{14}Si_1$ (Fig. 20) with potential cycling resulted from an increase in the electrode surface area due to buildup of the surface layer. The layer showed poor adherence to the electrode and if potential cycling was stopped for 10 minutes and then resumed, peaks A3 and C2 had decreased in height and then began to increase again. This could be attributed to dissolution of the surface layer into the electrolyte followed by further buildup of the layer when cycling was resumed. The rate of growth of the surface film was also dependent upon the applied potential sweep rate since the relative increase per cycle in i_p decreased with increasing sweep rate due to the shorter time spent in the potential regions of film growth (Table 7). With less oxide on the surface there was a greater probability that dissolution could occur. This was indeed indicated by the shift of the oxidation peaks to more positive potentials which in turn meant that the onset of passivation occurred later. Thus with more dissolution occurring the overall current density of the voltammogram was greater – which was observed experimentally.

A series of SEM micrographs of the glassy $Fe_{67}Co_{18}B_{14}Si_1$ surface after different numbers of potential cycles were obtained to show the progressive buildup of the surface layer on the electrode (Fig. 21).

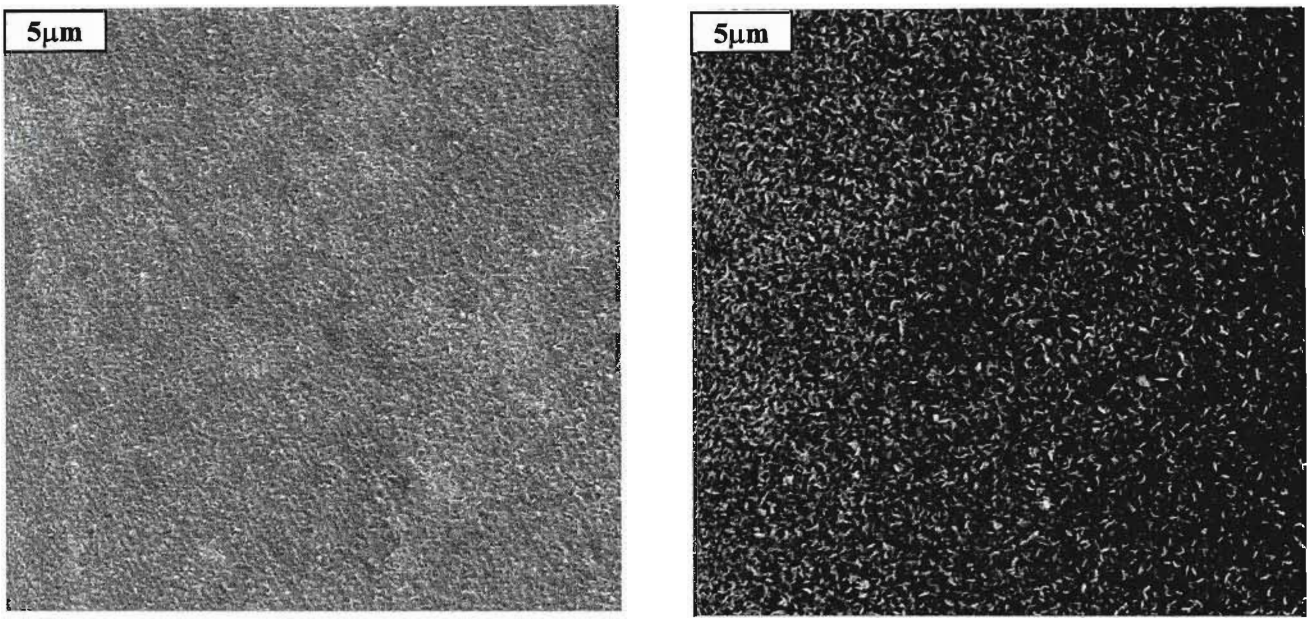

(a) 2 cycles showing coverage of the alloy substrate by small particles of uniform size (mag. x4000)

(b) 4 cycles showing enlargement of the particles and thickening of the surface layer (mag. x4000)

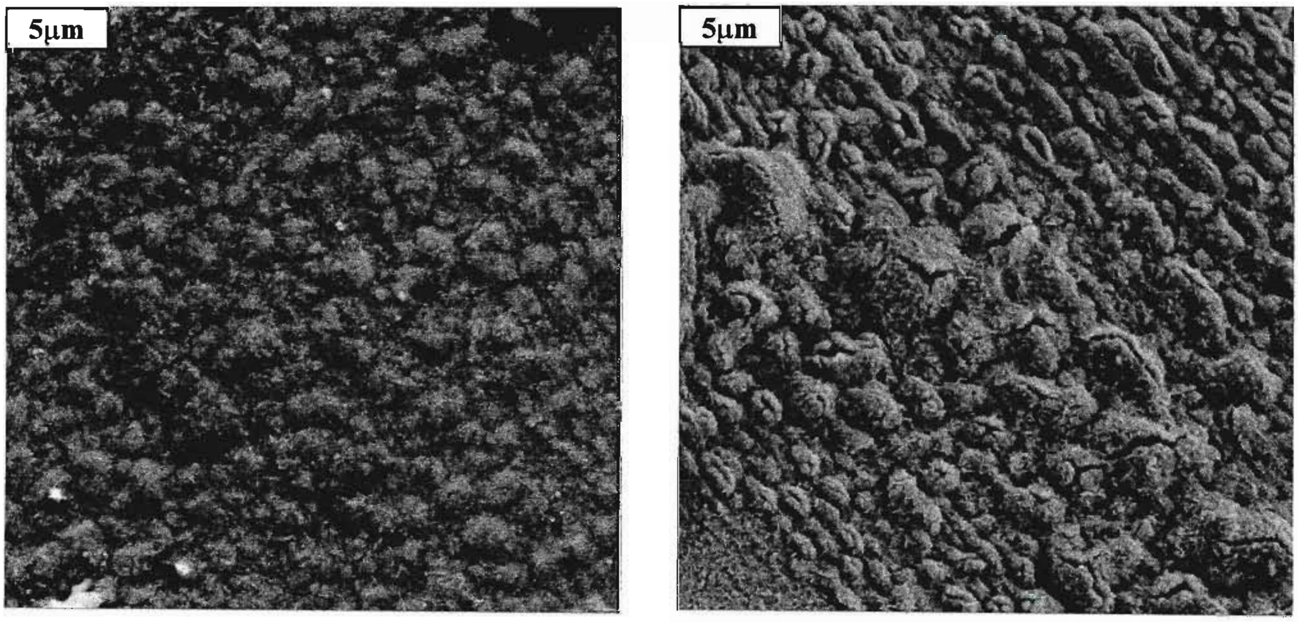

(c) 8 cycles showing a dense and compact layer with the development of small cracks within the layer (mag. x4000)

(d) 15 cycles showing further surface layer thickening to produce an uneven surface with more extensive crack formation (mag. x4000)

Fig. 21: SEM micrographs showing the buildup of the surface film on the glassy $Fe_{67}Co_{18}B_{14}Si_1$ electrode after different numbers of potential cycles between -1.72 and -0.05V in 1M KOH at 100mV/s.

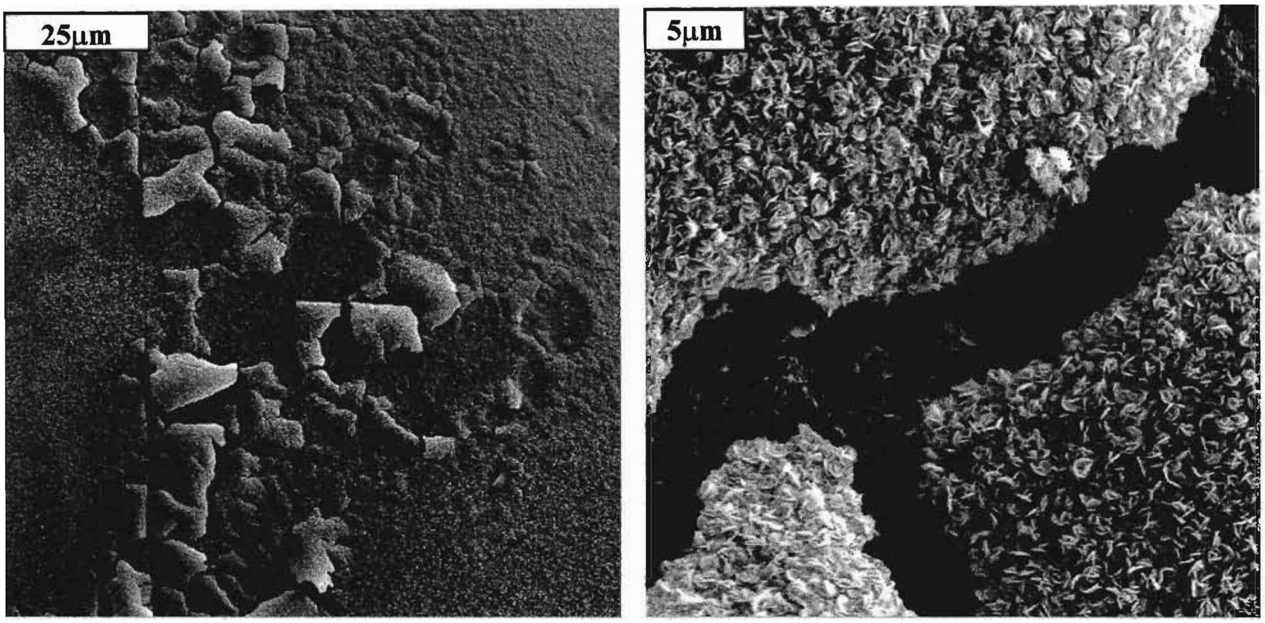

(e) 25 cycles showing more severe cracking and flaking of the alloy surface (mag. x500)

(f) enlargement of (e) showing a flaking portion of the surface layer with further crack formation within the main crack visible (mag. x4000)

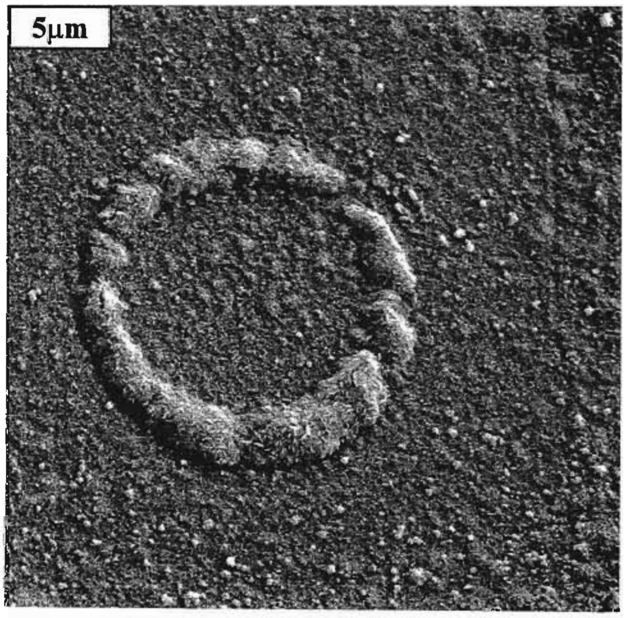

(g) enlargement of (e) in which a flaked portion of the alloy surface has lifted to reveal a raised circular region (mag. x4000)

Fig. 21: continued

After two cycles the alloy surface was covered by small particles of uniform size with substrate alloy still visible between the particles. Four cycles resulted in enlargement of the individual particles and general thickening of the layer. After eight cycles a thick and compact layer with an uneven surface had formed and small cracks were visible in the layer. After 15 cycles progressive thickening as well as more extensive cracking of the layer was observed. After 25 cycles sections of the surface layer began to flake and the flaked portions lifted to expose raised circular regions on the alloy substrate. These regions were similar to circular regions that have also been observed to form crystalline alloy surfaces that are referred to as nucleation exclusion zones. Graham [144] identified such regions on the surface of Fe electrodes in 0.5M NaOH. The circles on the crystalline surface had a smaller diameter (approximately 1μm) than those on the glassy $Fe_{67}Co_{18}B_{14}Si_1$ surface (5-15μm). No conclusive explanation as to why these regions form has been proposed. The distinct duplex nature of the surface film that formed on pure Fe was not apparent on the $Fe_{67}Co_{18}B_{14}Si_1$ alloy surface, possibly due to a continuum between the base and upper layer and the influence of the other alloy metal and metalloid components.

EDS analyses of the $Fe_{67}Co_{18}B_{14}Si_1$ surface after different numbers of potential cycles were obtained to monitor changes in the alloy surface concentration (Table 8). Again, the analyses were performed at fairly low magnification (x1000) and represent the general surface composition.

Table 8: EDS analysis of the glassy $Fe_{67}Co_{18}B_{14}Si_1$ surface after different numbers of CV cycles (100mV/s).

	Fe	**Co**	**Si**	**O**
Polished electrode surface	77.80	21.22	0.98	0
General analysis after 2 CV cycles	78.88	20.42	0.70	0
General analysis after 4 CV cycles	79.43	19.93	0.64	0
General analysis after 8 CV cycles	79.98	17.58	0.56	1.88
General analysis after 15 CV cycles	66.56	16.78	0.42	16.24
General analysis after 25 CV cycles	63.20	16.21	0.54	20.05
Spot analysis of a flake after 25 CV cycles	55.95	14.39	0.55	29.11
Spot analysis within a crack after 25 CV cycles	73.32	18.86	0.51	7.31

Oxygen was detected in the surface layer after 8 potential cycles when substantial thickening of the layer had occurred. With an increasing number of cycles the oxygen concentration increased progressively. Within the surface layer Fe enrichment and a corresponding Co depletion was detected in comparison to the base alloy substrate. Spot EDS analysis of a raised and flaking portion of the surface layer indicated that it had a significantly higher oxygen concentration than a spot EDS analysis within a crack suggesting that the surface layer was composed of an iron oxide. To avoid the interfering influence of the base alloy substrate in the analysis, flaking sections were scraped off the electrode surface and analysed separately by EDS. Results showed that the flaked portion consisted exclusively of Fe and O and it was suggested that these portions were composed of Fe_2O_3.

5.4 ELECTROCATALYSIS BY GLASSY $Fe_{67}Co_{18}B_{14}Si_1$ AND $Co_{66}Fe_4Si_{16}B_{12}Mo_2$ FOR THE HER

5.4.1 As-polished electrodes at different electrolyte temperatures

Tafel parameters, i_o and b, were obtained for hydrogen evolution at the as-polished glassy $Fe_{67}Co_{18}B_{14}Si_1$ electrode in 1M KOH at temperatures ranging between 25 and 70°C and the values obtained are listed in Table 9. These values were calculated from Tafel plots such as illustrated in Fig. 22.

Table 9: Kinetic data for hydrogen evolution on as-polished $Fe_{67}Co_{18}B_{14}Si_1$ in alkaline solution (1M KOH) at different temperatures.

T /°C	Tafel range / V	-b / mV	i_o / A.cm^{-2}	i_1^* / mA.cm^{-2}	$i_2^{\otimes}$ / mA.cm^{-2}	$i_3^{\oplus}$ / mA.cm^{-2}
25	-1.63 to -1.82	120 ± 7	(3.08 ± 0.80) x 10^{-5}	0.221 ± 0.055	0.560 ± 0.150	1.421 ± 0.431
30	-1.62 to -1.80	116 ± 8	(4.71 ± 0.93) x 10^{-5}	0.352 ± 0.038	0.903 ± 0.029	2.317 ± 0.080
40	-1.62 to -1.77	109 ± 5	(6.89 ± 0.58) x 10^{-5}	0.623 ± 0.044	1.629 ± 0.161	4.259 ± 0.600
50	-1.62 to -1.75	117±11	(8.92 ± 0.35) x 10^{-5}	0.747 ± 0.107	1.975 ± 0.431	5.219 ± 1.796
70	-1.61 to -1.74	123 ± 8	(1.55 ± 0.30) x 10^{-4}	1.061 ± 0.049	2.673 ± 0.020	6.732 ± 0.225

Nb. The b and i_o values reported were average values obtained from six Tafel plots obtained in independent experiments.

* E = -1.65V,$^{\otimes}$ E = -1.70V, $^{\oplus}$ E = -1.75V (vs. SSE)

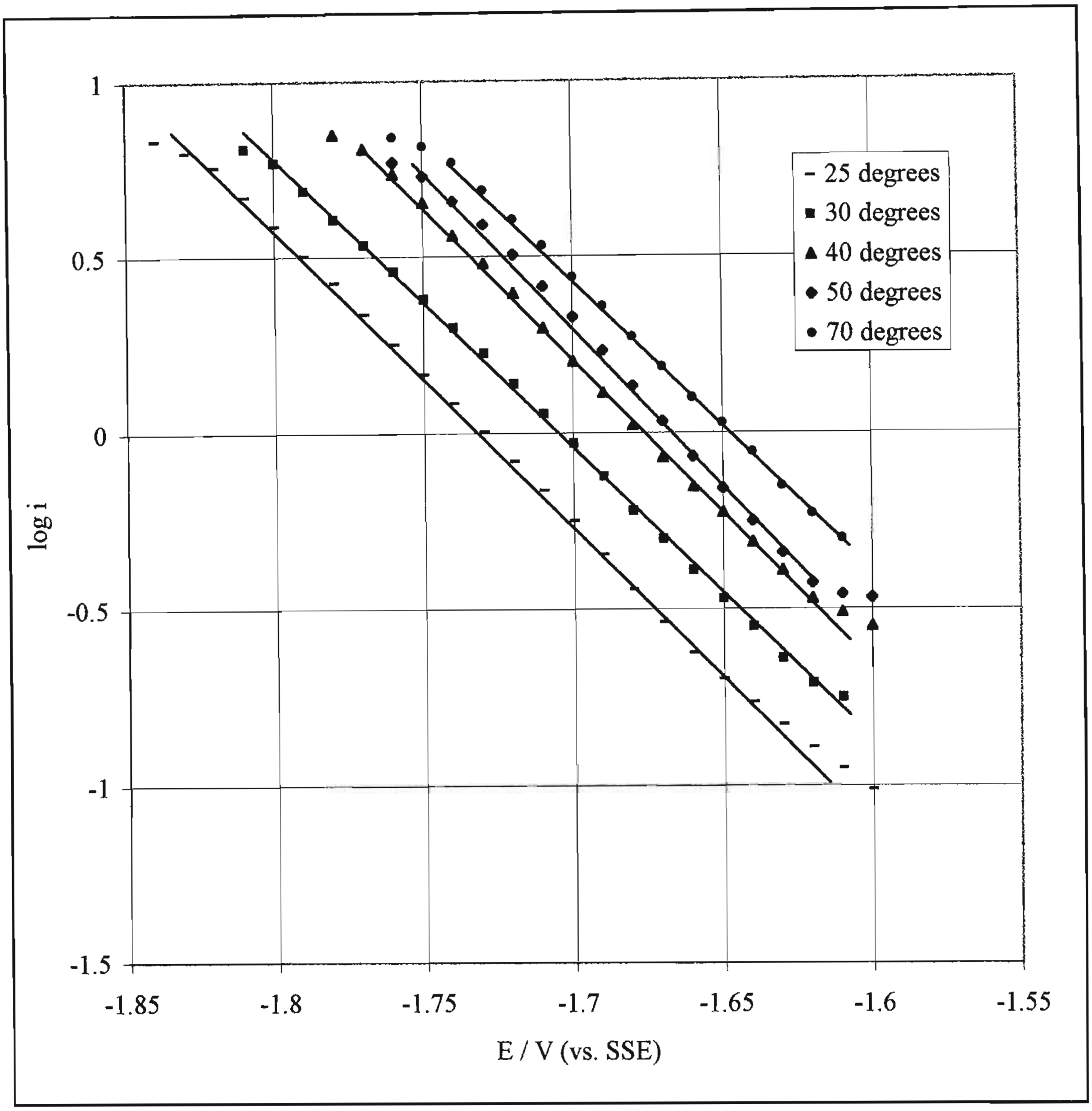

Fig. 22: Tafel plots of hydrogen evolution on the glassy $Fe_{67}Co_{18}B_{14}Si_1$ alloy surface in 1M KOH at different temperatures.

The $Fe_{67}Co_{18}B_{14}Si_1$ alloy displayed an improved electrocataytic activity for hydrogen evolution with increasing electrolyte temperature. Improved activity is indicated by an increase in the magnitude of the exchange current density, i_o at $\eta = 0$, and the current densities measured at different overpotentials within the linear Tafel region, i.e. -1.65V ($\eta = 0.10V$), -1.70V ($\eta = 0.15V$) and -1.75V ($\eta = 0.20V$). A high electrocatalytic activity is also associated with lower Tafel slope values. As the Tafel slope decreases in value the rate of increase of the current density in the Tafel region increases, i.e. there is an increase in the rate at which the HER occurs. The Tafel region of the $Fe_{67}Co_{18}B_{14}Si_1$ alloy spanned a potential range of approximately 0.2V but diffusion limited behaviour was reached more rapidly as the temperature was increased so that the upper potential limit of the Tafel region decreased. The Tafel slopes remained constant with an approximate value of 120mV obtained at each temperature tested. The constant Tafel slopes produced parallel current-voltage plots and consequently a constant rate of hydrogen evolution at each temperature. Electrochemical processes that occur in a multistep sequence often exhibit Tafel slopes of high value (~120mV) [146]. Tafel slopes that are independence of temperature do not correspond to the theoretical Tafel relation, $b = RT/\alpha nF$, which predicts that b should increase with increasing temperature. It is reported that the temperature dependence of Tafel slopes rarely represents the experimentally observed electrode-kinetic behaviour of electrochemical processes, in particular the supposed linear proportionality of b to T [5]. The exchange current density of the $Fe_{67}Co_{18}B_{14}Si$ alloy increased in a linear manner with increasing temperature from 3.08×10^{-5} A.cm^{-2} at 25°C to 15.5×10^{-5} A.cm^{-2} at 70°C. The current densities measured at potentials of -1.65, -1.70 and -1.75V showed a similar trend.

Tafel parameters obtained at the glassy $Co_{66}Fe_4Si_{16}B_{12}Mo_2$ electrode at different electrolyte temperatures are listed in Table 10 and the corresponding Tafel plots are shown in Fig. 23.

Table 10: Kinetic data for hydrogen evolution on the as-polished $Co_{66}Fe_4Si_{16}B_{12}Mo_2$ electrode in 1M KOH at different temperatures.

	High η region			Low η region					
T /°C	Tafel range /V	-b /mV	i_o /A.cm^{-2}	Tafel range / V	-b /mV	i_o /A.cm^{-2}	i_1* /mA.cm^{-2}	$i_2^{\otimes}$ /mA.cm^{-2}	$i_3^{\oplus}$ /mA.cm^{-2}
25	-1.74 to -1.88	103 ± 9	(1.54 ± 0.58) x10^{-5}	-1.61 to -1.74	158 ± 13	(8.25 ± 3.09) x 10^{-5}	0.267 ± 0.061	1.132 ± 0.398	9.734 ± 2.348
30	-1.73 to -1.86	115 ± 5	(4.60 ± 1.14) x10^{-5}	-1.64 to -1.73	157 ± 20	(1.22 ± 0.48) x 10^{-4}	0.435 ± 0.077	1.509 ± 0.256	15.109 ± 1.752
40	-1.73 to -1.85	126 ± 4	(8.63 ± 3.79) x10^{-5}	-1.62 to -1.73	146 ± 3	(1.77 ± 0.51) x 10^{-4}	0.637 ± 0.118	3.055 ± 0.472	18.414 ± 2.857
50	-1.74 to -1.84	134 ± 5	(1.91 ± 0.80) x 10^{-4}	-1.60 to -1.74	148 ± 9	(2.63 ± 0.43) x 10^{-4}	1.067 ± 0.241	5.012 ± 0.273	25.567 ± 2.939
70	-1.73 to -1.79	132 ± 4	(4.33 ± 0.64) x 10^{-4}	-1.62 to -1.73	159 ± 4	(7.62 ± 0.60) x10^{-4}	2.444 ± 0.591	11.328 ± 1.750	58.087 ± 5.255

* E = -1.64V, $^{\otimes}$E = -1.74V, $^{\oplus}$E = -1.84V (vs. SSE)

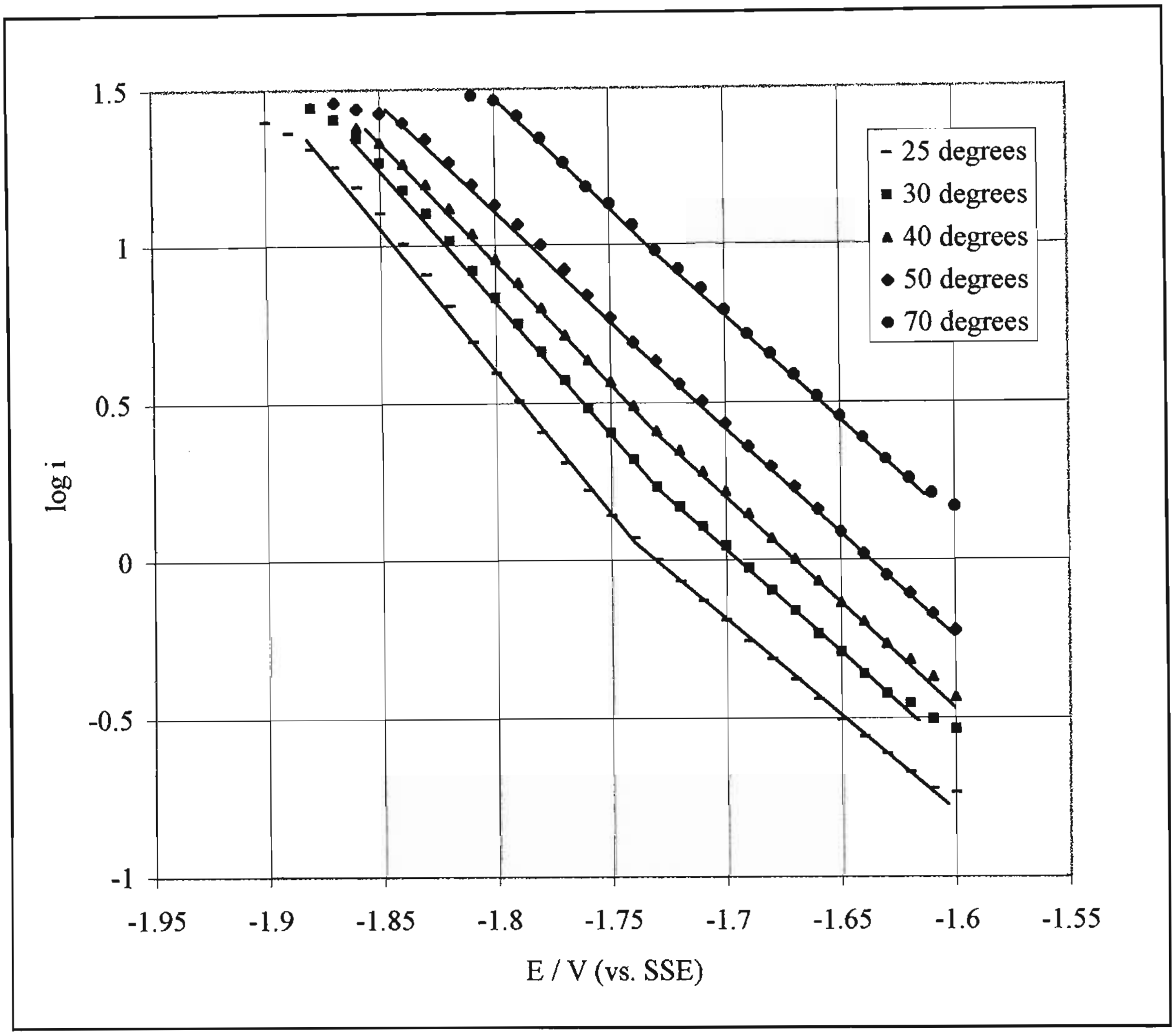

Fig. 23: Tafel plots of hydrogen evolution on the glassy $Co_{66}Fe_4Si_{16}B_{12}Mo_2$ alloy surface in 1M KOH at different temperatures.

Two distinct linear Tafel slopes were identified within the Tafel region that extended over a total potential range of 0.25V. The Tafel parameters from both regions are recorded in Table 10 and are labeled as the low overpotential region (extending from -1.64 to -1.74 at 25°C) and the high overpotential region (extending from -1.74 to -1.88 at 25°C). At all temperatures tested the high overpotential region had a lower Tafel slope and hence a higher electrocatalytic activity for hydrogen evolution than the low overpotential region. This behaviour is characteristic of a mechanism change between two parallel processes. When the high overpotential region has a higher slope than the low overpotential region then the phenomenon is generally characteristic of a change of mechanism between two processes in series [147]. Other glassy metal alloys compositions, such as $Co_{50}Ni_{25}Si_{15}B_{10}$, $Ni_{50}Co_{25}Si_{15}B_{10}$ and $Ni_{50}Co_{25}P_{15}B_{10}$ have also been reported to produce double Tafel slopes for the HER and display a lower activity at low overpotentials and an improved activity at higher overpotentials [68]. The change in slope indicates a possible change in the desorption mechanism [148] and/or the state of the adsorption intermediates on passing from low to high overpotentials [109]. The change in Tafel slope at the $Co_{66}Fe_4Si_{16}B_{12}Mo_2$ electrode occurred at a constant potential of -1.74V (vs. SSE) that remained unaffected by temperature. As outlined in section 2.4.2, the HER occurs by a two step pathway at an alloy surface due to the formation of the adsorbed hydrogen intermediates. The reaction is complex due to the fact that hydrogen desorption can occur by either a chemical or an electrochemical mechanism with either the hydrogen adsorption or desorption step forming the rate determining step. Further investigation would be required to determine the mechanism by which hydrogen evolution occurs at the glassy $Co_{66}Fe_4Si_{16}B_{12}Mo_2$ electrode surface in both the high and low overpotential regions.

In contrast with glassy $Fe_{67}Co_{18}B_{14}Si_1$, the Tafel slopes of the $Co_{66}Fe_4Si_{16}B_{12}Mo_2$ electrode in the high overpotential region increased slightly with increasing temperature, resulting in a convergence of the Tafel lines in this region. This response is in agreement with the classical form, $b = RT/\alpha nF$, which predicts that b should increase with increasing T and that the transfer coefficient, α, is a temperature independent parameter. In the low overpotential region the Tafel slope remained constant with increasing temperature, as was observed for the $Fe_{67}Co_{18}B_{14}Si_1$ alloy, producing parallel Tafel lines.

The i_o values of glassy $Co_{66}Fe_4Si_{16}B_{12}Mo_2$ in the high overpotential region were very similar to those of glassy $Fe_{67}Co_{18}B_{14}Si_1$ at temperatures of 25 to 40°C. However, the $Co_{66}Fe_4Si_{16}B_{12}Mo_2$ alloy showed a greater temperature dependence and produced greater i_o and consequently showed a higher electrocatalytic activity for hydrogen evolution than $Fe_{67}Co_{18}B_{14}Si_1$ at 50 and 70°C. The i_o values of $Co_{66}Fe_4Si_{16}B_{12}Mo_2$ increased from 1.54×10^{-5} (25°C) to 43.3×10^{-5} $A.cm^{-2}$ (70°C) in the high overpotential region and from 8.25×10^{-5} (25°C) to 76.2×10^{-5} $A.cm^{-2}$ (70°C) in the low overpotential region.

No literature Tafel parameters have been reported for hydrogen evolution at the glassy $Fe_{67}Co_{18}B_{14}Si_1$ and $Co_{66}Fe_4Si_{16}B_{12}Mo_2$ alloy surfaces, however, the values of the similar amorphous alloy compositions, $Fe_{78}Si_{11}B_{11}$ and $Fe_{60}Co_{20}B_{10}Si_{10}$, have been measured in 1M KOH at different temperatures and these values are reported in Table 11 for comparison with our values obtained for the glassy $Fe_{67}Co_{18}B_{14}Si_1$ (Table 9) and $Co_{66}Fe_4Si_{16}B_{12}Mo_2$ (Table 10) alloys.

Table 11: Literature Tafel parameters [68,69,71,95] for hydrogen evolution on glassy $Fe_{60}Co_{20}B_{10}Si_{10}$ and $Fe_{78}Si_{11}B_{11}$ alloys and polycrystalline Fe, Co and Pt in 1M KOH at different temperatures.

Electrode	**T / °C**	**i_o / A.cm^{-2}**	**-b / mV**	**Reference**
$Fe_{60}Co_{20}B_{10}Si_{10}$	25	1.0×10^{-6}	95	69
	50	4.8×10^{-5}	140	
	75	2.7×10^{-4}	150	
$Fe_{60}Co_{20}B_{10}Si_{10}$	30	$(6.86 \pm 3.02) \times 10^{-5}$	128 ± 7	68
	50	$(1.96 \pm 0.44) \times 10^{-4}$	125 ± 5	
	70	$(1.04 \pm 0.28) \times 10^{-3}$	132 ± 7	
	90	$(2.02 \pm 0.4) \times 10^{-3}$	166 ± 7	
$Fe_{60}Co_{20}B_{10}Si_{10}$	25	1.4×10^{-6}	97	71
$Fe_{78}Si_{11}B_{11}$	30	$(1.62 \pm 0.27) \times 10^{-5}$	137 ± 3	68
	50	$(1.51 \pm 0.38) \times 10^{-4}$	187 ± 10	
	70	$(3.09 \pm 0.62) \times 10^{-4}$	225 ± 11	
	90	1.37×10^{-4}	134 ± 38	
$Fe_{78}Si_{11}B_{11}$	25	1.0×10^{-6}	140	69
	50	5.0×10^{-5}	150	
	75	1.6×10^{-4}	155	
Fe	25	1.0×10^{-5}	135	69
	50	3.3×10^{-5}	140	
	75	4.0×10^{-5}	150	
Fe	30	$(9.38 \pm 2.33) \times 10^{-5}$	160 ± 6	68
	50	$(3.18 \pm 0.47) \times 10^{-4}$	165 ± 4	
	70	$(5.83 \pm 2.07) \times 10^{-4}$	182 ± 12	
	90	$(4.59 \pm 1.90) \times 10^{-4}$	190 ± 19	
Co	30	$(4.55 \pm 3.77) \times 10^{-7}$	76 ± 5	68
	50	$(2.29 \pm 0.54) \times 10^{-4}$	197 ± 7	
	70	$(5.49 \pm 2.59) \times 10^{-4}$	228 ± 27	
	90	$(1.93 \pm 0.51) \times 10^{-3}$	323 ± 27	
Pt	25	2.4×10^{-5}	120	69
	50	4.8×10^{-5}	150	
	75	3.3×10^{-4}	170	
Pt	30	$(3.16 \pm 2.68) \times 10^{-4}$	141 ± 45	68
	50	$(8.70 \pm 7.60) \times 10^{-4}$	131 ± 52	
	70	$(1.21 \pm 0.93) \times 10^{-3}$	131 ± 47	
	90	$(1.07 \pm 0.38) \times 10^{-3}$	172 ± 12	
Ni	25	1.5×10^{-5}	-	95

Discrepancies exist in the Tafel parameters reported for hydrogen evolution at the glassy $Fe_{60}Co_{20}B_{10}Si_{10}$ electrode. Alemu and Juttner [69] and Crousier et al. [71] obtained similar Tafel slopes and exchange currents at 25°C while Kreysa and Hakansson [68] obtained b and i_o values that were substantially larger at each temperature (Table 11). For example, at 25°C, Alemu and Juttner obtained i_o and b values of 1.0×10^{-6} A.cm^{-2} and 95 mV respectively while Kreysa and Hakansson obtained i_o and b values of 6.86×10^{-5} A.cm^{-2} and 128 mV. Inconsistencies were also found in the i_o values obtained at the glassy $Fe_{78}Si_{11}B_{11}$ electrode with the i_o values obtained by Alemu and Juttner showing a greater temperature dependence than the values obtained by Kreysa and Hakansson. These variations could possibly result from different surface preparation techniques. Alemu and Juttner and Kreysa and Hakansson did not describe their pretreatment procedure used prior to cathodic polarisation i.e. whether the alloy was tested in the as-quenched state, the dull or bright ribbon surface exposed to the electrolyte or if the alloy surface was prepared by mechanical or electrochemical polishing. The method of pretreatment will influence the results obtained, particularly when the as-quenched alloy forms a surface oxide film, and further investigation in which identical preparation techniques are used is required for confirmation of the results. Crousier et al. [71] tested the alloys in the as-quenched state with the bright surface of the ribbon exposed to the electrolyte without surface polishing. This differs from the pretreatment method used in this study in which the alloy surface was mechanically polished with Al_2O_3 powder in order to produce a reproducible electrode surface for each experiment. It is generally accepted that polishing of a metal surface generates stress (and hence stressed sites) in the surface, often by folding of the metal layers, and we suggest that these sites may serve as adsorption nuclei that enhance the activity of the electrode in comparison to its as-quenched state. Polishing also removes the surface oxide layer and could account for the greater i_o value of 3.08×10^{-5}A.cm^{-2} (25°C) obtained at the glassy $Fe_{67}Co_{18}B_{14}Si_1$ surface in comparison to the value of 1.4×10^{-6} A.cm^{-2} (25°C) obtained by Crousier et al. [71] for glassy $Fe_{60}Co_{20}Si_{10}B_{10}$. Karve et al. [149] studied the oxide layer that formed on the as-quenched glassy $Fe_{67}Co_{18}B_{14}Si_1$ surface by AES. It was found that the alloy surface was B-enriched and depleted in Co and Fe. The segregation of B was believed to prevent further oxidation and contribute to the corrosion resistance of $Fe_{67}Co_{18}B_{14}Si_1$ in the as-quenched state by preventing further corrosion of the metallic elements. A similar effect would also be predicted to occur on the as-quenched glassy $Co_{66}Fe_4Si_{16}B_{12}Mo_2$, $Fe_{60}Co_{20}B_{10}Si_{10}$ and $Fe_{78}Si_{11}B_{11}$ surfaces.

The i_o and b values obtained by both Alemu and Juttner [69] and Kreysa and Hakansson [68] for hydrogen evolution at glassy $Fe_{60}Co_{20}B_{10}Si_{10}$ show a far greater temperature dependence than the values obtained at the glassy $Fe_{67}Co_{18}B_{14}Si_1$ alloy tested in this study. This indicates that the $Fe_{60}Co_{20}B_{10}Si_{10}$ alloy displays a better electrocatalytic activity for the HER with increasing electrolyte temperature than the $Fe_{67}Co_{18}B_{14}Si_1$ alloy. The i_o and b values of glassy $Fe_{78}Si_{11}B_{11}$ [68,69] showed a similar temperature dependence to that of glassy

$Fe_{60}Co_{20}B_{10}Si_{10}$. The most significant difference between glassy $Fe_{60}Co_{20}B_{10}Si_{10}$, $Fe_{75}Si_{11}B_{11}$ and $Fe_{67}Co_{18}B_{14}Si_1$ is the metalloid Si concentration and it is suggested that the greater Si content is responsible for the superior activity of the $Fe_{60}Co_{20}B_{10}Si_{10}$ and $Fe_{78}Si_{11}B_{11}$ alloys for the HER.

The i_o values of glassy $Fe_{67}Co_{18}B_{14}Si_1$ were most similar to the values obtained for polycrystalline Fe [68,69] as both showed only a slight temperature dependence. The Tafel slopes of Fe, however, were greater in magnitude and increased with increasing temperature in comparison to $Fe_{67}Co_{18}B_{14}Si_1$ electrode. Tafel plots obtained by Alemu and Juttner [69] indicate that the Fe-based glassy $Fe_{60}Co_{20}B_{10}Si_{10}$ and $Fe_{75}Si_{11}B_{11}$ alloys are better electrocatalysts for hydrogen evolution than polycrystalline Fe. They reported that at a constant current density the overpotential of glassy $Fe_{78}Si_{11}B_{11}$ was 80mV lower than that of polycrystalline Fe. Addition of 20% Co to form glassy $Fe_{60}Co_{20}B_{10}Si_{10}$ resulted in a further 30mV decrease in overpotential at the same current density. With increasing temperature the i_o values of $Fe_{60}Co_{20}B_{10}Si_{10}$ became significantly greater than polycrystalline Fe. These results are also supported by Kreysa and Hakansson [68] who found that glassy $Fe_{60}Co_{20}B_{10}Si_{10}$ provided lower overvoltages for hydrogen evolution than polycrystalline Pt and Ni (good catalysts for hydrogen evolution). Therefore, the activity of glassy $Fe_{67}Co_{18}B_{14}Si_1$ for hydrogen evolution is most similar to polycrystalline Fe, while the addition of 10 wt% Si to the alloy results in a significant improvement in activity. The addition of 20 wt% Co + 10wt% Si to form glassy $Fe_{60}Co_{20}Si_{10}B_{10}$ results in a further increase in activity, possibly due to a synergistic interaction between the Co and Si components. Further investigation is required to determine the chemical mechanism by which these effects take place.

The i_o values of glassy $Co_{66}Fe_4Si_{16}B_{12}Mo_2$ (Table 10) were greater than both polycrystalline Fe and Co at the temperatures tested (Table 11) indicating that the activity of the glassy alloy for hydrogen evolution was higher than its metal components. The Tafel slopes of the glassy alloy were generally lower than Fe and Co indicating that the rate of hydrogen evolution was faster at the alloy surface. This was in agreement with observations made by Kreysa and Hakansson [68] for hydrogen evolution at $Co_{66}Fe_4Mo_2Si_{16}B_{12}$. They reported that the Tafel parameters of the glassy alloy did not correspond with either the pure Fe or Co metal components, however, they did not record the i_o and b values that they obtained and so direct comparisons between their results and those presented in Table 6 could not be made.

5.4.1.1 Arrhenius Plots

Activation energies were calculated from Arrhenius plots for the glassy $Fe_{67}Co_{18}B_{14}Si_1$ and $Co_{66}Fe_4Si_{16}B_{12}Mo_2$ alloys.
The Arrhenius equation is:

$$\ln k = \ln A - E_a/RT$$

where A is a pre-exponential factor (s^{-1}), k is the rate constant and E_a is the activation energy (kJ/mole) of a kinetically limited reaction. The apparent activation energies for hydrogen evolution on the glassy metal surfaces were calculated using the experimental i_o values (taken as a measure of the reaction rate at zero overpotential) at five different electrolyte temperatures tested using the following modification of the Arrhenius equation:

$$\ln i_o = \ln A - E_{a,\eta=0}/RT$$

If a plot of the natural logarithm of the exchange current density versus the inverse of time yields a straight line, then the value of the apparent activation energy, $E_{a,\eta=0}$, for hydrogen evolution can be obtained from the slope of the graph. Activation energies can also be calculated at different overpotentials to determine the relationship between E_a and η.

Linear relationships were obtained for plots of $\ln i_o$ vs. 1/T for hydrogen evolution ($\eta = 0$) at the glassy $Fe_{67}Co_{18}B_{14}Si_1$ (Fig. 24) and $Co_{66}Fe_4Si_{16}B_{12}Mo_2$ (Fig. 25) surfaces in 1M KOH. From the slopes of the graphs the values calculated were:

$Fe_{67}Co_{18}Si_1B_{14}$, $E_{a,\eta=0} = 29.71$ kJ/mole
$Co_{66}Fe_4Mo_2Si_{16}B_{12}$, $E_{a,\eta=0} = 42.97$ kJ/mole (low overpotential region)
51.41 kJ/mole (high overpotential region)

For comparison, $E_{a,\eta=0}$ values were also calculated using the i_o values reported in the literature for the glassy alloy of similar composition and the polycrystalline metal components. The values calculated were:

$Fe_{60}Co_{20}Si_{10}B_{10}$, $E_{a,\eta=0} = 95.64$ kJ/mole [69] and 53.82 kJ/mole [68]
$Fe_{78}Si_{11}B_{11}$, $E_{a,\eta=0} = 87.04$ kJ/mole [69]
Polycrystalline Fe, $E_{a,\eta=0} = 23.73$ kJ/mole [69] and 24.76 kJ/mole [68]
Co, $E_{a,\eta=0} = 119.58$ kJ/mole [68].
Pt, $E_{a,\eta=0} = 43.98$ kJ/mole [69] and 18.53 kJ/mole [68]
Ni, $E_{a,\eta=0} = 40.00$ kJ/mole [68]

A linear Arrhenius relationship from which $E_{a,\eta=0}$ could be calculated was not obtained for glassy $Fe_{78}Si_{11}B_{11}$ alloy using the i_o values obtained by Kreysa and Hakansson [68].

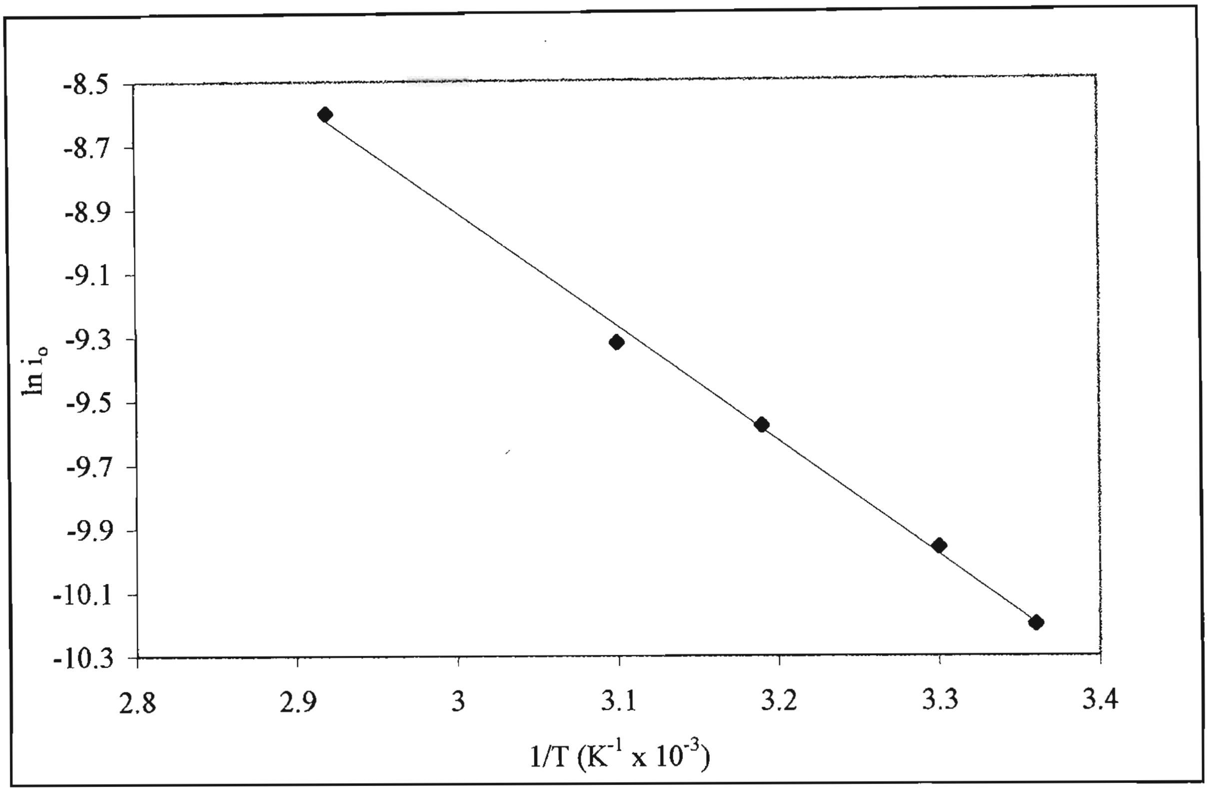

Fig. 24: Arrhenius plot for hydrogen evolution at the glassy $Fe_{67}Co_{18}B_{14}Si_1$ alloy surface in 1M KOH.

The apparent activation energy for hydrogen evolution on the polished glassy $Fe_{67}Co_{18}Si_1B_{14}$ surface was most similar to that of pure polycrystalline Fe and was much lower in magnitude than the values obtained at the glassy $Fe_{60}Co_{20}B_{10}Si_{10}$ and $Fe_{78}Si_{11}B_{11}$ electrode. The temperature effect for glassy $Co_{66}Fe_4Si_{16}B_{12}Mo_2$ was larger than that of $Fe_{67}Co_{18}Si_1B_{14}$, with greater $E_{a,\eta=0}$ values obtained in both the high and low overpotential regions of the former alloy.

We conclude that at a slow sweep rate for a kinetically controlled reaction, the value of the activation energy reflects the stability of the alloy. An alloy with a poorer tendency to passivate has a lower activation energy as the passive film formed prior to entry into the cathodic hydrogen evolution region is easier to break down. The more stable and compact the passive film the higher the activation energy required for its breakdown. The larger $E_{a,\eta=0}$ value of $Co_{66}Fe_4Si_{16}B_{12}Mo_2$ in comparison to $Fe_{67}Co_{18}B_{14}Si_1$ reflects the greater stability of the former alloy in the alkaline electrolyte. This could partially be attributed to the Mo content of the alloy. Mo has a beneficial effect in improving the corrosion resistance of Cr-containing crystalline alloys and would be predicted to have a similar effect in amorphous alloys [86]. If the addition of 2% Mo to the alloy results in the formation of a more compact and stable passive film, the activation energy for hydrogen evolution at the alloy surface will be increased, as we found.

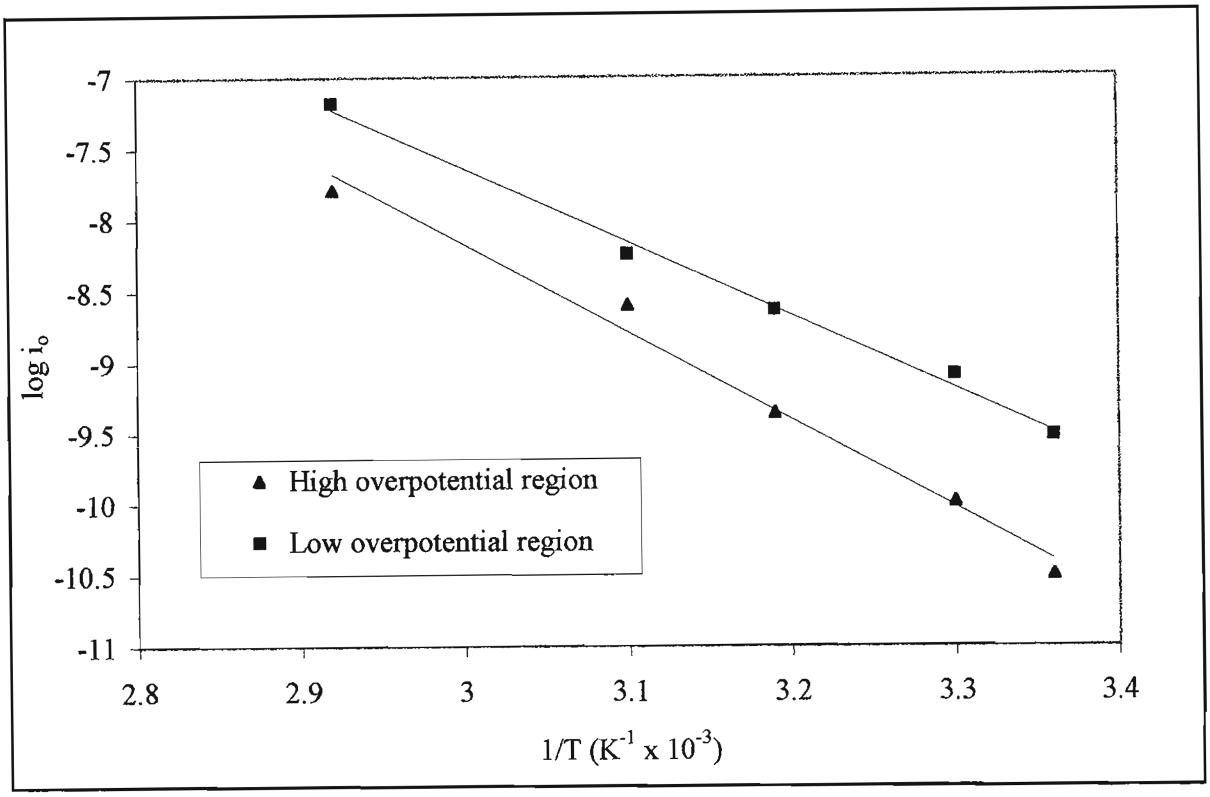

Fig. 25: Arrhenius plots for hydrogen evolution at the glassy $Co_{66}Fe_4Si_{16}B_{12}Mo_2$ alloy surface in 1M KOH.

5.4.2 *Ex situ* acid pretreatment

The electrocatalytic activity of a wide range of glassy alloy compositions can be improved for reactions such as hydrogen evolution and oxygen evolution by chemical pretreatment in comparison to their activity in the as-quenched and as-polished states. In electrocatalytic processes where the rate determining step is a surface reaction, the measured current density depends on both the inherent activity of the material and its real surface area. This is in contrast to mass transport controlled reactions where the current is independent of the surface roughness, provided that it is small compared to the diffusion layer thickness (about 10^{-2} cm). The rate of a catalytic reaction is proportional to the active surface area of the catalyst if transport phenomena are not rate determining. Thus, it is advantageous to get as much surface area as possible into a given volume without substantially increasing the electrode size. This is achieved using of porous electrode where the liquid can partially penetrate the intricate pore structure and makes contact with the solid over a larger surface area. Chemical pretreatment of glassy alloys with strong oxidising acids [96,119] increases their surface area by creating a roughened or porous surface and hence increases their apparent current density. Chemical pretreatment is generally believed to activate the surface by selectively dissolving surface oxides and one or more of the alloy components so that the effective surface area is increased. In contrast, it is reported that the activity of crystalline alloys is not enhanced by chemical pretreatment but rather that the electrode surface is deactivated or "poisoned" [119,150]. In this study of the influence of *ex situ* acid pretreatment with pure HF and HF/HNO_3 (ratio 1:4) mixtures on the activity of the glassy alloys for hydrogen evolution in 1M KOH was determined. Different treatment times and acid concentrations were tested.

5.4.2.1 Glassy $Fe_{67}Co_{18}B_{14}Si_1$

The Tafel parameters obtained after different *ex situ* acid pretreatments of the glassy $Fe_{67}Co_{18}B_{14}Si_1$ alloy surface are listed in Table 12. All HF and HF/HNO_3 acid treatments produced a slight increase in the exchange current density and caused the current densities to shift towards lower overpotentials in comparison to the as-polished surface. The Tafel plots obtained after pretreatment of $Fe_{67}Co_{18}B_{14}Si_1$ with HF of different concentrations and with a 0.5M HF/0.5M HNO_3 mixture for different time periods are shown in Fig. 26 and Fig. 27 respectively.

Table 12: Kinetic data for hydrogen evolution on glassy $Fe_{67}Co_{18}B_{14}Si_1$, in 1M KOH at 25°C, after different chemical pretreatments.

Chemical treatment	Treatment period /s	Tafel region /V	-b /mV	i_o /A.cm^{-2}	i_1* /mA.cm^{-2}	$i_2^{\otimes}$ /mA.cm^{-2}	$i_3^{\oplus}$ /mA.cm^{-2}
as-polished	-	-1.63 to -1.82	120 ± 7	(3.08 ± 0.80) x 10^{-5}	0.221 ± 0.055	0.560 ± 0.150	1.421 ± 0.431
0.5M HF	60	-1.63 to -1.83	122 ± 6	(4.40 ± 0.86) x 10^{-5}	0.270 ± 0.025	0.722 ± 0.048	1.926 ± 0.104
1.0M HF	60	-1.63 to -1.85	120 ± 6	(5.11 ± 0.56) x 10^{-5}	0.302 ± 0.028	0.777 ± 0.090	1.934 ± 0.293
2.0M HF	60	-1.64 to -1.86	118 ± 4	(6.60 ± 1.46) x 10^{-5}	0.447 ± 0.143	1.179 ± 0.356	3.108 ± 0.878
4.0M HF	60	-1.65 to -1.86	119 ± 4	(8.70 ± 2.41) x 10^{-5}	0.495 ± 0.107	1.279 ± 0.254	3.311 ± 0.614
8.0M HF	60	-1.64 to -1.83	114 ± 6	(9.05 ± 0.96) x 10^{-5}	0.751 ± 0.068	2.072 ± 0.142	5.718 ± 0.236
1.0M HF	30	-1.65 to -1.82	113 ± 7	(4.75 ± 0.42) x 10^{-5}	0.213 ± 0.007	0.596 ± 0.038	1.672 ± 0.180
1.0M HF	60	-1.63 to -1.85	120 ± 6	(5.19 ± 0.56) x 10^{-5}	0.302 ± 0.028	0.777 ± 0.090	1.934 ± 0.293
1.0M HF	300	-1.64 to -1.86	124 ± 5	(4.93 ± 0.35) x 10^{-5}	0.316 ± 0.032	0.802 ± 0.054	2.035 ± 0.067
1.0M HF	600	-1.65 to -1.84	122 ± 4	(5.85 ± 0.74) x 10^{-5}	0.326 ± 0.011	0.895 ± 0.016	2.455 ± 0.037
0.1M HF/ 0.1MHNO_3	60	-1.63 to -1.80	115 ± 2	(6.11 ± 0.34) x 10^{-5}	0.206 ± 0.023	0.591 ± 0.045	1.692 ± 0.089
0.5MHF/ 0.5MHNO_3	60	-1.63 to -1.80	117 ± 4	(8.82 ± 1.08) x 10^{-5}	0.306 ± 0.064	0.827 ± 0.141	2.232 ± 0.298
1.0M HF/ 1.0MHNO_3	60	-1.64 to -1.78	111 ± 3	(9.94 ± 0.88) x 10^{-5}	0.349 ± 0.027	0.977 ± 0.046	2.734 ± 0.081
0.5M HF/ 0.5MHNO_3	15	-1.63 to -1.80	123 ± 6	(5.77 ± 1.14) x 10^{-5}	0.266 ± 0.088	0.684 ± 0.184	1.563 ± 0.103
0.5M HF/ 0.5MHNO_3	30	-1.63 to -1.82	119 ± 8	(6.95 ± 1.08) x 10^{-5}	0.313 ± 0.019	0.773 ± 0.041	1.912 ± 0.090
0.5M HF/ 0.5MHNO_3	60	-1.63 to -1.81	117 ± 4	(8.82 ± 1.08) x 10^{-5}	0.306 ± 0.064	0.827 ± 0.141	2.232 ± 0.298

* E = -1.65V, $^{\otimes}$ E = -1.70V, $^{\oplus}$ E = -1.75V (vs. SSE)

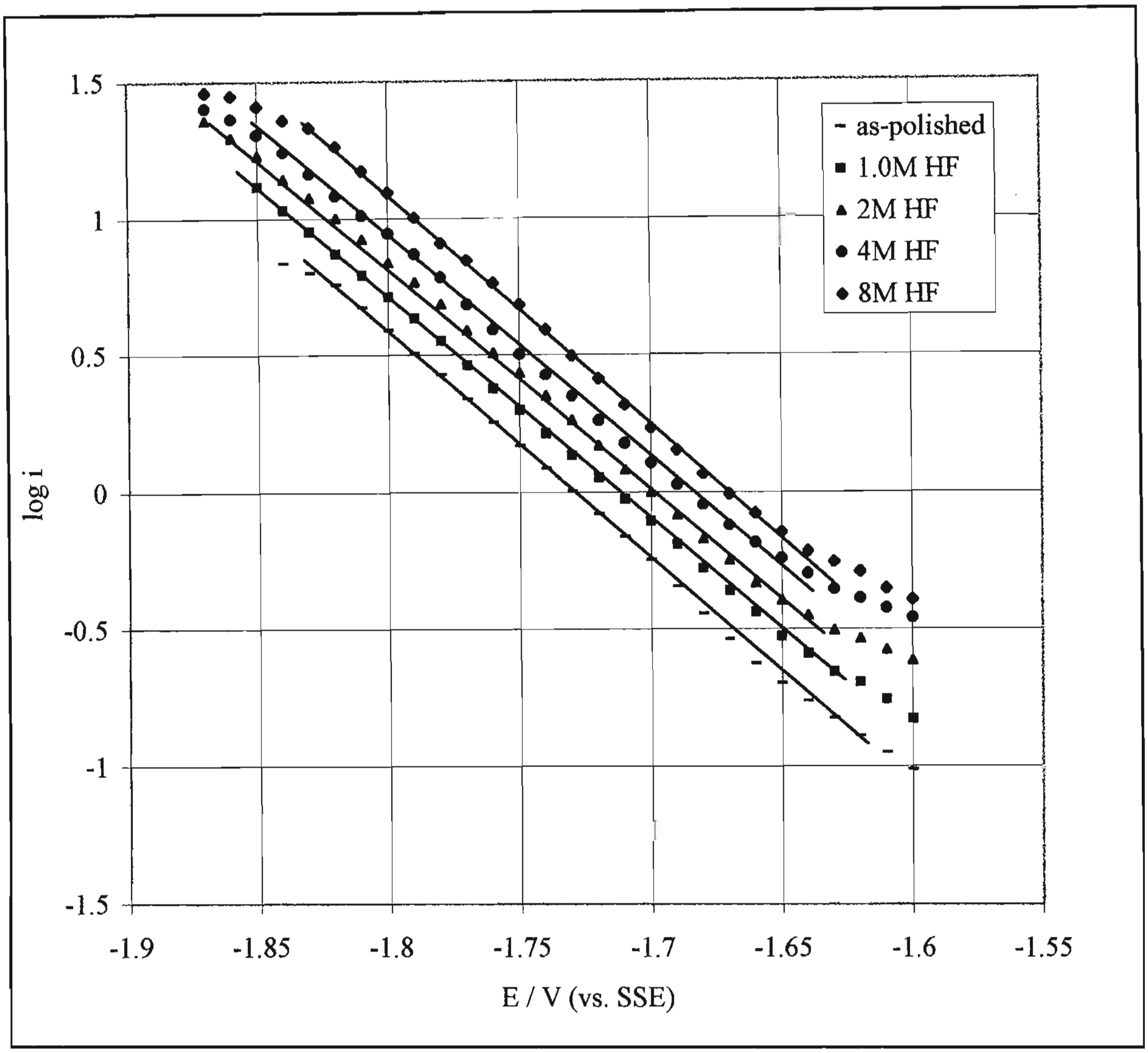

Fig. 26: Tafel plots for hydrogen evolution on glassy $Fe_{67}Co_{18}B_{14}Si_1$ after chemical pretreatment with HF at different concentrations for 1 minute.

Both HF and HF/HNO_3 pretreatment of glassy $Fe_{67}Co_{18}B_{14}Si_1$ produced an increase in the exchange current density of the alloy indicating that its activity for the HER was improved. As the immersion time and acid concentration were increased the alloy displayed a progressive increase in i_o, however, these values were only slightly greater than the i_o value obtained at the as-polished surface. HF/HNO_3 treatment was found to be more effective than pure HF in improving the activity of the alloy. A maximum i_o value of 9.94 x 10^{-5} $A.cm^{-2}$ was obtained after 1M HF/1M HNO_3 treatment for 1 minute which was only slightly greater than the i_o value of 3.08 x 10^{-5} $mA.cm^{-2}$ obtained at the as-polished electrode surface.

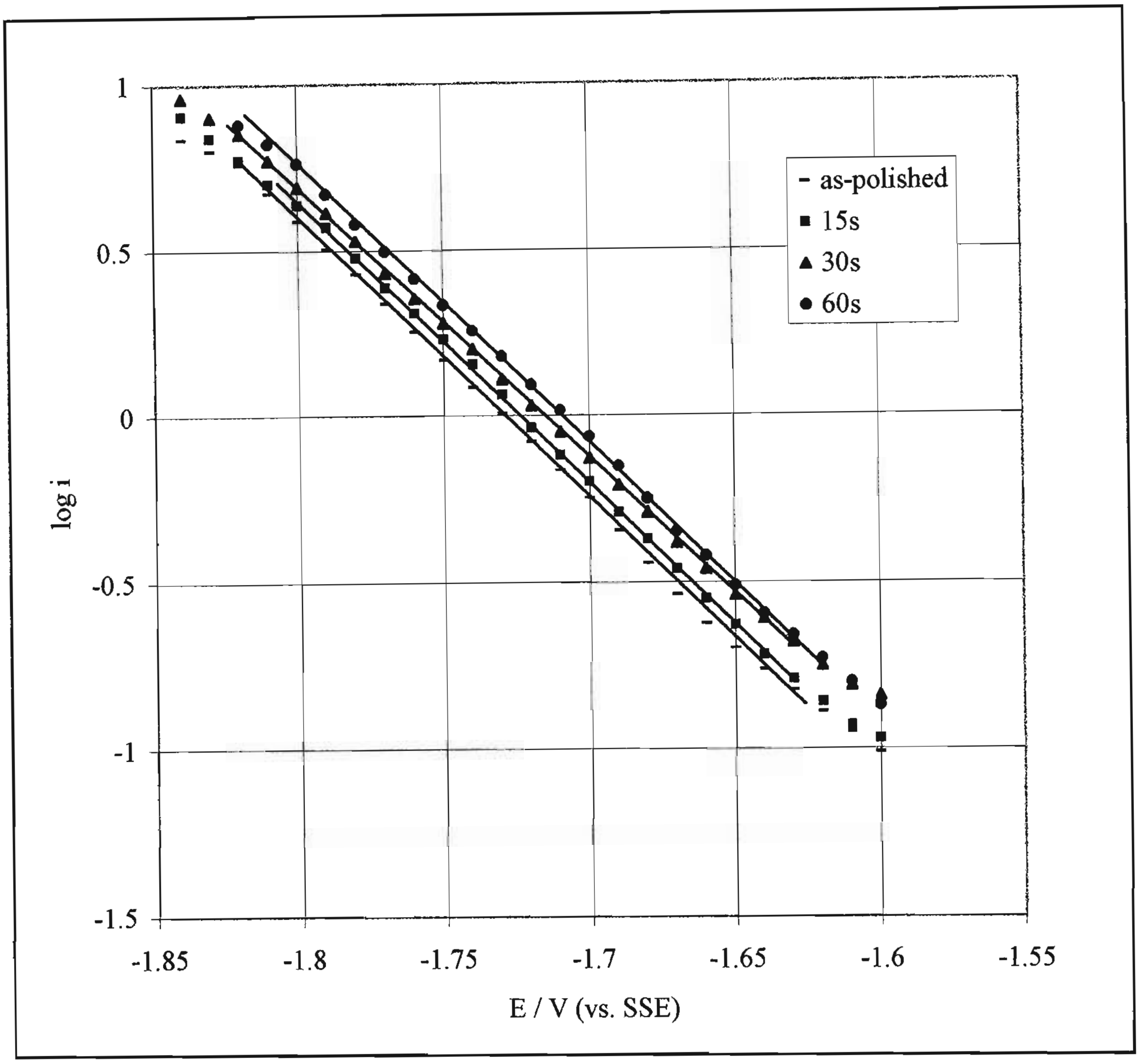

Fig. 27: Tafel plots for hydrogen evolution on the $Fe_{67}Co_{18}B_{14}Si_1$ alloy surface after chemical activation with a 0.5M HF/0.5M HNO_3 (1:4) mixture for different time periods.

Fig. 28 shows the variation in the i_o values of glassy $Fe_{67}Co_{18}B_{14}Si_1$ after pretreatment with HF of different concentrations. The increase in i_o was rapid for acid concentrations ranging between 0.5 and 4M and then increased only slightly with further increases in acid concentration (4M to 8M HF). The same trend in i_o increase was observed for the other acid treatments tested. A single Tafel slope of approximately 120mV was obtained after all the acid treatments tested which suggests that the mechanism of hydrogen evolution at the alloy surface remained unaffected.

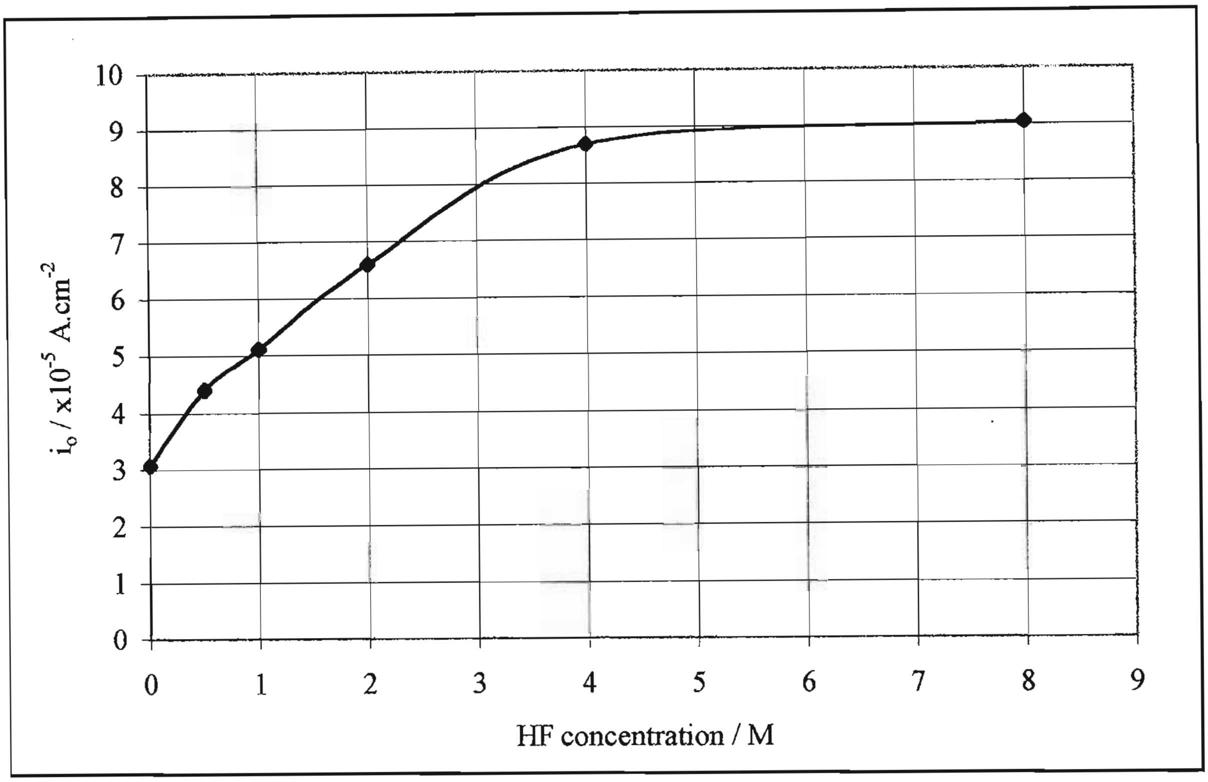

Fig. 28: Variation in the exchange current density for hydrogen evolution at the glassy $Fe_{67}Co_{18}B_{14}Si_1$ alloy surface resulting from HF pretreatments of different concentration.

Morphological changes in the glassy $Fe_{67}Co_{18}B_{14}Si_1$ alloy surface after the different treatments were determined by SEM analysis and a selection of the SEM micrographs obtained are shown in Fig. 29 and 30. Treatment with 1M HF (1 minute) resulted in an increase in the general surface roughness of the electrode with circular regions of localised attack that formed shallow depressions interspersed on the surface (Fig. 29a and b). After treatment with 8M HF (1min) a similar etch pattern was obtained but the general surface corrosion was more severe and an evenly spread surface deposit of particles was observed (Fig. 29c & d). The particles were very small and EDS analysis did not have a sufficiently high sensitivity for measuring their composition.

Fig. 30 shows the $Fe_{67}Co_{18}B_{14}Si_1$ surface after 0.5M HF/0.5M HNO_3 activation for different time periods. The alloy surface at low magnification (x500) (Fig. 30a) appeared similar to that produced by HF treatment with general surface roughening observed and circular regions of localised attack. However, enlargement of these regions revealed that an intricate mesh-like etch pattern fomed in which the acid appeared to have attacked the alloy surface in a discrete layer. Progressive disintegration of the alloy surface layer occurred with increasing immersion time and after 30 seconds only remnant portions of the alloy surface layer were present as round nodules (Fig. 30d).

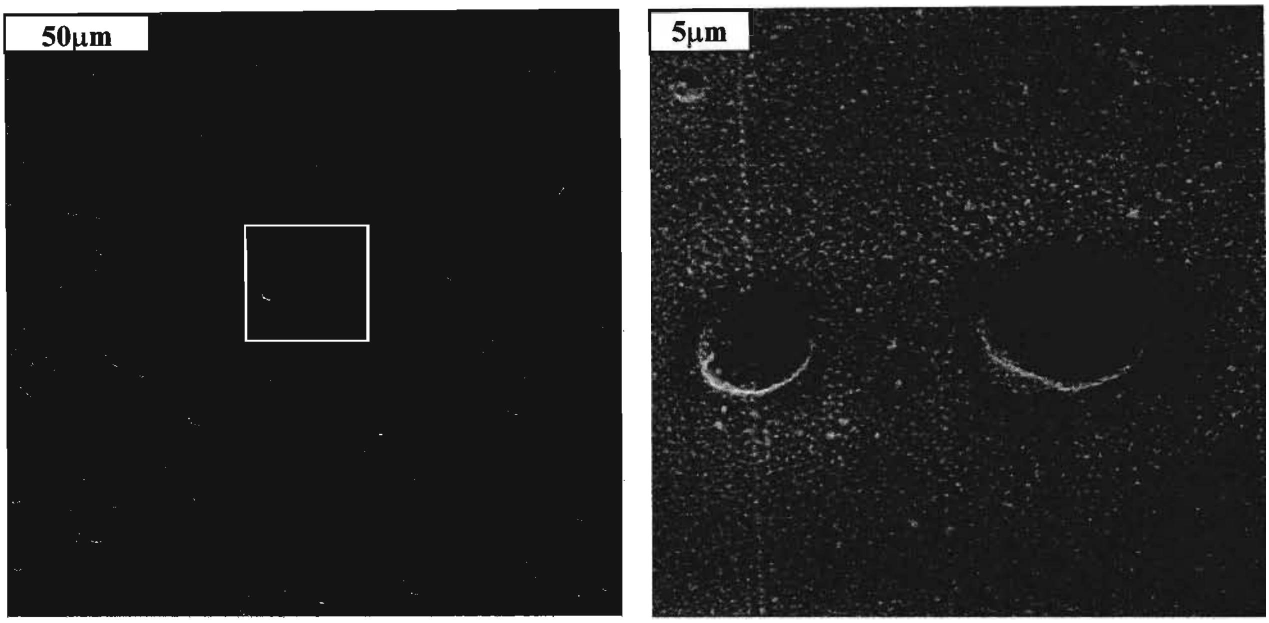

(a) 1M HF for 1 minute (mag. x500)

(b) enlargement of (a) (mag. x4000)

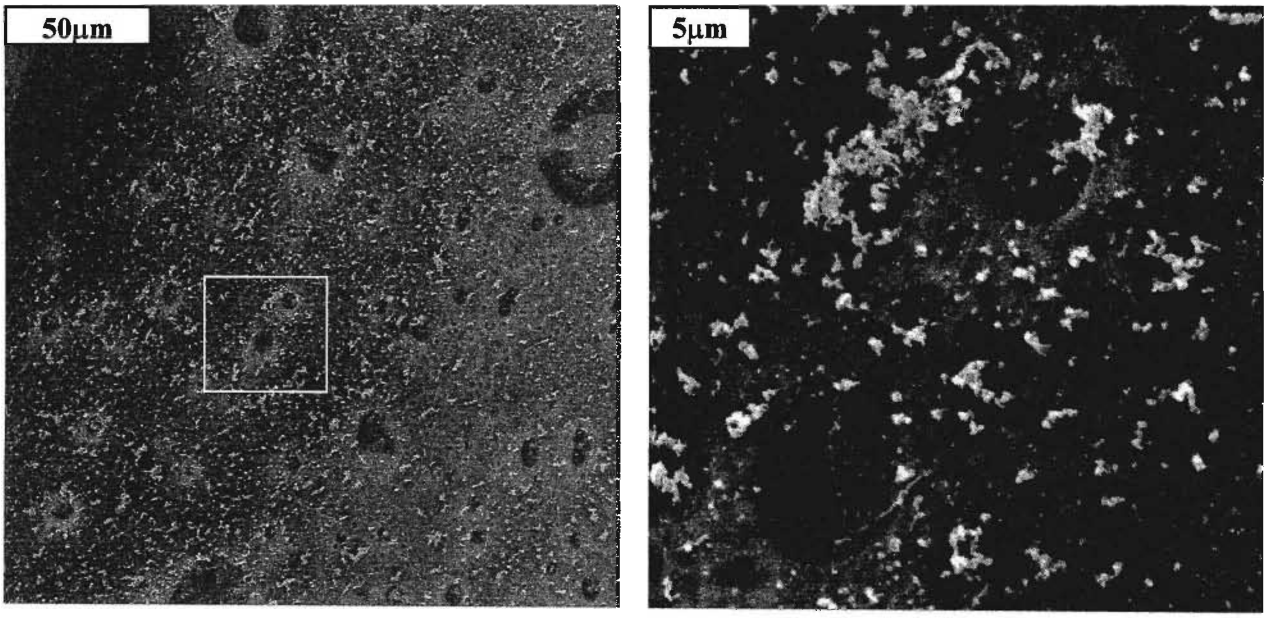

(c) 8 M HF for 1 minute (mag. x500)

(d) enlargement of (c) (mag. x4000)

Fig. 29: The glassy $Fe_{67}Co_{18}B_{14}Si_1$ surface after HF treatment.

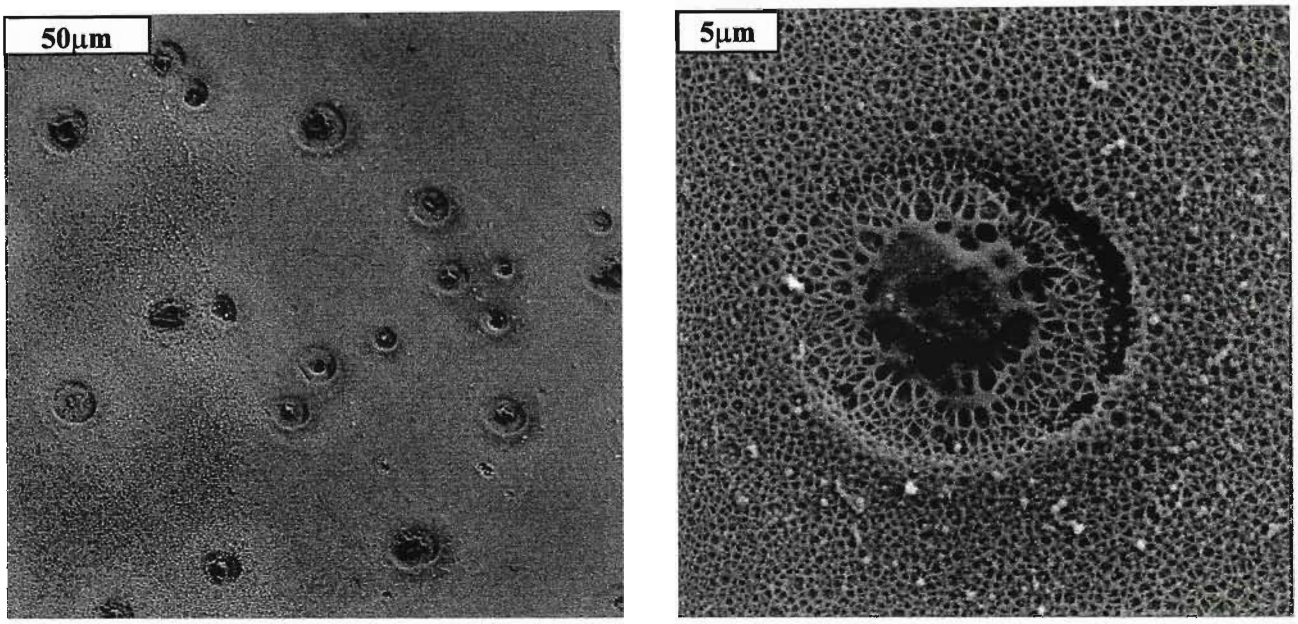

(a) 0.5M HF/0.5M HNO_3 treatment for 15 seconds (mag. x500)

(b) enlargement of (a) (mag. x4000)

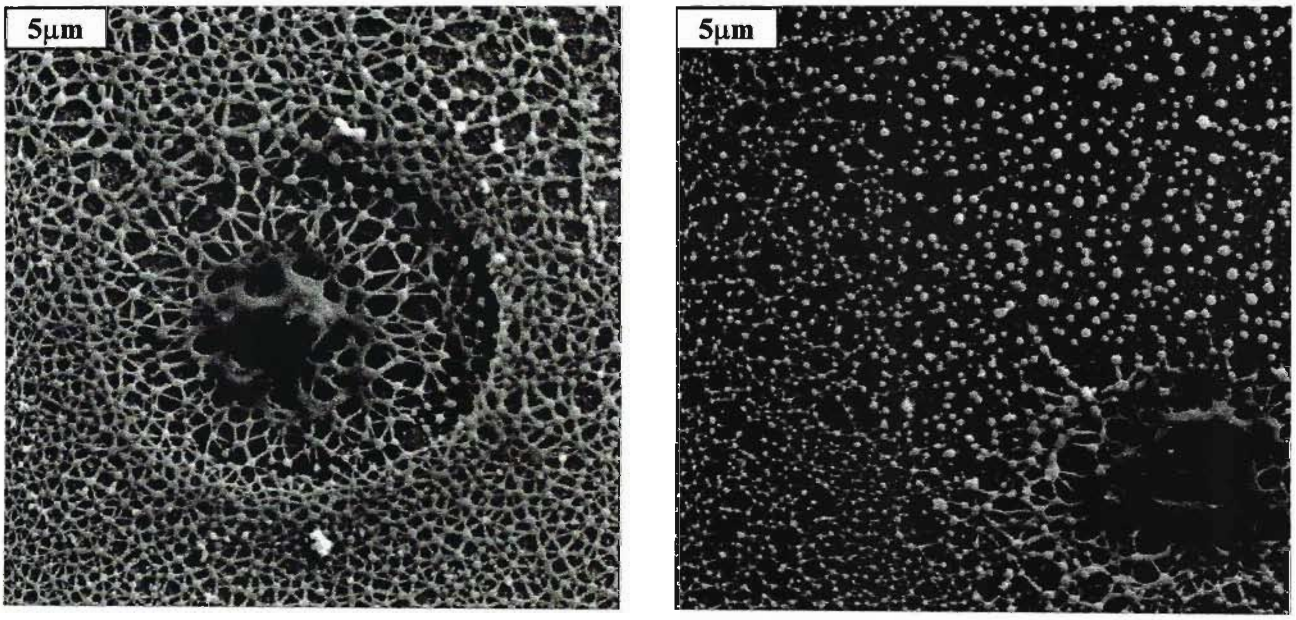

(c) 0.5 M HF/0.5M HNO_3 treatment for 30 seconds (mag. x4000)

(d) 0.5M HF/0.5M HNO_3 treatment for 1 minute (mag. x4000)

Fig. 30: The glassy $Fe_{67}Co_{18}B_{14}Si_1$ surface after HF/HNO_3 (1:4) treatment.

EDS analysis of the alloy surface after acid treatment revealed no significant variation in the alloy component concentrations in comparison to the as-polished surface. This indicates that treatment did not result in preferential dissolution of any one of the alloy components. The EDS results obtained are listed in Table 13.

Table 13: EDS analysis of the $Fe_{67}Co_{18}B_{14}Si_1$ alloy surface after different acid treatments.

	Fe	Co	Si
Polished electrode surface	77.80	21.22	0.98
1M HF (1min) treatment	77.83	21.08	1.09
1M HF / 1M HNO_3 (1min) treatment	78.54	20.09	1.37

Note: data presented as weight %.

Acid treatment with 1M HF (1min) produced no detectable change in the alloy component concentrations, while acid treatment with 1M HF/1M HNO_3 (1min) produced a slight increase of 0.74 wt% in Fe concentration, a 1.13 wt% decrease in Co concentration and a 0.39 wt% increase in Si concentration.

Based on these results it is suggested that the increase in the electrocatalytic activity of the $Fe_{67}Co_{18}B_{14}Si_1$ alloy for hydrogen evolution produced by acid pretreatment resulted from an increase in the electrode surface area (Fig. 30). The Tafel slope remained constant after the different treatments suggesting that there was no change in the mechanism of hydrogen evolution. This was also supported by the EDS results that reveal a change in the alloy surface component concentrations in comparison to the as-polished electrode surface. SEM analysis revealed a roughened alloy surface after acid treatment with a greater surface area at which hydrogen adsorption and evolution could occur. For all treatments the increase in i_o was initially rapid due to the increase in the electrode surface area. More severe treatments did not significantly enhance in the surface area, as can be seen from the SEM micrographs, and hence the i_o values for these treatments showed a relatively smaller increase in value. Machida et al. [119] also suggested that chemical etching of amorphous alloys with acids such as HF and HNO_3 improved their electrocatalytic properties by enlarging the active electrode surface area.

It should be noted that acid activation of the $Fe_{67}Co_{18}B_{14}Si_1$ alloy surface was a very destructive technique that damaged the alloy surface and created a visible etch. With increasing acid concentration and immersion time the severity of the etch increased. Treatment with 1M HF/1M HNO_3 for 5 minutes was found to destroy the alloy sample by etching through the entire ribbon thickness. Clearly this is undesirable as repeated activation treatments would destroy the sample and would not produce a stable and long-life catalyst. It can be concluded that due to the very small increase in the activity of the alloy resulting from acid pretreatment in comparison to the severity of the etch produced, acid pretreatment does not form a viable activation procedure.

An anodic polarisation curve of the $Fe_{67}Co_{18}B_{14}Si_1$ electrode after the most activating acid activation with 1M HF/1M HNO_3 (1 minute) was obtained to investigate the influence of acid pretreatment on the corrosion properties of the alloy (Fig. 31). The corrosion parameters obtained from the curve are listed in Table 14.

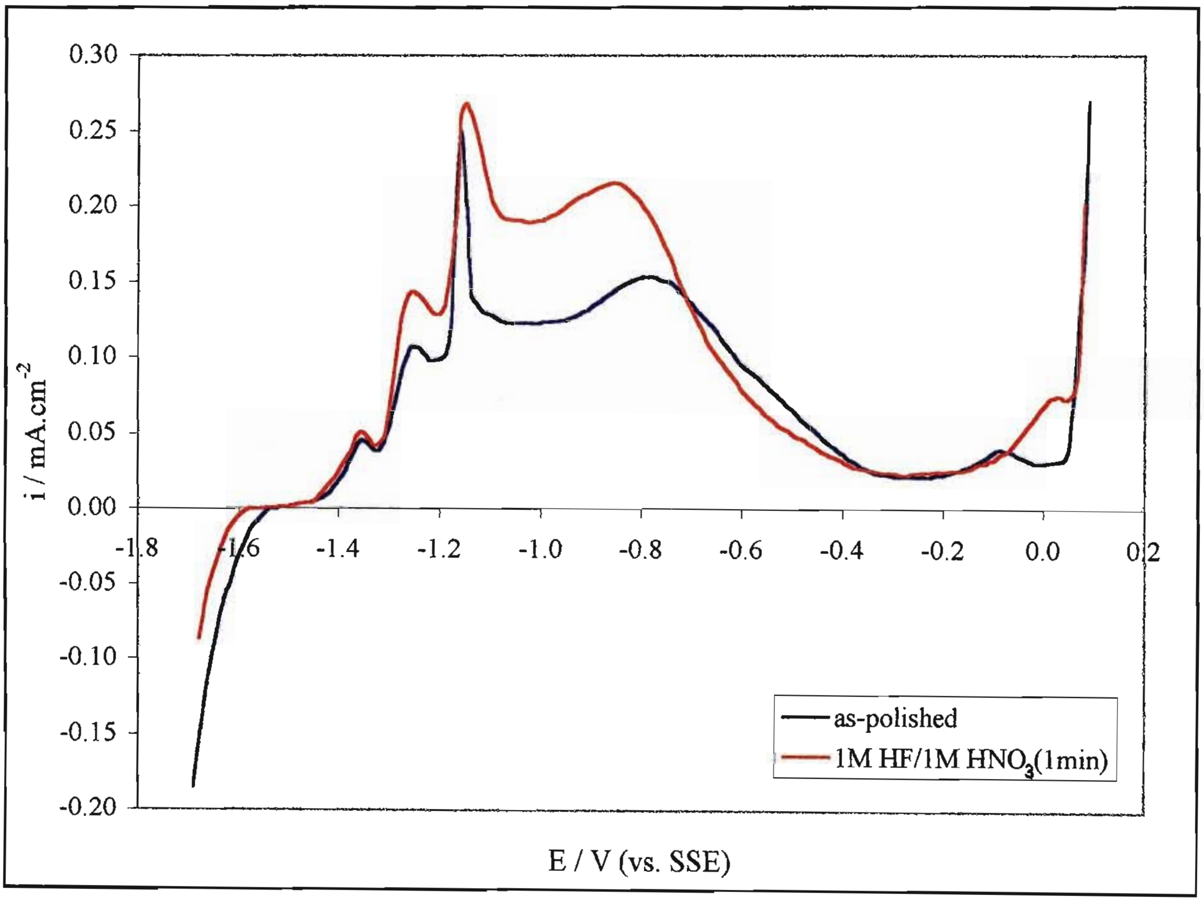

Fig. 31: Typical anodic polarisation curves of the glassy $Fe_{67}Co_{18}B_{14}Si_1$ alloy in the as-polished state and after acid pretreatment prior to cathodic polarisation in 1M KOH at 25°C.

Table 14: Corrosion parameters obtained from anodic polarisation curves of glassy $Fe_{67}Co_{18}B_{14}Si_1$ in the as-polished state and after acid pretreatment.

	E_{corr}	E_{pp}	E_{Flade}	E_{tr}	i_{pp}	i_p
as-polished	-1.53	-1.16	-0.36	0.04	0.251	2.09×10^{-2}
1M HF/1M HNO_3 (1 min)	-1.59	-1.15	-0.36	0.05	0.268	2.33×10^{-2}

Nb. The corrosion parameters are average values obtained from an average of six independent experiments.

shape of the anodic polarisation curve of the acid treated and as-polished $Fe_{67}Co_{18}B_{14}Si_1$ electrodes were similar, however there was an increase in the current density of the three anodic peaks at potentials of -1.35, -1.25 and -1.16V and in the current density of the broad anodic peak ranging between potentials of -1.07 and -0.73V. The passive region (-0.37 to -0.14V) maintained a constant density at both electrode surfaces. E_{corr} shifted towards a more negative potential after acid treatment and E_{tr} maintained a constant potential. The similarity in the shape of the two curves indicates that acid treatment produced a surface area increase but did not change the surface properties of the electrode or significantly reduce its corrosion resistance in comparison to the as-quenched state. The surface area increase led to an increase in apparent current densities in the different regions of the anodic polarisation curve (because current density calculations were based on the geometric surface area of the electrode and not the actual effective area).

5.4.2.2 Glassy $Co_{66}Fe_4Si_{16}B_{12}Mo_2$

The Tafel parameters obtained in 1M KOH after acid activation of the glassy $Co_{66}Fe_4Mo_2Si_{16}B_{12}$ electrode are listed in Table 15. The $Co_{66}Fe_4Mo_2Si_{16}B_{12}$ alloy displayed a greater stability in the acid medium than the $Fe_{67}Co_{18}B_{14}Si_1$ composition and so longer acid treatment times of 1M HF (10min) and 1M HF/HNO_3 (10min) were also tested. Both HF and HF/HNO_3 treatments were effective in improving the alloy activity for the HER as can be seen from the increase in the Tafel plot current densities in Fig. 32. The Tafel plots obtained from 1M HF 1 and 5 minute treatments were omitted from the graphs for clarity as they are very similar to those of the as-polished alloy. Tafel plots of increasing current density were obtained after acid treatments in the order 1M HF (1min) < 1M HF (5min) < 8M HF (1min) < 1M HF/1M HNO_3 (1min) < 1M HF (10 min) < 1M HF/1M HNO_3 (5 min) < 1M HF/1M HNO_3 (10 min). Double Tafel slopes were obtained for the treated surfaces with exceptions occurring for 1M HF (10min) and 8M HF (1min) treatments which produced single slopes. The shapes of the Tafel plots were the same as those obtained at the as-polished surface with greater activities for hydrogen evolution occurring in the high overpotential region. A maximum activity was obtained after 1M HF/1M HNO_3 treatment for 10 minutes with i_o values of 28.7×10^{-5} and 46.6×10^{-5} $A.cm^{-2}$ obtained at 25°C in the high and low overpotential regions respectively. The i_o values increased significantly and were 18.6 and 5.6 times greater than the values obtained at the as-polished electrode in the high and low overpotential regions respectively.

Table 15: Kinetic data for hydrogen evolution on glassy $Co_{66}Fe_4Si_{16}B_{12}Mo_2$ in 1M KOH at 25°C, after different chemical treatments.

		High η region			Low η region					
Chemical treatment	Treatment period /s	Tafel region / V	-b /mV	i_o /A.cm^{-2}	Tafel region / V	-b /mV	i_o /A.cm^{-2}	i_{1*} / mA.cm^{-2}	$i_2^{\otimes}$ / mA.cm^{-2}	$i_3^{\oplus}$ / mA.cm^{-2}
As-polished	-	-1.74 to -1.88	103 ± 9	(1.54 ± 0.58) x10^{-5}	-1.61 to -1.74	158 ± 13	(8.25 ± 3.09) x 10^{-5}	0.267 ± 0.061	1.132 ± 0.398	9.734 ± 2.348
1M HF	60	-1.71 to -1.84	143 ± 11	(2.14 ± 0.89) x 10^{-5}	-1.62 to -1.71	177 ± 5	(5.20 ± 0.97) x 10^{-5}	0.181 ± 0.006	0.791 ± 0.240	3.927 ± 0.803
1M HF	300	-1.72 to -1.88	112 ± 7	(3.80 ± 0.42) x 10^{-5}	-1.62 to -1.72	131 ± 2	(3.66 ± 0.28) x 10^{-5}	0.177 ± 0.008	1.046 ± 0.041	8.183 ± 1.408
1M HF	600	-1.59 to -1.85	143 ± 5	(1.22 ± 0.80) x 10^{-4}				0.535 ± 0.052	2.602 ± 0.342	12.667 ± 2.095
8M HF	60	-1.61 to -1.86	134 ± 4	(5.42 ± 1.20) x 10^{-5}				0.328 ± 0.063	1.590 ± 0.171	8.467 ± 1.112
1M HF/ 1M HNO_3	60	-1.71 to -1.86	141 ± 9	(9.61 ± 2.13) x 10^{-5}	-1.59 to -1.71	170 ± 19	(1.43 ± 0.25) x 10^{-4}	0.502 ± 0.043	2.035 ± 0.088	10.983 ± 0.571
1M HF/ 1M HNO_3	300	-1.70 to -1.87	155 ± 6	(2.38 ± 0.82) x 10^{-4}	-1.60 to -1.71	180 ± 10	(2.83 ± 0.74) x 10^{-4}	0.767 ± 0.112	3.535 ± 0.595	16.302 ± 3.170
1M HF/ 1M HNO_3	600	-1.71 to -1.85	166 ± 5	(2.87 ± 0.53) x 10^{-4}	-1.61 to -1.71	218 ± 17	(4.66 ± 0.45) x 10^{-4}	1.214 ± 0.035	3.582 ± 0.318	14.182 ± 2.428

* E = -1.64V, $^{\otimes}$ E = -1.74V, $^{\oplus}$E = -1.84V (vs.SSE)

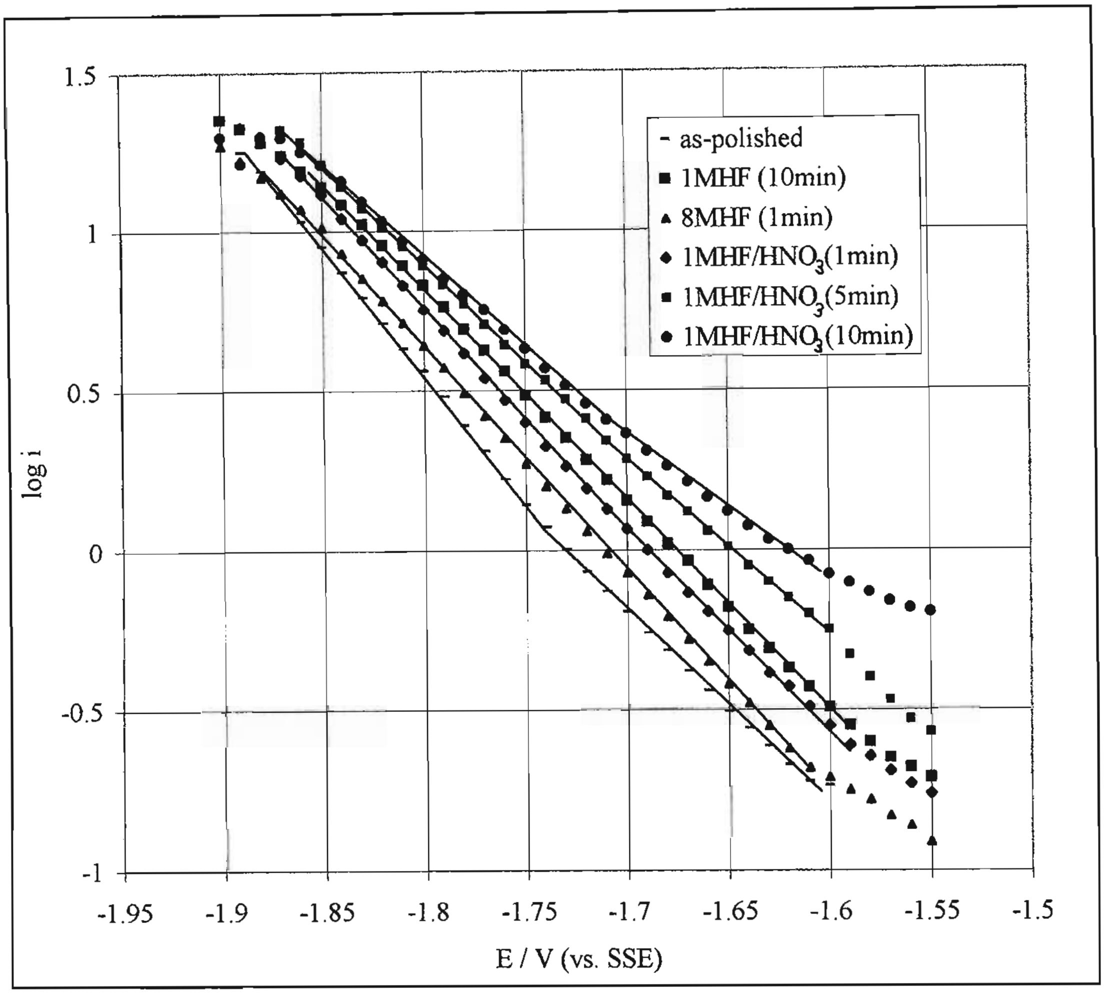

Fig. 32: Tafel plots for hydrogen evolution on the glassy $Co_{66}Fe_4Si_{16}B_{12}Mo_2$ electrode after chemical pretreatment with different acids.

A visible etch was only produced in the $Co_{66}Fe_4Si_{16}B_{12}Mo_2$ alloy surface after more severe acid treatments (1M HF/1M HNO_3 for 5 and 10 minutes) indicating this alloy composition had a higher resistant to corrosion in an acid medium than the $Fe_{67}Co_{18}B_{14}Si_1$ alloy. SEM micrographs of the acid pretreated $Co_{66}Fe_4Mo_2Si_{16}B_{12}$ surfaces are shown in Fig. 33. Treatment with 8M HF (1 minute) produced a roughened surface and a surface deposit that created a patterned effect (Fig. 33a). A very light etch resulted from 1M HF/HNO_3 (1 minute) treatment and occurred preferentially along the polish lines created by the 0.5 μm Al_2O_3 paste (Fig. 33b). Treatment with 1M HF/1M HNO_3 (10 minutes) produced a highly roughened surface with a fine porous structure in comparison to the smooth as-quenched surface. A larger electrode surface area supported a greater number of active sites at which hydrogen adsorption and evolution could occur and resulted in an increase in the apparent current density of the alloy, as observed for the $Fe_{67}Co_{18}B_{14}Si_1$. The i_o values of glassy $Co_{66}Fe_4Mo_2Si_{16}B_{12}$ were significantly greater than the values obtained for the $Fe_{67}Co_{18}B_{14}Si_1$

electrode after acid pretreatment because a porous surface with a much greater surface area was produced for the former alloy.

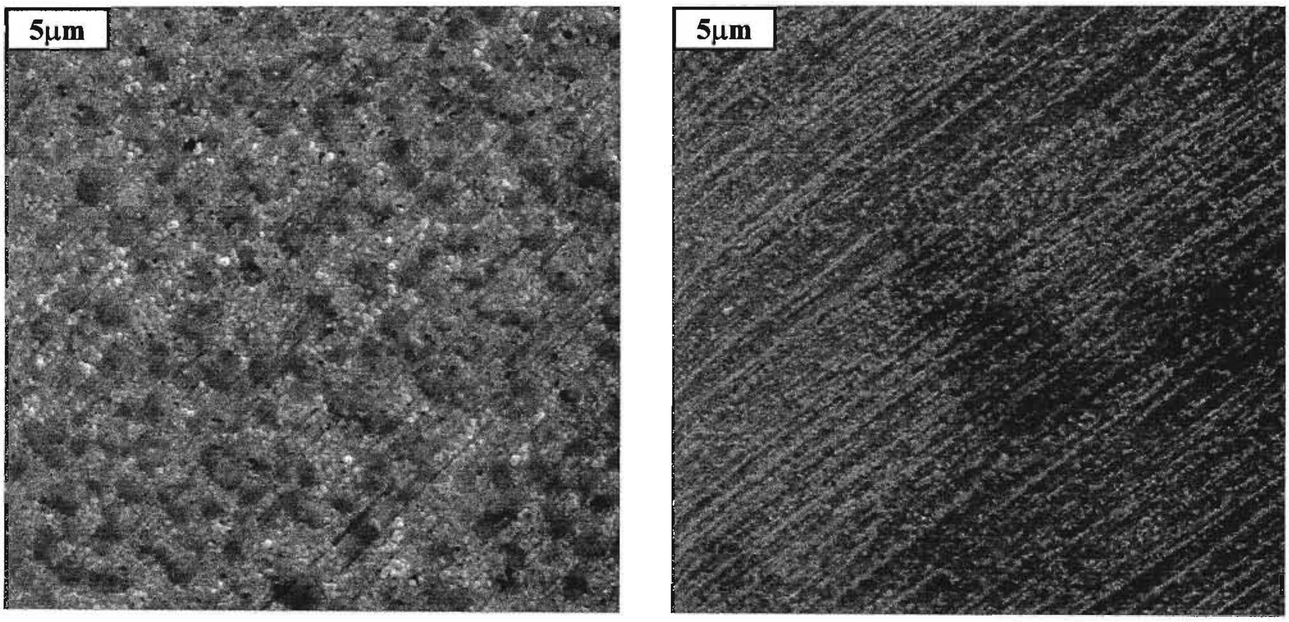

(a) 8M HF treatment for 1 minute (mag. x4000)

(b) 1M HF/1M HNO_3 treatment for 1 minute (mag. x4000)

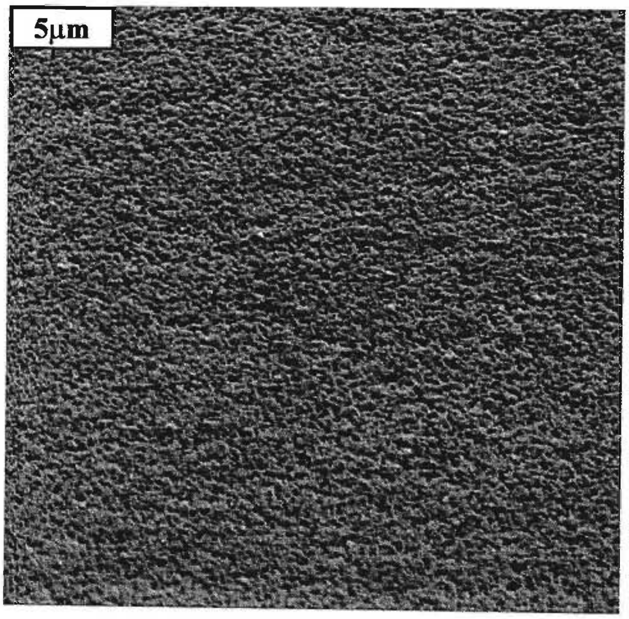

(c) 1M HF / 1M HNO_3 treatment for 10 minutes (mag. x4000)

Fig. 33: The $Co_{66}Fe_4Si_{16}B_{12}Mo_2$ electrode surface after different acid pretreatments.

The porous surface enhanced the electrode surface area so that the electrolyte was able to make contact with the substrate over a much larger surface area. Consequently the apparent current density increased and the electrocatalytic activity of the alloy for the HER improved. Cahan et al. [151] suggested that at a highly porous alloy surface little current is effectively produced inside the pores. The increased activity, particularly when the product is a gas, results from a large number of surface menisci for which there are sections where the layer of solution is very thin, i.e. δ has been made very small ($\sim 10^{-5}$cm) by physical means and not by stirring. It is in these areas that high limiting currents per meniscus are produced. Overall, the total current per external geometric area is several orders of magnitude higher than that for the corresponding situation at a planar electrode surface, and this explanation clearly is also consistent with experimental facts found in the present work.

The apparent current densities at a porous alloy surface are greatly enhanced in comparison to a smooth polished surface if the current densities measured are based on the geometric electrode area. A direct comparison of the actual current densities is difficult to calculate due to the difficulty of estimating the true surface area. The polished glassy alloy surfaces were smooth and correspond closely with the geometric areas of the electrodes whereas the surface areas of the porous and roughened electrodes were substantially increased in comparison to the geometric areas. A qualitative indication of the roughness factor is obtained from the SEM pictures but these do not provide a quantitative evaluation of this parameter [152]. An estimate of surface roughness is important in interpretation of data at catalytic surfaces. Comparison of the role of the electrocatalyst independent of the effect of surface area remains a challenge in this field. Other complicating factors associated with electrocatalytic reactions at porous surfaces have also been reported [89]. Within the pore structure a variation in the local hydroxyl ion concentration during the electrodic reaction may result in a modification in the local reversible potential. The porous structure may produce other effects, especially at high current, such as ohmic drop or loss of active surface area due to the occlusion of gases. Factors such as these lead to uncertainties in the interpretation of the experimental results. Catalyst design should aim at maximising the surface area of the electrode rather than increasing the size of the electrode to obtain a maximum current density. An increased surface roughness may result in an increase in the Tafel slope and polarisation curves at ideal porous electrodes possess a double Tafel slope. Both these effects were noted at the HF/HNO_3 treated $Co_{66}Fe_4Si_{16}B_{12}Mo_2$ electrode.

Acid pretreatment of glassy $Co_{66}Fe_4Si_{16}B_{12}Mo_2$ was found to have a less detrimental effect on the alloy surface than an equivalent treatment of the $Fe_{67}Co_{18}B_{14}Si_1$ electrode. The surface etch on the $Co_{66}Fe_4Si_{16}B_{12}Mo_2$ electrode was less severe and there were no signs of the circular regions of localised attack. While the two alloy compositions had a similar activity for hydrogen evolution in the as-polished state at 25°C, acid treatment was much more effective in activating the $Co_{66}Fe_4Si_{16}B_{12}Mo_2$ composition for HER. Exchange current densities that were 18.6 and 5.6 times greater in the high and low overpotential regions respectively than the values obtained at the as-polished $Co_{66}Fe_4Si_{16}B_{12}Mo_2$ electrode were obtained while an i_o value that was only 3.2 times greater was obtained for the $Fe_{67}Co_{18}B_{14}Si_1$ alloy after the most activating treatment. It was concluded that the glassy $Co_{66}Fe_4Mo_2Si_{16}B_{12}$ composition produced a superior and more durable electrocatalyst for the HER after acid pretreatment (1M HF/1M HNO_3, 10 minutes) than the glassy $Fe_{67}Co_{18}B_{14}Si_1$ alloy.

The i_o values of the acid activated $Co_{66}Fe_4Si_{16}B_{12}Mo_2$ electrode (1M HF/1M HNO_3, 10 minutes) were higher than the polycrystalline Fe and Co components of the alloy and were also found to be higher than both polycrystalline Ni [95] or Pt [69] at 25°C (Table 7). These results indicated that this glassy alloy composition formed a potentially excellent electrocatalytst for the HER after suitable surface pretreatment.

An anodic polarisation curve of glassy $Co_{66}Fe_4Si_{16}B_{12}Mo_2$ electrode after the most activating acid pretreatment (1M HF/1M HNO_3, 10 minutes) was obtained and compared with the curve at the as-polished surface (Fig. 34). The corrosion parameters obtained from the curves are listed in Table 16.

Table 16: Corrosion parameters obtained from anodic polarisation curves of glassy $Co_{66}Fe_4Si_{16}B_{12}Mo_2$ in the as-polished state and after acid pretreatment.

	E_{corr}	E_{pp}	E_{Flade}	E_{tr}	i_{pp}	i_p
as-polished	-1.55	-1.23	-0.21	0.03	0.223	4.73×10^{-2}
1M HF/1M HNO_3 (10 minutes)	-1.55	-1.22	-0.12	-0.03	0.250	1.14×10^{-1}

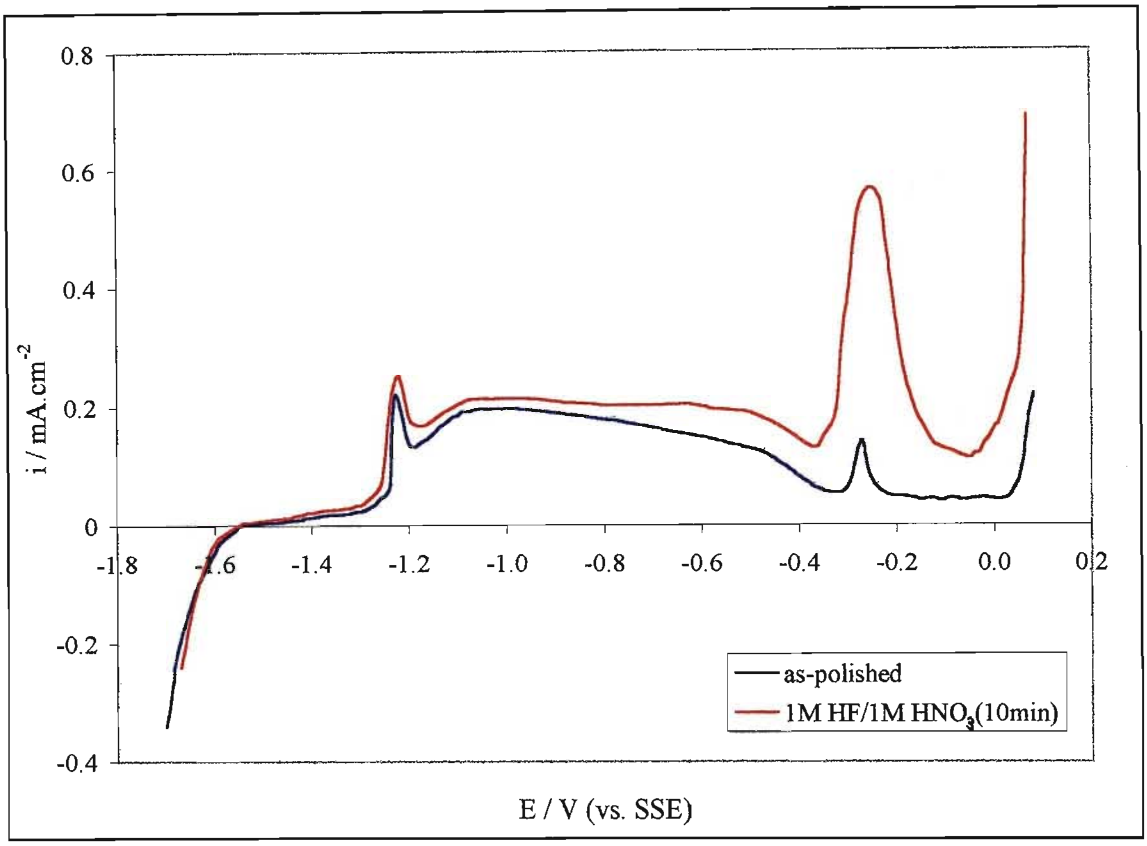

Fig. 34: Typical anodic polarisation curves of the glassy $Co_{66}Fe_4Si_{16}B_{12}Mo_2$ alloy in the as-polished state and after acid pretreatment prior to cathodic polarisation in 1M KOH at 25°C.

The shape of the anodic polarisation curve of glassy $Co_{66}Fe_4Si_{16}B_{12}Mo_2$ was not greatly affected by acid treatment with all anodic peaks occurring at approximately the same potentials as the as-polished electrode peaks. The E_{corr} and E_{tr} values were not altered by the treatment. Acid treatment produced an increase in the current densities in all regions of the anodic polarisation curve with a substantial increase current density obtained at the peak occurring at -0.24V. The anodic polarisation curves indicate that, as for the $Fe_{67}Co_{18}B_{14}Si_1$ alloy, acid treatment did not influence the corrosion properties of the alloy but produced a surface area increase and consequently a greater apparent current density.

5.4.3 *In situ* anodic pretreatment

5.4.3.1 Glassy $Fe_{67}Co_{18}B_{14}Si_1$

The influence of *in situ* surface activation on the electrocatalytic activity of glassy $Fe_{67}Co_{18}B_{14}Si_1$ for HER was determined in the basic media to compare its effectiveness with *ex situ* acid activation. The Tafel parameters, i_o and b, obtained after anodic oxidation at different constant current densities prior to cathodic polarisation in the hydrogen evolution region are listed in Table 17 and the corresponding Tafel plots are shown in Fig. 35. The current densities obtained from the Tafel plots at -1.65 ($\eta = 0.1$V), -1.70 ($\eta = 0.15$V) and -1.75 V ($\eta = 0.2$V) are also included in the Table 17.

Table 17: Kinetic data for hydrogen evolution on glassy $Fe_{67}Co_{18}B_{14}Si_1$ in 1M KOH at 25°C after anodic oxidation *in situ* at different constant current densities for 2 minutes.

Anodic Treatment /µA.cm^{-2}	Tafel region /V	-b /mV	i_o /A.cm^{-2}	i_1^{*} /mA.cm^{-2}	$i_2^{\otimes}$ /mA.cm^{-2}	$i_3^{\oplus}$ /mA.cm^{-2}
As-polished	-1.63 to -1.82	120 ± 7	(3.08 ± 0.80) x 10^{-5}	0.221 ± 0.055	0.560 ± 0.150	1.421 ± 0.431
10	-1.66 to -1.78	117 ± 5	(3.83 ± 0.43) x 10^{-5}	0.308 ± 0.009	0.820 ± 0.026	2.185 ± 0.094
50	-1.66 to -1.79	113 ± 3	(4.87 ± 1.52) x 10^{-5}	0.313 ± 0.070	0.848 ± 0.172	2.300 ± 0.525
100	-1.66 to -1.79	119 ± 9	(5.16 ± 1.22) x 10^{-5}	0.334 ± 0.096	0.853 ± 0.166	2.184 ± 0.432
300	-1.66 to -1.78	124 ± 9	(6.27 ± 1.17) x 10^{-5}	0.359 ± 0.028	0.936 ± 0.089	2.440 ± 0.274
500	-1.66 to -1.78	131 ± 8	(7.04 ± 1.05) x 10^{-5}	0.378 ± 0.035	0.973 ± 0.077	2.511 ± 0.225
750	-1.67 to -1.81	113 ± 5	(3.36 ± 0.13) x 10^{-5}	0.290 ± 0.026	0.769 ± 0.084	2.042 ± 0.289
1000	-1.66 to -1.81	115 ± 9	(2.97 ± 0.95) x 10^{-5}	0.226 ± 0.042	0.599 ± 0.070	1.600 ± 0.150
2000	-1.66 to -1.81	109 ± 6	(2.55 ± 1.00) x 10^{-5}	0.214 ± 0.063	0.559 ± 0.143	1.530 ± 0.310
3000	-1.66 to -1.81	106 ± 7	(2.20 ± 0.53) x 10^{-5}	0.192 ± 0.019	0.543 ± 0.040	1.402 ± 0.066

* E = -1.65V, $^{\otimes}$ E = -1.70V, $^{\oplus}$ E = -1.75V (vs. SSE)

Anodic treatment improved the activity of the glassy $Fe_{67}Co_{18}B_{14}Si_1$ alloy for the HER in comparison to the as-quenched state as can be seen from the resulting increase in the current densities, however the increases were found to be small and the Tafel plots fall close together. The Tafel plots obtained after anodic treatments of 10, 50, 2000 and 3000 µA.cm^{-2} were omitted from the graph for clarity as they were very similar to those obtained at the as-polished electrode. The activity of the alloy for hydrogen evolution increased with an increasing magnitude of anodic current to a maximum level that corresponded to a treatment of 500µA.cm^{-2}. Treatments with oxidation currents greater than 500µA.cm^{-2} led to a decrease in the activity of the alloy and treatments of 2000 and 3000 µA.cm^{-2} resulted in lower current densities than those obtained at the as-polished surface.

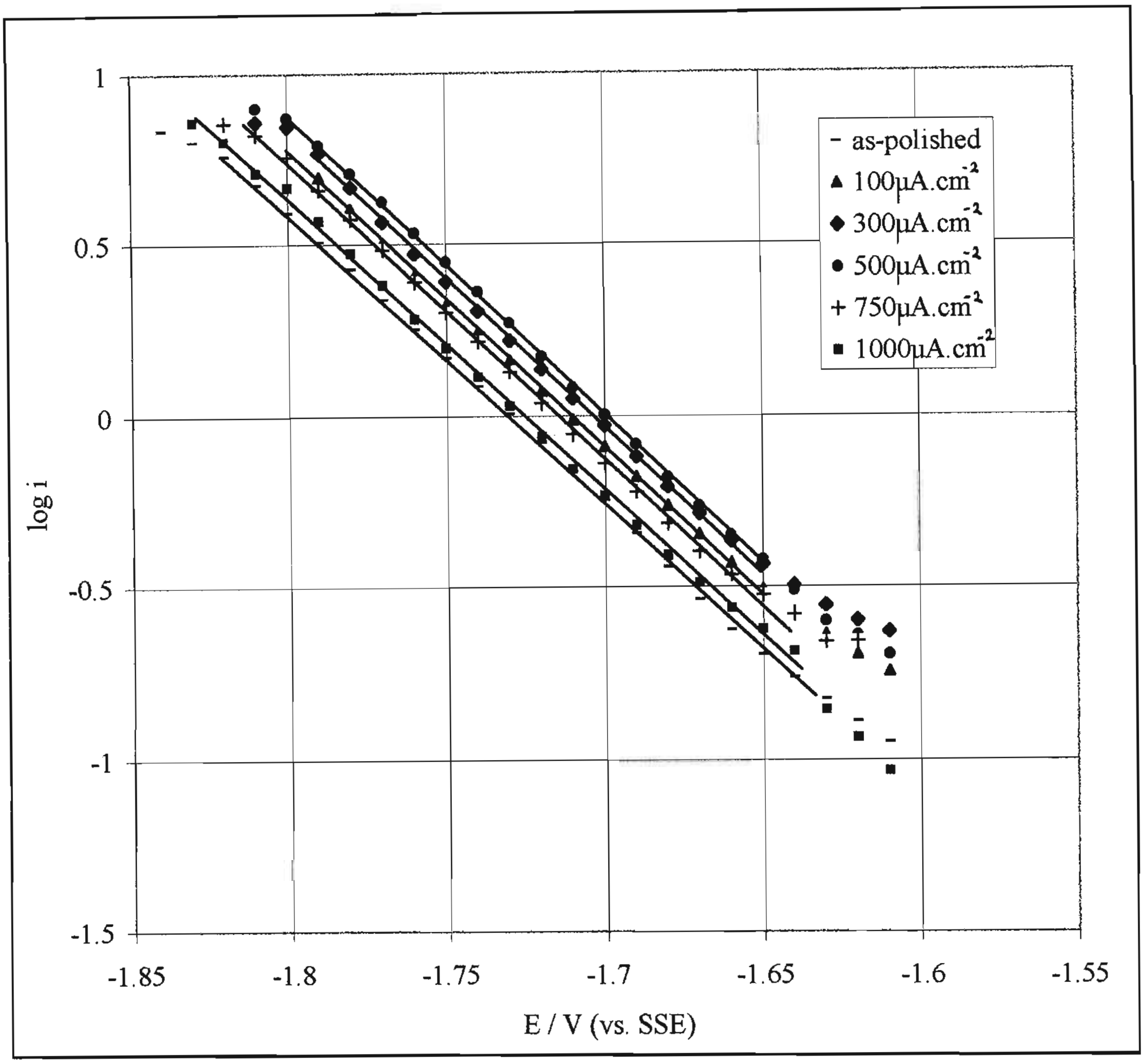

Fig. 35: Tafel plots for hydrogen evolution on the glassy $Fe_{67}Co_{18}B_{14}Si_1$ electrode after *in situ* anodic oxidation at constant current densities for 2 minutes in 1M KOH at 25°C.

The variation in the i_o values for hydrogen evolution at the glassy $Fe_{67}Co_{18}B_{14}Si_1$ electrode resulting from the different anodic treatments are illustrated in Fig. 36. The i_o values increased to a maximum value of 7.04 x 10^{-5} A.cm^{-2}, corresponding to a treatment of 500μA.cm^{-2}, after which they decreased. Anodic treatments of 750, 1000, 2000 and 3000 μA.cm^{-2} produced i_o values that were lower in value than that of the as-polished electrode. A single Tafel slope was obtained for each anodic treatment that increased slightly to a maximum value of 131mV (500μA.cm^{-2}) after which the slope decreased with a further increase in the anodic current density.

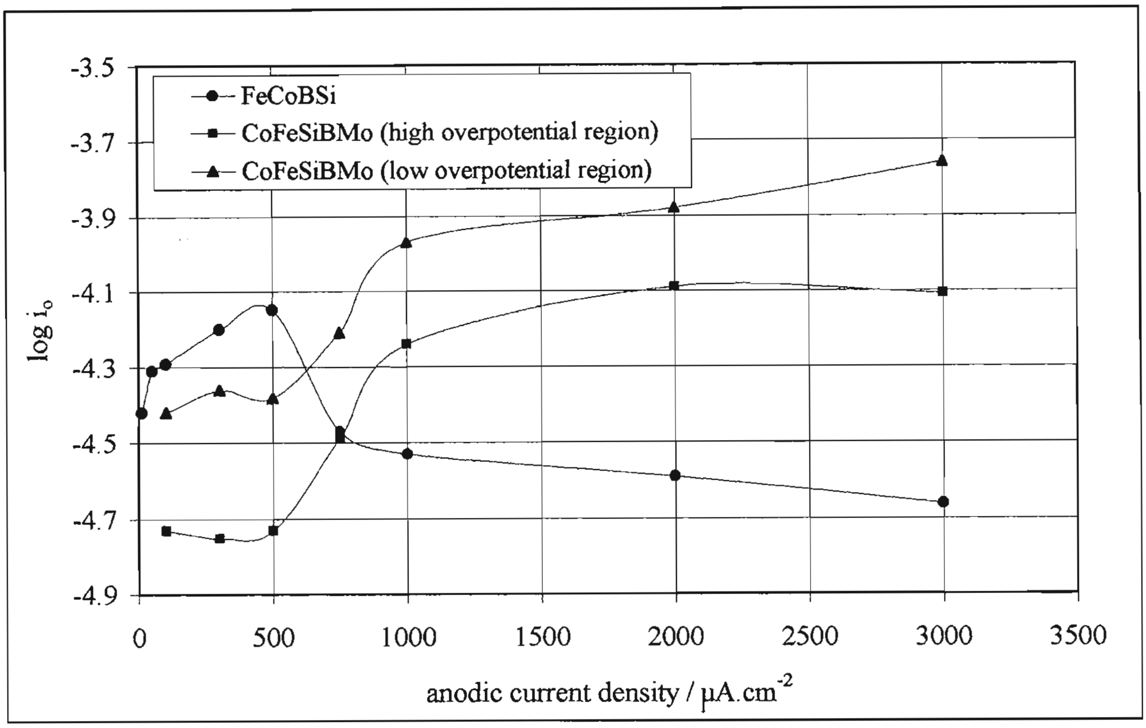

Fig. 36: Exchange current densities obtained for hydrogen evolution after anodic oxidation of the $Fe_{67}Co_{18}B_{14}Si_1$ and $Co_{66}Fe_4Si_{16}B_{12}Mo_2$ electrodes at constant current density in 1M KOH at 25°C.

The influence of the anodic treatment time on the activity of the $Fe_{67}Co_{18}B_{14}Si_1$ alloy was also investigated using the most activating anodic treatment of 500µA.cm^{-2}. The Tafel parameters obtained for treatment times of 2, 10 and 30 minutes are listed in Table 18 and the corresponding Tafel plots are shown in Fig. 37.

Table 18: Kinetic data for hydrogen evolution at the glassy $Fe_{67}Co_{18}B_{14}Si_1$ electrode, in 1M KOH at 25°C, after *in situ* anodic oxidation at 500µA.cm^{-2} for different times.

	High η region			Low η region					
500 /µA.cm^{-2} treatment	Tafel region /V	-b /mV	i_o /A.cm^{-2}	Tafel region /V	-b /mV	i_o /A.cm^{-2}	i_1* mA.cm^{-2}	$i_2^{\otimes}$ mA.cm^{-2}	$i_3^{\oplus}$ mA.cm^{-2}
2 min	-1.63 to -1.80	131 ± 8	(7.04 ± 1.05) x 10^{-5}	-	-	-	0.378 ± 0.035	0.973 ± 0.077	2.511 ± 0.225
10 min	-1.72 to -1.84	140 ± 6	(9.76 ± 3.03) x 10^{-5}	-1.59 to -1.72	104 ± 5	(3.76 ± 1.47) x 10^{-5}	0.313 ± 0.095	0.848 ± 0.252	2.300 ± 2.590
30 min	-1.72 to -1.85	144 ± 6	(9.62 ± 1.99) x 10^{-5}	-1.59 to -1.72	111 ± 5	(4.21 ± 0.06) x 10^{-5}	0.334 ± 0.056	0.853 ± 0.135	2.184 ± 0.248

* E = -1.65V, $^{\otimes}$ E = -1.70V, $^{\oplus}$ E = -1.75V (vs. SSE)

An increasing treatment time was found to have little influence on the activity of the alloy for hydrogen evolution i.e. the magnitude of the current densities did not increase, resulting in almost superimposable Tafel plots. Treatment times of 10 and 30 minutes did, however, produce two distinct, although not very different, Tafel slopes in comparison to the single slope produced for a treatment time of two minutes. The two slopes occurred in the potential ranges of -1.59 to -1 72V and -1.72 to -1.85V in the low and high potential regions respectively. The alloy displayed a greater activity for hydrogen evolution in the low overpotential region as lower Tafel slope values were obtained in this region.

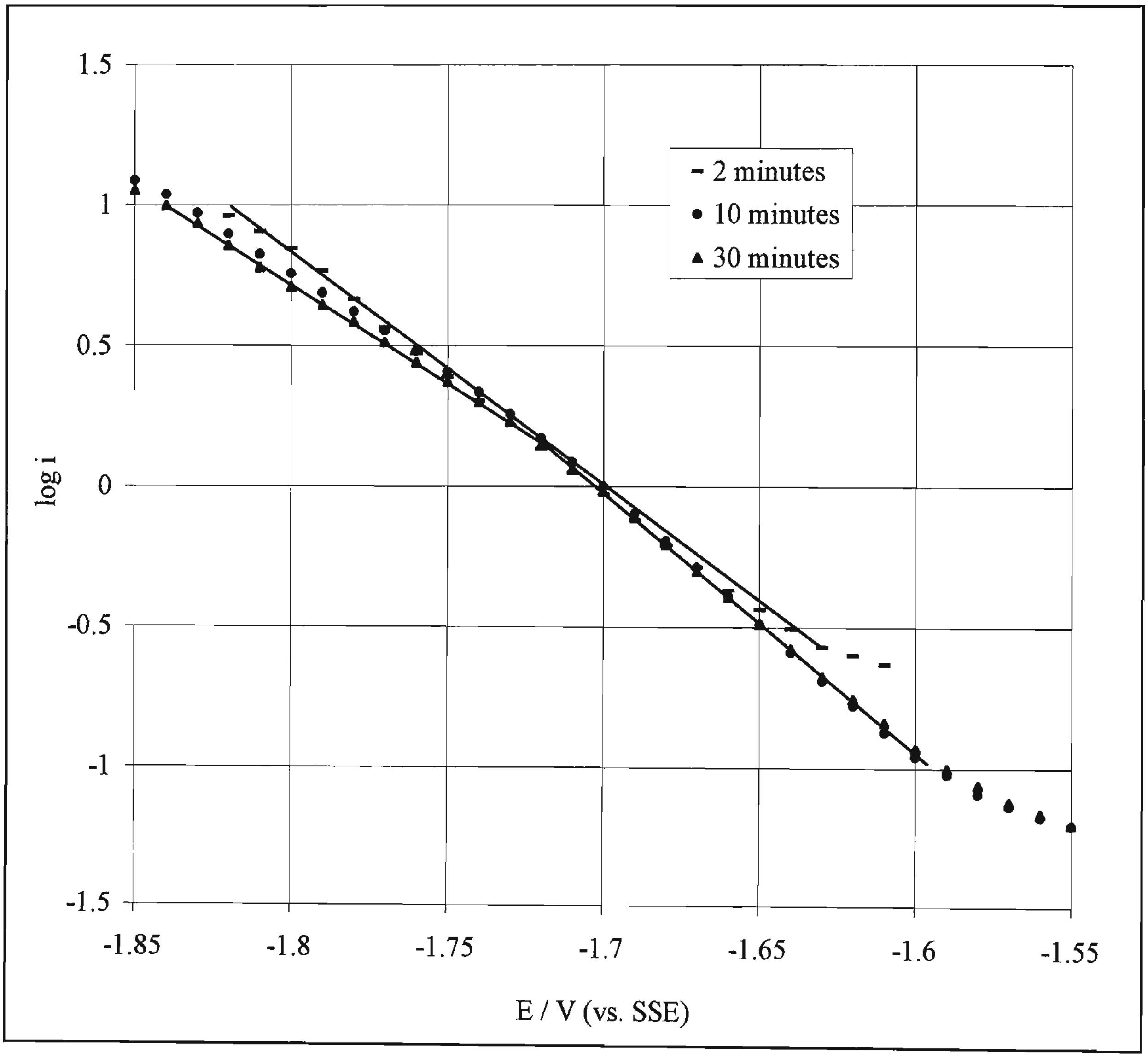

Fig. 37: Tafel plots for hydrogen evolution on the glassy $Fe_{67}Co_{18}B_{14}Si_1$ electrode after *in situ* anodic oxidation at $500\mu A.cm^{-2}$ for different times.

Oxygen bubbles formed on the electrode surface for anodic treatments of 1000μA.cm^{-2} and greater that had to be tapped off prior to the commencement of cathodic polarisation. Anodic treatment also resulted in the formation of a very faint orange/brown layer on the electrode surface that became darker as the magnitude of the anodic oxidation current was increased. This layer was not fully reduced by subsequent cathodic polarisation and was still visible on completion of the HER. The layer was very fine and could not be scraped off and analysed separately by EDS. The electrode surface was examined under the SEM microscope after the different anodic treatments and the SEM micrographs obtained after treatments of 500 (2min) and 3000 μA.cm^{-2} (2min) are shown in Fig. 38.

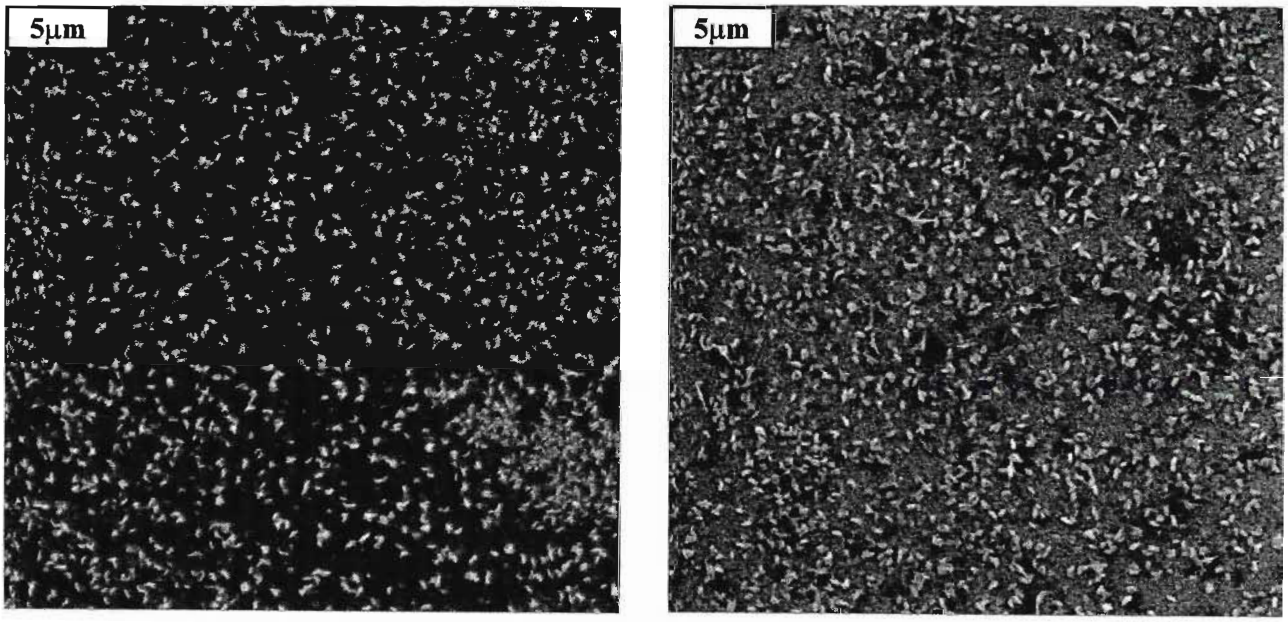

(a) 500 μA.cm^{-2} for 2 minutes (mag. x4000)

(b) 3000 μA.cm^{-2} for 2 minutes (mag. x4000)

Fig. 38: SEM micrographs of the glassy $Fe_{67}Co_{18}B_{14}Si_1$ electrode after anodic oxidation at constant current densities.

A layer of surface particles was visible on the electrode surface that probably caused the faint orange colouration. An anodic treatment of 500μA.cm^{-2} resulted in the formation of large particles that were sparsely distributed on the electrode surface. A treatment of 3000μA.cm^{-2} resulted in the formation of a dense layer of particles that totally covered the alloy surface and consisted of two distinct particle sizes. Large and sparsely distributed particles, similar to those formed at 500μA.cm^{-2}, were visible as well as a dense layer of extremely small particles that totally covered the alloy substrate.

It is suggested that the particles provided hydrogen adsorption sites that were different from the sites on the smooth and polished amorphous surface. Different adsorption sites altered the strength of the surface-hydrogen bond interaction and therefore influenced the rate of hydrogen evolution. The formation of different adsorption sites is also supported by the change in the Tafel slope resulting from the different anodic treatments. It appears that the larger particles improved the activity of the alloy for hydrogen evolution by providing catalytically active surface sites and also by increasing the electrode surface area at which the HER could occur. The compact layer of small particles only formed for anodic treatments greater than 500μA.cm^{-2} and appeared to provide different adsorption site that inhibited the HER in comparison to the as-polished alloy surface. The decreased activity was indicated by lower Tafel currents obtained for anodic treatments of 750, 1000 2000 and 3000μA.cm^{-2}. Furthermore, the anodic polarisation curve of the as-polished glassy $Fe_{67}Co_{18}B_{14}Si_1$ electrode (Fig. 17) showed two distinct passive regions of different current density. The region of higher current density occurred at more cathodic potentials (-1.11 to -0.50V) and decreased to a passive region of much lower current density prior to the onset of oxygen evolution. The two regions indicate that a change in the nature of the passive film or a restructuring of the passive film occurred as the potential becomes more anodic. Anodic treatments of lower oxidation current produced a higher activity for the HER than the second layer of dense particles that formed at higher oxidation currents. Further investigation of the nature of the surface sites and the chemical mechanism by which hydrogen evolution occurs at anodically treated surfaces is required.

The results obtained from EDS analysis of the $Fe_{67}Co_{18}B_{14}Si_1$ electrode after anodic treatments of different oxidation current are listed in Table 19.

Table 19: EDS analysis of the glassy $Fe_{67}Co_{18}B_{14}Si_1$ surface after different anodic treatments.

	Fe	Co	Si
Polished electrode surface	77.80	21.22	0.98
500 μA.cm^{-2} (2min) anodic treatment	80.23	19.08	0.69
3000 μA.cm^{-2} (2min) anodic treatment	81.45	17.84	0.71

Fe enrichment on the alloy surface was detected after anodic pretreatment in comparison to the polished alloy surface. An anodic treatment at 500μA.cm^{-2} (2min) resulted in a 2.43 wt% increase in Fe and a proportional 2.14 wt% decrease in Co on the alloy surface. A treatment of 3000μA.cm^{-2} (2min) resulted in a 3.65 wt% increase in Fe and a 3.38 wt% decrease in Co. These quantitative EDS results indicate that an Fe-enriched layer of surface particles was formed by anodic treatment. Surface analysis techniques such as AES or XPS would be required to determine the composition of the surface particles.

In situ surface activation of glassy $Fe_{67}Co_{18}B_{14}Si_1$ was less effective than acid pretreatment in activating the alloy surface for the HER, i.e. a maximum i_o value of 9.94×10^{-5} A.cm^{-2} resulted from the most activating acid treatment (1M HF/1M HNO_3, 1 minute) as compared to a value of 7.04×10^{-5} A.cm^{-2} after anodic treatment (500μA.cm^{-2}, 2 minutes). Although less effective than acid activation, anodic activation was also less destructive and would produce a more durable electrocatalyst. Consequently, anodic treatment is the recommended method of activation for glassy $Fe_{67}Co_{18}B_{14}Si_1$ alloy.

No kinetic parameters are available in the literature for hydrogen evolution at the glassy $Fe_{67}Co_{18}B_{14}Si_1$ electrode surface after anodic oxidation, however, the values reported for the similar glassy $Fe_{60}Co_{20}B_{10}Si_{10}$ composition are recorded in Table 20 for comparison. Glassy $Fe_{60}Co_{20}B_{10}Si_{10}$ was tested after *in situ* anodic oxidation of the bright (upper) ribbon surface of the alloy in the as-queched state.

Table 20: Literature Tafel parameters [70,71] for hydrogen evolution on glassy $Fe_{60}Co_{20}B_{10}Si_{10}$ in KOH at 25°C after *in situ* anodic oxidation at different current densities for 2 minutes.

Electrode	Electrolyte	Anodic treatment / μA.cm^{-2}	i_o / A.cm^{-2}	b / mV	Reference
$Fe_{60}Co_{20}B_{10}Si_{10}$	1M KOH	As-quenched	1.38×10^{-6}	97	71
		10	2.00×10^{-6}	133	
		50	1.58×10^{-6}	118	
		100	4.79×10^{-6}	112	
		300	6.31×10^{-6}	120	
		500	2.82×10^{-5}	135	
		2000	2.75×10^{-5}	137	
		3000	1.10×10^{-5}	111	
$Fe_{60}Co_{20}B_{10}Si_{10}$	30 wt% KOH	200	1.6×10^{-3}	71	70
		500	1.1×10^{-3}	77	
		1000	2.3×10^{-3}	77	
		2000	2.1×10^{-3}	80	
		5000	1.0×10^{-3}	99	

Huot et al. [70] found that *in situ* anodic treatment of glassy $Fe_{60}Co_{20}B_{10}Si_{10}$ at 25°C in 30 wt% KOH at constant current densities resulted in a very minor improvement in the activity of the alloy for hydrogen evolution in comparison to the as-quenched state. However, a substantial improvement in activity resulted at 70°C after the same anodic treatments (in particular for a treatment of 1mA.cm^{-2} (2 minutes)). This is in agreement with the results obtained at the glassy $Fe_{67}Co_{18}B_{14}Si_1$ electrode in this study, which showed only a slight improvement in activity after anodic treatment at 25°C in comparison to the as-polished electrode. The results obtained by Crousier et al. [71] indicated that anodic treatment of glassy $Fe_{60}Co_{20}B_{10}Si_{10}$ resulted in a much greater increase in the activity of the alloy for hydrogen evolution than the $Fe_{67}Co_{18}B_{14}Si_1$ composition after the same treatment. A maximum i_o value of 28.2 x 10^{-6} A.cm^{-2} was obtained at glassy $Fe_{60}Co_{20}B_{10}Si_{10}$ after a treatment of 500μA.cm^{-2} (2 minutes) compared with the i_o value of 1.38 x 10^{-6} A.cm^{-2} obtained at the as-quenched electrode. The Tafel slope of glassy $Fe_{60}Co_{20}B_{10}Si_{10}$ also increased in value from 97 mV in the as-quenched state to 135mV after an anodic treatment of 500μA.cm^{-2}. This was greater than the increase obtained at the glassy $Fe_{67}Co_{18}B_{14}Si_1$ electrode in this study and suggests that the greater Si content of $Fe_{60}Co_{20}B_{10}Si_{10}$ was responsible for its superior activity. Both glassy $Fe_{60}Co_{20}B_{10}Si_{10}$ and $Fe_{67}Co_{18}B_{14}Si_1$ showed an increase in i_o to a maximum value corresponding to an anodic treatment of 500μA.cm^{-2}, after which the i_o value decreased. This indicates that the electrochemical responses of the two alloys were very similar due to their similar compositions and that the greater Si content was responsible for a superior electrocatalytic activity.

Hout et al. [70] proposed that anodic pretreatment of glassy $Fe_{60}Co_{20}B_{10}Si_{10}$ at a constant current density in 30 wt% KOH resulted in the formation of a black surface layer of Fe_3O_4 by a dissolution-precipitation mechanism involving Fe(II) species. Subsequent cathodic reduction prior to the onset of hydrogen evolution created a porous Fe layer (identified by x-ray diffraction) on which hydrogen evolution occurred. It was proposed that an increased electrode surface area was responsible for the greater activity of the anodically treated alloy surface. SEM analysis (x20 000) showed that the layer of Fe particles coalesced and increased in size during the first thousand seconds of hydrogen evolution. This resulted in a decrease in the effective surface area of the alloy and hence a decrease in the current density for hydrogen evolution. The Fe particles that formed on the $Fe_{60}Co_{20}B_{10}Si_{10}$ electrode were similar to the compact layer of fine particles observed on the $Fe_{67}Co_{18}B_{14}Si_1$ surface after an anodic treatment of 3000μA.cm^{-2} (Fig. 38b), however, the scanning electron microscope used in this study did not have a sufficiently high resolving power to be able to distinguish individual particles at a x20 000 magnification. The growth of Fe particles with a high catalytic activity has also been reported to form on the surface of Fe-based amorphous alloys after thermal treatment [23,153].

5.4.3.2 $Co_{66}Fe_4Si_{16}B_{12}Mo_2$

The Tafel parameters obtained for hydrogen evolution after *in situ* anodic oxidation of the $Co_{66}Fe_4Si_{16}B_{12}Mo_2$ electrode at different constant current densities are listed in Table 21 and the corresponding Tafel plots are shown in Fig. 39.

The Tafel plots for treatments of 100 and 300 $\mu A.cm^{-2}$ were omitted as they produced only slight increases in current density and overlapped with the Tafel plot of the as-polished electrode. The electrocatalytic activity of the glassy $Co_{66}Fe_4Si_{16}B_{12}Mo_2$ composition increased as the anodic current density was increased. This is in contrast to results obtained for the $Fe_{67}Co_{18}B_{14}Si_1$ alloy. Double Tafel slopes were obtained for all anodic treatments occurring between potentials of -1.60 to -1.72V and -1.72 to -1.88V in the low and high overpotential regions respectively. The Tafel slopes in the high overpotential region maintained a constant value of approximately 120mV while the values in the low overpotential region varied more erratically but showed a general trend towards an increase in value. The activity of the alloy was greater in the high overpotential region for all treatments tested i.e. the current densities increased more rapidly with increasing overpotential in the high overpotential region. The variation in the i_o values resulting from the different anodic treatments are show in Fig 36. The i_o values, and hence the electrocatalytic activity of the alloy for the HER, showed the most rapid increase for treatments ranging between 500 and 1000 $\mu A.cm^{-2}$ in both the high and low overpotential regions. Maximum i_o values of 7.68 x 10^{-5} and 17.5 x 10^{-5} $A.cm^{-2}$ were obtained in the high and low overpotential regions after a treatment of 3000 $\mu A.cm^{-2}$ and were 4.99 and 2.12 times greater than the values obtained at the as-polished alloy surface at 25°C.

SEM micrographs obtained after anodic treatments of 500, 1000 and 3000$\mu A.cm^{-2}$ are shown in Fig. 40. Treatment resulted in the formation of small particles on the alloy surface. The particles maintained a constant size but increased in density as the magnitude of the anodic current was increased. A dense layer formed after an anodic treatment of 3000 $\mu A.cm^{-2}$ though which the base alloy was barely visible (Fig. 40c). A very faint orange surface colouration was also visible after treatments greater than 500$\mu A.cm^{-2}$. EDS analysis did not detect variations (>0.4%) in component concentrations of the treated alloy surfaces in comparison to the as-polished surface, possibly due to the extreme thinness of the particle layer. The layer was much lighter but appeared similar to that formed on the $Fe_{67}Co_{18}B_{14}Si_1$ surface after the same anodic treatment. Due to the constancy of the Tafel slope values and the increase in i_o resulting from increased anodic oxidation treatments, it appears that the mechanism of hydrogen evolution remained unchanged and that enhanced electrocatalytic activity resulted from an increased electrode surface area.

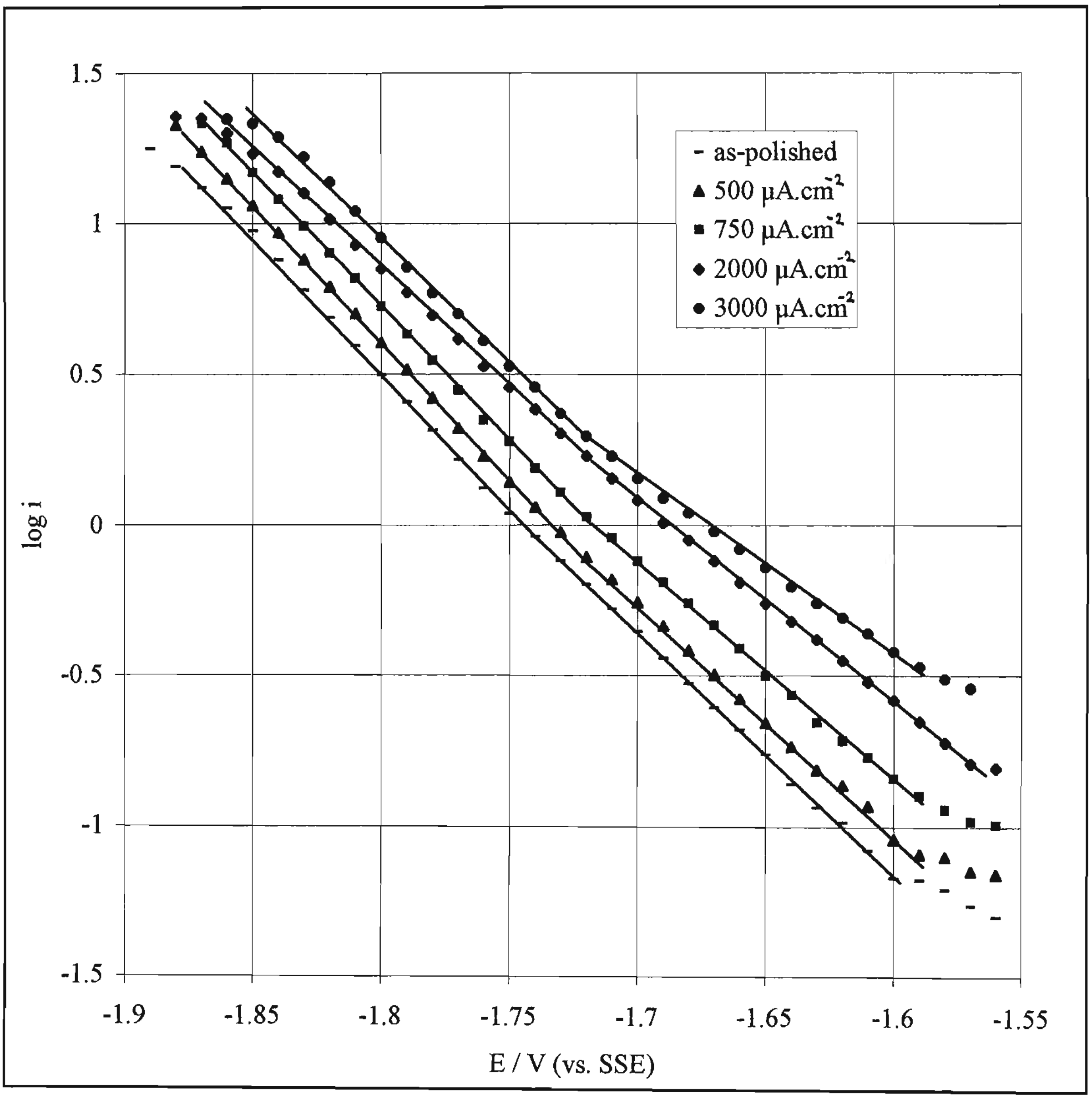

Fig. 39: Tafel plots for hydrogen evolution on the glassy $Co_{66}Fe_4Si_{16}B_{12}Mo_2$ electrode after *in situ* anodic oxidation at constant current densities for 2 minutes in 1M KOH at 25°C.

Table 21: Kinetic data for hydrogen evolution on glassy $Co_{66}Fe_4Si_{16}B_{12}Mo_2$ in 1M KOH at 25°C after anodic oxidation *in situ* at constant current densities for 2 minutes.

	High η region			Low η region					
Anodic Treatment /μA.cm^{-2}	Tafel region /V	-b /mV	i_o /A.cm^{-2}	Tafel region /V	-b /mV	i_o /A.cm^{-2}	i_1* /mA.cm^{-2}	$i_2^{\otimes}$ /mA.cm^{-2}	$i_3^{\oplus}$ /mA.cm^{-2}
as-polished	-1.74 to -1.88	103 ± 9	(1.54 ± 0.58) x10^{-5}	-1.61 to -1.74	158 ± 13	(8.25 ± 3.09) x 10^{-5}	0.267 ± 0.061	1.132 ± 0.398	9.734 ± 2.348
100	-1.72 to -1.89	120 ± 13	(1.88 ± 0.39) x 10^{-5}	-1.60 to -1.72	149 ± 15	(3.77 ± 1.92) x 10^{-5}	0.143 ± 0.054	0.775 ± 0.064	5.291 ± 0.209
300	-1.72 to -1.88	112 ± 6	(1.77 ± 0.19) x 10^{-5}	-1.59 to -1.72	136 ± 8	(4.36 ± 0.56) x 10^{-5}	0.155 ± 0.057	0.890 ± 0.233	7.379 ± 2.771
500	-1.72 to -1.88	106 ± 4	(1.86 ± 0.98) x 10^{-5}	-1.59 to -1.72	129 ± 4	(4.13 ± 1.52) x 10^{-5}	0.189 ± 0.010	1.127 ± 0.044	9.333 ± 1.361
750	-1.72 to -1.87	113 ± 5	(3.23 ± 0.40) x 10^{-5}	-1.59 to -1.72	137 ± 2	(6.12 ± 0.81) x 10^{-5}	0.276 ± 0.031	1.518 ± 0.053	11.991 ± 0.238
1000	-1.72 to -1.86	128 ± 5	(5.76 ± 1.23) x 10^{-5}	-1.60 to -1.72	167 ± 16	(1.08 ± 0.32) x 10^{-4}	0.331 ± 0.072	1.652 ± 0.158	11.262 ± 0.623
2000	-1.72 to -1.86	129 ± 2	(8.18 ± 0.18) x 10^{-5}	-1.57 to -1.72	153 ± 7	(1.31 ± 0.22) x 10^{-4}	0.481 ± 0.062	2.322 ± 0.146	14.844 ± 1.549
3000	-1.72 to -1.84	120 ± 3	(7.68 ± 1.90) x 10^{-5}	-1.60 to -1.72	164 ± 4	(1.75 ± 0.36) x 10^{-4}	0.640 ± 0.131	2.642 ± 0.626	19.693 ± 5.838

* E = -1.64V, $^{\otimes}$ E = -1.74V, $^{\oplus}$E = -1.84V (vs.SSE)

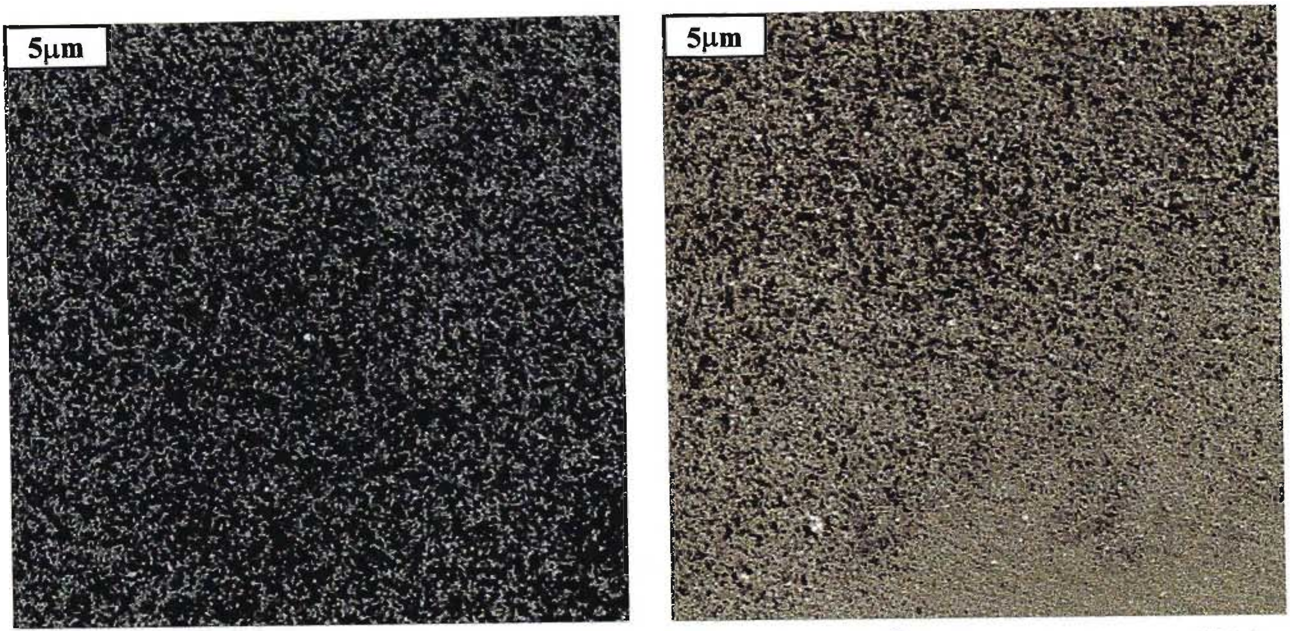

(a) 500 μA.cm^{-2} for 2 minutes (mag. x4000)

(b) 1000 μA.cm^{-2} for 2 minutes (mag. x4000)

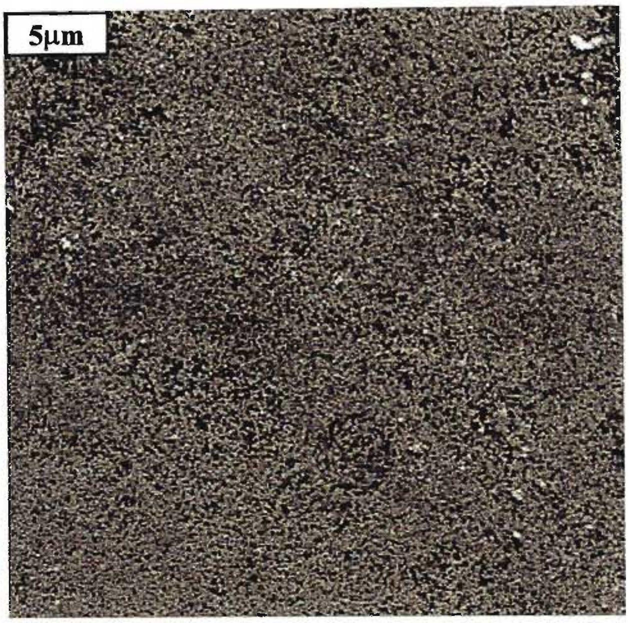

(c) 3000 μA.cm^{-2} for 2 minutes (mag. x4000)

Fig. 40: SEM micrographs of the glassy $Co_{66}Fe_4Si_{16}B_{12}Mo_2$ electrode after anodic oxidation at constant current densities.

In situ surface activation of glassy $Co_{66}Fe_4Si_{16}B_{12}Mo_2$ was significantly less effective than acid activation in enhancing the rate of hydrogen evolution at the alloy surface. Maximum i_o values of 28.7 x 10^{-5} and 46.6 x 10^{-5} A.cm^{-2} were obtained after acid pretreatment (1M HF/1M HNO_3, 10 minutes) of the alloy as compared with maximum values of 7.68 x 10^{-5} and 17.7 x 10^{-5} A.cm^{-2} after anodic pretreatment (3000μA.cm^{-2}, 2 minutes) in the high and low overpotential regions respectively. The high activity of the acid treated surface was attributed to its porous structure and the large electrode surface area resulting at which the HER could occur. It was concluded that both anodic and acidic pretreatment enhanced the electrocatalytic activity of glassy $Co_{66}Fe_4Si_{16}B_{12}Mo_2$ for the HER in comparison to the as-polished state with the most effective and recommended activation pretreatment being 1M HF/1M HNO_3 for 10 minutes.

5.4.4 Conclusions

1. Both glassy $Co_{66}Fe_4Si_{16}B_{12}Mo_2$ and $Fe_{67}Co_{18}B_{14}Si_1$ displayed a poor corrosion resistance in 1M KOH. The electrochemical response of glassy $Fe_{67}Co_{18}B_{14}Si_1$ was similar to that of polycrystalline Fe. Potential cycling between the hydrogen and oxygen evolution regions resulted in buildup of a surface layer, possible Fe_2O_3, with progressive disintegration of the alloy occurring by flaking of the layer.

2. The glassy $Co_{66}Fe_4Si_{16}B_{12}Mo_2$ and $Fe_{67}Co_{18}B_{14}Si_1$ alloys displayed a similar electrocatalytic activity for hydrogen evolution in the as-polished state at 25°C. Both these alloy compositions displayed a lower activity for hydrogen evolution than the similar glassy $Fe_{60}Co_{20}Si_{10}B_{10}$ and $Fe_{75}Si_{11}B_{11}$ compositions. The main difference between the alloys was the metalloid Si content and it was suggested that Si enhanced the activity of the glassy alloys for HER.

3. The activity of both the as-polished glassy $Fe_{67}Co_{18}B_{14}Si_1$ and $Co_{66}Fe_4Mo_2Si_{16}B_{12}$ surfaces increased as with increasing electrolyte temperature. The $Co_{66}Fe_4Si_{16}B_{12}Mo_2$ alloy displayed a greater temperature dependence for hydrogen evolution than the $Fe_{67}Co_{18}B_{14}Si_1$ alloy. The $Fe_{67}Co_{18}B_{14}Si_1$ alloy produced a single Tafel slope that remained constant (approximately 120mV) at all temperatures. The Tafel region of the $Co_{66}Fe_4Mo_2Si_{16}B_{12}$ alloy consisted of two slopes that were divided into regions defined as low and high overpotential regions. At all temperatures the high overpotential region displayed a higher activity for hydrogen evolution, i.e. the current density increased most rapidly with increasing overpotential. The change in Tafel slope indicated that a possible change in hydrogen evolution reaction mechanism or in the adsorption intermediates occurred on passing from low to high overpotentials.

4. A larger activation energy was obtained at glassy $Co_{66}Fe_4Si_{16}B_{12}Mo_2$ electrode than the $Fe_{67}Co_{18}B_{14}Si_1$ electrode which reflects the greater stability of the former alloy in 1M KOH. The $Fe_{67}Co_{18}B_{14}Si_1$ alloy displayed a poorer tendency to passivate and had a lower activation energy as the passive film formed prior to entry into the cathodic hydrogen evolution region was easier to break down. The $Co_{66}Fe_4Si_{16}B_{12}Mo_2$ alloy had a relatively more stable and compact passive film so that a higher activation energy was required for its breakdown.

5. Anodic pretreatment was more effective in improving the activity of glassy $Co_{66}Fe_4Si_{16}B_{12}Mo_2$ for the HER than the $Fe_{67}Co_{18}B_{14}Si_1$ composition. The $Co_{66}Fe_4Si_{16}B_{12}Mo_2$ alloy showed a progressive increase in activity with an increase in oxidation current. This was attributed to the formation of Fe-rich particles on the amorphous surface which provided a greater number of adsorption sites at which the HER could occur. The $Fe_{67}Co_{18}B_{14}Si_1$ alloy displayed the greatest activity after a treatment of 500μA.cm^{-2}, after which the activity of the alloy decreased. This was attributed to the formation of two types of surface particles. A deposit of larger surface particles, formed at 500μA.cm^{-2}, provided catalytically active sites while a smaller and more dense layer of particles, formed at 750 to 3000μA.cm^{-2}, inhibited the HER in comparison to the as-polished surface.

6. Pure HF was less effective than the HF/HNO_3 mixture in improving the electrocatalytic activity of both glassy $Fe_{67}Co_{18}B_{14}Si_1$ and $Co_{66}Fe_4Si_{16}B_{12}Mo_2$ for the HER. Glassy $Co_{66}Fe_4Si_{16}B_{12}Mo_2$ displayed a maximum activity for hydrogen evolution after immersion in 1M HF/1M HNO_3 (10 minutes). A porous surface with a greatly enhanced surface area was observed by SEM and no changes in the alloy component concentrations were detected in comparison to the as-polished electrode. This surface displayed a higher activity for hydrogen evolution than the polycrystalline Fe and Co components of the alloy and was also more active than polycrystalline Ni and Pt. Acid treatment of glassy $Fe_{67}Co_{18}B_{14}Si_1$ was a destructive technique that would form a more stable and long-life catalyst.

7. Anodic polarisation curves of both acid treated $Fe_{67}Co_{18}B_{14}Si_1$ (1M HF/1M HNO_3, 1 minute) and $Co_{66}Fe_4Mo_2Si_{16}B_{12}$ (1M HF/1M HNO_3, 10 minute) indicated that treatment increased the surface area of the electrodes and had little affect on the corrosion properties of the alloys. The shapes of the acid treatment curves remained constant and increases in the apparent current densities resulted in all regions of the curves (because current densities calculated were based on the geometric electrode areas).

5.5 ELECTROCATALYSIS BY GLASSY $Fe_{40}Ni_{40}P_{14}B_6$ AND $Fe_{40}Ni_{40}B_{20}$ FOR THE HER

5.5.1 As-polished electrodes at different electrolyte temperatures

$Fe_{40}Ni_{40}P_{14}B_6$

The Tafel parameters obtained for hydrogen evolution at the glassy $Fe_{40}Ni_{40}P_{14}B_6$ electrode at the five different electrolyte temperatures tested are listed in Table 22 and the corresponding Tafel plots are shown in Fig. 41.

Table 22: Kinetic data for hydrogen evolution at the glassy $Fe_{40}Ni_{40}P_{14}B_6$ electrode in 1M KOH at different temperatures.

	High η region			Low η region					
T/ °C	Tafel range /V	-b/ mV	i_o /A.cm^{-2}	Tafel range / V	-b/ mV	i_o /A.cm^{-2}	i_1*/ mA.cm^{-2}	$i_2^{\otimes}$/ mA.cm^{-2}	$i_3^{\oplus}$/ mA.cm^{-2}
25	-1.71 to -1.83	72 ± 3	(4.57 ± 1.76) x 10^{-7}	-1.63 to -1.71	127 ± 9	(6.11 ± 0.73) x 10^{-6}	0.052 ± 0.011	0.125 ± 0.014	0.462 ± 0.102
30	-1.71 to -1,83	86 ± 7	(2.02 ± 0.99) x 10^{-6}	-1.63 to -1.71	133 ± 10	(1.02 ± 0.29) x 10^{-5}	0.080 ± 0.021	0.181 ± 0.044	0.650 ± 0.114
40	-1.70 to -1.81	97 ± 4	(3.32 ± 0.81) x 10^{-6}	-1.62 to -1.70	175 ± 11	(1.87 ± 0.55) x 10^{-5}	0.098 ± 0.015	0.211 ± 0.035	0.781 ± 0.049
50	-1.70 to -1.81	124 ± 18	(1.34 ± 0.48) x 10^{-5}	-1.63 to -1.70	189 ± 17	(5.44 ± 2.85) x 10^{-5}	0.183 ± 0.062	0.335 ± 0.304	1.074 ± 0.740
70	-1.71 to -1.81	141 ±15	(6.06 ± 2.31) x 10^{-5}	-1.63 to -1.71	193 ± 10	(1.26 ± 0.31) x 10^{-4}	0.515 ± 0.083	0.922 ± 0.242	2.119 ± 0.477

* E = -1.65V, $^{\otimes}$ E = -1.70V, $^{\oplus}$ E = -1.75V (vs. SSE)

In the linear Tafel region two slopes were obtained with potentials ranging between -1.63 to -1.71V in the low overpotential region and -1.71 to -1.83V in the high overpotential region. With increasing temperature the two distinguishable Tafel regions were maintained and the Tafel lines shifted towards appreciably lower overpotentials. Double Tafel slopes have also been obtained by Gennero de Chialvo and Chialvo [89] for hydrogen evolution on crystalline Ni and $Ni_{1-x}Mo_x$ (x = 0 to 25) alloys in 2M NaOH at 30°C and by Lian et al. [109] for hydrogen evolution at glassy $Ni_{50}Co_{25}P_{15}B_{10}$ and $Ni_{50}Co_{25}Si_{15}B_{10}$ alloys and crystalline Ni in 1M KOH at 25°C.

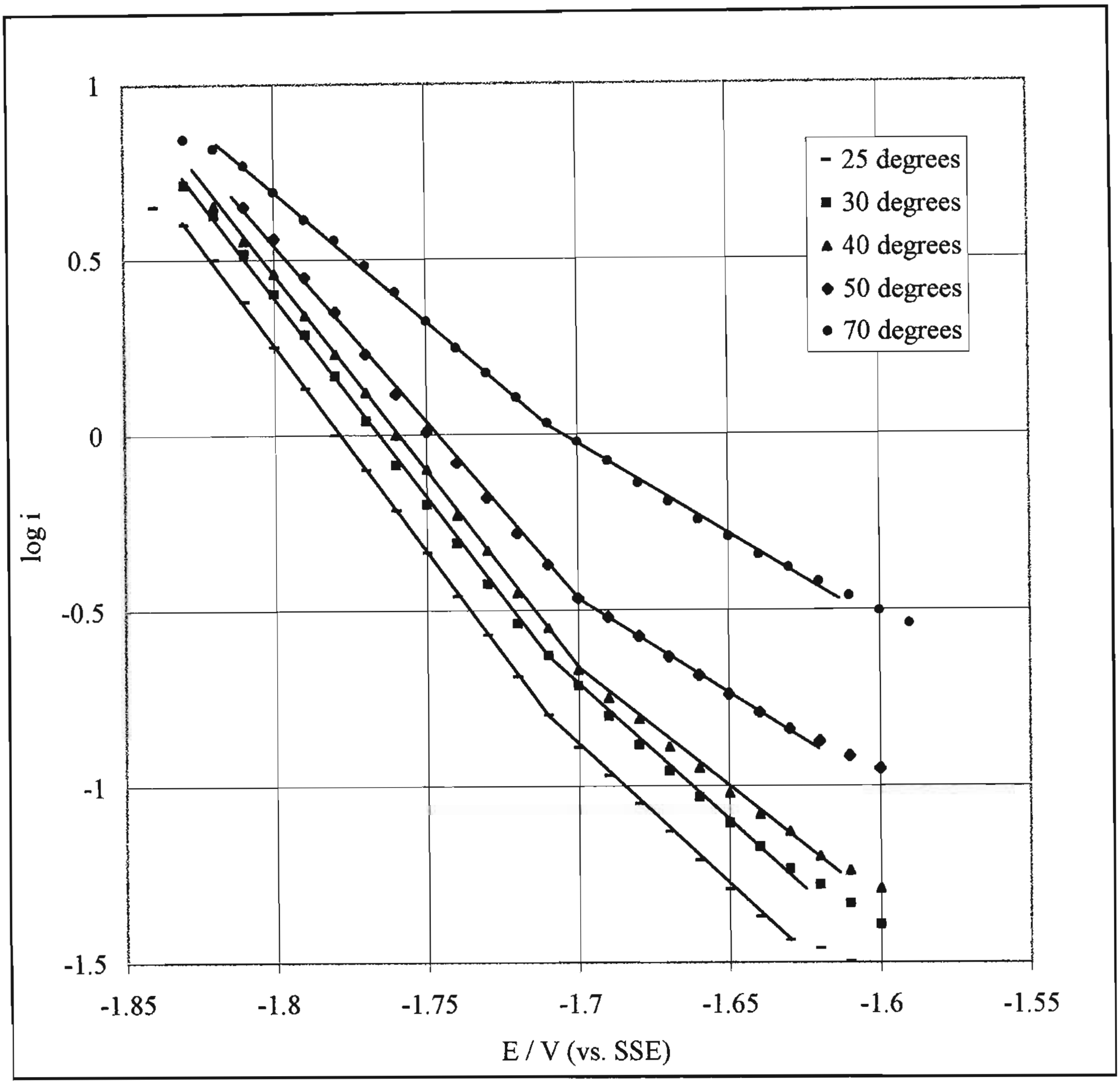

Fig. 41: Tafel plots of hydrogen evolution on the glassy $Fe_{40}Ni_{40}P_{14}B_6$ electrode in 1M KOH at different temperatures.

In both the high and low overpotential regions the Tafel slopes of glassy $Fe_{40}Ni_{40}P_{14}B_6$ increased with increasing temperature in accordance with the Tafel relation resulting in a convergence of the Tafel lines and a reduction in the rate of hydrogen evolution. At all temperatures the electrocatalytic activity of the alloy was greatest in the high overpotential region, i.e. further away from the corrosion potential, with the current density increasing most rapidly with increasing potential. The i_o values increased in an exponential manner with increasing temperature, increasing from 0.46 x 10^{-6} (25°C) to 60.6 x 10^{-6} $A.cm^{-2}$ (70°C) in the high overpotential region and from 0.61 x 10^{-5} (25°C) to 12.6 x 10^{-5} $A.cm^{-2}$ (70°C) in the low overpotential region. Temperature increase significantly improved the electrocatalytic efficiency of glassy $Fe_{40}Ni_{40}P_{14}B_6$ for the HER the exponential variation of i_o suggests that the reaction was an activation controlled process rather than a diffusion controlled reaction.

$Fe_{40}Ni_{40}B_{20}$

The Tafel parameters obtained at the glassy $Fe_{40}Ni_{40}B_{20}$ electrode for hydrogen evolution at the different electrolyte temperatures are listed in Table 23. The Tafel plots from which the kinetic parameters were calculated are shown in Fig. 42.

Table 23: Kinetic data for hydrogen evolution at the glassy $Fe_{40}Ni_{40}B_{20}$ electrode in 1M KOH at different temperatures.

	High η region			Low η region					
T/ °C	Tafel range /V	-b /m V	i_o /A.cm^{-2}	Tafel range /V	-b /mV	i_o/ A.cm^{-2}	i_1*/ mA.cm^{-2}	$i_2^{\otimes}$/ mA.cm^{-2}	$i_3^{\oplus}$/ mA.cm^{-2}
25	-1.75 to -1.89	117 ± 5	(5.56 ± 1.28) x 10^{-6}	-1.63 to -1.75	164 ± 9	(1.62 ± 0.73) x 10^{-5}	0.066 ± 0.011	0.275 ± 0.041	2.012 ± 0.469
30	-1.74 to -1.87	114 ±14	(8.55 ± 2.10) x 10^{-6}	-1.63 to -1.74	139 ± 17	(2.25 ± 0.91) x 10^{-5}	0.092 ± 0.045	0.472 ± 0.081	3.575 ± 0.222
40	-1.75 to -1.88	126 ±10	(1.88 ± 0.70) x 10^{-5}	-1.65 to -1.75	153 ± 13	(5.91 ± 0.95) x 10^{-5}	0.238 ± 0.098	0.894 ± 0.208	5.535 ± 1.552
50	-1.75 to -1.89	129 ±15	(3.01 ± 1.46) x 10^{-5}	-1.64 to -1.75	184 ± 11	(1.03 ± 0.75) x 10^{-4}	0.466 ± 0.120	1.408 ± 0.368	8.302 ± 3.776
70	-1.75 to -1.85	130 ± 6	(5.83 ± 2.90) x 10^{-5}	-1.63 to -1.75	197 ± 21	(2.41 ± 1.88) x 10^{-4}	0.658 ± 0.396	1.809 ± 0.541	10.706 ± 1.673

* E = -1.65V, $^{\otimes}$ E = -1.75V, $^{\oplus}$ E = -1.85V (vs. SSE)

Two linear Tafel regions with different slopes were also obtained at the glassy $Fe_{40}Ni_{40}B_{20}$ electrode at each temperature tested. The low overpotential region ranged between potentials of -1.63 to -1.75V in the low overpotential region and -1.75 to -1.89V (25°C) in the high overpotential region. The activity the alloy for hydrogen evolution was greatest in the high overpotential region as was the case for the $Fe_{40}Ni_{40}P_{14}B_6$ alloy. Slight increases in the Tafel slope values occurred with increasing temperature that were much lower than the increases obtained at the $Fe_{40}Ni_{40}P_{14}B_6$ electrode. An exception to this occurred at 30°C in the low overpotential region for which a substantially lower slope of 139mV was obtained. Consequently, the Tafel lines of glassy $Fe_{40}Bi_{40}B_{20}$ appear parallel and do not converge in the manner observed for the $Fe_{40}Ni_{40}P_{14}B_6$ alloy. Constant slopes indicate that the rate of hydrogen evolution remains constant at each temperature. The i_o values of glassy $Fe_{40}Ni_{40}B_{20}$ increased from 5.56 x 10^{-6} (25°C) to 58.3 x 10^{-6} (70°C) in the high overpotential region and from 1.62 x 10^{-5} (25°C) to 24.1 x 10^{-5} A.cm^{-2} (70°C) in the low overpotential region. The increase in the i_o values was not as high as that observed at the $Fe_{40}Ni_{40}P_{14}B_6$ electrode.

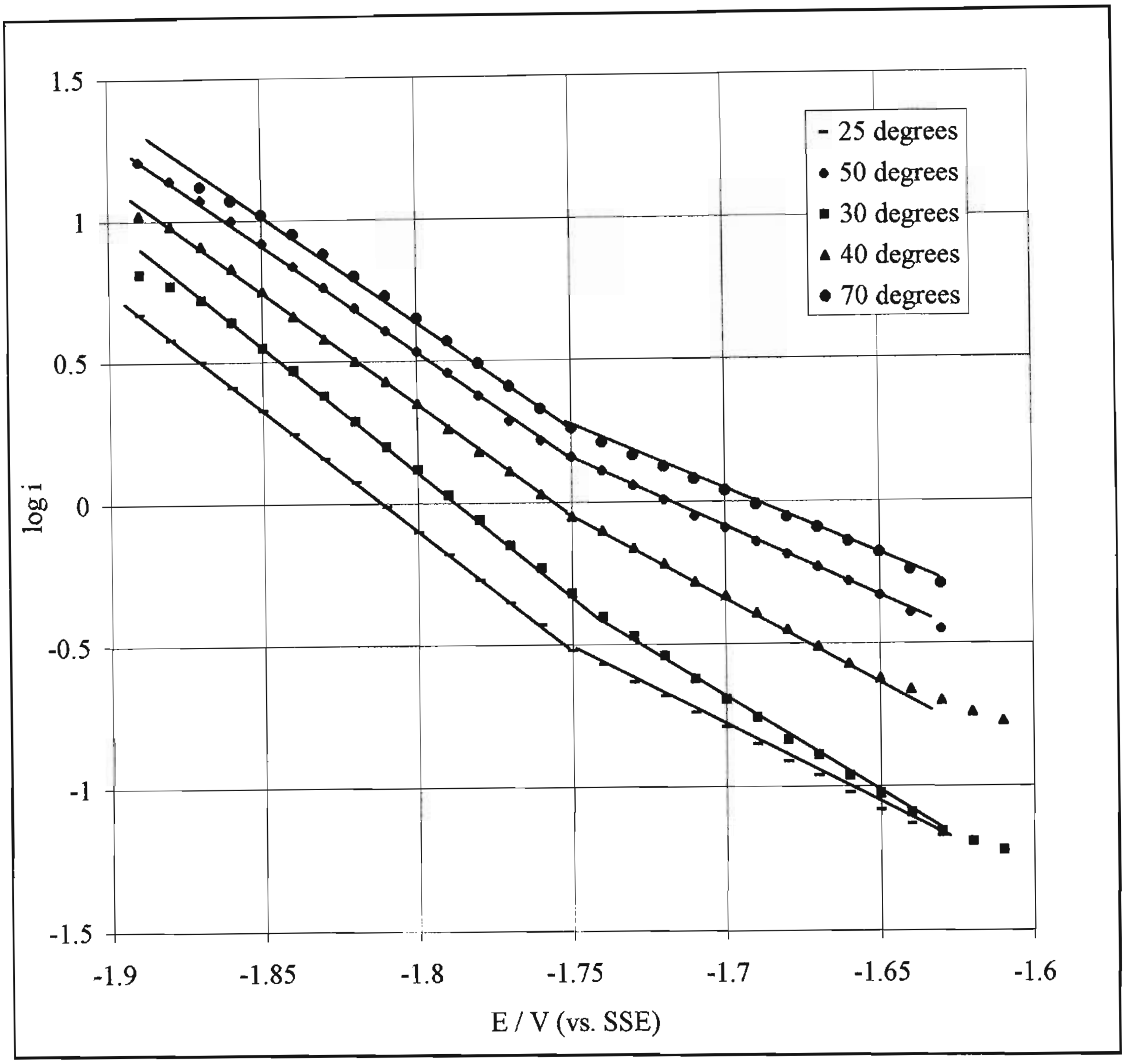

Fig. 42: Tafel plots for hydrogen evolution on the glassy $Fe_{40}Ni_{40}B_{20}$ alloy surface in 1M KOH at different temperatures.

The results indicate that the P-containing glassy $Fe_{40}Ni_{40}P_{14}B_6$ alloy displayed a greater temperature dependence for hydrogen evolution than the P-free $Fe_{40}Ni_{40}B_{20}$ composition, with the Tafel slopes and exchange current densities of the former alloy increasing more rapidly with increasing temperature. Lian et al. [109] investigated the influence of metalloid elements, P and Si, on the electrocatalytic activity of glassy $Ni_{50}Co_{25}P_{15}B_{10}$ and $Ni_{50}Co_{25}Si_{15}B_{10}$ for the HER in 1M KOH at 25°C. Consistent with our results it was reported that the glassy P-containing alloy produced lower Tafel slopes in both overpotential regions than the Si-containing alloy causing the current densities of the P-containing composition to increase more rapidly with increasing overpotential. Podesta et al. [110] reported that the electrocatalytic activity of different amorphous Ni-Co-P alloys (prepared by electroless deposition) for hydrogen evolution in base increased as the P content of the alloy was increased. Contrary findings were reported by Shervedani and Lasia [154] and Paseka [112] who found the Ni-P electrodes (prepared by electrodeposition) of lower P content displayed a higher activity for hydrogen evolution in 1M NaOH at 25°C. Such findings indicate that the influence of metalloid P on the electrocatalytic activity of glassy alloys has not yet been resolved and further investigation of its effect is clearly required.

Linear plots of $\ln i_o$ vs. 1/T were obtained for hydrogen evolution ($\eta = 0$) at both the glassy $Fe_{40}Ni_{40}P_{14}B_6$ and $Fe_{40}Ni_{40}B_{20}$ surfaces. The apparent activation energies calculated from the slopes of the graphs were:

$Fe_{40}Ni_{40}P_{14}B_6$, $E_{a,\eta=0}$ = 57.50 kJ/mole (low overpotential region)
$E_{a,\eta=0}$ = 87.64 kJ/mole (high overpotential region)
$Fe_{40}Ni_{40}B_{20}$, $E_{a,\eta=0}$ = 52.30 kJ/mole (low overpotential region)
$E_{a,\eta=0}$ = 44.65 kJ/mole (high overpotential region)

The activation energies of the two alloys showed a close similarity in the low overpotential region. In the high overpotential region the P-containing alloy had a substantially lower $E_{a,\eta=0}$ value for hydrogen evolution than the P-free alloy.

The Tafel parameters reported in the literature for hydrogen evolution at the glassy $Fe_{40}Ni_{40}P_{14}B_6$ and $Fe_{40}Ni_{40}B_{20}$ electrodes at different electrolyte temperatures are listed in Table 24 for comparison with the values obtained in this study. Only single Tafel slopes and i_o values were reported in the literature [68,71] for hydrogen evolution at the glassy $Fe_{40}Ni_{40}P_{14}B_6$ and $Fe_{40}Ni_{40}B_{20}$ surfaces. In general the kinetic parameters in the lower overpotential region are less commonly reported in literature. The i_o value reported [71] for hydrogen evolution at the glassy $Fe_{40}Ni_{40}P_{14}B_6$ surface (25°C) corresponded closely with the value obtained in this study in the high overpotential region while the Tafel slope reported were approximately 40mV higher than the slope obtained in this study. Crousier et al. [71] tested the alloy in the as-quenched state and did not polish the surface prior to cathodic polarisation which could possibly account for the differences in slope values. The Tafel parameters obtained by Kreysa and Hakanson [68] for hydrogen evolution at glassy $Fe_{40}Ni_{40}B_{20}$ displayed an erratic variation with increasing temperature and the i_o and b values were higher at all temperatures than the values obtained in this study. No other Tafel parameters were available in the literature for hydrogen evolution at the glassy $Fe_{40}Ni_{40}B_{20}$ and $Fe_{40}Ni_{40}P_{14}B_6$ electrode surfaces. Glassy $Fe_{40}Ni_{40}P_{14}B_6$ had lower i_o values in both overpotential regions than polycrystalline Fe [68,69] and Ni [68,95] at all temperatures tested indicating that the glassy alloy had a lower activity for hydrogen evolution than either of its pure metal components. The i_o values of glassy $Fe_{40}Ni_{40}B_{20}$ were lower than polycrystalline Ni at the different temperatures tested indicating that this alloy composition had a lower activity for hydrogen evolution in the as-quenched state than Ni. The glassy alloy displayed a greater temperature dependence for hydrogen evolution than polycrystalline Fe.

Table 24: Tafel parameters [68,69,70,71,93,95,155] reported for hydrogen evolution on glassy $Fe_{40}Ni_{40}B_{20}$ and $Fe_{40}Ni_{40}P_{14}B_6$ alloys and polycrystalline Ni and Fe in base at different temperatures.

Electrode	Electrolyte	T / °C	i_o / A.cm^{-2}	-b / mV	Reference
$Fe_{40}Ni_{40}B_{20}$	1M KOH	30	(1.34 ± 0.34) x10^{-4}	174 ± 7	68
		50	(1.48 ± 0.44) x10^{-4}	184 ± 10	
		70	(5.30 ± 1.70) x10^{-5}	230 ± 14	
		90	(1.07 ± 0.19) x 10^{-3}	188 ± 8	
$Fe_{40}Ni_{40}P_{14}B_6$	1M KOH	25	1.2 x 10^{-7}	109	71
$Fe_{40}Ni_{40}P_{14}B_6$	1M KOH	25	4.57 x 10^{-7} (high η region)	72 (high η)	this work
			6.11 x 10^{-6} (low η region)	127 (low η)	
$Fe_{40}Ni_{40}B_{20}$	1M KOH	30	8.55 x 10^{-6} (high η region) 2.25 x 10^{-5} (low η region)	114 (high η) 139 (low η)	this work
		50	3.01 x 10^{-5} (high η region) 1.03 x 10^{-4} (low η region)	129 (high η) 184 (low η)	
		70	5.83 x 10^{-5} (high η region) 2.41 x 10^{-4} (low η region)	130 (high η) 197 (low η)	
Ni	1M KOH	30	(1.02 ± 0.78) x 10^{-4}	146 ± 19	68
		50	(1.28 ± 0.18) x 10^{-4}	159 ± 3	
		70	(1.37 ± 0.19) x 10^{-4}	159 ± 3	
		90	(1.37 ± 0.32) x 10^{-4}	147 ± 5	
Ni	1M NaOH	25	2 x 10^{-5}	165	155
Ni	1M KOH	25	1.5 x 10^{-5}	-	95
Ni	30wt% KOH	70	3.2 x 10^{-4}	106	93
Fe	1M KOH	25	1.0 x 10^{-5}	135	70
		50	3.3 x 10^{-5}	140	
		75	4.0 x 10^{-5}	150	
Fe	1M KOH	30	(9.38 ± 2.33) x 10^{-5}	160 ± 6	69
		50	(3.18 ± 0.47) x 10^{-4}	165 ± 4	
		70	(5.83 ± 2.07) x 10^{-4}	182 ± 12	
		90	(4.59 ± 1.90) x 10^{-4}	190 ± 19	

5.5.2 *Ex situ* acid pretreatment

Glassy $Fe_{40}Ni_{40}P_{14}B_6$

The influence of different acid treatments on the electrocatalytic activity of glassy $Fe_{40}Ni_{40}P_{14}B_6$ for the HER prior to cathodic polarisation in 1M KOH was determined. The kinetic parameters calculated for each of the treatments are listed in Table 25. The $Fe_{40}Ni_{40}P_{14}B_{20}$ alloy composition was stable in the acid medium and treatments with 1M HF and 1M HF/1M HNO_3 of up to 10 minutes were tested. All acid treatments increased the activity of the alloy and a selection of the Tafel lines obtained are shown in Fig. 43. HF treatments were most effective in increasing the activity of the alloy in the order 1M HF (1min) < 4M HF (1min) < 8M HF (1min) < 1M HF (10min) while HF/HNO_3 mixtures were most effective in the order 1M HF/1M HNO_3 (1min) < 2M HF/2M HNO_3 (1min) < 1M HF/1M HNO_3 (10min). Double Tafel plots consisting of two distinct slopes were obtained for each treatment with the change in slope occurring at a constant potential of -1.71V. The current densities in the high overpotential region increased more rapidly with increasing potential than those in the low overpotential region indicating that the alloy was more active for hydrogen evolution in the high overpotential region. The exception to this was observed after a 1M HF/1M HNO_3 (10 minutes) treatment which produced in a higher activity for hydrogen evolution in the low overpotential region. The Tafel slopes remained constant in the high overpotential region for all treatments (approximately 75mV), maintaining a value that was similar to the as-polished alloy at 25°C. Constant slopes were also obtained in the low overpotential region of the HF-treated surfaces (about 130mV) while a decrease in the slope resulted from HF/HNO_3 treatments of increasing severity. The constant Tafel slopes indicated that the rate of hydrogen evolution was not affected by acid treatment. Therefore, the nature of the active sites and the mechanism of hydrogen evolution remained constant. The greatest improvement in activity resulted from acid treatment with 1M HF/1M HNO_3 for 10 minutes. The i_o value increased from 0.46×10^{-6} (as-polished, 25°C) to 16.2×10^{-6} A.cm^{-2} in the high overpotential region and from 6.11×10^{-6} (as polished, 25°C) to 10.5×10^{-6} A.cm^{-2} in the low overpotential region. The i_o value was 35.4 times greater after acid treatment than at the as-polished electrode in the high overpotential region.

Table 25: Kinetic data for hydrogen evolution on glassy $Fe_{40}Ni_{40}P_{14}B_6$, in 1M KOH at 25°C, after different chemical pretreatments.

		High η region			Low η region					
Chemical treatment	Treatment period /s	Tafel Region /V	-b /mV	i_o /A.cm^{-2}	Tafel Region /V	-b /mV	i^o /A.cm^{-2}	i_1* /mA.cm^{-2}	$i_2^{\otimes}$ /mA.cm^{-2}	$i_3^{\oplus}$ /mA.cm^{-2}
As-polished	0	-1.71 to -1.83	72 ± 3	$(4.57 \pm 1.76) \times 10^{-7}$	-1.63 to -1.71	127 ± 9	$(6.11 \pm 0.73) \times 10^{-6}$	0.052 ± 0.011	0.125 ± 0.014	0.462 ± 0.102
1M HF	60	-1.71 to -1.85	75 ± 3	$(9.62 \pm 1.74) \times 10^{-7}$	-1.64 to -1.71	125 ± 5	$(6.05 \pm 0.65) \times 10^{-6}$	0.044 ± 0.005	0.135 ± 0.019	0.524 ± 0.064
4M HF	60	-1.71 to -1.81	81 ± 6	$(1.63 \pm 0.49) \times 10^{-6}$	-1.63 to -1.71	132 ± 3	$(6.26 \pm 0.32) \times 10^{-6}$	0.054 ± 0.015	0.162 ± 0.006	0.609 ± 0.065
8M HF	60	-1.71 to -1.82	79 ± 9	$(3.23 \pm 1.04) \times 10^{-6}$	-1.64 to -1.71	140 ± 5	$(6.55 \pm 0.08) \times 10^{-6}$	0.065 ± 0.056	0.176 ± 0.059	0.666 ± 0.123
1M HF	600	-1.71 to -1.81	69 ± 1	$(4.59 \pm 0.22) \times 10^{-6}$	-1.65 to -1.71	129 ± 3	$(8.01 \pm 0.32) \times 10^{-6}$	0.067 ± 0.004	0.210 ± 0.020	0.878 ± 0.081
1MHF/ $1MHNO_3$	60	-1.71 to -1.85	71 ± 2	$(1.58 \pm 0.38) \times 10^{-6}$	-1.64 to -1.71	121 ± 15	$(6.47 \pm 1.82) \times 10^{-6}$	0.061 ± 0.009	0.143 ± 0.022	0.521 ± 0.113
2MHF/ $2MHNO_3$	60	-1.71 to -1.82	85 ± 4	$(2.05 \pm 0.56) \times 10^{-6}$	-1.63 to -1.71	112 ± 11	$(8.61 \pm 2.80) \times 10^{-6}$	0.071 ± 0.001	0.186 ± 0.025	0.613 ± 0.074
1MHF/ $1MHNO_3$	600	-1.70 to -1.78	67 ± 4	$(1.62 \pm 0.42) \times 10^{-5}$	-1.62 to -1.70	75 ± 2	$(1.05 \pm 1.23) \times 10^{-5}$	0.264 ± 0.025	1.269 ± 0.100	4.770 ± 0.510

* E = -1.65V , $^{\otimes}$E = -1.70V , $^{\oplus}$ E = -1.75V (vs.SSE)

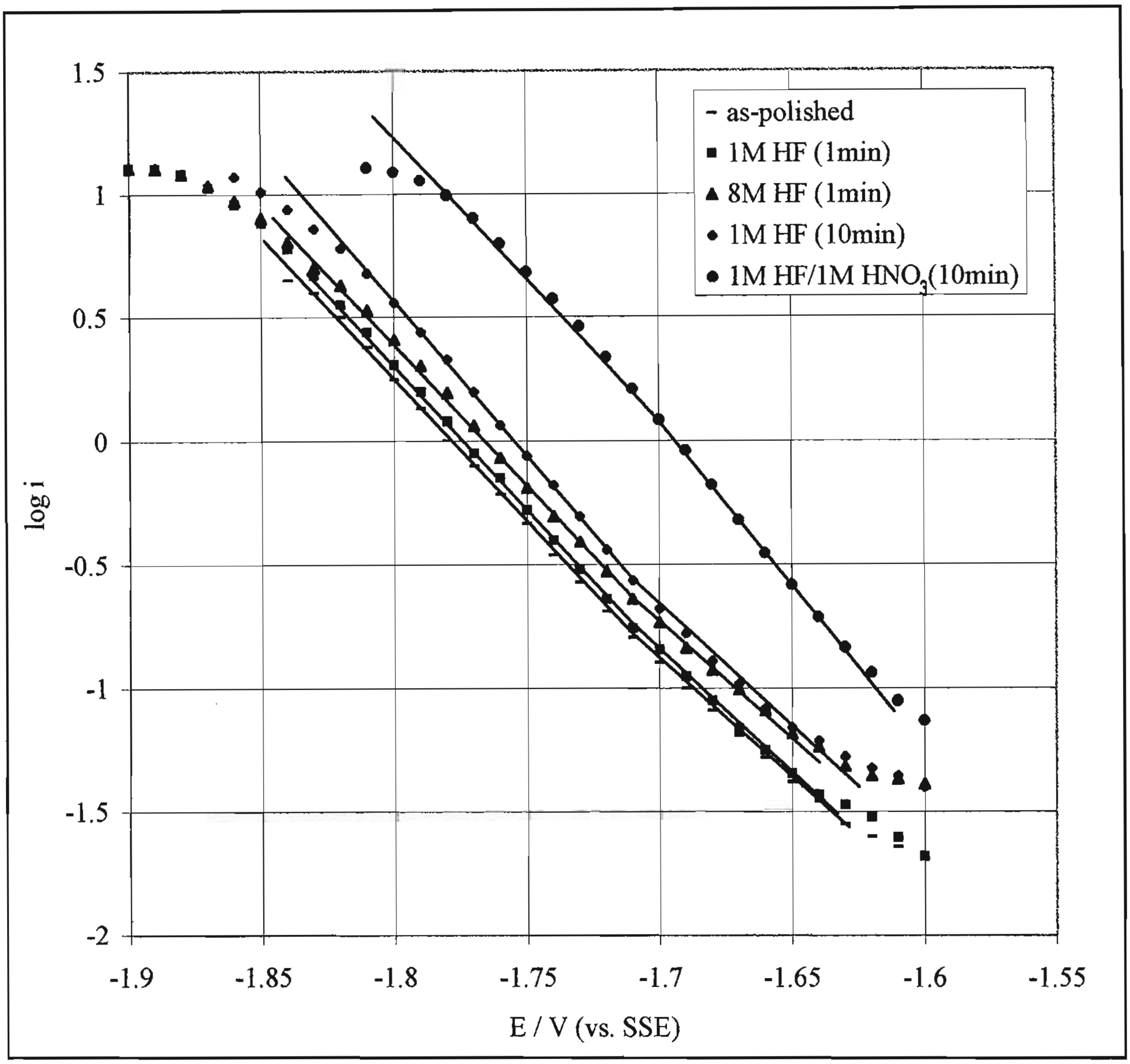

Fig. 43: Tafel plots for hydrogen evolution on glassy $Fe_{40}Ni_{40}P_{14}B_6$ in 1M KOH after different chemical treatments *ex situ*.

Glassy $Fe_{40}Ni_{40}B_{20}$

Identical acid pretreatments were also performed on the glassy $Fe_{40}Ni_{40}B_{20}$ alloy to compare the effectiveness of acid activation with the similar $Fe_{40}Ni_{40}P_{14}B_6$ alloy composition. The kinetic parameters for hydrogen evolution at the glassy $Fe_{40}Ni_{40}B_{20}$ surface after different acid pretreatments are listed in Table 26.

Table 26: Kinetic data for hydrogen evolution on glassy $Fe_{40}Ni_{40}B_{20}$ in 1M KOH at 25°C, after different chemical pretreatments.

		High η region			Low η region					
Chemical treatment	Treatment period /s	Tafel Region /V	-b /mV	i_o /A.cm^{-2}	Tafel region /V	-b /mV	i_o /A.cm^{-2}	i* /mA.cm^{-2}	$i_2^{\otimes}$ /mA.cm^{-2}	$i_3^{\oplus}$ /mA.cm^{-2}
As-polished	0	-1.75 to -1.89	117 ± 5	(5.56 ± 1.28) x 10^{-6}	-1.63 to -1.75	164 ± 9	(1.62 ± 0.73) x 10^{-5}	0.066 ± 0.011	0.275 ± 0.041	2.012 ± 0.469
1M HF	60	-1.75 to -1.93	118 ± 3	(6.05 ± 1.37) x 10^{-6}	-1.63 to -1.75	163 ± 9	(2.32 ± 0.12) x 10^{-5}	0.084 ± 0.013	0.304 ± 0.027	2.129 ± 0.059
4M HF	60	-1.76 to -1.93	120 ± 7	(7.61 ± 2.86) x 10^{-6}	-1.63 to -1.76	211 ± 24	(4.17 ± 0.88) x 10^{-5}	0.124 ± 0.024	0.356 ± 0.067	2.430 ± 0.290
8M HF	60	-1.76 to -1.93	139 ± 3	(2.17 ± 0.28) x 10^{-5}	-1.62 to -1.76	250 ± 16	(1.01 ± 0.82) x 10^{-4}	0.255 ± 0.006	0.610 ± 0.041	3.197 ± 0.223
1M HF	600	-1.75 to -1.92	113 ± 8	(6.82 ± 3.93) x 10^{-6}	-1.64 to -1.75	164 ± 17	(2.43 ± 0.13) x 10^{-5}	0.100 ± 0.022	0.402 ± 0.094	3.152 ± 0.264
1M HF/ 1M HNO_3	60	-1.75 to -1.94	121 ± 4	(7.68 ± 1.31) x 10^{-6}	-1.62 to -1.75	190 ± 37	(3.02 ± 0.83) x 10^{-5}	0.102 ± 0.008	0.339 ± 0.032	2.280 ± 0.300
2M HF/ 2M HNO_3	60	-1.76 to -1.95	133 ± 5	(1.46 ± 0.39) x 10^{-5}	-1.65 to -1.76	208 ± 43	(5.19 ± 3.87) x 10^{-5}	0.159 ± 0.069	0.467 ± 0.103	2.611 ± 0.284
1M HF/ 1M HNO_3	600	-1.76 to -1.93	141 ± 1	(2.32 ± 1.73) x 10^{-5}	-1.64 to -1.76	188 ± 12	(5.25 ± 0.66) x 10^{-5}	0.179 ± 0.155	0.589 ± 0.351	3.002 ± 1.631

* E = -1.65V, $^{\otimes}$ E = -1.75V, $^{\oplus}$ E = -1.85V (vs. SSE)

The response of the glassy $Fe_{40}Ni_{40}B_{20}$ alloy to acid treatment was very similar to the $Fe_{40}Ni_{40}P_{14}B_6$ alloy with similar trends in the Tafel lines obtained. All treatments produced an increase in the activity of the alloy in comparison to the as-polished state and the HF/HNO_3 mixture was found to be more effective in the activating the electrode surface than pure HF. Double Tafel slopes were also obtained with the alloy displaying the highest activity for hydrogen evolution in the high overpotential region. HF treatments resulted in an increase in alloy activity in the order 1M HF (1min) < 4M HF (1min) < 1M HF (10min) < 8M HF (1min). The Tafel plots obtained for HF/HNO_3 treatments of different concentration and time are shown in Fig. 44 from which it can be seen that treatments of increasing effectiveness occurred in the order 1M HF/1M HNO_3 (1min) < 2M HF/2M HNO_3 (1min) < 1M HF/1M HNO_3 (10min).

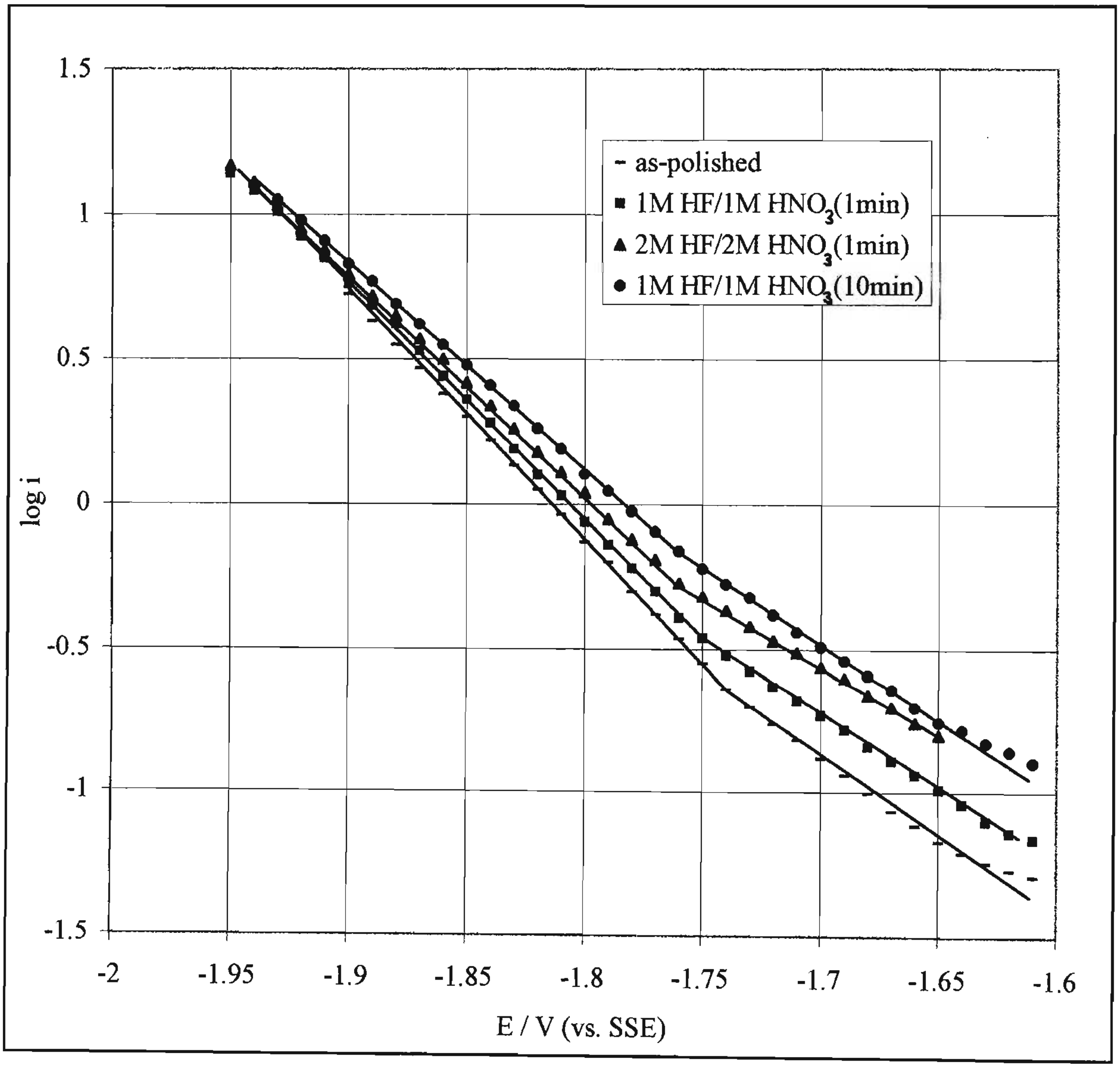

Fig. 44: Tafel plots for hydrogen evolution on the $Fe_{40}Ni_{40}B_{20}$ alloy surface after different chemical treatments *ex situ*.

The Tafel slopes increased in value in the high overpotential region as the severity of the HF and HF/HNO_3 treatments was increased, resulting in a pronounced convergence of the Tafel lines towards a common point as can be seen in Fig. 44. As for the $Fe_{40}Ni_{40}P_{14}B_6$ alloy, a maximum electrocatalytic activity for hydrogen evolution was obtained after pretreatment with 1M HF/1M HNO_3 (10 minutes), however, the increase was substantially lower than that obtained for the $Fe_{40}Ni_{40}P_{14}B_6$ composition. The i_o values of glassy $Fe_{40}Ni_{40}B_{20}$ increased from 5.56×10^{-6} (as-polished, 25°C) to 23.2×10^{-5} $A.cm^{-2}$ in the high overpotential region and from 1.62×10^{-5} (as-polished, 25°C) to 5.25×10^{-5} $A.cm^{-2}$ in the low overpotential region. This corresponded to i_o values that were 4.2 and 3.2 times greater than those of the as-polished electrode after acid treatment in the high and low overpotential regions respectively.

The i_o values of glassy $Fe_{40}Ni_{40}P_{14}B_6$ after acid pretreatment (1M HF/1M HNO_3, 10 minutes) compared closely with polycrystalline Fe [69] (Table 24). The Tafel slopes of the glassy alloy were lower than Fe resulting in a greater rate of current increase at the alloy surface and consequently a greater overall activity for the HER. The i_o values and hence the electrocatalytic activity of glassy $Fe_{40}Ni_{40}P_{14}B_6$ remained lower than that of polycrystalline Ni. After the same acid pretreatment the i_o values of glassy $Fe_{40}Ni_{40}B_{20}$ were greater than Fe in both overpotential regions indicating that the electrocatalytic activity of this alloy was greater than polycrystalline Fe. The i_o values of $Fe_{40}Ni_{40}B_{20}$ were greater than the value reported for polycrystalline Ni by Spriano et al. [95] at 25°C but lower than the value obtained by Kreysa and Hakansson [68] at 30°C. Although there were discrepancies in the i_o literature values reported at the Ni electrode the results indicate that the activity of the acid treated $Fe_{40}Ni_{40}B_{20}$ electrode was improved to levels comparable with polycrystalline Ni.

5.5.2.1 SEM/EDS analysis

The influence of the acid treatment on the electrode surface was investigated by SEM analysis and a selection of the micrographs obtained are shown in Fig. 45. HF treatment resulted in "blister" formation on both the glassy $Fe_{40}Ni_{40}P_{14}B_6$ and $Fe_{40}Ni_{40}B_{20}$ electrodes. Tiny blisters covering the $Fe_{40}Ni_{40}P_{14}B_6$ electrode can be seen after 1M HF treatment (1 minute) (Fig. 45a). The diameter of the blisters increased as the acid concentration was increased (Fig. 45b). After 8M HF treatment (1 minute) the blisters appeared to rupture and flake in a discrete layer that exposed a second underlying layer of the alloy and created an unusual mesh-like surface that consisted of the remnant upper layer (Fig. 45c). Further enlargement of the surface (x 7000) showed signs of surface roughening of the second layer (Fig. 45d), however, blistering and flaking of the second layer was not observed within the treatment range tested. It is predicted that prolonged acid treatment would result in the successive removal of layers of the alloy.

An explanation for the blister formation on the glassy $Fe_{40}Ni_{40}P_{14}B_6$ and $Fe_{40}Ni_{40}B_{20}$ electrodes after HF treatment is based on findings by Gilman [117]. Gilman found that when fractured portions of the glassy $Fe_{40}Ni_{40}P_{14}B_6$ and $Fe_{40}Ni_{40}B_{20}$ alloys were viewed under an electron microscope, micron-sized voids were observed within the bulk alloy structure. The voids were believed to form within the bulk alloy during rapid quenching of the melt. Cathodic polarisation in the hydrogen evolution region resulted in hydrogen adsorption at an electrode surface and therefore the possibility that the adsorbed atoms could diffuse into the bulk alloy and accumulate within these defect sites. Both glassy $Fe_{40}Ni_{40}P_{14}B_6$ and $Fe_{40}Ni_{40}B_{20}$ are reported to be susceptible to hydrogen absorption and embrittlement [70,84, 109,114,156]. It is proposed that the voids acted as traps for atomic hydrogen as it diffused into the alloy in much the same way as hydrogen is trapped in interstices in crystalline materials. When atomic hydrogen combined to form molecular hydrogen an increase of pressure within the void resulted. Pressure buildup in the bulk structure contributed to embrittlement of the alloy and reduced its fracture stress while pressure buildup near the alloy surface resulted in the formation of visible blisters due to expansion of the voids and their eventually rupture so that the hydrogen gas could escape.

Gas irradiation-induced blister formation has been reported to occur in glassy alloys [157]. Helium irradiation of glassy $Fe_{40}Ni_{40}P_{14}B_6$ and $Fe_{40}Ni_{40}B_{20}$ resulted in blister formation that was very similar in appearance to the blisters that formed on our HF treated alloy surfaces. This phenomenon has also been explained on the basis of helium absorption and entrapment in small interstitial holes within the bulk alloy structure. Near the alloy surface an increase in the gas pressure within the holes causes them to increase in size and eventually blister and rupture. Irradiation with hydrogen and argon gas produced the same bubbling effect as that observed for He irradiation.

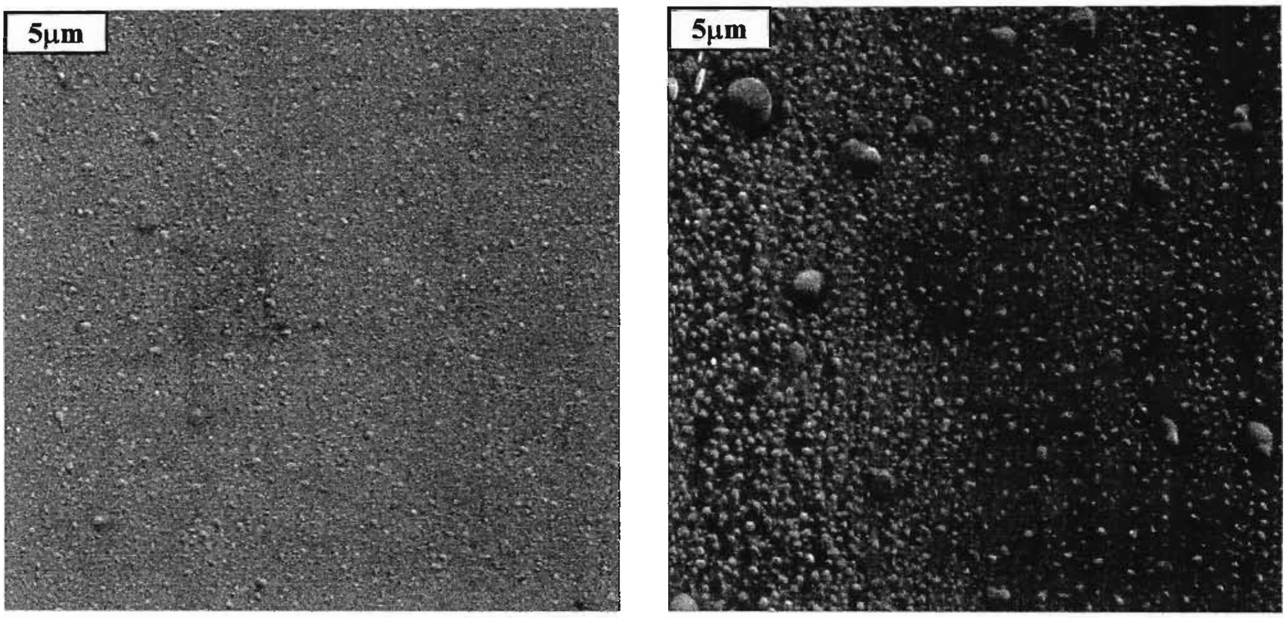

(a) 1M HF for 1 minute (mag. x4000) (b) 4M HF for 1 minute (mag. x4000)

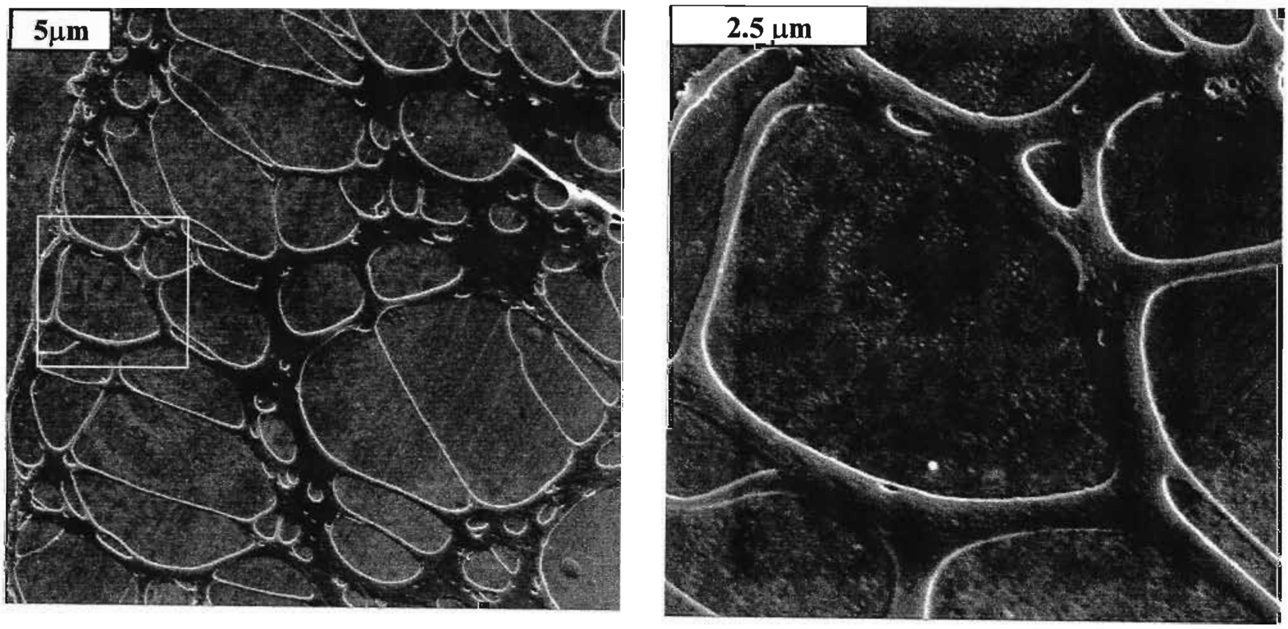

(c) 8M HF for 1 minute (mag. x4000) (d) enlargement of (c) (mag. x7000)

Fig. 45: The glassy $Fe_{40}Ni_{40}P_{14}B_6$ alloy surface after acid treatment with HF.

Treatment with HF/HNO_3 mixtures created a very different etch pattern to that produced by acid treatment with pure HF. Fig. 46 compares the SEM micrographs obtained from portions of the $Fe_{40}Ni_{40}P_{14}B_6$ and $Fe_{40}Ni_{40}B_{20}$ electrode surfaces after acid pretreatment with 1M HF/1M HNO_3 (10 minutes). The $Fe_{40}Ni_{40}P_{14}B_6$ surface (Fig. 46a) was highly roughened and numerous small craters produced a porous structure and a greatly enhanced surface area in comparison to its as-polished state. The size of the craters increased as the concentration and duration of the acid treatment was increased. Only general surface roughening was observed on the $Fe_{40}Ni_{40}B_{20}$ electrode (Fig. 46b) after an equivalent acid treatment and the surface lacked the porous and cratered structure of the $Fe_{40}Ni_{40}P_{14}B_6$ electrode. Therefore the surface area produced by acid treatment of the glassy $Fe_{40}Ni_{40}B_{20}$ electrode was substantially lower than the surface area of the $Fe_{40}Ni_{40}P_{14}B_6$ electrode.

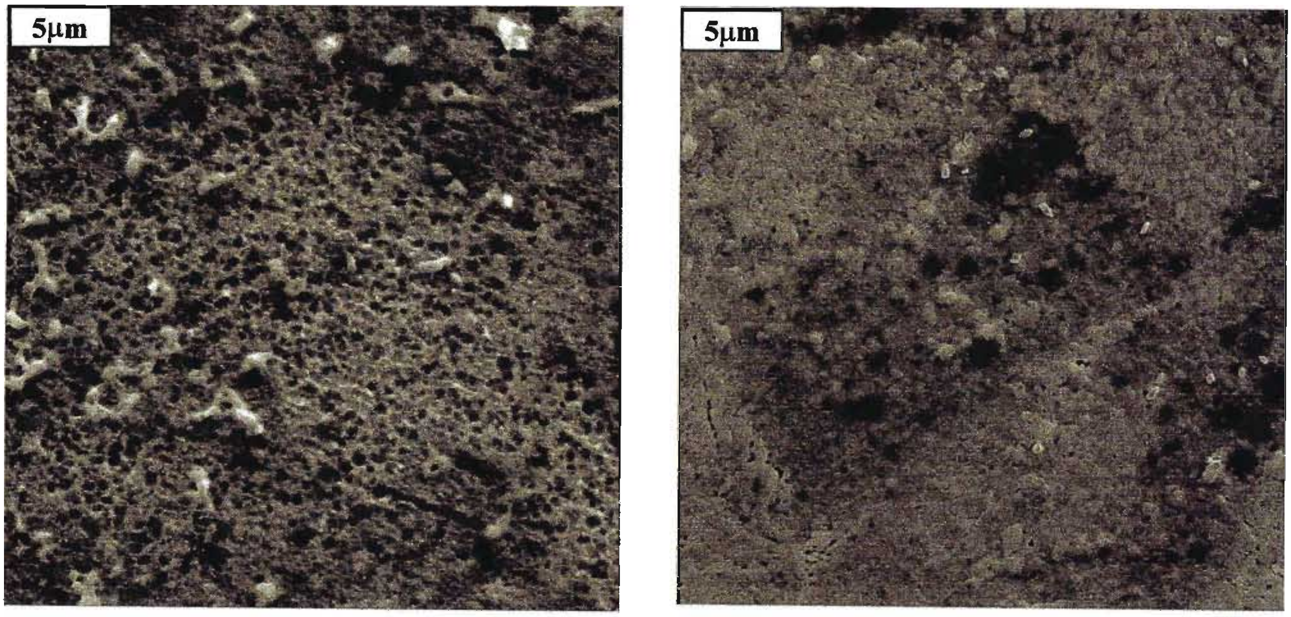

(a) $Fe_{40}Ni_{40}P_{14}B_6$ (mag. x4000)

(b) $Fe_{40}Ni_{40}B_{20}$ (mag. x4000)

Fig. 46: The glassy $Fe_{40}Ni_{40}P_{14}B_6$ and $Fe_{40}Ni_{40}B_{20}$ alloy surfaces after acid treatment with 1M HF/1M HNO_3 for 10 minutes.

EDS analyses of the general electrode surfaces after different acid treatments were obtained to monitor changes in the alloy surface composition produced by the different treatments and the values obtained are listed in Table 27.

Table 27: EDS analysis of the $Fe_{40}Ni_{40}P_{14}B_6$ alloy surface after different chemical treatments.

	Fe	**Ni**	**P**
Polished electrode	41.05	42.15	16.80
1M HF/1M HNO_3 (1min) treatment	43.73	43.12	13.15
1M HF/1M HNO_3 (10min) treatment	44.95	44.50	10.55

HF/HNO_3 treatment selectively leached P from the alloy surface and resulted in a corresponding enriched of Fe and Ni. After treatment with 1M HF/1M HNO_3 (1 minute) the P concentration decreased by 3.65 wt% and after 10 minutes a further 2.60 wt% decrease resulted. It is proposed that metalloid P at the polished alloy surface inhibited the HER. HF/HNO_3 treatment resulted in selective dissolution of the P component from the alloy and produced a porous and roughened electrode surface as well as removing the inhibiting P component. A change in the Tafel slope for hydrogen evolution after acid treatment indicated that a possible change in the adsorption sites or the mechanism of hydrogen evolution had occurred. These results are also supported by the finding that HF/HNO_3 treatment of the P-free alloy did not create a porous surface.

Treatments with HF produced no detectable changes in the surface compositions of glassy $Fe_{40}Ni_{40}P_{14}B_6$ and $Fe_{40}Ni_{40}B_{20}$ in comparison to the as-polished state. It appears that HF treatment activated the glassy $Fe_{40}Ni_{40}P_{14}B_6$ and $Fe_{40}Ni_{40}B_{20}$ alloys by increasing the electrode surface areas and creating a greater number of adsorption sites. The Tafel slopes of the HF-treated surfaces remained constant while the i_o values increased, indicating that the activity of the alloys for hydrogen evolution increased while the adsorption sites and the mechanism of the reaction was unchanged.

Helfand et al. [142] detected P-enrichment in the near-surface region of amorphous $Co_{80}P_{20}$ and $Ni_{80}P_{20}$ by XPS analysis. Shervedani and Lasia [154] reported that P was partially leached from amorphous Ni-P alloys by acid treatment to produce a porous electrode surface with an enhanced surface area and consequently a higher apparent current density. These findings are in agreement with the results obtained in this study. It was also reported that B was leached from the alloy surface by acid treatment, however in this study it was not possible to detect changes in the B concentration using the EDS surface analysis technique.

Lian et al. [109] found that the glassy Ni-based $Ni_{50}Co_{25}P_{15}B_{10}$ and $Ni_{50}Co_{25}Si_{15}B_{10}$ alloys displayed an enhanced activity for hydrogen evolution in 1M KOH at 25°C after chemical treatment with HF and HF/HNO_3 mixtures in comparison to the as-polished electrodes. Surface enrichment of the metalloids P, Si and B were also detected on the polished electrode surfaces prior to acid pretreatment. It was proposed that hydrogen adsorption occurred at the

Ni and Co metal sites and that the surface metalloid elements inhibited the recombination of adsorbed hydrogen to form molecular hydrogen. At metalloid enriched surfaces molecular hydrogen formation was proposed to occur by an electrochemical desorption reaction. Chemical treatment selectively leached the metalloid surface elements to create a Co and Ni enriched surface at which molecular hydrogen formation occurred predominantly by recombination of adsorbed hydrogen atoms. For treatments that only partially leached the metalloid component from the alloy surface a combination of the recombination and electrochemical desorption reactions was proposed to occur. Crystalline Co_2Ni and Ni_2Co alloy compositions that did not contain metalloid elements displayed a higher activity for hydrogen evolution in the as-polished state but did not show a similar increase in activity to the glassy alloys after acid treatment [109]. Indeed, chemical pretreatment was reported to deactivate or "poison" the crystalline alloy surface. These finding were also supported by Kumagai et al. [150] who reported that crystalline alloys could not be activated by HF treatment.

5.5.2.2 Anodic polarisation curves

Anodic polarisation curves of the HF and HF/HNO_3 treated $Fe_{40}Ni_{40}P_{14}B_6$ and $Fe_{40}Ni_{40}B_{20}$ electrodes are shown in Fig. 47 and Fig. 48 and the corrosion parameters obtained from the curves are listed in Table 28.

Table 28: Corrosion parameters obtained from anodic polarisation curves of the glassy $Fe_{40}Ni_{40}P_{14}B_6$ and $Fe_{40}Ni_{40}B_{20}$ electrodes in the as-polished state and after acid pretreatment.

	E_{corr}	E_{pp}	E_{Flade}	E_{tr}	i_{pp}	i_p
$Fe_{40}Ni_{40}P_{14}B_6$						
as-polished	-1.16	-1.03	-0.90	-0.04	7.93×10^{-3}	4.91×10^{-3}
1M HF (10 minutes)	-1.33	-0.96	-0.71	-0.03	3.62×10^{-2}	1.32×10^{-2}
1M HF/1M HNO_3 (10 minutes)	-1.33	-0.97	-0.71	-0.03	5.80×10^{-2}	1.82×10^{-2}
$Fe_{40}Ni_{40}B_{20}$						
as-polished	-1.14	-1.02	-0.96	-0.01	8.65×10^{-3}	6.32×10^{-3}
1M HF (10 minutes)	-1.29	-1.05	-0.89	-0.03	2.02×10^{-2}	1.44×10^{-2}
1M HF/1M HNO_3 (10 minutes)	-1.28	-1.05	-0.90	-0.04	2.78×10^{-2}	1.82×10^{-2}

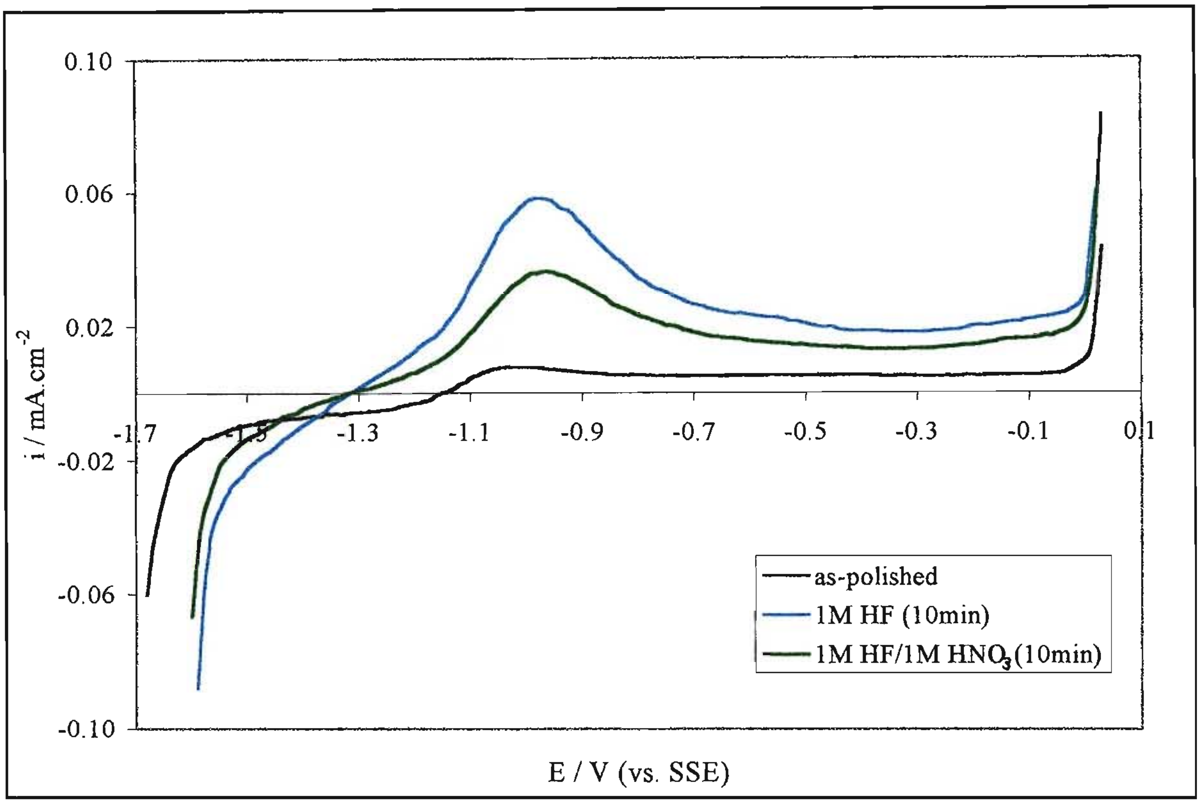

Fig. 47 Typical anodic polarisation curves of glassy $Fe_{40}Ni_{40}P_{14}B_6$ in the as-polished state and after acid pretreatment prior to cathodic polarisation in 1M KOH at 25°C.

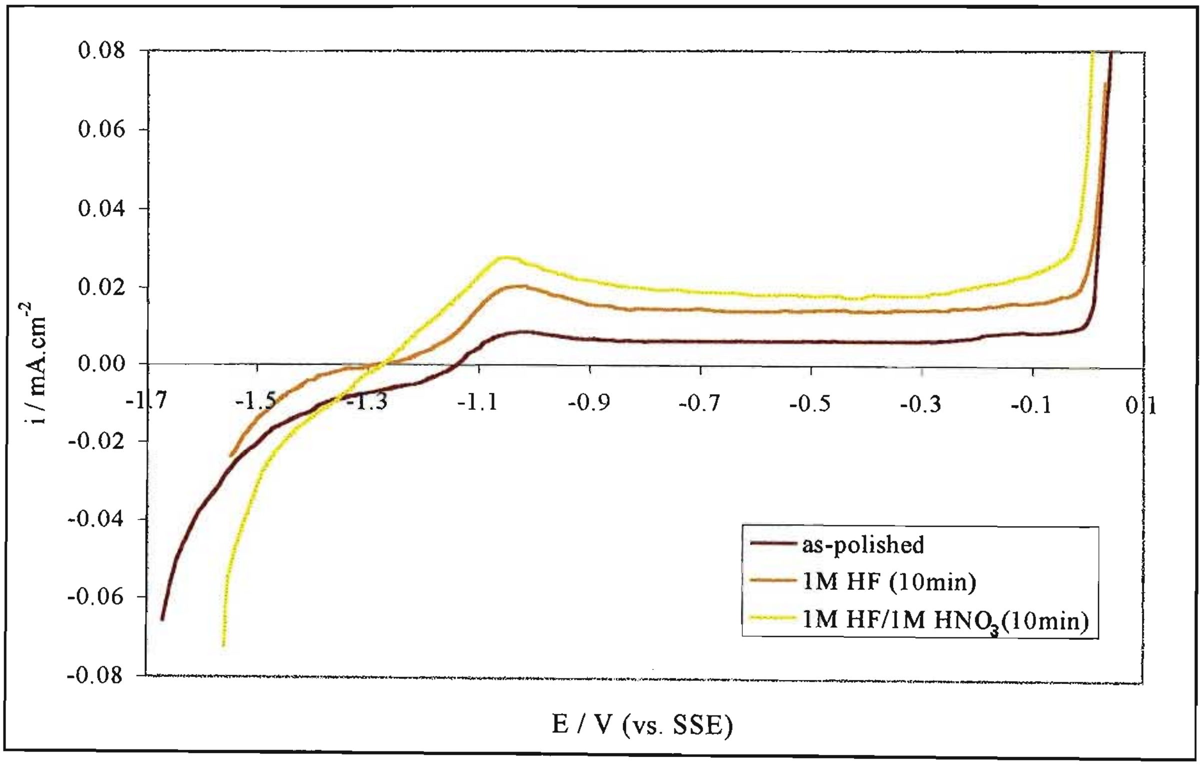

Fig. 48: Typical anodic polarisation curves of glassy $Fe_{40}Ni_{40}B_{20}$ in the as-polished state and after acid pretreatment prior to cathodic polarisation in 1M KOH at 25°C.

The anodic polarisation curves of the as-polished $Fe_{40}Ni_{40}P_{14}B_6$ and $Fe_{40}Ni_{40}B_{20}$ electrodes were almost identical. Acid treatments with pure HF and HF/HNO_3 mixtures did not alter the shapes of the curves and the active anodic peaks occurred at similar potentials to those of the as-polished surface for both alloys. Acid treatments increased the current densities in all regions of the curve and for both alloys HF/HNO_3 treatment produced a greater increase in the current densities than pure HF. The increased current densities indicate that acid treatment enhanced the electrode surface area and produced greater apparent current densities. The current densities at the $Fe_{40}Ni_{40}P_{14}B_6$ alloy were greater than $Fe_{40}Ni_{40}B_{20}$ after both HF and HNO_3 treatments in all potential regions. This finding supports that SEM observations which showed that the surface area of the acid treated $Fe_{40}Ni_{40}P_{14}B_6$ electrode was substantially greater than the $Fe_{40}Ni_{40}B_{20}$ electrode after the same treatment, resulting in greater apparent current densities for the former alloy. For both alloy compositions E_{corr} shifted towards more negative potential and E_{Flade} towards more positive potentials in comparison to the as-polished state. This resulted in a broader active peak and a larger potential range over which dissolution of the alloys could occur, reducing the corrosion resistance of the alloys in comparison to their as-quenched state.

5.5.3 *In situ* anodic pretreatment

Glassy $Fe_{40}Ni_{40}P_{14}B_6$

The Tafel parameters obtained for hydrogen evolution after *in situ* anodic oxidation of the $Fe_{40}Ni_{40}P_{14}B_6$ alloy at different constant current densities are listed in Table 29 and a selection of Tafel plots obtained are shown in Fig. 49.

Anodic pretreatment produced a small increase in the activity of glassy $Fe_{40}Ni_{40}P_{14}B_6$ for hydrogen evolution in comparison to the as-polished surface as can be seen from the Tafel plots in Fig. 49. A maximum activity was obtained after an anodic treatment of $300\mu A.cm^{-2}$. The i_o values increased from 4.57×10^{-7} (as-polished, 25°C) to 14.8×10^{-7} ($300\mu A.cm^{-2}$) in the high overpotential region and from 6.11×10^{-6} (as-polished, 25°C) to 18.0×10^{-6} $A.cm^{-2}$ ($300\mu A.cm^{-2}$) in the low overpotential region. The i_o values were 3.2 and 2.9 times greater than the values obtained in the high and low overpotential regions of the as-polished electrode. The increase in activity for hydrogen evolution was much lower than the increase obtained at the 1M HF/1M HNO3 (10 minute) treated surface. Double Tafel slopes were obtained that maintained constant values of approximately 75mV and 128mV in the high and low overpotential regions respectively. These were close to the values obtained at the polished surface at 25°C.

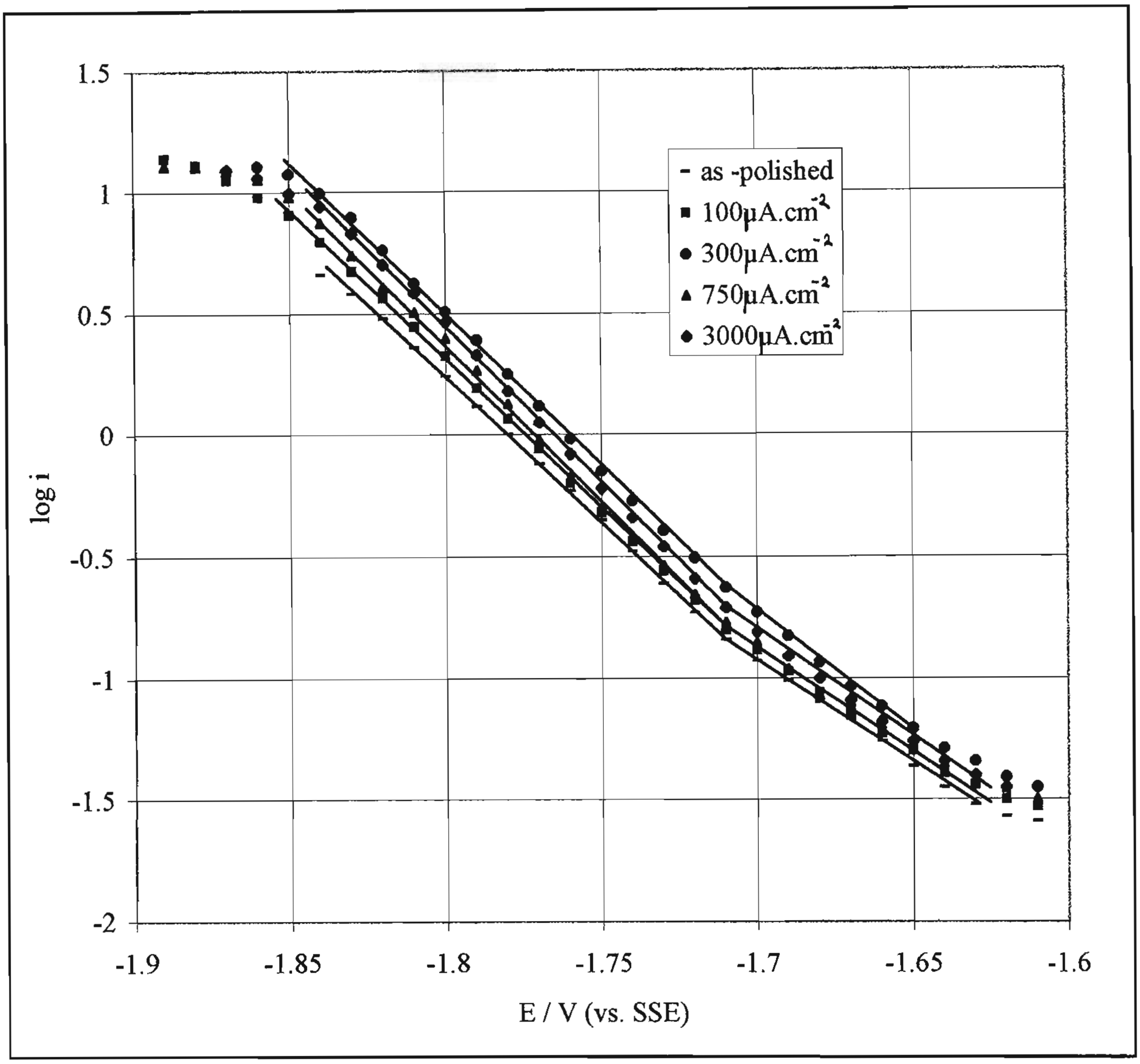

Fig. 49: Tafel plots for hydrogen evolution on the glassy $Fe_{40}Ni_{40}P_{14}B_6$ electrode after *in situ* anodic oxidation at constant current densities for 2 minutes in 1M KOH at 25°C.

SEM analysis of the alloy surface after anodic oxidation at current densities of $750\mu A.cm^{-2}$ and greater revealed that a fine and evenly distributed layer of extremely small surface particles formed. No particle layer was detected for treatments of $500\mu A.cm^{-2}$ or less and the only indication of surface change was a slight roughening along the edges of the Al_2O_3 polish lines. It is proposed that the surface particles provided surface sites for hydrogen adsorption that enhanced the surface area of the electrode resulting in a greater current density in comparison to the as-polished surface.

Table 29: Kinetic data for hydrogen evolution on glassy $Fe_{40}Ni_{40}P_{14}B_6$ in 1M KOH at 25°C after *in situ* anodic oxidation at different current densities for 2 minutes.

	High η region			Low η region					
Anodic Treatment /μA.cm^{-2}	Tafel Region /V	-b /mV	i_o /A.cm^{-2}	Tafel Region /V	-b /mV	i_o /A.cm^{-2}	i_1* /mA.cm^{-2}	$i_2^{\otimes}$ /mA.cm^{-2}	$i_3^{\oplus}$ /mA.cm^{-2}
As-polished	-1.71 to -1.83	72 ± 3	(4.57 ± 1.76) x 10^{-7}	-1.63 to -1.71	127 ± 9	(6.11 ± 0.73) x 10^{-6}	0.052 ± 0.011	0.125 ± 0.014	0.462 ± 0.102
10	-1.73 to -1.82	77 ± 5	(6.52 ± 2.44) x 10^{-7}	-1.66 to -1.73	130 ± 20	(9.59 ± 7.00) x 10^{-6}	0.051 ± 0.016	0.144 ± 0.013	0.590 ± 0.016
50	-1.73 to -1.84	76 ± 2	(6.39 ± 0.42) x 10^{-7}	-1.67 to -1.76	140 ± 20	(1.23 ± 0.18) x 10^{-5}	0.047 ± 0.028	0.123 ± 0.019	0.492 ± 0.044
100	-1.72 to -1.85	73 ± 4	(8.40 ± 2.45) x 10^{-7}	-1.64 to -1.72	131 ± 25	(1.35 ± 0.72) x 10^{-5}	0.059 ± 0.025	0.119 ± 0.026	0.450 ± 0.070
300	-1.71 to -1.84	81 ± 2	(1.48 ± 0.30) x 10^{-6}	-1.65 to -1.71	137 ± 18	(1.80 ± 0.53) x 10^{-5}	0.061 ± 0.009	0.176 ± 0.021	0.729 ± 0.074
500	-1.71 to -1.84	79 ± 4	(1.05 ± 3.39) x 10^{-6}	-1.66 to -1.71	140 ± 6	(1.22 ± 0.23) x 10^{-5}	0.058 ± 0.010	0.115 ± 0.036	0.428 ± 0.162
750	-1.71 to -1.84	71 ± 6	(7.33 ± 3.65) x 10^{-7}	-1.66 to -1.71	128 ± 16	(5.37 ± 1.22) x 10^{-6}	0.047 ± 0.006	0.152 ± 0.040	0.529 ± 0.103
1000	-1.72 to -1.84	75 ± 5	(6.56 ± 3.31) x 10^{-7}	-1.67 to -1.72	118 ± 9	(5.25 ± 0.84) x 10^{-6}	0.038 ± 0.018	0.130 ± 0.028	0.556 ± 0.086
2000	-1.71 to -1.84	77 ± 3	(6.96 ± 4.23) x 10^{-7}	-1.68 to -1.71	109± 7	(4.90 ± 0.81) x 10^{-6}	0.050 ± 0.014	0.114 ± 0.027	0.464 ± 0.103
3000	-1.71 to -1.84	73 ± 3	(6.05 ± 2.24) x 10^{-7}	-1.66 to -1.71	119± 11	(5.28 ± 0.30) x 10^{-6}	0.044 ± 0.012	0.134 ± 0.016	0.577 ± 0.110

* E = -1.65, $^{\otimes}$ E = -1.70, $^{\oplus}$ E = -1.75 (vs. SSE)

The variation in the i_o values with the applied anodic oxidation current are shown in Fig. 50. A maximum i_o value, and hence a maximum electrocatalytic activity for hydrogen evolution, was obtained after an anodic treatment of 300 μA.cm^{-2} in both the high and low overpotential regions. No explanations could be provided as to why the activity of the alloy increased to a maximum level and then decreased because the changes in the electrode surface resulting from anodic treatment at 300 μA.cm^{-2} were too small to be detected within the resolving power of the SEM. No surface composition changes were detected by EDS after anodic treatment either.

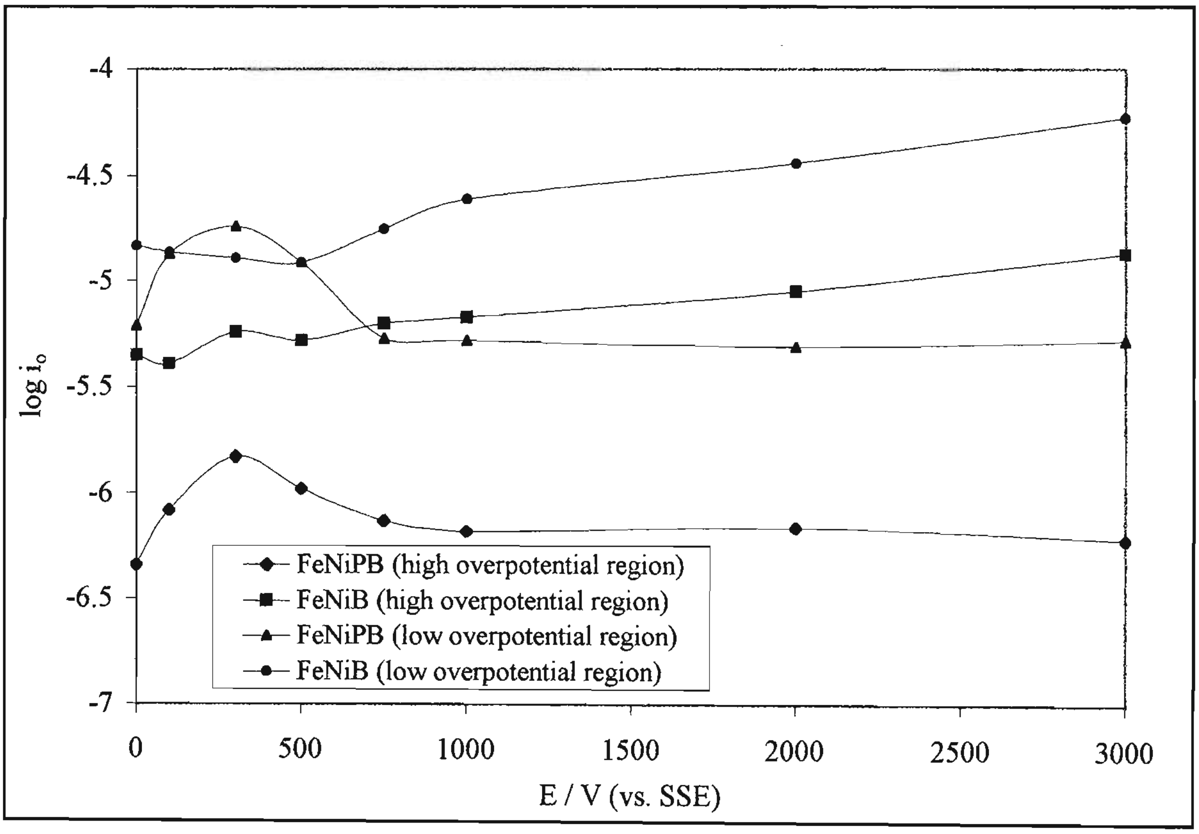

Fig. 50: Exchange current densities obtained for the HER after anodic oxidation of the glassy $Fe_{40}Ni_{40}P_{14}B_6$ and $Fe_{40}Ni_{40}B_{20}$ alloys at constant current density in 1M KOH at 25°C.

For comparison the kinetic parameters reported in the literature [71] for hydrogen evolution at the glassy $Fe_{40}Ni_{40}P_{14}B_6$ electrode after *in situ* anodic oxidation are listed in Table 30.

Table 30: Literature Tafel parameters [71] for hydrogen evolution on glassy $Fe_{40}Ni_{40}P_{14}B_6$ in 1M KOH at 25°C after *in situ* anodic oxidation at different current densities for 2 minutes.

Electrode	Electrolyte	Anodic treatment / μA.cm^{-2}	i$_o$ / A.cm^{-2}	b / mV	Reference
$Fe_{40}Ni_{40}P_{14}B_6$	1MKOH, 25°C	as-quenched	1.20×10^{-7}	109	71
		10	4.16×10^{-7}	133	
		100	3.31×10^{-7}	108	
		300	2.88×10^{-6}	133	
		500	2.09×10^{-6}	118	
		1000	1.58×10^{-6}	112	
$Fe_{40}Ni_{40}P_{14}B_6$	1MKOH, 25°C	as-polished	4.57×10^{-7} (high η) 6.11×10^{-6} (low η)	72 127	this work
		10	6.52×10^{-7} (high η) 9.59×10^{-6} (low η)	77 130	
		100	8.40×10^{-7} (high η) 1.35×10^{-5} (low η)	73 131	
		300	1.48×10^{-6} (high η) 1.80×10^{-5} (low η)	81 137	
		500	1.05×10^{-6} (high η) 1.22×10^{-5} (low η)	79 140	
		1000	6.56×10^{-7} (high η) 5.25×10^{-6} (low η)	75 118	

Only a single set of Tafel parameters was reported by Crousier et al. [71] for hydrogen evolution at the glassy $Fe_{40}Ni_{40}P_{14}B_6$ electrode in contrast to the double slope obtained in this work. Crousier et al. found that *in situ* anodic oxidation improved the activity of the alloy for hydrogen evolution in comparison to the as-quenched state. The literature i$_o$ values compare closely with the values obtained in the high overpotential region of this study. The exchange current density also showed a similar trend in which a maximum value was obtained after an anodic treatment of 300 μA.cm^{-2} followed by a decrease in the value. These observations led Crousier et al. to conclude that the activation process affected the catalyst surface rather than the electronic state of the surface. No mechanism suggesting how anodic treatment activated the alloy was proposed nor were reasons offered as to why oxidation currents greater than 300 μA.cm^{-2} suppressed the HER. The b values of both sets of results remained approximately constant and equal to those of the untreated alloy, however, the literature Tafel slopes were 40-50mV higher than the values obtained in this study, possibly due to differences in the alloy surface preparation. Crousier et al. tested the alloy in the as-quenched state with no surface polishing while in this study the results were obtained at a polished alloy surface. Anodic oxidation of polycrystalline Ni has also been reported [158] to modify the crystalline surface and enhance the activity of the metal for hydrogen evolution. The overpotential of Ni for hydrogen evolution decreased with an increasing oxidation current to a maximum value after which there was a similar increase in overpotential [158].

Glassy $Fe_{40}Ni_{40}B_{20}$

The influence of *in situ* anodic oxidation at constant current density on the Tafel parameters of glassy $Fe_{40}Ni_{40}B_{20}$ for hydrogen evolution are listed in Table 31. The $Fe_{40}Ni_{40}B_{20}$ alloy displayed a progressive increase in activity as the magnitude of the oxidation current was increased to a maximum activity that corresponded to a treatment of 3000 $\mu A.cm^{-2}$ (Fig. 51). This contrasted with the $Fe_{40}Ni_{40}P_{14}B_6$ alloy for which a maximum activity was obtained after a treatment of $300\mu A.cm^{-2}$, i.e. an order of magnitude current density variation. Double Tafel slopes were obtained and the slopes remained constant for each treatment with values of approximately 110mV and 157mV obtained in the high and low overpotential regions respectively. These slopes were similar to those obtained at the as-polished alloy surface at 25°C. As for glassy $Fe_{40}Ni_{40}P_{14}B_6$, the increase in activity resulting from anodic treatment was small. The i_o values changed from 5.56×10^{-6} (as-polished, 25°C) to 11.4×10^{-5} $A.cm^{-2}$ ($3000\mu A.cm^{-2}$) in the high overpotential region and from 1.62×10^{-5} (as-polished, 25°C) to 6.42×10^{-5} $A.cm^{-2}$ ($3000\mu A.cm^{-2}$) in the low overpotential region. These values showed an increase that was only 2.1 and 4.0 times greater than the as-polished electrode in the high and low overpotential regions respectively.

SEM analysis detected a fine surface layer on the glassy $Fe_{40}Ni_{40}B_{20}$ electrode for anodic treatments of $1000\mu A.cm^{-2}$ and greater. No individual surface particles could be distinguished and the layer was much finer than the layer that formed on the $Fe_{40}Ni_{40}P_{14}B_6$ surface after equivalent treatment. It is proposed that the surface layer provided adsorption sites for hydrogen and enhanced the surface area of the electrode in comparison to the as-quenched electrode, increasing the apparent rate of hydrogen evolution.

Table 31: Kinetic data for hydrogen evolution on glassy $Fe_{40}Ni_{40}B_{20}$ in 1M KOH at 25°C after *in situ* anodic oxidation at different current densities for 2 minutes.

	High η region			Low η region					
Anodic treatment /μA.cm^{-2}	Tafel Region /V	-b /mV	i_o /A.cm^{-2}	Tafel Region /V	-b /mV	i_o /A.cm^{-2}	i_1* /mA.cm^{-2}	$i_2^{\otimes}$ /mA.cm^{-2}	$i_3^{\oplus}$ /mA.cm^{-2}
As-polished	-1.75 to – 1.89	117 ± 5	(5.56 ± 1.28) x 10^{-6}	-1.63 to -1.75	164 ± 9	(1.62 ± 0.73) x 10^{-5}	0.066 ± 0.011	0.275 ± 0.041	2.012 ± 0.469
100	-1.74 to – 1.90	119 ± 5	(7.08 ± 0.83) x 10^{-6}	-1.64 to -1.74	154 ± 11	(1.73 ± 0.65) x 10^{-5}	0.077 ± 0.021	0.340 ± 0.042	2.381 ± 0.131
300	-1.74 to – 1.91	113 ± 4	(6.60 ± 1.08) x 10^{-6}	-1.64 to -1.74	157 ± 10	(2.05 ± 0.31) x 10^{-5}	0.089 ± 0.009	0.390 ± 0.013	3.026 ± 0.326
500	-1.74 to – 1.90	110 ± 7	(6.72 ± 1.24) x 10^{-6}	-1.65 to -1.74	152 ± 2	(2.10 ± 0.24) x 10^{-5}	0.094 ± 0.006	0.415 ± 0.034	3.384 ± 1.006
750	-1.74 to – 1.91	109 ± 6	(6.65 ± 3.19) x 10^{-6}	-1.64 to -1.74	148 ± 5	(1.97 ± 0.70) x 10^{-5}	0.093 ± 0.055	0.445 ± 0.218	3.740 ± 1.916
1000	-1.74 to – 1.90	102 ± 3	(5.49 ± 0.35) x 10^{-6}	-1.64 to -1.74	143 ± 20	(2.00 ± 0.83) x 10^{-5}	0.099 ± 0.022	0.503 ± 0.029	4.970 ± 0.439
2000	-1.74 to – 1.88	106 ± 6	(7.89 ± 1.70) x 10^{-6}	-1.65 to -1.74	161 ± 26	(3.30 ± 0.96) x 10^{-5}	0.138 ± 0.004	0.596 ± 0.040	5.437 ± 0.741
3000	-1.75 to – 1.91	110 ± 6	(1.14 ± 0.30) x 10^{-5}	-1.63 to -1.75	187 ± 9	(6.42 ± 2.35) x 10^{-5}	0.220 ± 0.064	0.752 ± 0.095	6.118 ± 0.609

* E = -1.65V, $^{\otimes}$ E = -1.75V, $^{\oplus}$ E = -1.85V (vs. SSE)

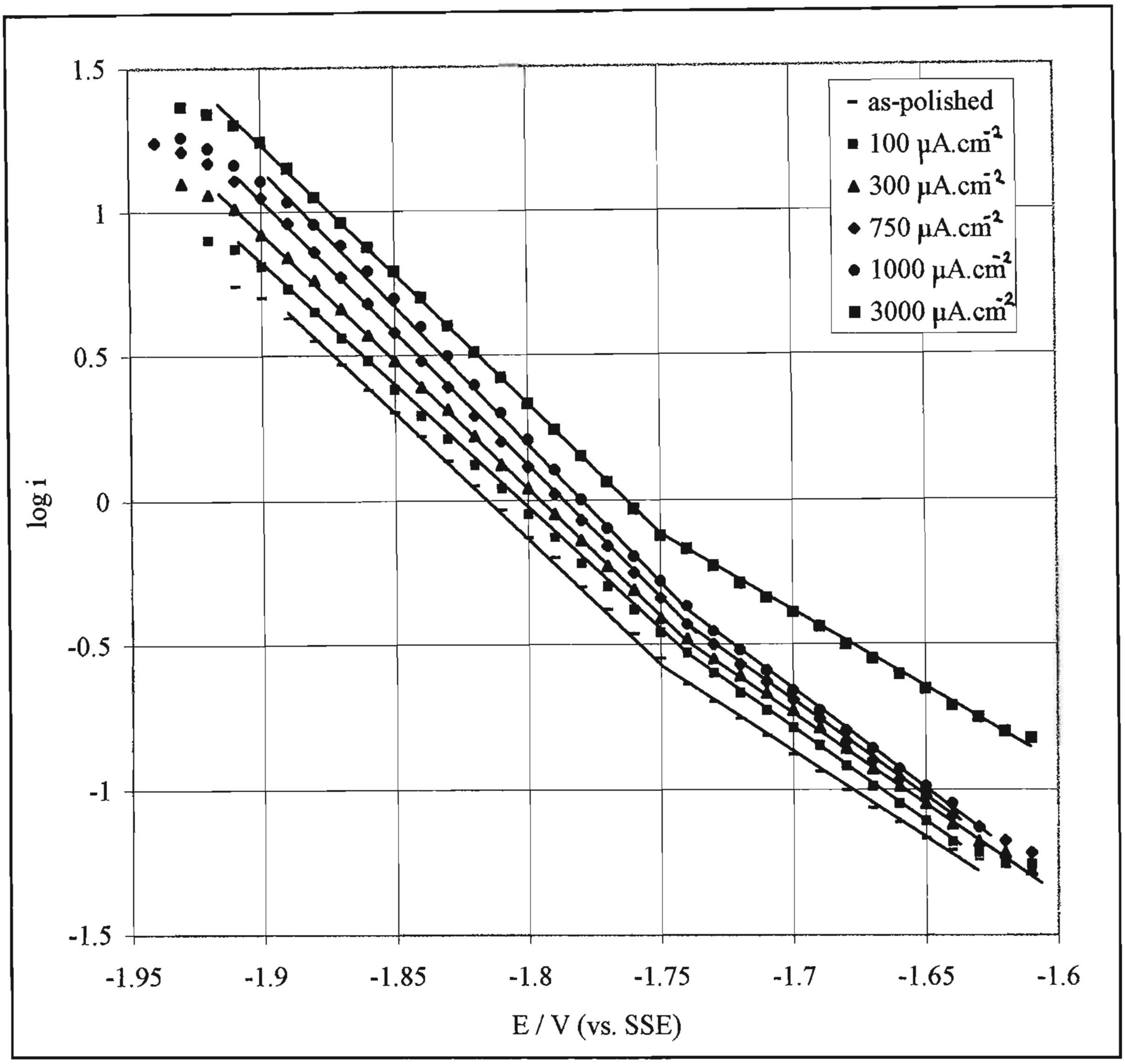

Fig. 51: Tafel plots for hydrogen evolution on the glassy $Fe_{40}Ni_{40}B_{20}$ electrode after *in situ* anodic oxidation at constant current densities for 2 minutes in 1M KOH at 25°C.

The activity of glassy $Fe_{40}Ni_{40}P_{14}B_6$ alloy, which showed the greatest improvement after an anodic treatment of 300μA.cm^{-2} for 2 minutes, remained lower than that of polycrystalline Fe [68,69] and Ni [68,95] at 25°C (Table 20). The i_o values of $Fe_{40}Ni_{40}B_{20}$ were greatest after an anodic treatment of 3000μA.cm^{-2} (2 minutes) and increased to values greater than Fe, indicating that the anodically treated alloy had a greater activity for hydrogen evolution than Fe. The i_o values of $Fe_{40}Ni_{40}B_{20}$ were greater than Ni [95] in the low overpotential region and lower than Ni in the high overpotential region at 25°C.

5.5.4 Conclusions

1. The glassy $Fe_{40}Ni_{40}P_{16}B_6$ alloy displayed a larger temperature dependence for hydrogen evolution than the $Fe_{40}Ni_{40}B_{20}$ alloy with the Tafel slopes and exchange current densities of the former composition showing a greater increase with increasing temperature.

2. HF treatment enhanced the activity of both the $Fe_{40}Ni_{40}P_{16}B_6$ and $Fe_{40}Ni_{40}B_{20}$ alloys by increasing the electrode surface roughness. The Tafel slopes remained constant at values similar to the as-polished electrodes and no changes in the alloy surface concentrations were detected by EDS after treatment. This indicated that the mechanism of hydrogen evolution remained unchanged by HF treatment and that the increased activity resulted from an increased electrode surface area. These findings were in contrast to the glassy $Zr_{74}Ti_{19}Cu_2Fe_5$ alloy for which 1M HF (10 seconds) treatment produced a highly porous electrode surface by dissolution of the Zr component to produce an electrode with a much greater activity for hydrogen evolution than the as-polished surface.

3. The glassy $Fe_{40}Ni_{40}P_{14}B_6$ and $Fe_{40}Ni_{40}B_6$ alloys appeared to be susceptible to hydrogen absorption as evidenced by blister formation after acid pretreatment with HF.

4. HF/HNO_3 treatment produced a much greater increase in the activity of the $Fe_{40}Ni_{40}P_{14}B_6$ alloy for hydrogen evolution than the $Fe_{40}Ni_{40}B_{20}$ composition. Selective dissolution of the P-enriched $Fe_{40}Ni_{40}P_{14}B_6$ surface created a porous electrode with a high surface area. A roughened rather than a porous surface was produced by an equivalent treatment of the P-free alloy and did not display a similarly large increase in activity.

5. The anodic polarisation curves of the acid treated $Fe_{40}Ni_{40}P_{14}B_6$ and $Fe_{40}Ni_{40}B_{20}$ alloys were very similar in the as-polished state indicating that P was unimportant as regards the redox properties of these alloys. The anodic polarisation curves of the acid treated (HF and HF/HNO_3) $Fe_{40}Ni_{40}P_{14}B_6$ and $Fe_{40}Ni_{40}B_{20}$ electrodes showed that greater current densities were obtained in all regions of the curve while the shape of the curves remained the same as the as-polished surfaces. In addition, the current densities of the acid treated $Fe_{40}Ni_{40}P_{14}B_6$ electrode were greater than the $Fe_{40}Ni_{40}B_{20}$ electrode in all regions of the curve after identical treatment. These findings supported the SEM observations that showed that the surface area of the $Fe_{40}Ni_{40}P_{14}B_6$ alloy was greater after acid treatment than the $Fe_{40}Ni_{40}B_{20}$ alloy and hence the apparent current density (calculated using the geometrical electrode surface area) was also greater.

6. Anodic treatment improved the activity of both the $Fe_{40}Ni_{40}P_{14}B_6$ and $Fe_{40}Ni_{40}B_{20}$ alloys for hydrogen evolution but was less effective than acid treatment. Slight surface roughening

was detected by SEM after anodic treatment of the glassy surfaces that appeared to increase the surface area of the electrode and produce higher apparent current densities. The Tafel slopes remained constant for both alloys for the different treatments indicating that the mechanism of hydrogen evolution was not affected.

7. The glassy $Fe_{40}Ni_{40}P_{14}B_6$ and $Fe_{40}Ni_{40}B_{20}$ alloys were less active for hydrogen evolution in their as-polished state than their polycrystalline Fe and Ni components. The $Fe_{40}Ni_{40}P_{14}B_6$ alloy was more active than Fe after acid pretreatment (1M HF/1M HNO_3, 10 minutes) but less active than pure Ni. The $Fe_{40}Ni_{40}B_{20}$ alloy displayed an improved activity after the same acid pretreatment to levels greater than both Fe and Ni.

5.6 ELECTROCATALYSIS BY GLASSY $Zr_{74}Ti_{19}Cu_2Fe_5$ FOR THE HER

5.6.1 The as-polished electrode at different electrolyte temperatures

The electrocatalytic efficiency of glassy $Zr_{74}Ti_{19}Cu_2Fe_5$ for the HER was determined on the basis of electrochemical data obtained from cathodic polarisation curves obtained in 1M KOH at 25°C. The Tafel parameters, i_o ($\eta = 0$) and b, were calculated from the Tafel plots at five different electrolyte temperatures and are listed in Table 32. The current densities obtained within the Tafel region at potentials of -1.80 ($\eta = 0.15V$), -1.92 ($\eta = 0.27V$) and -2.05V ($\eta = 0.4V$) were also included for comparison. These values were obtained from Tafel plots such as illustrated in Fig. 52. Two distinct Tafel slopes were obtained at each temperature ranging between potentials of -1.82 to -1.90 and -1.90 to -2.12V (25°C) in the high and low overpotential regions respectively. The intercept potential of the two slopes did not remain constant but shifted towards more negative potentials as the temperature increased, changing from -1.90V (25°C) to -1.96V (70°C). Higher slope values were recorded in the low overpotential region for each of the temperatures tested indicating that the electrocatalytic activity of the alloy was lower in this potential region. The alloy displayed the highest activity for hydrogen evolution in the high overpotential region, i.e. further away from the corrosion potential. The change in Tafel slope indicated that a possible change in the desorption mechanism for hydrogen evolution occurred due to specific adsorption sites whose surface coverage was dependant on potential. This was supported by SEM analysis of the polished alloy surface which showed that it was non-uniform, with nodules of crystalline Zr embedded in the alloy substrate (Fig. 15c). The nodules could have provided alternate adsorption sites that produced the change in Tafel slope. Similar inhomogeneities on the glassy $Co_{66}Fe_4Si_{16}B_{12}Mo_2$, $Fe_{40}Ni_{40}B_{20}$ and $Fe_{40}Ni_{40}P_{14}B_6$ surfaces were not detected, however it has been reported [12,17,85] that very small crystallites can also form in glassy alloys that are not visible under an electron microscope. For electrolyte temperatures of 25-

50°C, the Tafel slopes remained constant in both regions with values of approximately 148mV and 194mV obtained in the high and low overpotential regions respectively. The constant slopes meant that parallel Tafel plots were obtained so that the rate of current increase was constant at each temperature. The exception to this trend occurred at 70°C in the low overpotential region for which a substantially higher Tafel slope of 249mV was obtained, resulting in a greatly reduced rate of current increase. This result was reproducible and was attributed to the formation of excess hydrogen bubbles at elevated temperature that adhered to the alloy surface and reduced the available surface area at which the HER could occur and therefore reduced the overall rate of the reaction.

Table 32: Kinetic data for hydrogen evolution on glassy $Zr_{74}Ti_{19}Cu_2Fe_5$ in 1M KOH at different electrolyte temperatures.

	High η region			Low η region					
T/ °C	Tafel range /V	-b /mV	i_o /mA.cm^{-2}	Tafel range /V	-b /mV	i_o /mA.cm^{-2}	i_1*/ mA.cm^{-2}	$i_2^{\otimes}$/ mA.cm^{-2}	$i_3^{\oplus}$/ mA.cm^{-2}
25	-1.90 to -2.12	153 ± 12	(4.02 ± 1.44) x 10^{-6}	-1.82 to -1.90	187 ± 11	(9.96 ± 3.29) x 10^{-6}	0.067 ± 0.016	0.267 ± 0.076	1.714 ± 0.610
30	-1.91 to -2.12	149 ± 7	(4.86 ± 1.26) x 10^{-6}	-1.79 to -1.91	218 ± 12	(1.08 ± 0.26) x 10^{-5}	0.085 ± 0.015	0.288 ± 0.051	2.079 ± 0.414
40	-1.92 to -2.08	140 ± 6	(5.27 ± 1.05) x 10^{-6}	-1.80 to -1.92	194 ± 24	(1.27 ± 0.49) x 10^{-5}	0.096 ± 0.021	0.330 ± 0.052	2.578 ± 0.546
50	-1.92 to -2.09	158 ± 9	(7.46 ± 2.51) x 10^{-6}	-1.75 to -1.92	185 ± 9	(1.53 ± 0.31) x 10^{-5}	0.110 ± 0.022	0.410 ± 0.416	2.835 ± 1.001
70	-1.96 to -2.12	141 ± 4	(3.96 ± 1.11) x 10^{-6}	-1.79 to -1.96	249 ± 19	(3.93 ± 0.80) x 10^{-5}	0.116 ± 0.040	0.232 ± 0.091	1.441 ± 0.608

* E = -1.80V, $^{\otimes}$ E = -1.92V, $^{\oplus}$ E = -2.05V (vs. SSE)

The $Zr_{74}Ti_{19}Cu_2Fe_5$ alloy displayed a much lower activity for hydrogen evolution in the as-quenched state than the other glassy alloy compositions tested. The overpotentials required for hydrogen evolution at the $Zr_{74}Ti_{19}Cu_2Fe_5$ surface were lower (more negative) than those of the other alloy compositions tested. This has been attributed to the formation of thin passivating Zr and Ti oxide layers that suppress the HER [93,95,96,97]. Although temperature increase improved the activity of the alloy for HER, the increase in the current densities were much lower than those obtained at the other glassy alloy surfaces and the Tafel plots fell close together. Exchange current densities in the high overpotential region did not change with increasing temperature with values of 4.02 x 10^{-6} A.cm^{-2} (25°C) and 3.96 x 10^{-6} (70°C) obtained. A slight increase occurred in the low overpotential region with the value changing from 9.96 x 10^{-6} (25°C) to 15.3 x 10^{-6} A.cm^{-2} (50°C). At 70°C a substantially higher i_o value of 39.3 x 10^{-6} A.cm^{-2} was obtained but this was attributed to interference from the hydrogen bubbles. No visual change in the $Zr_{74}Ti_{19}Cu_2Fe_5$ electrode surface occurred during hydrogen evolution at each temperature.

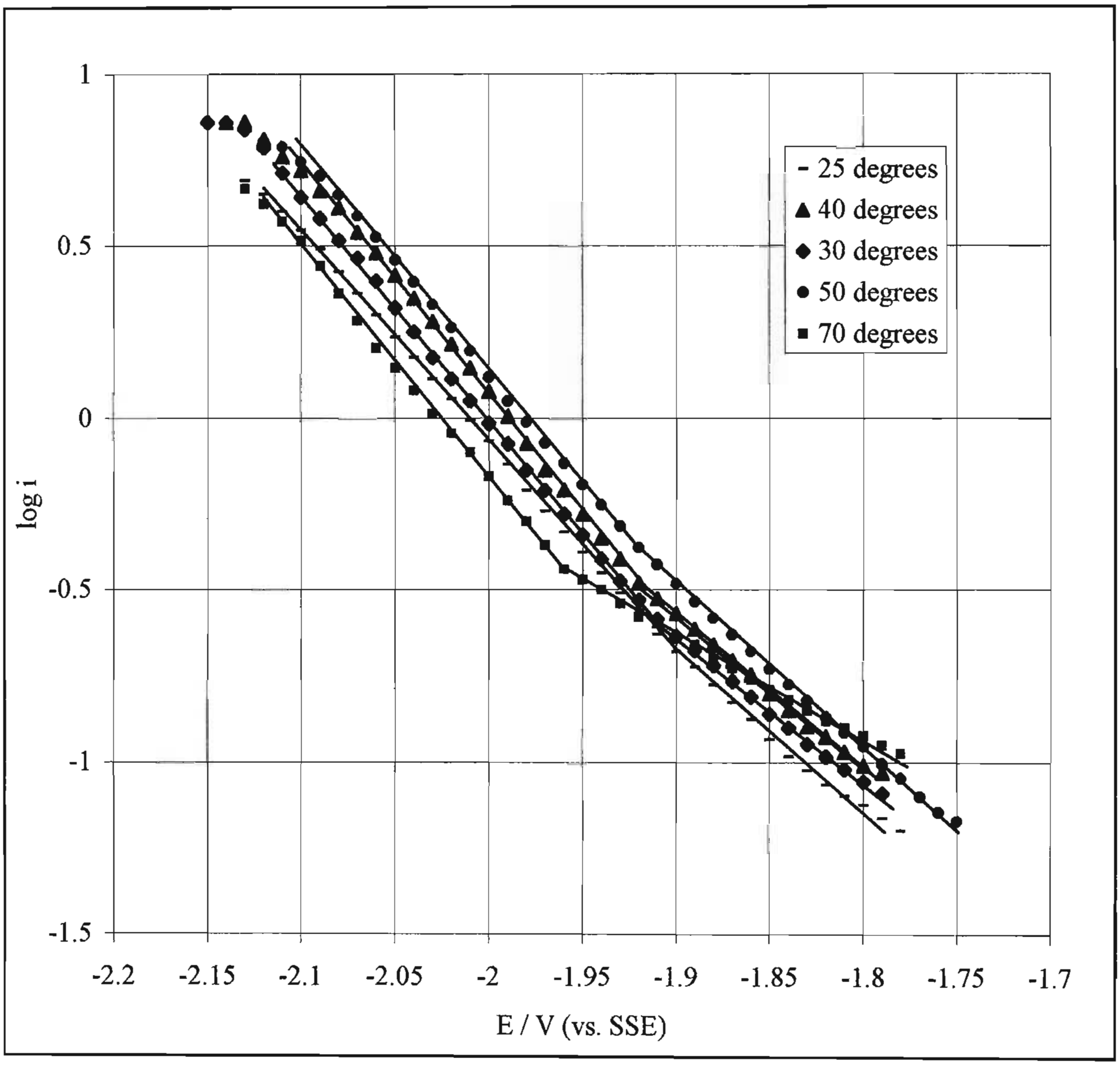

Fig. 52: Tafel plots of hydrogen evolution on the glassy $Zr_{74}Ti_{19}Cu_2Fe_5$ electrode in 1M KOH at different electrolyte temperatures.

Linear plots of $\ln i_o$ vs. 1/T were obtained for hydrogen evolution (η=0) at the glassy $Zr_{74}Ti_{19}Cu_2Fe_5$ electrode (Fig. 53) and from the slope of the graphs apparent activation energies of 21.62 and 12.99 kJ/mole were calculated. The i_o value obtained at 70°C from the high overpotential region of the Tafel slope was omitted from the graph as a linear Arrhenius relation was not obtained when this value was included.

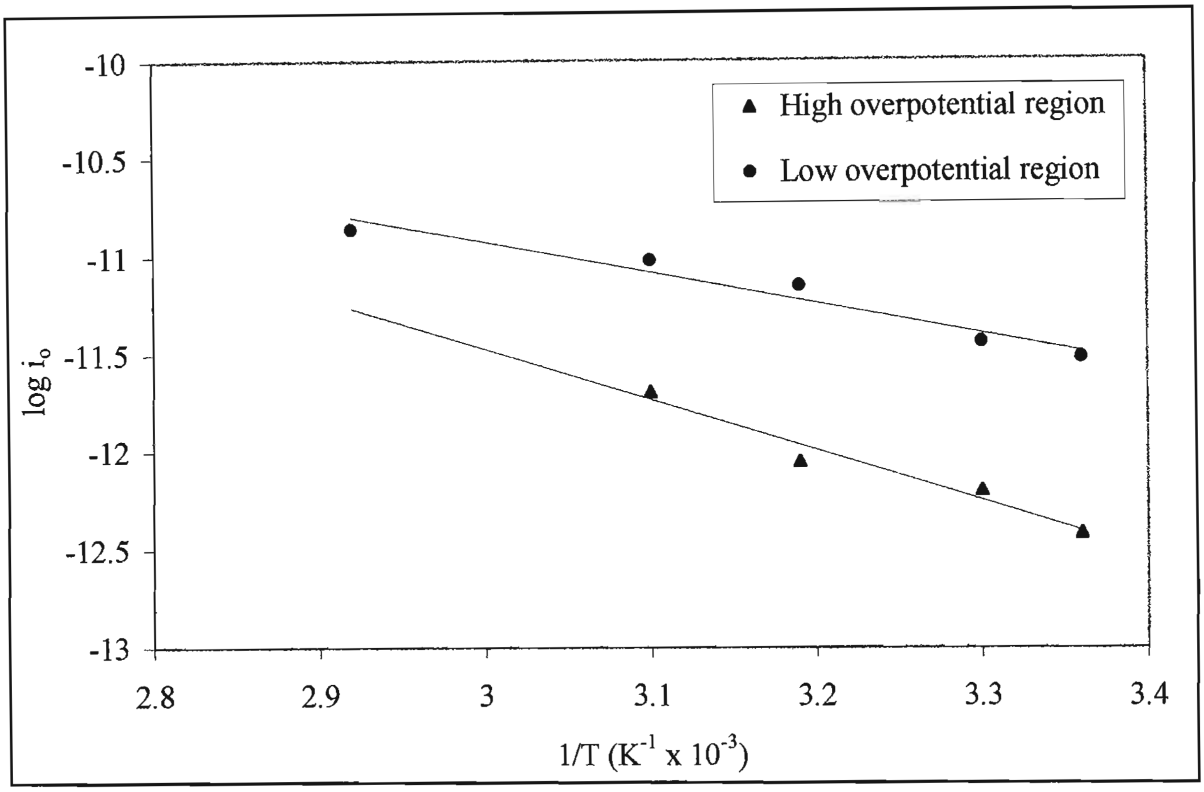

Fig. 53: Arrhenius plot for hydrogen evolution at glassy $Zr_{74}Ti_{19}Cu_2Fe_5$ in 1M KOH.

Literature Tafel parameters are reported for hydrogen evolution at polycrystalline Pt and Ni in Table 33 for comparison with the results obtained at the glassy $Zr_{74}Ti_{19}Cu_2Fe_5$ electrode (Table 32). The $Zr_{74}Ti_{19}Cu_2Fe_5$ alloy produced two Tafel slopes in comparison to the single slopes reported at the polycrystalline Ni [68,95] and Pt [68,97] electrodes. In the as-polished state the $Zr_{74}Ti_{19}Cu_2Fe_5$ electrode displayed a lower activity for hydrogen evolution at the temperatures tested in both the high and low overpotential regions than pure Ni and Pt, i.e. lower i_o values were obtained for the $Zr_{74}Ti_{19}Cu_2Fe_5$ alloy. In both cases the Tafel slopes of $Zr_{74}Ti_{19}Cu_2Fe_5$ were similar in the high overpotential region while higher slopes were obtained in the low overpotential region than those of Ni or Pt.

Table 33: Literature Tafel parameters [68,95,97] for hydrogen evolution at polycrystalline Pt and Ni electrodes in 1M KOH.

Electrode	Temperature / °C	i_o / A.cm^{-2}	b / mV	References
Ni	25	1.5×10^{-5}	-	95
Ni	30	$(1.02 \pm 0.78) \times 10^{-4}$	146 ± 19	68
	50	$(1.28 \pm 0.18) \times 10^{-4}$	159 ± 3	
	70	$(1.37 \pm 0.19) \times 10^{-4}$	159 ± 3	
	90	$(1.37 \pm 0.32) \times 10^{-4}$	147 ± 5	
Pt	25	2.4×10^{-5}	120	97
	50	4.8×10^{-5}	150	
	75	3.3×10^{-4}	170	
Pt	30	$(3.16 \pm 2.68) \times 10^{-4}$	141 ± 45	68
	50	$(8.70 \pm 7.60) \times 10^{-4}$	131 ± 52	
	70	$(1.21 \pm 0.93) \times 10^{-3}$	131 ± 47	
	90	$(1.07 \pm 0.38) \times 10^{-3}$	172 ± 12	

5.6.2 *Ex situ* acid pretreatment

The electrocatalytic activity of glassy $Zr_{74}Ti_{19}Cu_2Fe_5$ alloy was low in the as-polished state and so different acid pretreatments were tested to determine their effectiveness in activating the alloy surface. The kinetic parameters obtained at the acid treated electrodes prior to cathodic polarisation in 1M KOH are listed in Table 34. The treatment times and acid concentrations tested vary greatly according to the alloy composition being tested. For example, acid treatment with 1M HF for some minutes was reported to be necessary for effective activation of glassy $Zr_{67}Ni_{33}$, Ti-Cu and Zr-Cu [119] surfaces while only 10s immersion was required for the glassy $Zr_{67}Pd_{33}$ alloy [97]. The glassy $Zr_{74}Ti_{19}Cu_2Fe_5$ alloy composition was highly reactive in HF and so the treatment times were limited to 10s. The alloy was less reactive in the 1M HF/1M HNO_3 mixture and so a longer treatment time of one minute was also tested.

A substantial increase in the electrocatalytic activity of the $Zr_{74}Ti_{19}Cu_2Fe_5$ alloy for hydrogen evolution was found to result from acid treatment and the Tafel plots obtained are shown in Fig. 54. Acid treatment with pure HF was more effective in activating the $Zr_{74}Ti_{19}Cu_2Fe_5$ alloy than the HF/HNO_3 mixture. The order in which acid treatment increased the activity of the alloy was

Table 34: Kinetic data for hydrogen evolution on the glassy $Zr_{74}Ti_{19}Cu_2Fe_5$ electrode in 1M KOH at 25°C after different chemical treatments.

		High η region			Low η region					
Chemical treatment	Treatment period /s	Tafel region /V	-b /mV	i_o /A.cm^{-2}	Tafel Region /V	-b /mV	i_o /A.cm^{-2}	i_1* /mA.cm^{-2}	$i_2^{\otimes}$ /mA.cm^{-2}	$i_3^{\oplus}$ /mA.cm^{-2}
As-polished	0	-1.90 to –2.12	153 ± 12	$(4.02 \pm 1.44) \times 10^{-6}$	-1.82 to -1.90	187 ± 11	$(9.96 \pm 3.29) \times 10^{-6}$	0.067 ± 0.016	0.267 ± 0.076	1.714 ± 0.610
0.1M HF	10	-1.88 to -2.08	176 ± 6	$(1.13 \pm 0.24) \times 10^{-5}$	-1.76 to -1.88	259 ± 10	$(2.36 \pm 0.73) \times 10^{-5}$	0.095 ± 0.013	0.322 ± 0.097	1.944 ± 0.461
0.5M HF	10	-1.75 to -2.04	165 ± 4	$(4.19 \pm 1.19) \times 10^{-5}$	-	-	-	0.343 ± 0.100	1.806 ± 0.530	10.925 ± 3.270
1.0M HF	10	-1.76 to -2.02	172 ± 6	$(7.86 \pm 2.40) \times 10^{-5}$	-	-	-	0.693 ± 0.170	3.583 ± 1.124	21.305 ± 8.250
1M HF/ 1M HNO_3	10	-1.90 to -2.09	180 ± 5	$(9.32 \pm 2.33) \times 10^{-6}$	-1.76 to -1.90	267 ± 39	$(2.50 \pm 0.32) \times 10^{-5}$	0.094 ± 0.008	0.277 ± 0.047	1.557 ± 0.162
1M HF/ 1M HNO_3	60	-1.76 to -2.11	188 ± 4	$(2.28 \pm 0.35) \times 10^{-5}$	-	-	-	0.144 ± 0.021	0.627 ± 0.099	3.088 ± 0.540

* E = -1.80V, $^{\otimes}$E = -1.92V, $^{\oplus}$E = -2.05V (vs.SSE)

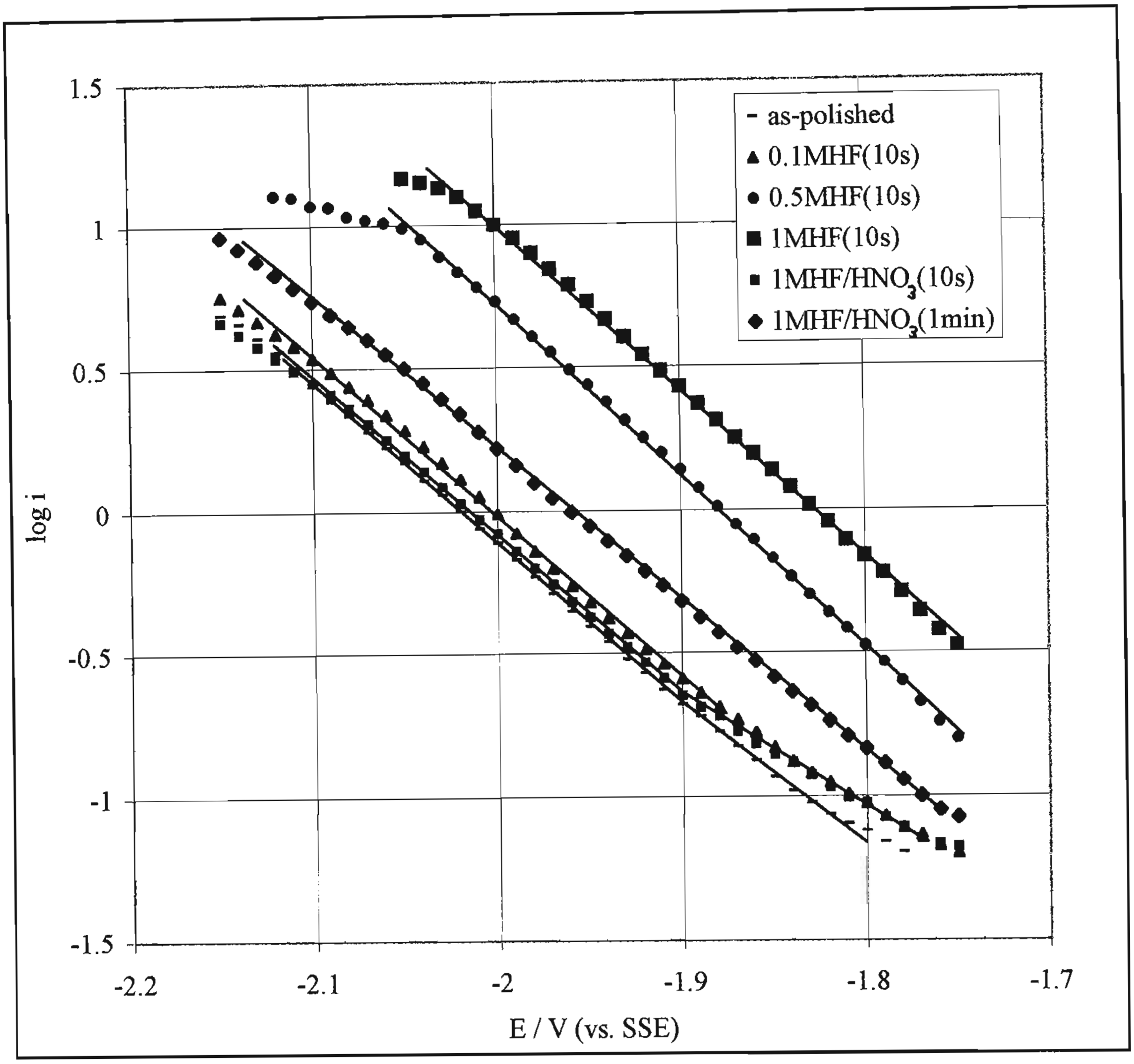

Fig. 54: Tafel plots for hydrogen evolution on the $Zr_{74}Ti_{19}Cu_2Fe_5$ alloy surface after different chemical treatments.

1M HF/HNO_3 (10s) < 0.1M HF (10s) < 1M HF/HNO_3 (1min) < 0.5M HF (10s) < 1M HF (10s). This contrasted with the glassy $Fe_{40}Ni_{40}B_{20}$, $Fe_{40}Ni_{40}P_{14}B_6$ and $Co_{66}Fe_4Si_{16}B_{12}Mo_2$ compositions for which HF/HNO_3 pretreatment produced the greatest increase in activity. HF/HNO_3 treatment had a severe effect on the glassy $Fe_{67}Co_{18}B_{14}Si_1$ alloy, producing a deep etch in the electrode, although the treatment was not, interestingly, as effective in activating the $Zr_{74}Ti_{19}Cu_2Fe_5$ composition. The less severe acid treatments, 0.1M HF (10s) and 1M HF/1M HNO_3 (10s), of the $Zr_{74}Ti_{19}Cu_2Fe_5$ alloy produced two distinct Tafel slopes. More severe treatments, i.e. higher acid concentrations and longer etch times, produced single slopes with an average slope of approximately 176mV obtained that remained constant for each treatment. The slopes obtained at the treated alloy surface were about 20mV higher in value than the slope at the as-polished surface at 25°C in the high overpotential region, indicating that a possible change in the hydrogen adsorption sites resulted from acid treatment. The i_o values increased linearly with increasing HF concentration, changing from 4.02×10^{-6} A.cm^{-2} (as-polished, 25°C) to 78.6×10^{-6} A.cm^{-2} (1MHF, 10s) after the most activating treatment. Treatment with HF/HNO_3 mixtures produced a less marked increase in the Tafel current densities with a maximum i_o value of 22.8×10^{-6} A.cm^{-2} obtained after one minute immersion. Acid treatment with 1M HF (10s) and 1M HF/1M HNO_3 (60s) produced i_o values that were 2.3 and 19.6 times greater than at the as-polished surface respectively.

5.6.2.1 SEM/EDS analysis

Both acid treatments produced a visible etch in the alloy surface and a light mottled orange/brown surface layer. The layer was extremely thin and could not be removed for separate analysis. Subsequent cathodic polarisation reduced the layer to form a dull metallic grey alloy surface. The slight surface etch was produced by the acid treatments that was easily polished out with Al_2O_3 on completion of the reaction. A selection of SEM micrographs of the treated alloy surfaces are shown in Fig. 55. Treatment with 0.1M HF produced a roughened and uneven alloy surface (Fig. 55a). The surface became highly porous after treatment with 1M HF for 10s (Fig. 55b). Treatment with 1M HF/1M HNO_3 (10s) produced a roughened surface with a surface deposit and did not appear porous (Fig. 55c). When the treatment was extended to one minute a fine porous structure was produced (Fig. 55d). Although both 1M HF (10s) and 1M HF/1M HNO_3 treatments (1 minute) produced porous surfaces, the HF treated surface was significantly more active for the HER. This suggests that, as for the $Co_{66}Fe_4Si_{16}B_{12}Mo_2$ alloy, HF activation created more than simply a surface area effect with the possibility of partial surface crystallisation and the production of catalytically active screw and/or step dislocations on the alloy surface. More severe acid attack was noted around the Zr nodules in comparison to the general alloy surface (Fig. 55e). Regions were also visible where the Zr nodules had been totally etched off and all that remained were the smooth regions that surrounded the nodules. As the severity of the treatment was increased it was noted that the number of nodules etched off the alloy surface increased. It is concluded that the second adsorption site created by the crystalline Zr nodules was selectively removed by acid treatments. My explanation of the slope change is that a homogeneous alloy surface was produced, in comparison to the as-polished surface, that consisted predominantly of a single type of hydrogen adsorption site and resulted in single Tafel slopes as opposed to the double slopes obtained at the as-polished surface.

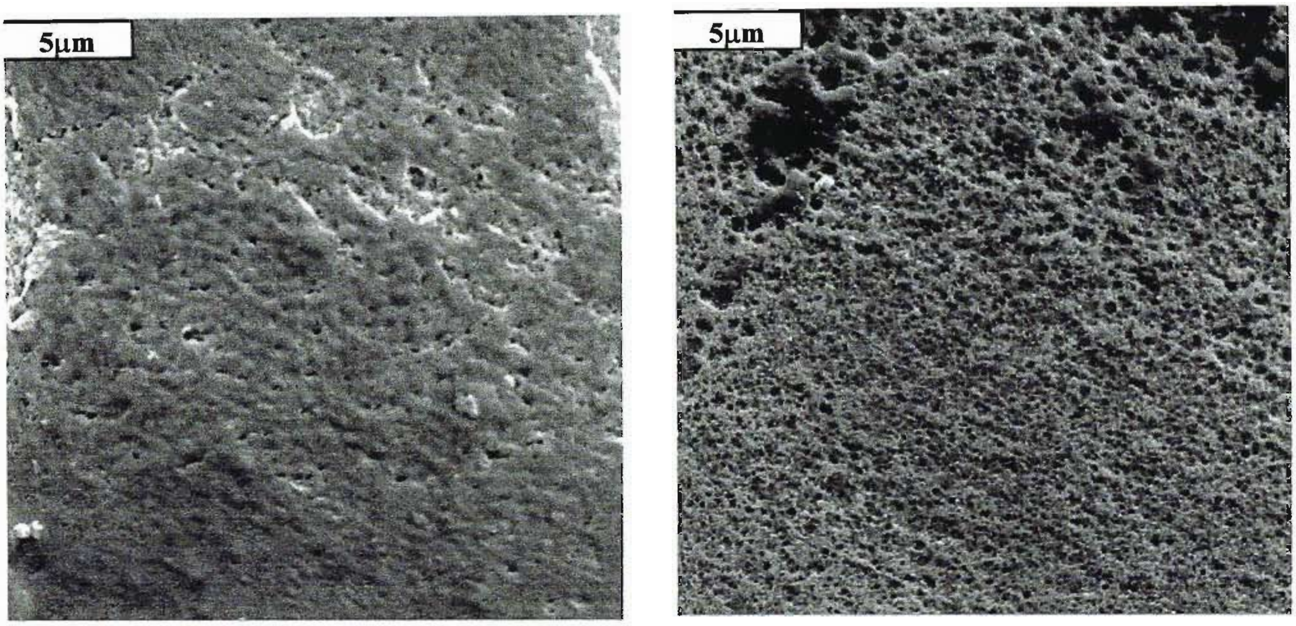

(a) 0.1M HF for 10 seconds (mag. x 4000)

(b) 1M HF for 10 seconds (mag. x4000)

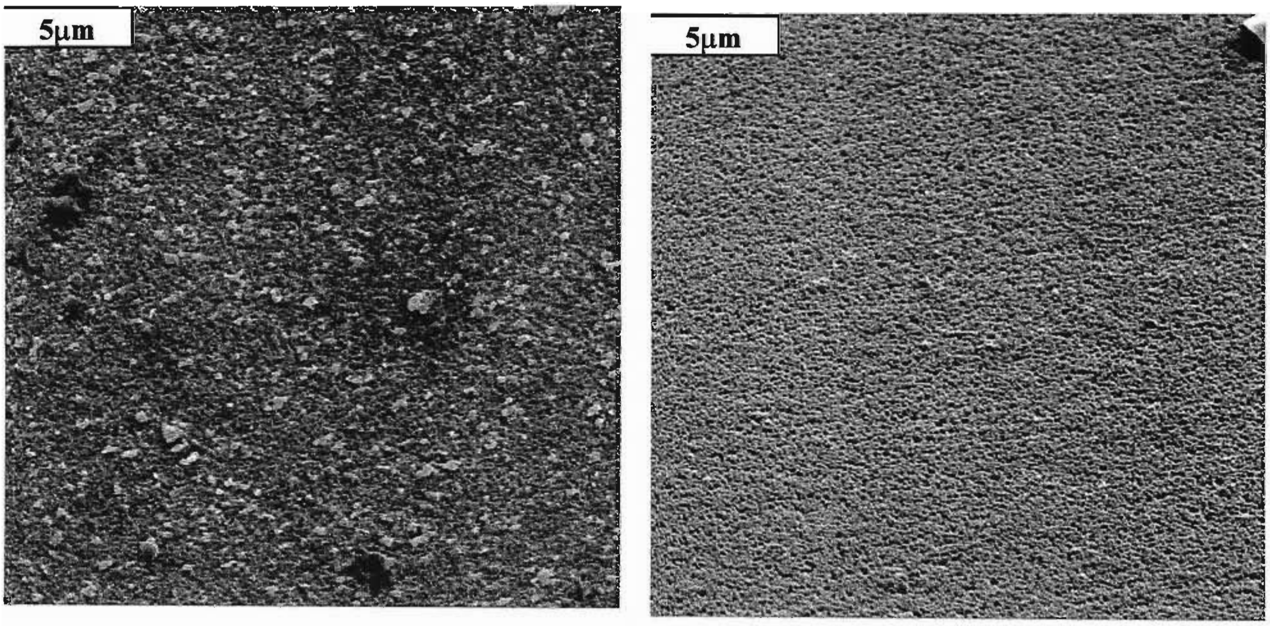

(c) 1M HF / 1M HNO_3 for 10 seconds (mag. x4000)

(d) 1M HF / 1M HNO_3 for 1 minute (mag. x4000)

Fig. 55: The glassy $Zr_{74}Ti_{19}Cu_2Fe_5$ surface after different acid pretreatments.

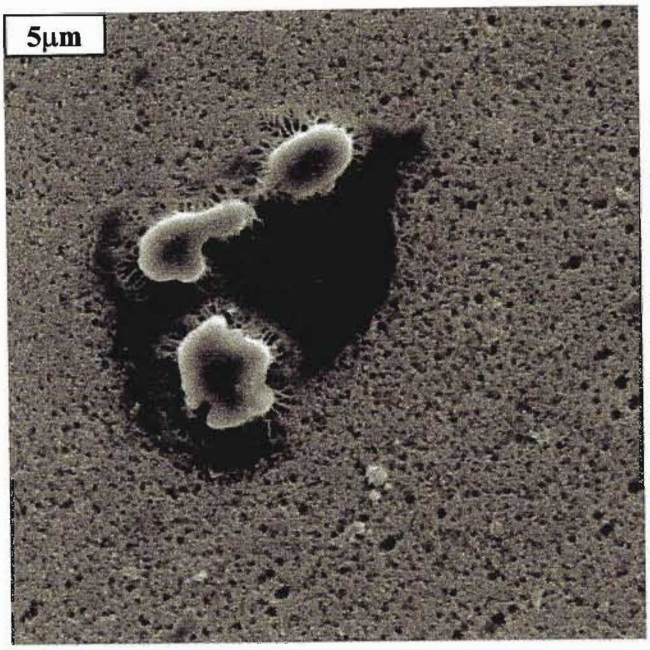

(e) 1M HF for 10 seconds, showing more severe etching around the Zr nodules (mag. x4000)

Fig. 55: Continued

EDS analyses of the general $Zr_{74}Ti_{19}Cu_2Fe_5$ surface were obtained after the different acid pretreatments to determine if changes in the alloy surface composition were produced. The results obtained are listed in Table 35.

Table 35: EDS analysis of the $Zr_{74}Ti_{19}Cu_2Fe_5$ electrode after different chemical pretreatments.

	Zr	Ti	Cu	Fe
Polished electrode surface	73.22	19.71	1.24	5.83
0.1M HF (10s) treatment	71.28	20.15	2.33	6.24
0.5M HF (10s) treatment	68.95	21.88	2.89	6.28
1.0M HF (10s) treatment	65.36	24.04	3.35	7.25
1M HF/1M HNO_3 (10s) treatment	73.77	19.48	1.86	4.89
1M HF/1M HNO_3 (60s) treatment	70.34	21.13	2.41	6.12

A progressive decrease in the surface Zr concentration resulted from HF treatment of increasing concentration. A maximum decrease in the surface Zr content of 7.86 wt% resulted from 1.0M HF treatment (1 minute) in comparison to the polished alloy surface. Treatment with 1M HF/1M HNO_3 (10 seconds) did not produce a detectable change in the alloy concentrations while the one minute treatment produced a 2.88 wt% decrease in the Zr content. It is suggested that preferential dissolution of the Zr component of the alloy created the porous alloy surface and resulted in a corresponding enrichment of the Ti, Cu and Fe components. Dissolution of the Zr-component from Zr-based glassy alloys after HF treatment to produce of a porous alloy surface has been widely reported in the literature [70]. Porous surfaces displaying a Zr and Ti deficiency were obtained after HF-treatment of the glassy $Zr_{64}Ni_{36}$ [95], $Zr_{67}Ni_{33}$ [93] and $Ti_{50}Cu_{50}$, $Ti_{65}Cu_{35}$ and $Zr_{67}Cu_{33}$ [119] alloys. The HF-treated Zr-Ni surfaces were Ni enriched while the Ti-Cu and Zr-Cu surfaces were Cu enriched due to preferential leaching of Zr and Ti components.

The kinetic parameters of Zr-based alloys for the HER that have been obtained in alkaline electrolytes in both their as-quenched states and after acid treatment are listed in Table 36 for comparison with the results obtained in Table 36.

Table 36: Literature Tafel parameters [93,95] reported for hydrogen evolution at glassy Zr-based alloys in base in their as-quenched state and after HF treatment.

Electrode	Electrolyte	Treatment	i_o / A.cm^{-2}	-b / mV	Reference
$Zr_{74}Ti_{19}Cu_2Fe_5$	1M KOH, 25°C	as-polished	4.02×10^{-6} (high η region)	153	this work
		1.0M HF, 10s	7.86×10^{-5}	172	
$Zr_{64}Ni_{36}$	1M KOH, 25°C	as-quenched	4.5×10^{-7}	120-150	95
		0.01M HF, 60s	1.6×10^{-3}	120-150	
		1M HF, 60s	4.4×10^{-3}	120-150	
$Zr_{48}Ni_{27}Al_{25}$	1M KOH, 25°C	as-quenched	1.2×10^{-8}	120-150	95
		0.01M HF, 60s	2.2×10^{-3}	120-150	
$Zr_{67}Ni_{33}$	30wt% KOH, 70°C	as-quenched	1.1×10^{-4}	107	93
		1M HF, 10s	5.8×10^{-4}	190	
		1M HF, 30s	1.7×10^{-4}	107	
		1M HF, 60s	1.1×10^{-4}	114	
		1M HF, 120s	5.5×10^{-5}	102	

The electrocatalytic activity of the glassy $Zr_{64}Ni_{36}$ and $Zr_{48}Ni_{27}Al_{25}$ [95] alloys were lower than the $Zr_{74}Ti_{19}Cu_2Fe_5$ alloy prior to surface treatment in 1M KOH at 25°C. This was, in part, attributed to differences in the surface preparation of the alloys. The $Zr_{64}Ni_{36}$ and $Zr_{48}Ni_{27}Al_{25}$ alloys were tested in the as-quenched state while the $Zr_{74}Ti_{19}Cu_2Fe_5$ alloy was polished with Al_2O_3 prior to cathodic polarisation. The as-quenched surfaces were smooth and lacked surface sites for hydrogen adsorption, resulting in a lower activity. Electrode polishing increased the defect nature of the alloy surface and created stressed sites that served as adsorption sites for hydrogen and enhanced the activity of the alloy. The poor electrocatalytic activity of the as-quenched Zr-based glassy alloys was attributed to their high corrosion resistance and the presence of a tenacious surface oxide film consisting of ZrO_2 [93,95,96] that inhibits the HER. The high corrosion resistance of the $Zr_{74}Ti_{19}Cu_2Fe_5$ alloy was apparent from the anodic polarisation curve (section 5.2) which showed no active region in 1M KOH and underwent spontaneous passivation. Tafel slopes of approximately 150mV were obtained for the glassy $Zr_{64}Ni_{36}$, $Zr_{48}Ni_{27}Al_{25}$ and $Zr_{74}Ti_{19}Cu_2Fe_5$ alloys (in the high overpotential region) at 25°C prior to surface pretreatment. After acid treatment the Tafel slopes of the $Zr_{64}Ni_{36}$ and $Zr_{48}Ni_{27}Al_{25}$ alloys remained unchanged while a 30mV increase in slope resulted for the $Zr_{74}Ti_{19}Cu_2Fe_5$ alloy.

The most activating pretreatment of the glassy $Zr_{74}Ti_{19}Cu_2Fe_5$ electrode resulted from immersion in 1M HF for 10 seconds (Table 36). In contrast to the as-polished glassy alloy surface, acid pretreatment produced a single Tafel slope. The i_o value of acid treated glassy $Zr_{74}Ti_{19}Cu_2Fe_5$ was greater than polycrystalline Ni at 25°C [95] indicating that the activity of the alloy for the HER was higher (Table 33). The i_o value of acid treated $Zr_{74}Ti_{19}Cu_2Fe_5$ was also higher than polycrystalline Pt at 25°C, however the Tafel slope of the glassy alloy was 52mV higher than Pt indicating that the rate of hydrogen evolution at the alloy surface was slower than at the Pt surface. There was general agreement in the literature that the as-polished and as-quenched alloy surfaces displayed a lower activity for hydrogen evolution than the polycrystalline components of the alloy and that acid treatment enhanced the activity of the alloy to levels greater than the individual alloy components. These findings are consistent with the results obtained for hydrogen evolution at the glassy $Zr_{74}Ti_{19}Cu_2Fe_5$ alloy in this study.

Hout et al. [70] found that HF treatment of Zr-based amorphous alloys resulted in selective dissolution of the Zr component, giving rise to an increase in the surface concentrations of the other alloying components and increasing the surface porosity. An improved activity for hydrogen evolution was obtained for the treated alloys in comparison with the as-quenched state. Spriana et al. [95] found that the activity of the glassy $Zr_{64}Ni_{36}$ and $Zr_{48}Ni_{27}Al_{25}$ alloys in the as-quenched state were lower than polycrystalline Ni, i.e. low i_o values and higher Tafel slopes were obtained for the glassy alloy compositions. However, HF treatment resulted in a substantial improvement in the activity of the glassy alloys for hydrogen evolution to levels that were greater than polycrystalline Ni. This was attributed to the removal of the inhibiting oxide film from the as-quenched alloy surfaces. HF treatment of the glassy $Zr_{48}Ni_{27}Al_{25}$ created a highly porous surface by preferential leaching of the Al component while treatment of the $Zr_{64}Ni_{36}$ alloy resulted in dissolution of the Zr-component to produce a Ni-enriched surface. XRD indicated that particles of crystalline Ni formed on the alloy surface and that these contributed to the high activity of the alloy. Another finding was that the hydrogen gas produced by oxidation of the Al and Zr components and by cathodic polarisation in the hydrogen evolution region was absorbed by the amorphous phase and resulted in the formation of Zr hydride.

Treatment of glassy $Zr_{48}Ni_{27}Al_{25}$ in 25wt% KOH at 70°C (24 to 96 hours) prior to cathodic polarisation in 1M KOH was reported to be an effective activation pretreatment. Preferential leaching of the Al component of the alloy occurred producing a porous surface consisting of small Ni particles that displayed a high activity for the HER [95]. Leaching was found to be less effective than HF pretreatment, possibly due to the presence of the passivating Zr oxide film on the alloy surface that hindered the leaching reaction.

Similar results and explanations have been obtained in other independent studies. Machida et al. [96] reported that the Zr-Ni-containing amorphous alloys displayed a poor activity for hydrogen evolution in the as-quenched state in 1M NaOH at 30°C due to the passivating ZrO_2 film. After pretreatment in 1M HF the activity of the alloy was significantly improved by removal of the oxide film and an increased roughness of the alloy surface. After acid treatment the activity of the amorphous alloy was greater than that of pure Ni with a hydrogen overpotential 115mV more positive than Ni obtained at $200mA.cm^{-2}$.

Huot and Brossard [93,99] found that the amorphous $Zr_{67}Ni_{33}$ alloy had a high activity for hydrogen evolution in the as-quenched state at 70°C in 30wt% KOH and that chemical treatment with 1M HF produced only a slight increase in catalytic activity. This would support the findings by Spriana et al. [95] where concentrated alkali at elevated temperatures improved the catalytic activity of the alloy by preferential leaching of one of the alloy components to create a porous surface. Changes in the electrode surface morphology and composition resulted from acid treatment, with general surface roughening, crevice formation and a reduction in the Zr surface concentration detected by SEM and x-ray microanalysis (EDAX). Chemical activation was proposed to occur by dissolution of the surface oxide layer(s), followed by selective dissolution of the Zr component of the alloy. Zr hydride formation resulting from hydrogen generation was also detected, resulting in a loss of ductility and contributing to embrittlement of the alloy. Acid treatment was also linked to the deactivation of the alloy surface during cathodic polarisation in the hydrogen evolution region, in which a decrease in the current density occurred until a steady state was attained. This was attributed to Zr hydride formation on the alloy surface that inhibited the HER. The hydride layer was assumed to remove potential active sites at which hydrogen discharge could occur.

5.6.2.2 Anodic polarisation curves

Anodic polarisation curves of the acid activated $Zr_{74}Ti_{19}Cu_2Fe_5$ surfaces were compared with the as-polished surface to determine how the corrosion properties of the alloy were affected by the treatment. The anodic polarisation curves of the HF and HF/HNO_3 treated surfaces are shown in Fig. 56 and Fig. 57 respectively and the corrosion parameters obtained from the curves are listed in Table 37.

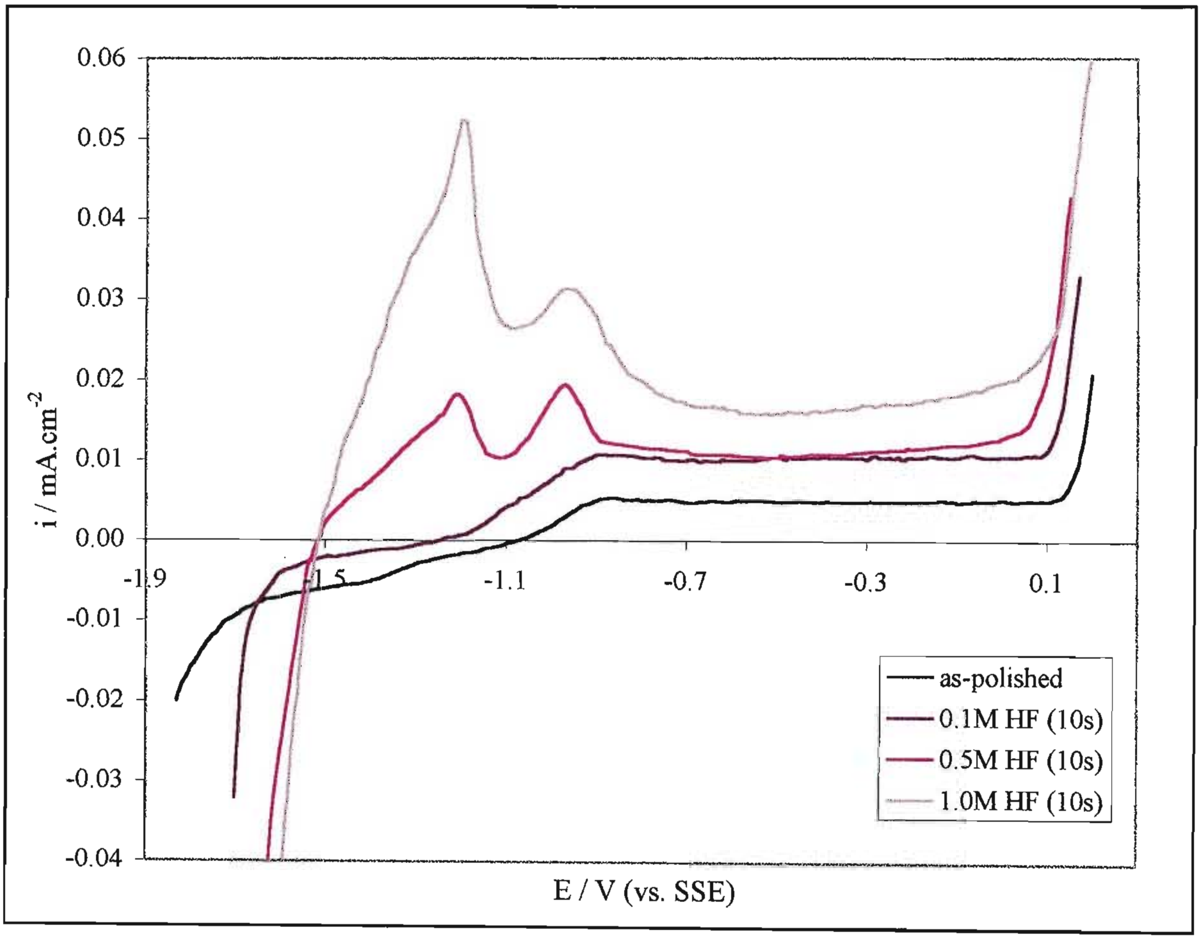

Fig. 56: Typical anodic polarisation curves of the glassy $Zr_{74}Ti_{19}Cu_2Fe_5$ alloy in 1M KOH (25°C) in the as-polished state and after *ex situ* HF pretreatments.

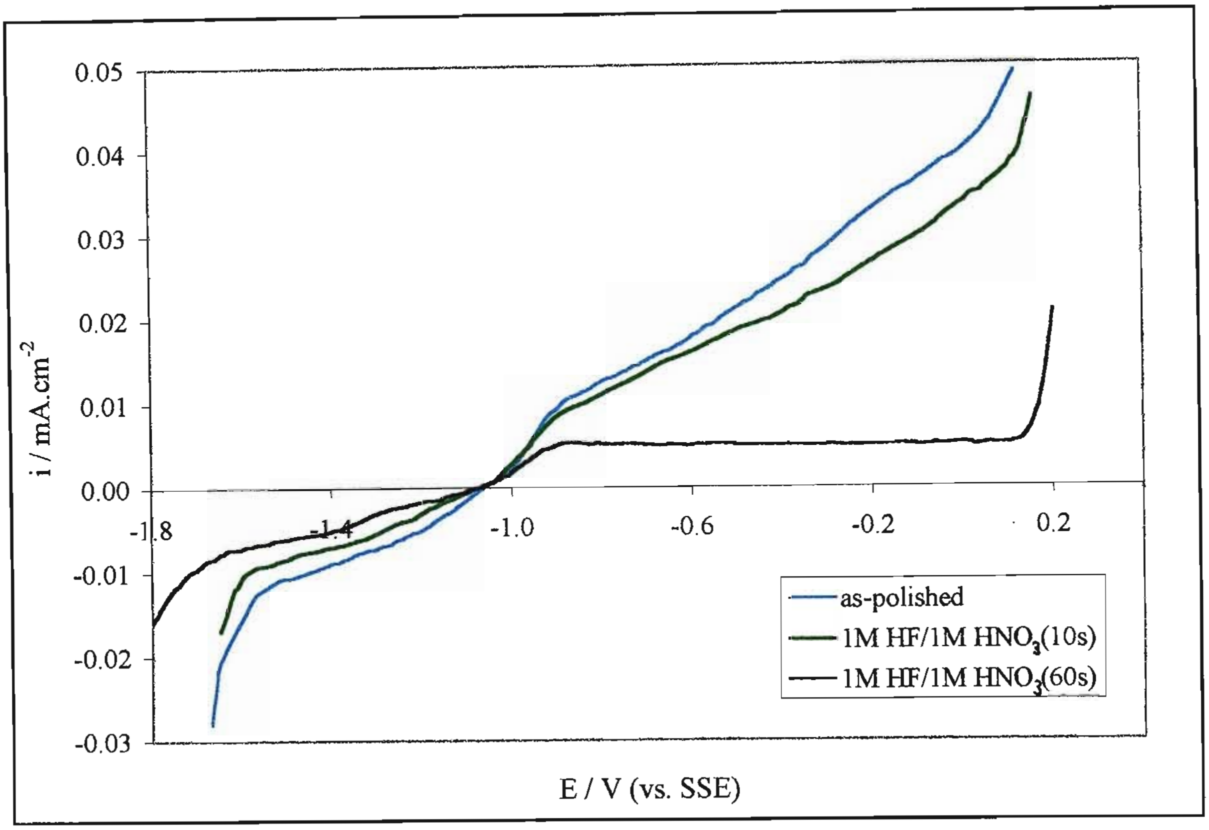

Fig. 57: Typical anodic polarisation curves of the glassy $Zr_{74}Ti_{19}Cu_2Fe_5$ alloy in 1M KOH (25°C) in the as-polished state and after *ex situ* HF/HNO_3 treatments.

Table 37: Corrosion parameters obtained from anodic polarisation curves of glassy $Zr_{74}Ti_{19}Cu_2Fe_5$ in the as-polished state and after acid pretreatment.

	E_{corr}	E_{pp}	E_{Flade}	E_{tr}	i_{pp}	i_p
as-polished	-1.07	-	-	0.13	-	4.93×10^{-3}
0.1M HF (10s)	-1.26	-	-	0.09	-	1.11×10^{-2}
0.5M HF (10s)	-1.52	-1.21	-0.89	0.05	1.83×10^{-2}	1.13×10^{-2}
1.0M HF (10s)	-1.52	-1.19	-0.76	0.06	5.20×10^{-2}	1.64×10^{-2}
1M HF/1M HNO_3 (10s)	-1.07	-	-	0.12	-	-
1M HF/1M HNO_3 (60s)	-1.07	-	-	0.05	-	-

The anodic polarisation curve of the as-polished $Zr_{74}Ti_{19}Cu_2Fe_5$ electrode showed no active region and the alloy passivated spontaneously in 1M KOH. After 0.1M HF (10s) treatment the current densities increased at potentials more anodic than E_{corr} but the shape of the curve remained unchanged (Fig. 56). After 0.5M HF (10s) treatment an active region consisting of two anodic peaks at potentials of -1.20 and -0.97V formed and the current density of the passive region was further increased. The two peaks indicate that primary and secondary active-passive transitions occur with increasing potential. Higher current densities were obtained in all regions of the anodic polarisation curve after 1.0M HF treatment and the curve maintained a similar shape to that of the 0.5M treated surface. As the acid concentration was increased the E_{corr} values shifted towards more negative potentials. The formation of active peaks after acid treatment indicate that the corrosion resistance of the glassy $Zr_{74}Ti_{19}Cu_2Fe_5$ alloy was reduced in comparison to its as-polished state. The increased current densities would also, in part, also reflect the increased surface area of the acid treated electrode which were found to be porous and greatly increased when viewed by SEM.

The HF/HNO_3 treated $Zr_{74}Ti_{19}Cu_2Fe_5$ surfaces displayed a monotonic increase in current density (Fig. 57) when anodically polarised and a passive region was not obtained at potentials more positive than E_{corr}. Thus HF/HNO_3 treatment greatly reduced the corrosion resistance of the alloy in comparison to its as-polished state and is not a suitable activation pretreatment, findings which are not unexpected. The E_{corr} values were unchanged by the treatment.

5.6.3 *In situ* anodic pretreatment

In view of the dramatic effect on HER shown by prior *ex situ* (acidic) oxidation of the glassy $Zr_{74}Ti_{19}Cu_2Fe_5$ surface it would clearly be instructive to investigate *in situ* surface activation in the basic medium. The influence of *in situ* anodic oxidation on the electrocatalytic activity of the glassy $Zr_{74}Ti_{19}Cu_2Fe_5$ alloy for hydrogen evolution prior to cathodic polarisation in 1M KOH was determined, as distinct from prior oxidation in acid media. The kinetic parameters obtained after anodic oxidation at different constant current densities are listed in Table 38 and the corresponding Tafel plots are shown in Fig. 58. As the Tafel plots fall close together, the Tafel lines obtained for treatments of 750 and 2000μA.cm^{-2} were omitted from the graph for clarity.

A progressive increase in the Tafel current densities resulted from anodic treatments of increasing magnitude. Double Tafel slopes were obtained for all treatments and the potential at which the slopes intercepted maintained a constant value of -1.90V. This contrasts with the single slope that was obtained at the acid treated surfaces. The double slope indicated that the inhomogeneities present on the alloy were not removed by anodic treatment as was the case for the acid treatment. For all anodic treatments the alloy had lower Tafel slopes in the high overpotential region and hence displayed a greater activity for hydrogen evolution in this region as was the case at the as-polished electrode surface. The Tafel slopes showed a general increase in value with an increasing anodic oxidation current in the high overpotential region so that the Tafel lines converged towards a common point at high potentials. The i_o values increased progressively with an increasing oxidation current, changing from 4.02 x 10^{-6} (as-polished, 25°C) to 33.1 x 10^{-5} A.cm^{-2} (3000μA.cm^{-2}) and from 9.96 x 10^{-6} (as-polished, 25°C) to 70.1 x 10^{-6} A.cm^{-2} (3000μA.cm^{-2}) in the high and low overpotential regions respectively.

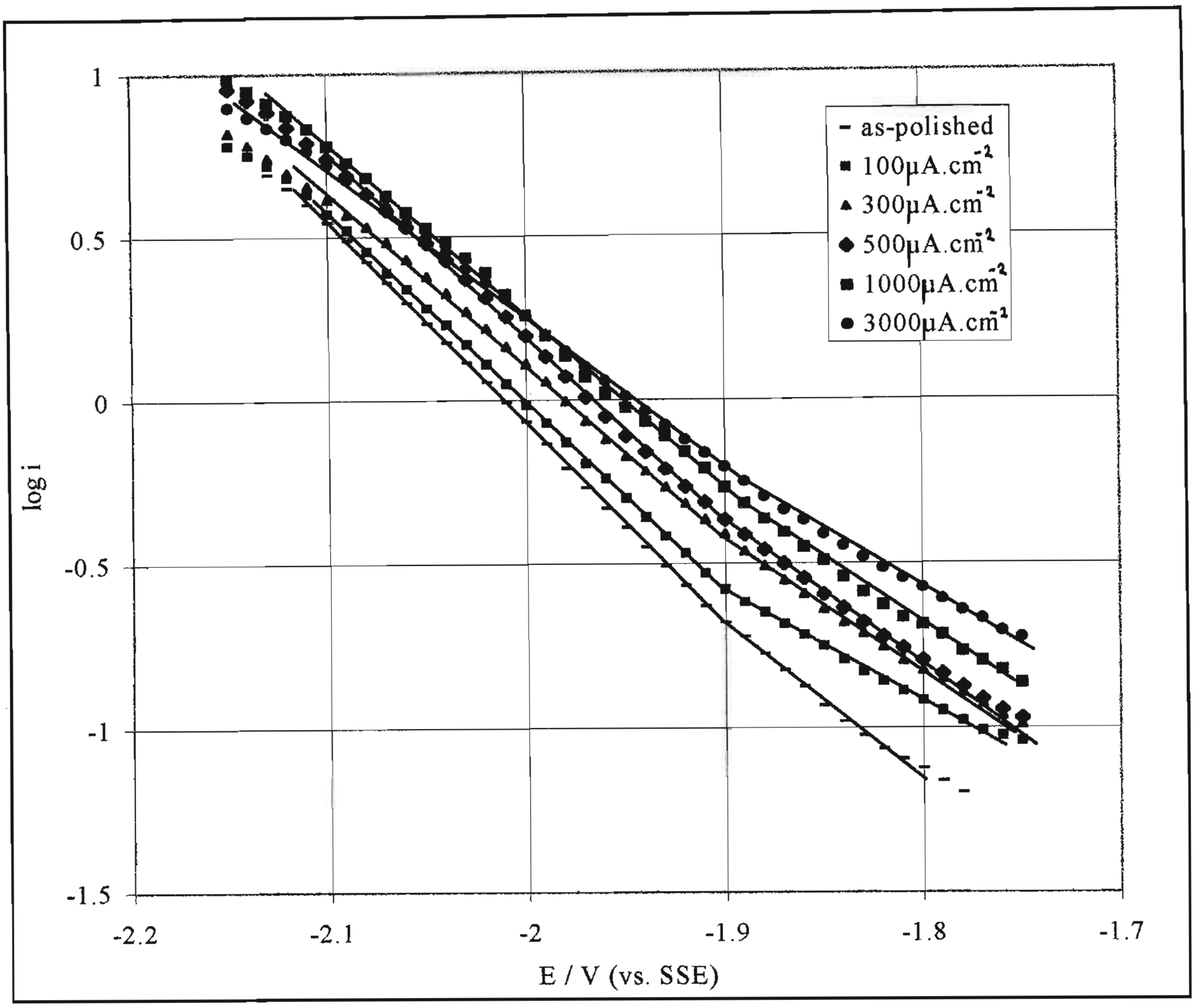

Fig. 58: Tafel plots for hydrogen evolution on the glassy $Zr_{74}Ti_{19}Cu_2Fe_5$ electrode after *in situ* anodic oxidation at constant current densities for 2 minutes in 1M KOH at 25°C.

These i_o values were 8.2 and 7.0 times greater in the high and low overpotential regions after the most activating anodic treatment than the values obtained at the as-polished surface. This increase was not as great as the increase obtained after HF treatment (10 seconds) of glassy $Zr_{74}Ti_{19}Cu_2Fe_5$ for which an i_o value 19.6 times greater than that of the as-polished electrode surface was obtained. The increase in i_o resulting from anodic treatment of the $Zr_{74}Ti_{19}Cu_2Fe_5$ alloy was much greater than the increase obtained for equivalent treatments of the glassy $Fe_{67}Co_{18}B_{14}Si_1$, $Co_{66}Fe_4Si_{16}B_{12}Mo_2$, $Fe_{40}Ni_{40}P_{14}B_6$ and $Fe_{40}Ni_{40}B_{20}$ alloys also tested in this study. This indicates that the $Zr_{74}Ti_{19}Cu_2Fe_5$ composition was more effectively activated by anodic treatment than the other alloy compositions. The variation in the i_o value obtained after anodic treatments of different magnitude is shown in Fig. 59. The i_o value increased most rapidly for anodic treatments of up to 500μA.cm^{-2}, after which the rate of increase slowed.

Table 38: Kinetic data for hydrogen evolution on the glassy $Zr_{74}Ti_{19}Cu_2Fe_5$ electrode in 1M KOH at 25°C after *in situ* anodic oxidation at different current densities for 2 minutes.

	High η region			Low η region					
Anodic treatment /μA.cm^{-2}	Tafel region /V	-b /mV	i_o /A.cm^{-2}	Tafel region /V	-b /mV	i_o /A.cm^{-2}	i_1* mA.cm^{-2}	$i_2^{\otimes}$ mA.cm^{-2}	$i_3^{\oplus}$ mA.cm^{-2}
0	-1.90 to -2.12	153 ± 12	$(4.02 \pm 1.44) \times 10^{-6}$	-1.82 to -1.90	187 ± 11	$(9.96 \pm 3.29) \times 10^{-6}$	0.067 ± 0.016	0.267 ± 0.076	1.714 ± 0.610
100	-1.90 to -2.11	166 ± 14	$(6.17 \pm 1.08) \times 10^{-6}$	-1.77 to -1.90	300 ± 16	$(3.30 \pm 0.66) \times 10^{-5}$	0.134 ± 0.018	0.275 ± 0.121	1.587 ± 0.708
300	-1.90 to -2.10	183 ± 11	$(1.55 \pm 0.72) \times 10^{-5}$	-1.80 to -1.90	256 ± 32	$(4.04 \pm 0.88) \times 10^{-5}$	0.152 ± 0.025	0.467 ± 0.104	2.410 ± 0.453
500	-1.90 to -2.10	180 ± 11	$(1.75 \pm 0.46) \times 10^{-5}$	-1.76 to -1.90	253 ± 23	$(4.47 \pm 1.53) \times 10^{-5}$	0.164 ± 0.042	0.536 ± 0.099	2.946 ± 0.396
750	-1.90 to -2.09	190 ± 8	$(2.04 \pm 0.41) \times 10^{-5}$	-1.80 to -1.90	266 ± 19	$(4.07 \pm 0.68) \times 10^{-5}$	0.178 ± 0.033	0.535 ± 0.110	2.654 ± 0.640
1000	-1.89 to -2.11	213 ± 10	$(2.23 \pm 0.58) \times 10^{-5}$	-1.75 to -1.89	259 ± 17	$(3.17 \pm 1.03) \times 10^{-5}$	0.196 ± 0.030	0.658 ± 0.133	3.336 ± 0.542
2000	-1.89 to -2.08	204 ± 2	$(3.25 \pm 0.85) \times 10^{-5}$	-1.79 to -1.89	294 ± 20	$(7.76 \pm 2.42) \times 10^{-5}$	0.251 ± 0.063	0.633 ± 0.089	2.987 ± 1.004
3000	-1.88 to -2.12	209 ± 24	$(3.31 \pm 0.48) \times 10^{-5}$	-1.75 to -1.88	283 ± 25	$(7.01 \pm 0.62) \times 10^{-5}$	0.268 ± 00.031	0.744 ± 0.256	3.403 ± 1.443

* E = -1.80V, $^{\otimes}$ E = -1.92V, $^{\oplus}$ E = -2.05V (vs.SSE)

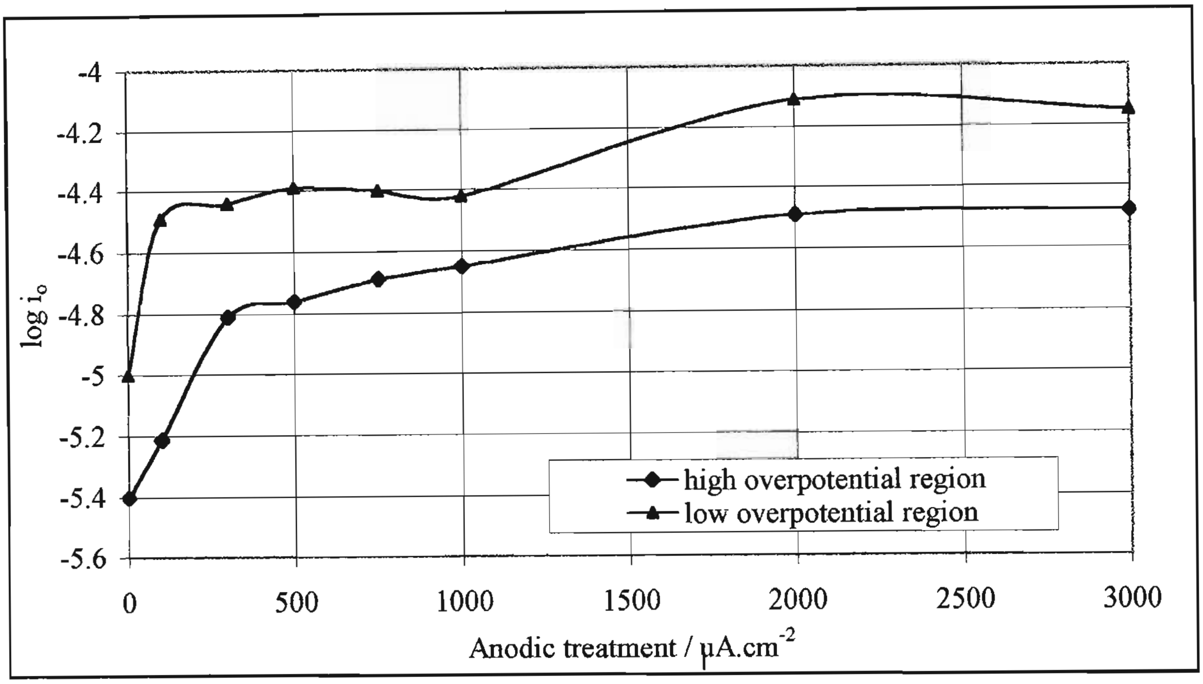

Fig. 59: Exchange current densities obtained for hydrogen evolution after anodic oxidation of glassy $Zr_{74}Ti_{19}Cu_2Fe_5$ at different constant current densities in 1M KOH at 25°C.

5.6.3.1 SEM/EDS analysis

SEM analysis showed that anodic oxidation resulted in the formation of discrete patches of deposit on the alloy surface. The size of the patches increased as the magnitude of the oxidation current was increased. The base alloy substrate was visible in areas surrounding the patches and the Al_2O_3 polish lines could be seen on the electrode surface. An SEM micrograph of a portion of the $Zr_{74}Ti_{19}Cu_2Fe_5$ electrode surface after an anodic treatment of $3000\mu A.cm^{-2}$ is shown in Fig. 60 in which a large region of deposit was surrounded by smaller regions of deposit. EDS did not have sufficient sensitivity to detect any differences in the deposit concentrations in comparison to the as-polished surface. It is suggested that the surface deposit formed by anodic oxidation was an oxide that provided new and catalytically active surface sites that were supported on the amorphous substrate. A change in the nature of the surface sites was indicated by a change in the Tafel slopes resulting from anodic pretreatment. The oxide also increased the surface area and increased the apparent current density at the electrode.

From these results it was concluded that anodic oxidation of the glassy $Zr_{74}Ti_{19}Cu_2Fe_5$ electrode, prior to cathodic polarisation in 1M KOH, was effective in increasing the activity of the alloy in comparison to its as-quenched state. Further investigation of the electrode surface, the nature of the active sites and the mechanism by which the reaction occurs is required. Acid pretreatment was found to be more effective than anodic treatment in activating the electrode surface.

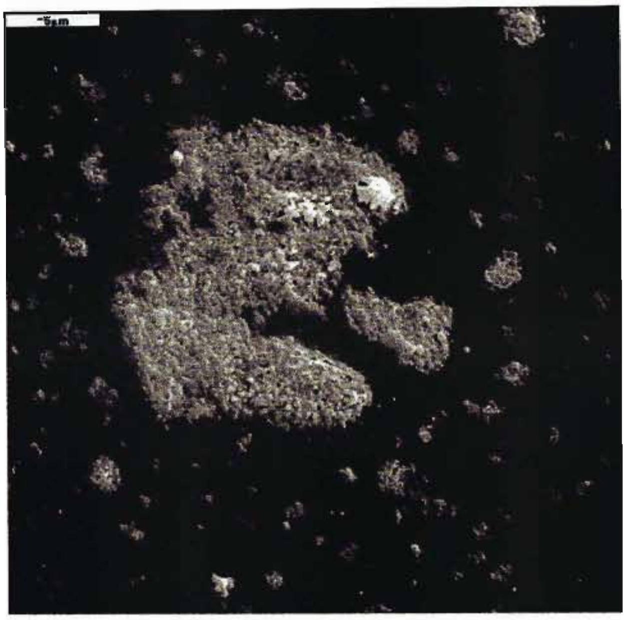

Fig. 60: The $Zr_{19}Ti_{19}Cu_2Fe_5$ alloy surface after *in situ* anodic oxidation at 3000μA.cm^{-2} for 2 minutes (mag. x4000).

The most activating anodic pretreatment of 3000μA.cm^{-2} (2 minutes) produced double Tafel slopes at the glassy $Zr_{74}Ti_{19}Cu_2Fe_5$ electrode in comparison to the single slopes reported for polycrystalline Ni and Pt (Table 34). The i_o values of $Zr_{74}Ti_{19}Cu_2Fe_5$ were higher than Ni [95] and Pt [97] in both overpotential regions at 25°C, however the Tafel slopes were also substantially higher at the glassy alloy surface. Tafel slopes that were 89mV and 163mV higher in value than Pt were obtained at the $Zr_{74}Ti_{19}Cu_2Fe_5$ electrode in the high and low overpotential regions respectively, resulting in a slower rate of hydrogen evolution at the glassy alloy surface.

5.6.3.2 Anodic polarisation curves

The anodic polarisation curves obtained after *in situ* electrochemical pretreatment of the $Zr_{74}Ti_{19}Cu_2Fe_5$ alloy are shown in Fig. 61 and the approximate corrosion parameters obtained from the curves are listed in Table. 39.

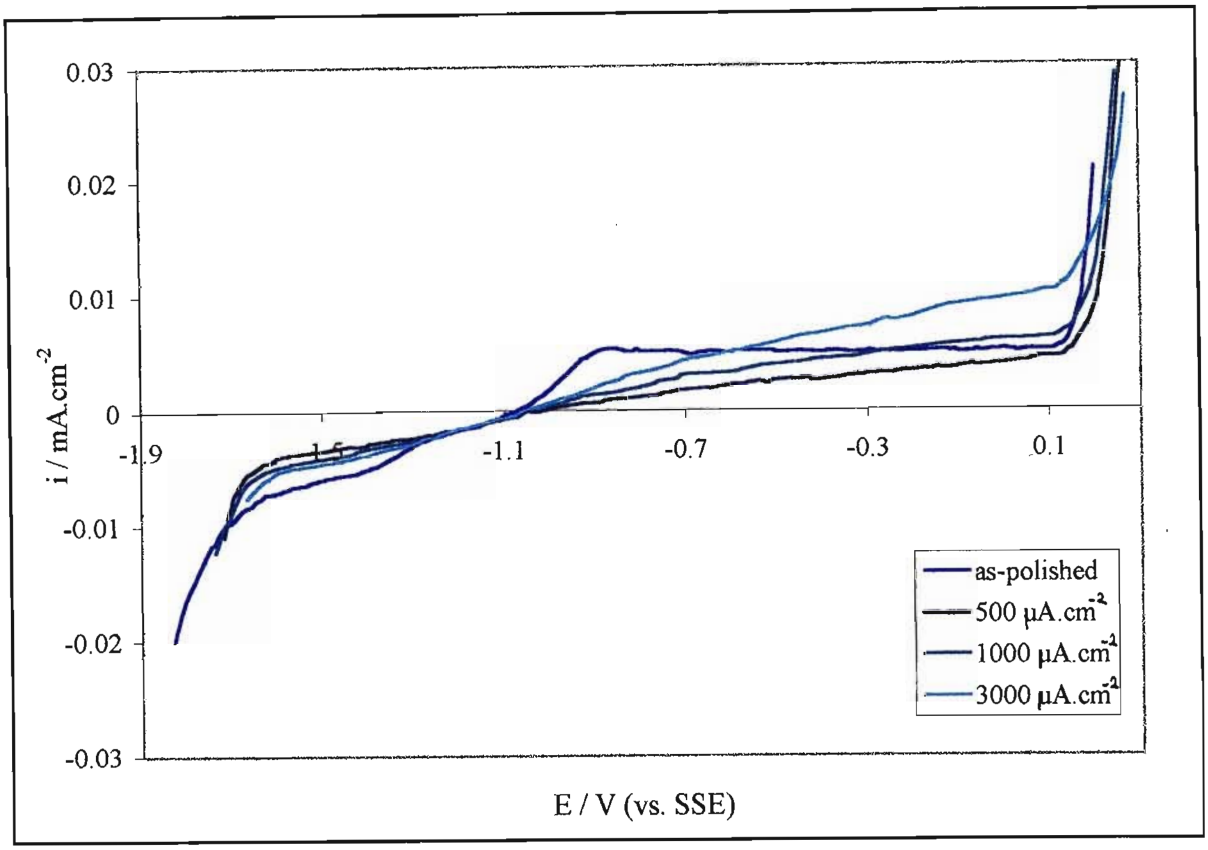

Fig. 61 Typical anodic polarisation curves of the glassy $Zr_{74}Ti_{19}Cu_2Fe_5$ electrode in 1M KOH (25°C) after *in situ* anodic oxidation at different current densities.

Table 39: Corrosion parameters obtained from anodic polarisation curves of glassy $Zr_{74}Ti_{19}Cu_2Fe_5$ in the as-polished state and after anodic oxidation at different current densities.

	E_{corr}	E_{tr}	i_p
as-polished	-1.07	0.13	4.93×10^{-3}
500 $\mu A.cm^{-2}$	-1.05	0.12	-
1000 $\mu A.cm^{-2}$	-1.05	0.15	-
3000 $\mu A.cm^{-2}$	-10.5	0.12	-

The anodic polarisation curves of the anodically oxidised $Zr_{74}Ti_{19}Cu_2Fe_5$ surfaces showed that the treatment altered the surface properties of the alloy in comparison to its as-polished state but did not produce a substantial increase in current density. The current densities of the curves obtained for anodic treatments of 500 $\mu A.cm^{-2}$ and less were lower than those of the as-polished surface. The current densities of the anodically oxidised surfaces at potentials higher than E_{corr} were not constant and increased with increasing potential, in comparison to the as-polished surface which maintained a constant current density. The E_{corr} and E_{tr} values were not affected significantly by anodic oxidation indicating that the treatment did not have a detrimental effect on the corrosion resistance of the $Zr_{74}Ti_{19}Cu_2Fe_5$ alloy.

5.6.4 Conclusions

1. An increase in temperature (25 to 70°C) produced a minor increase in the activity of the glassy $Zr_{74}Ti_{19}Cu_2Fe_5$ alloy which was not as great as the increase obtained at the glassy $Fe_{67}Co_{18}B_{14}Si_1$, $Co_{66}Fe_4Si_{16}B_{12}Mo_2$, $Fe_{40}Ni_{40}P_{14}B_6$ and $Fe_{40}Ni_{40}B_{20}$ surfaces. This was attributed to highly passivating Zr oxide and Ti oxide surface films that inhibited the HER.

2. Acid pretreatment produced a large increase in the activity of the $Zr_{74}Ti_{19}Cu_2Fe_5$ alloy for hydrogen evolution in comparison to its as-polished state, with the greatest increase resulting from 1M HF (10 seconds) treatment. Activation was attributed to removal of the inhibiting oxide layer and the formation of a porous surface with a greatly enhanced area at which the HER could occur. The electrolyte was able to partially penetrate the surface pores and make contact with the substrate over a much larger surface area, consequently resulting in a higher apparent current density. The different mechanisms by which hydrogen adsorption and evolution can occur are listed in section 2.4.2. EDS analysis revealed that acid treatment resulted in preferential dissolution of the Zr component at the alloy. Partial crystallisation of the alloy surface with the production of a greater number of surface defect sites at which hydrogen adsorption could occur may also have contributed to the increase in activity of the alloy.

3. Acid pretreatment with pure HF was more effective in improving the activity of glassy $Zr_{74}Ti_{19}Cu_2Fe_5$ for the HER than the HF/HNO_3 mixture. This contrasted with the glassy $Co_{66}Fe_4Si_{16}B_{12}Mo_2$, $Fe_{40}Ni_{40}P_{14}B_6$ and $Fe_{40}Ni_{40}B_{20}$ alloys for which HF/HNO_3 pretreatment was more effective.

4. Single Tafel slopes resulted from acid treatments of glassy $Zr_{74}Ti_{19}Cu_2Fe_5$ with 0.5M HF (10s), 1.0M HF (10s) and 1M HF/1M HNO_3 (1min). This was attributed to preferential removal of the Zr nodules (as observed by SEM analysis) to production of a more homogeneous alloy surface with only single adsorption sites at which hydrogen adsorption and evolution could occur.

5. Acid pretreatment reduced the corrosion resistance of glassy $Zr_{74}Ti_{19}Cu_2Fe_5$ in comparison to its as-polished state. The as-polished surface passivated spontaneously in 1M KOH. After acid treatment an active region formed and the current densities increased in all regions of the anodic polarisation curve. The increased current densities can, in part, be attributed to the

porous alloy surface that resulted in greater apparent current densities (because current densities were calculated based on the geometrical electrode area).

6. *In situ* anodic oxidation of the glassy $Zr_{74}Ti_{19}Cu_2Fe_5$ electrode, prior to cathodic polarisation in 1M KOH, resulted in a progressive increase in the activity of the alloy for hydrogen evolution as the magnitude of the oxidation current was increased. A surface deposit, possibly an oxide, consisting of discrete patches formed on the alloy surface and became larger as the oxidation current was increased. The surface layer appeared to provide catalytically active surface sites and also enhanced the surface area of the electrode at which the HER could occur. Further investigation of the composition of the surface deposit and the mechanism by which anodic treatment activates the alloy surface is required. Anodic treatment was much more effective in improving the activity of the glassy $Zr_{74}Ti_{19}Cu_2Fe_5$ alloy than equivalent treatments of the $Fe_{67}Co_{18}B_{14}Si_1$, $Co_{66}Fe_4Si_{16}B_{12}Mo_2$, $Fe_{40}Ni_{40}P_{14}B_6$ and $Fe_{40}Ni_{40}B_{20}$ electrodes.

7. The anodic polarisation curves of the anodically oxidised $Zr_{74}Ti_{19}Cu_2Fe_5$ surfaces showed that the treatment altered the surface properties of the alloy in comparison to its as-polished state but did not reduce the corrosion resistance of the alloy.

8. In the as-polished state the $Zr_{74}Ti_{19}Cu_2Fe_5$ electrode displayed a lower activity for hydrogen evolution than polycrystalline Ni or Pt at the different temperatures tested. Acid pretreatment of the glassy surface (1M HF, 10 seconds) produced i_o values that were higher, and hence a catalytic activity that was greater, than both Ni and Pt. After anodic treatment of $Zr_{74}Ti_{19}Cu_2Fe_5$ at an oxidation current of $3000\mu A.cm^{-2}$ the i_o values of the glassy alloy were higher than both Ni and Pt, however the Tafel slopes were also substantially higher at the glassy alloy surface which resulted in a slower rate of hydrogen evolution.

SUMMARY

Effective mounting and handling methods for the thin glassy metal alloy ribbons were developed and tested successfully. The anodic polarisation curves of the alloys in their as-polished state indicated that the glassy $Fe_{67}Co_{18}B_{14}Si_1$ and $Co_{66}Fe_4Si_{16}B_{12}Mo_2$ compositions displayed the poorest corrosion resistance in base with higher active and passive current densities obtained for both alloys in comparison to the other alloy compositions tested. The voltammetric response of glassy $Fe_{67}Co_{18}B_{14}Si_1$ was very similar to that of polycrystalline Fe. Progressive buildup and flaking of an oxide layer on the $Fe_{67}Co_{18}B_{14}Si_1$ surface, possibly an iron oxyhydroxide, resulted in the eventual disintegration of this alloy. The glassy $Fe_{40}Ni_{40}P_{14}B_6$ and $Fe_{40}Ni_{40}B_{20}$ alloys exhibited similar polarisation curves in their as-polished state and an active to passive transition. The $Zr_{74}Ti_{19}Cu_2Fe_5$ alloy displayed the greatest corrosion resistance in the as-polished state and no active region was obtained.

In the as-polished state the most corrosion resistant composition, $Zr_{74}Ti_{19}Cu_2Fe_5$, displayed the poorest activity for hydrogen evolution and only a minor improvement resulted from increasing electrolyte temperature in comparison to the other glassy alloys tested. This was attributed to the formation of passivating Zr oxide and Ti oxide surface films that inhibited the HER. The least corrosion resistant compositions, $Fe_{67}Co_{18}B_{14}Si_1$ and $Co_{66}Fe_4Si_{16}B_{12}Mo_2$, showed the highest activity for hydrogen evolution in their as-polished state and a larger temperature dependence than the $Zr_{74}Ti_{19}Cu_2Fe_5$ alloy.

Cathodic polarisation of glassy $Co_{66}Fe_4Si_{16}B_{12}Mo_2$, $Fe_{40}Ni_{40}P_{14}B_6$, $Fe_{40}Ni_{40}B_{20}$ and $Zr_{74}Ti_{19}Cu_2Fe_5$ in the hydrogen evolution region resulted in Tafel plots that consisted of two different Tafel slopes that were divided into regions defined as the low and high overpotential regions. At all temperatures and after surface activation, the high overpotential region displayed a higher activity for hydrogen evolution, i.e. a greater rate of increase in the current density with increasing potential, than the low overpotential region. The $Zr_{74}Ti_{19}Cu_2Fe_5$ alloy surface was inhomogeneous with some nodules of crystalline Zr embedded in the amorphous substrate, highlighting the difficulty associated with manufacturing an amorphous alloy with a homogeneous structure. This provided two distinctly different hydrogen adsorption sites and was possibly the reason for the change in Tafel slope.

The hydrogen evolution Tafel parameters for the $Fe_{67}Co_{18}B_{14}Si_1$ and $Co_{66}Fe_4Si_{16}B_{12}Mo_2$ electrodes were similar, in the as-polished state. Acid pretreatment of glassy $Fe_{67}Co_{18}B_{14}Si_1$ resulted in a slight increase in the activity of this alloy and was a destructive procedure that rapidly etched through the entire ribbon thickness and destroyed the sample. A large improvement in the activity of the $Co_{66}Fe_4Si_{16}B_{12}Mo_2$ alloy resulted from acid treatment (1M HF/1M HNO_3, 10 minutes) and a porous electrode surface was produced. The i_o values of acid treated $Co_{66}Fe_4Si_{16}B_{12}Mo_2$ were higher than the polycrystalline Fe and Co components of the alloy and were also found to be higher than both polycrystalline Ni or Pt at 25°C, indicating that this glassy alloy composition formed a potentially excellent electrocatalytst for the HER. The anodic polarisation curves of the acid treated $Fe_{67}Co_{18}B_{14}Si_1$ and $Co_{66}Fe_4Si_{16}B_{12}Mo_2$ surfaces maintained similar shapes but greater current densities than the curves of the as-polished surfaces. This was attributed to the increased electrode surface areas produced by acid treatment and the fact that the current densities calculated were based on geometrical areas and not actual effective areas, resulting in an apparent increase in the current densities.

The activity of the $Zr_{74}Ti_{19}Cu_2Fe_5$ alloy was substantially improved by acid pretreatment in comparison to the as-polished state. Acid treatment with HF resulted in selective dissolution of the Zr component of the alloy, producing a porous surface with a large surface area at which hydrogen adsorption and evolution could occur. The $Zr_{74}Ti_{19}Cu_2Fe_5$ alloy displayed a lower activity for hydrogen evolution in the as-polished state than polycrystalline Ni and Pt but a greater activity was obtained after acid pretreatment with 1M HF for 10 seconds. The disadvantage associated with the acid pretreated surface was a reduction in the corrosion resistance of the alloy in-comparison to its as-polished state. HF pretreatment resulted in an anodic polarisation curve with an active region and the HF/HNO_3 treated surface showed no sign of passivation with a progressive increase in the current density occurring for potentials more positive than E_{corr}. Current densities were higher in all regions of the curves after acid treatment in comparison to their as-polished state. This was attributed to the increased surface area of the electrode and possibly to the removal of a passivating surface oxide film.

The activity of the $Fe_{40}Ni_{40}P_{14}B_6$ alloy for hydrogen evolution was lower than the $Fe_{40}Ni_{40}B_{20}$ alloy in the as-polished state. P-enrichment in the near surface region of the $Fe_{40}Ni_{40}P_{14}B_6$ electrode, detected by EDS, possibly inhibited the reaction. The activity of the $Fe_{40}Ni_{40}P_{14}B_6$ electrode was significantly improved by acid treatment, in particular 1M HF/1M HNO_3 treatment for 10 minutes, whereas the $Fe_{40}Ni_{40}B_{20}$ composition displayed a much smaller increase in activity after the same treatment. SEM/EDS analysis revealed that the acid pretreated $Fe_{40}Ni_{40}P_{14}B_6$ surface was porous and that preferential dissolution of the P component occurred. Only a slight degree of surface roughening was obtained after an equivalent pretreatment of the P-free alloy. The anodic polarisation curves of the acid treated surfaces maintained the same shape but displayed greater current densities in all regions of the curve than for the as-polished electrode. In all cases the current densities of the $Fe_{40}Ni_{40}P_{14}B_6$ alloy were greater than the $Fe_{40}Ni_{40}B_{20}$ alloy after equivalent treatments. This was attributed to the greater surface area of the $Fe_{40}Ni_{40}P_{14}B_6$ electrode and hence a greater apparent current density. Both alloy compositions were susceptible to hydrogen absorption as indicated by blister formation and rupturing on the alloy surfaces after HF treatment.

For all the glassy alloy compositions tested, *ex situ* chemical pretreatment was more effective than *in situ* anodic pretreatment in activating the electrode surface for the HER. Anodic treatment ($3000\mu A.cm^{-2}$) was most effective in activating the $Zr_{74}Ti_{19}Cu_2Fe_5$ electrode in comparison to the other glassy alloy compositions and did not have a detrimental effect on the corrosion resistance of the alloy. The anodic polarisation curves indicated that current densities of similar magnitude to the as-polished surface were obtained. The current densities of the anodically treated surfaces were not constant, as was the case for the as-polished electrode, but varied between E_{corr} and E_{tr}, indicating that changes in the surface properties of the alloy had occurred. Further investigation into the nature of these changes and the mechanism by which anodic treatment activates the alloy surface for the HER is required. Although less effective than acid treatment in activating the glassy alloy surfaces, anodic treatment was not a destructive activation procedure and resulted in a more stable and long-life catalyst. In this regard it would form the preferred technique for activating the glassy alloy surfaces for the HER.

SUGGESTIONS FOR FUTURE WORK

---

1. A great deal of further research and systematic investigation into the influence of the glassy metal surface structure and electronic structure on the electrochemical properties of the alloys is required as the investigations published to date are sparse and not comprehensive. There has been little attention directed towards the study of the electronic properties of the passive films formed on glassy alloys, possibly due to the fact that a large number of studies have concentrated on Cr-containing alloys that form very thin passive films that are difficult to analyse with respect to their electronic properties [94]. Passivity models such as the Point Defect Model of Macdonald [57], developed for polycrystalline alloys, may lead to a greater understanding of the complex processes involved in glassy alloys, after suitable modification.

2. Systematic comparisons between the glassy alloys and equivalent crystalline alloy compositions would provide a greater understanding of the influence of amorphous structure on the corrosion and electrocatalytic properties of the glassy alloys.

3. The preliminary characterisation of the corrosion and catalytic properties of the glassy alloys tested in this study was conducted in a 1M KOH electrolyte. It would be useful to extend the experiments to include a range of other electrolyte media such. as H_2SO_4, HCl, $KHSO_4$, $NaHSO_4$ or $NaClO_4$. The influence of pH change on the corrosion and catalytic properties of the alloys could thereby be determined.

4. An extremely wide range of glassy alloy systems and different reaction types remains to be investigated. Crystalline gold has been extensively studied and is found to display a very wide range of electrocatalytic activities, especially in base. The use of gold as an electrocatalyst for a diversity of reaction types such as alcohol oxidation, aldehyde oxidation, carbohydrate oxidation, hydrocarbon oxidation/reduction, oxidation/reduction of nitrogen, amino acid oxidation, oxidation/reduction of gases such as CO, N_2O, O_2, or oxidation/reduction of inorganic compounds in aqueous acids and bases has been investigated by different researchers [159]. A number of different reactions such as these could be investigated at glassy alloy electrocatalyst surfaces and compared with the well-researched polycrystalline metals such as Au and Pt. The kinetic parameters of the $Fe(CN)_6^{3-/4-}$ redox couple, that has been widely investigated at crystalline alloy and metal surfaces, could be

obtained at the glassy alloy electrodes to gain insight into the role of the amorphous structure [160].

5. The glassy $Fe_{67}Co_{18}B_{14}Si_1$ alloy tested in this study displayed a lower activity for the HER in 1M KOH than the similar glassy alloy compositions, $Fe_{60}Co_{20}Si_{10}B_{10}$ [68,69] and $Fe_{75}Si_{11}B_{11}$ [69,71]. On this basis it was suggested that Si addition improved the electrocatalytic activity of the glassy alloys for hydrogen, however further investigation into the influence exerted by Si as well as the other metalloid components is required.

6. SEM analysis revealed that surface pretreatment, in particular acid pretreatment, greatly enhanced the surface area of the electrodes in comparison to their as-polished state. This resulted in an increase in the apparent current densities and hence in the electrocatalytic activity of the alloys because current densities were calculated based on geometrical electrode areas. It would be useful to obtain estimates of the real surface area of the pretreated electrodes so as to determine the electrocatalytic activity of the alloys independent of the surface area effect. A method such as that used by Simpraga et al. [161] could be used to evaluate the true electrode surface.

7. Fe and Ni-based Cr-containing glasses have been reported to display a high corrosion resistance, in particular to pitting corrosion [45]. The Cr content of the glassy alloy required to suppress pitting varied according to the glassy alloy composition but was in general < 8% Cr and was lower than the content required in ferritic stainless steels [67,82]. The pitting corrosion resistance of the glassy alloys could be tested by the addition of ions such as Cl^-, PO_4^{3-}, CN^-, Br^- or F^- and the measurement of pitting potentials. Pitting potentials could be obtained in both acidic and basic electrolytes although these values have been most commonly obtained in an acid medium. The interaction between the aggressive anions and the passive films formed on glassy alloy surface has not been extensively studied and it is suggested that this is because the role of the metalloid elements in film formation and stability is not clearly understood [94]. A study such as this could throw some light on the problem.

8. A more detailed analysis of the cyclic voltammetric responses of the glassy alloys would provide greater insight into the species and processes responsible for the various peaks, e.g. by varying: the potential range scanned in the anodic and cathodic directions to determine the interdependence of peaks, the sweep rate to determine the sweep rate dependence of the peaks (2mV/s to 10V/s), the rotation rate of a rotating ring disc electrode to detect any solution species produced at the oxidation and reduction peaks and the electrolyte temperature to determine its influence on the peak shapes and positions. Hydrogen adsorption at many metal and alloy surfaces can clearly be detected on cyclic voltammograms as distinct peaks that occur at potentials just positive of the hydrogen evolution potential. The potentials at which

hydrogen adsorption peaks on glassy alloys occur could be used to calculate and compare ΔG^0_{ads} values. Comparisons between the ΔG^0_{ads} values of crystalline and amorphous materials would provide an indication of how hydrogen adsorbs on the different surfaces.

9. Further investigation of the influence of chemical pretreatment on the surface properties of the glassy alloys is required, in particular the glassy $Zr_{74}Ti_{19}Cu_2Fe_5$ composition which displayed a decrease in corrosion resistance after both HF and HF/HNO_3 pretreatment. Preferential leaching of Zr from the alloy surface and the possible removal of passivating Zr oxide and Ti oxide surface films reduced the corrosion resistance of the alloy in comparison with its as-polished state (as indicated by the formation of two distinct active peaks on the APC). Further electrochemical and SEM/EDS analyses of the active and passive potential regions of the treated surface would provide greater insight into the changes in surface morphology and composition resulting from acid treatment.

10. Further investigation of the mechanism by with anodic oxidation activates the glassy alloy surfaces is required. Anodic pretreatment produced a surface deposit that provided catalytically active sites for the HER in comparison with the as-polished electrode for each of the alloy compositions tested. The surface layer was very fine and compositional changes in comparison to the as-polished electrode were not be detected by EDS. The composition of these surface layers could be determined using surface analysis techniques such as AES or XPS.

11. Investigation into possible mechanisms of hydrogen evolution at the glassy alloy surfaces could be conducted. Certain mechanistic possibilities and rate determining steps for the HER can be used to calculate different reaction orders and Tafel slopes which can then be compared with the values obtained experimentally from Tafel plots [2]. Kinetic parameters of the elementary steps of the HER and of the net reaction could be evaluated in a similar manner to that of Chialvo [89]. The significance of the change in Tafel slope on moving from low to higher overpotentials requires further investigation.

REFERENCES

---

[1] A.J. Bard, L.R. Faulkner, *Electrochemical Methods, Fundamentals and Applications*, John Wiley and Sons Inc, New York, p.26, Ch.8 (1980).

[2] Southampton Electrochemistry Group, *Instrumental Methods in Electrochemistry*, ed. T.K. Kemp, Ellis Harwood Limited, Chichester, p. 26, 32, 183-189, 206, 234, 236-240, 368 (1985).

[3] P.H. Rieger, *Electrochemistry*, Prentice-Hall Inc., Englewood Cliffs, New Jersey, p. 273, 281 (1987).

[4] H.B. Oldham, J.C. Myland, *Fundamentals of Electrochemical Science*, Academic Press Inc., San Diego, p. 173 (1994).

[5] *Modern Aspects of Electrochemistry, No 16*, ed. B.E. Conway, R.E White, J.O'M. Bockris, Plenum Press, New York and London, Ch. 2 (1985).

[6] J. Tafel, *Z. Phys. Chem.*, **50**, 641 (1905).

[7] J. O'M. Bockris, A.K. Reddy, *Modern Electrochemistry*, Plenum Press, New York, Vol. 2, p. 1328, 1351 (1977).

[8] D.P. Gregory, *Modern Aspects of Electrochemistry, No. 10*, J. O'M. Bockris, B.E. Conway, Plenum Press, New York, p. 239 (1975).

[9] A.A. Balandin, *Advances in Catalysis, Vol. 10*, ed. D.D. Eley, W.E. Frankenberg, V.I. Komarewsky, P.B. Weisz, Academic Press, New York, p. 120 (1958).

[10] W.E. Brower, M.S. Matyjaszczyk, T.L. Pettit, G.V.Smith, *Nature*, **301**, 497 (1983).

[11] W. Klement, R.H. Willems, P. Duwez, *Nature*, **187**, 869 (1960), in ref. [13].

[12] M.D. Archer, C.C. Corke, B.H. Harji, *Electrochimica Acta*, **32**, 13 (1987).

[13] P. Ramachandrarao, *Metallic Glasses, Production, Properties and Applications*, ed. T.R. Anantharaman, Trans Tech Publications, Netherlands, p. 31 (1984).

[14] J.J. Gilman, *Science*, **208**, 856 (1980).

[15] R.B. Diegle, *Proc. 4th Int. Conf. Rapidly Quenched Metals*, ed. T. Masumoto, K. Suzuki, Japan Institue of Metals, Sendai, **2**, p. 1457 (1982).

[16] J.L. Walter, F. Bacon, F.E. Luborsky, *Mater. Sci. Engng*, **24**, 239 (1976), in ref. [12].

[17] A. Brunsch, *J. Appl. Phys.*, **50**, 7603 (1979), in ref. [12].

[18] H. Kaneko, Y. Fujino, S. Yamaguchi, K, Asami, K. Hashimoto, M. Hirabayashi, *Corros. Sci.*, **23**, 1207 (1983).

[19] K. Asami, M. Kikuchi, K. Hashimoto, *Corros. Sci.*, **39**, 95 (1997).

[20] C. Grant, R. McKim, *New Scientist*, 637 (1982).

[21] H.G. Suzuki, K. Yamamoto, *Mater. Sci. Engng.*, **33**, 57 (1978), in ref. [12].

[22] F.E. Luborsky, J.L.Walter, *J. Appl. Phys.*, **47**, 3648 (1976), in ref. [12].

[23] M. Peuckert, A. Baiker, *J. Chem. Soc. Faraday Trans. 1*, **81**, 2797 (1985).

[24] A.L.Greer, *Science*, **267**, 1947 (1995).

[25] M.H. Cohen, D. Turnbull, *Nature*, **189**, 131 (1961), in ref. [14].

[26] D.E. Polk, *Acta. Metall.*, **20**, 485 (1972).

[27] A. Peker, W.L. Johnson, *Appl. Phys. Lett.*, **63**, 2342 (1993).

[28] P. Chaudhari, D. Turnbull, *Science*, **199**, 11 (1978).

[29] S. Lele, *Metallic Glasses, Production, Properties and Applications*, ed. T.R. Anantharaman, Trans Tech Publications, Netherlands, p. 81 (1984).

[30] J.D. Bernal, *Nature*, **183**, 141 (1959), in ref. [28,29].

[31] M.H. Cohen, D. Turnbull, *Nature*, **203**, 964 (1964), in ref. [28,29].

[32] J.L. Finney, J. Wallace, *J. Non-Cryst. Solids*, **43**, 165 (1981), in ref. [29].

[33] D.E. Polk, *J. Non-Cryst. Solids*, **5**, 365 (1971), in ref. [28,29].

[34] M.N. Candrasekharaiah, *Metallic Glasses, Production, Properties and Applications*, ed. T.R. Anantharaman, Trans Tech Publications, Netherlands, p. 269 (1984).

[35] C. Suryanarayana, *Metallic Glasses, Production, Properties and Applications*, ed. T.R. Anantharaman, Trans Tech Publications, Netherlands, p. 249 (1984).

[36] P. Rama Rao, V.M. Radhakrishnan, *Metallic Glasses, Production, Properties and Applications*, ed. T.R. Anantharaman, Trans Tech Publications, Netherlands, p. 225 (1984).

[37] T.K.G. Namboodhiri, *Metallic Glasses, Production, Properties and Applications*, ed. T.R. Anantharaman, Trans Tech Publications, Netherlands, p. 203 (1984).

---

[38] M.T. Thomas, D.R. Baer, Proc. *4th Int. Conf. Rapidly Quenched Metals*, ed. T. Masumoto, K. Suzuki, Japan Institute of Metals, Sendai, p. 1453 (1982).

[39] K. Hashimoto, T. Masumoto, *Mater. Sci. and Engng*, **23**, 285 (1976).

[40] K. Hashimoto, K. Osada, T. Masumoto, S. Shimodaira, *Corros. Sci.*, **16**, 71 (1976).

[41] M. Naka, K. Hashimoto, T. Masumoto, *J. Non-Cryst. Solids*, **28**, 403 (1978), in ref. [12].

[42] A. Kawashima, K. Asami, K. Hashimoto, *J. Non-Cryst. Solids*, 70, 69 (1985).

[43] R.B. Diegle, D.M. Lineman, *J. Electrochem. Soc.*, **131**, 106 (1984).

[44] M. Naka, K, Hashimoto, T. Masumoto, *J. Japan Inst. Met.*, **38**, 835 (1974), in ref. [12].

[45] M. Naka, K. Hashimoto, T. Masumoto, *Corrosion*, **32**, 146 (1976).

[46] T. Masumoto, K. Hashimoto, *Annual Review of Materials Science*, **8**, 215 (1978).

[47] P. Cadet, M. Keddam, H. Takenouti, *Proc. 4th Int. Conf. Rapidly Quenched Metals*, ed. T. Masumoto, K. Suzuki, Japan Institute of Metals, Sendai, p. 1447 (1982).

[48] C. Yoon, D.L. Cocke, *J. Non-Cryst. Solids*, **79**, 217 (1986).

[49] D.L. Cocke, C. Yoon, *Rapidly Quenched Metals*, ed. S. Steeb, H. Warlimont, Elsevier Science Publishers, Lausanne, p. 1497 (1985).

[50] M. Naka, K. Hashimoto, T. Masumoto, *J. Non-Cryst. Solids*, **30**, 29 (1978).

[51] M. Naka, K. Hashimoto, T. Masumoto, *J. Non-Cryst. Solids*, **31**, 355 (1979) in [12].

[52] K. Hashimoto, A. Asami, *Corros. Sci.*, **19**, 251 (1979).

[53] R.B. Diegle, *Corrosion*, **35**, 250 (1979).

[54] K. Hashimoto, M. Naka, K. Asami, T. Masumoto, *Corros. Sci.*, **19**, 165 (1979), in ref. [12].

[55] A. Kawashima, T. Sato, K. Hashimoto, *J. Non-Cryst. Solids*, **70**, 55 (1985).

[56] A. Kawashima, K. Hashimoto, T. Masumoto, *Corrosion*, **36**, 577 (1980).

[57] D.D. Macdonald, *J. Electrochem. Soc.*, **139**, 3434 (1992).

[58] S.M. Gravano, S. Torchio, F. Mazza, E. Angelini, M. Baricco, *Corros. Sci.*, **33**, 1227 (1992).

[59] P.P. Karve, M.G. Thube, S.K. Kulkarni, A.S. Nigavekar, *Solid State Communications*, **50**, 1027 (1984).

[60] S.M. Gravano, S. Torchio, E. Angelini, C. Antonione, M. Baricco, *Corros. Sci.*, **32**, 509 (1991).

---

[61] T.M. Devine, *J. Electrochem. Soc.*, **124**, 38 (1977).

[62] Y. Massiani, J. Crousier, *Surface Science*, **162**, 801 (1985).

[63] Y. Massiani, P. Gas, J. Crousier, J. Bernardini, *Appl. Surface Sci.*, **20**, 132 (1984).

[64] R.M. Latanision, J.C. Turn, C.R. Compeau, Third Int. Conf. on Mechanical Behaviour of Materials, ed. K.J. Miller, R.F. Smith, Pergamon Press, Oxford, p. 475 (1979).

[65] R.B. Diegle, *Corrosion*, **36**, 362 (1980).

[66] S. Virtanen, H. Bohni, *Corros. Sci.*, **31**, 333 (1990).

[67] C.K. Hanham, Y. Waseda, K.T. Aust, *Mater. Sci. Engng.*, **45**, 71 (1980), in ref. [12].

[68] G. Kreysa, B. Hakansson, *J. Electroanal. Chem.*, **201**, 61 (1986).

[69] H. Alemu, K. Juttner, *Electrochimica Acta*, **33**, 1101 (1988).

[70] J.Y. Huot, M. Trudeau, L. Brossard, R. Schulz, *J. Electrochem. Soc.*, **136**, 2224 (1989).

[71] J. Crousier, J.P. Crousier, F. Bellucci, *Electrochimica Acta*, **38**, 821 (1993).

[72] N.R. Sorensen, F.J. Hunkeler, R.M. Latanision, *Corrosion*, **40**, 619 (1984).

[73] R.S. Chaudhary, T.K.G. Namboodhiri, I.B. Singh, *Bulletin of Electrochemistry*, **6**, 859 (1990).

[74] K. Asami, K. Hashimoto, T. Masumoto, S. Shimodaira, *Corros. Sci.*, **16**, 909 (1976).

[75] K. Hashimoto, M. Naka, J. Noguchi, K. Asami, T. Masumoto, *Proc. 4th Inter. Symp. on Passivity of Metals*, ed. R.P. Frankenthal, J. Krugar, Electrochemical Society, New Jersey, p. 156 (1978), in ref. [12].

[76] T.P. Moffat, W.F. Flanagan, B.D. Lichter, *Proc. 9th Int. Cong. Met. Corros., Toronto*, Vol. 3, p. 454 (1984), in ref. [12].

[77] K. Asami, M. Naka, K. Hashimoto, T. Masumoto, *J. Electrochem. Soc.*, **127**, 2130 (1980).

[78] H. Kaneko, Y. Fujino, S. Yamaguchi, K. Asami, K. Hashimoto, M. Hirabayashi, *Corros. Sci.*, **23**, 1207 (1983).

[79] H. Brookes, F. Graham, *J. Chem. Soc. Faraday Trans*, **89**, 547 (1993).

[80] G. Okamoto, *Corros. Sci.*, **13**, 471 (1973).

[81] K. Teramoto, K. Asami, K. Hashimoto, *Corros. Engng.*, **27**, 57 (1978).

[82] R.B. Diegle, J.E. Slater, *Corrosion*, **32**, 155 (1976).

[83] J.C. Turn Jr, R.M. Latanision, *Corrosion*, **39**, 271 (1983).

---

[84] M.D. Archer, R.J. McKim, *Corrosion*, **39**, 91 (1983).

[85] K. Kovacs, J. Farkas, L. Takacs, M.Z. Awad, A. Vertes, L. Kiss, A. Lovas, *J. Electrochem. Soc.*, **129**, 695 (1982).

[86] F.J Graham, M.Sc Thesis, University of Natal, Durban, p. 19, 24, 233 (1986).

[87] P.P. Karve, S.K. Kulkarni, *Corros. Sci.*, **25**, 1091 (1985).

[88] D.L. Cocke, *J. Metals*, 70 (1986).

[89] M.R. Gennero de Chialvo, A.C. Chialvo, *J. Electroanal. Chem.*, **448**, 87 (1998).

[90] R. Schlogel, R. Wiesendanger, A. Baiker, *J. Catal.*, **108**, 452 (1987).

[91] J. Barber, S. Morin, B.E. Conway, *J. Electroanal. Chem.*, **446**, 125 (1998).

[92] F.G. Will, *J. Electrochem. Soc.*, **112**, 451 (1965).

[93] J.Y. Huot, L. Brossard, *Int. J. Hydrogen Energy*, **12**, 599 (1987).

[94] P.C. Searson, P.V. Nagarkar, R.M. Latanision, *Modern Aspects of Electrochemistry*, No. 21, ed. J. O'M. Bockris, B.E. Conway, R.E. White, Plenum Press, New York, p. 121 (1990).

[95] S. Spriano, M. Baricco, C. Antonione, E. Angelini, F. Rosalbino, P. Spinelli, *Electrochimica Acta*, **39**, 1781 (1994).

[96] K. Machida, M. Enyo, T. Toyoshima, K. Miyahara, K. Kai, K. Suzuki, *Bull. Chem. Soc. Jpn*, **56**, 3393 (1983).

[97] M. Enyo, T. Yamazaki, K. Kai, K. Suzuki, *Electrochimica Acta*, **28**, 1573 (1983).

[98] M. Naka, K. Hashimoto, T. Masumoto, I. Okamoto, *Proc. 4th Int. Conf. on Rapidly Quenched Metals*, ed. T. Masumoto, K. Suzuki, Japan Institute of Metals, Sendai, p. 1431 (1982).

[99] J.Y. Huot, M. Trudeau, L. Brossard, R, Schulz, *Int. J. Hydrogen Energy*, **14**, 319 (1989).

[100] A. Yokoyama, H. Komiyama, H. Inoue, T. Masumoto, H.M. Kimura, *J. Catal.*, **68**, 355 (1981).

[101] R. Schlogel, *Rapidly Quenched Metals*, ed. S. Steeb, H. Warlimont, Elsevier Publishers, Lausanne, p. 1723 (1985).

[102] R.B. Diegle, *J. Non-Cryst. Solids*, **61**, 601 (1984), in ref. [101].

[103] E. Endoh, H. Otouma, T. Morimoto, Y. Oda, *Int. J. Hydrogen Energy*, **12**, 473 (1987).

[104] D.W. Kirk, S.J. Thorpe, H. Suzuki, *Int. J. Hydrogen Energy*, **22**, 493 (1997).

[105] D. Huerta, K.E. Heusler, *J. Non-Cryst. Solids*, **56**, 261 (1983).

[106] M. Nagumo, T. Takahashi, *Mater. Sci. Engng.*, **23**, 257 (1976).

---

[107] U. Linker, W. Plieth, *Werkst. Korros.*, **34**, 391 (1983).

[108] E.R. Gonzalez, G. Tremilliosi-Filho, M.J. Giz, *Curr. Top. Electrochem.*, **2**, 167 (1993).

[109] K. Lian, D.W. Kirk, S.J. Thorpe, *Electrochimica Acta*, **36**, 537 (1991).

[110] J.J. Podesta, R.C.V. Piatti, A.J. Arvia, P. Ekdunge, K. Juttner, G. Kreysa, *Int. J. Hydrogen Energy*, **17**, 9 (1992).

[111] I. Paseka, J. Velicka, *Electrochimica Acta*, **42**, 237 (1997).

[112] I. Paseka, *Electrochimica Acta*, **40**, 1633 (1995).

[113] B.E. Conway, L. Bai, M.A. Sattar, *Int. J. Hydrogen Energy*, **12**, 607 (1987).

[114] L. Vracar, B.E. Conway, *J. Electroanal. Chem.*, **227**, 253 (1990).

[115] H.S. Tong, J.E. Macur, *Corrosion*, **38**, 464 (1982).

[116] K. Machida, M. Enyo, G. Adachi, J. Shiokawa, *Electrochimica Acta*, **29**, 807 (1984).

[117] J.J. Gilman, *Phys. Today*, **28**, 46 (1975).

[118] A. Yokoyama, H. Komiyama, H, Inoue, T. Masumoto, H.K, Kimura, *Scr. Metall.*, **15**, 365 (1981), in ref. [12].

[119] K. Machida, M. Enyo, K. Kai, K. Suzuki, *J. Less-Common Metals*, **100**, 377 (1984), in ref. [12].

[120] N. Kumagai, Y. Samata, A. Kawashima, K. Asami, K. Hashimoto, *Corrosion, Electrochemistry and Catalysis of Metallic Glasses*, ed. R.B. Diegle, K. Hashimoto, The Electrochemical Society, Pennington, New Jersey, p. 390 (1988).

[121] K. Lian, S.J. Thorpe, D.W. Kirk, *Electrochimica Acta*, **37**, 169 (1992).

[122] K. Lian, S.J. Thorpe, D.W. Kirk, *Electrochimica Acta*, **37**, 2029 (1992).

[123] M. Hara, K. Asami, K. Hashimoto, T. Masumoto, *Electrochimica Acta*, **31**, 481 (1986).

[124] M. Hara, K. Hashimoto, T. Masumoto, *Proc. 4th Int. Conf. on Rapidly Quenched Metals*, ed. T. Masumoto, K. Suzuki, Japan Institute of Metals, Sendai, p. 1423 (1982).

[125] K. Hashimoto, N. Kumagai, H. Yoshioka, H. Habazaki, K. Kawashima, K. Asami, B.P. Zhang, *Mater. Sci. Engng*, **A133**, 22 (1991).

[126] K. Machida, M. Enyo, *Chem. Lett.*, 75 (1985), in ref. [12].

[127] A. Kawashima, K. Hashimoto, *Proc. 4th Int. Conf. on Rapidly Quenched Metals*, ed. T. Masumoto, K. Suzuki, Japan Institute of Metals, Sendai, p. 1427 (1981).

[128] K. Machida, M. Enyo, *Bull. Chem. Soc. Jpn.*, **58**, 2043 (1985).

[129] K. Machida, K. Nishimura, M. Enyo, *J. Electrochem. Soc.*, **133**, 2522 (1986).

---

[130] S. Yoshida, H. Yamashita, T. Funabiki, T. Yonezawa, *J. Chem. Soc.,Faraday Trans. 1*, **80**, 1435 (1984).

[131] S. Yoshida, H. Yamashita, T. Funabiki, T. Yonezawa, *J. Chem. Soc.,Chem. Commun.*, 964 (1982).

[132] A, Yokoyama, H. Komiyama, H. Inoue, *Proc. 4th Int. Conf. on Rapidly Quenched Metals*, ed. T. Masumoto, K. Suzuki, Japan Institute of Metals, Sendai, p. 1419 (1981).

[133] R. Hauert, P. Oelhafen, R. Schlogl, H.J. Guntherodt, *Solid State Communications*, **55**, 583 (1985).

[134] A. Yokoyama, H. Komiyama, H. Inoue, T. Masumoto, H. Kimura, *J. Non-Cryst. Solids*, **61**, 619 (1984).

[135] G. Kisfaludi, K. Lazar, Z. Schay, L. Gaczi, C. Fetzer, G. Konczos, A. Lovas, *Appl. Surface Sci.*, **24**, 225 (1985).

[136] J. Kupka, A. Budniok, *J. Appl. Electrochem.*, **20**, 1015 (1990).

[137] C.H.L. Tonkinson, M.Sc. Thesis, University of Natal, Durban, p. 154 (1993).

[138] B. MacDougall, M.J. Graham, *Electrochim. Acta,* **26**, 705 (1981).

[139] S.J. Thorpe, J. Paprocki, K.T. Aust, *Corrosion,* **41**, 385 (1985).

[140] M. Islam, *Corrosion,* **36**, 158 (1980).

[141] W.D. France, Jr., *J. Electrochemical Soc.,* **114**, 818 (1967).

[142] M.A. Helfand, C.R. Clayton, R.B. Diegle, N.R. Sorenson, *J. Electrochem. Soc.*, **139**, 2121 (1992).

[143] J.I Goldstein, D.E.Newbury, P.Echlin, D.C. Roy, C. Fiori, E. Lifshin, *Scanning Electron Microscopy and x-ray Microsnalysis*, Plenum Press, New York, Ch. 3 (1983).

[144] F. Graham, PhD Thesis, University of Natal, Durban, p. 131, 133, 182, 203, 218 (1994).

[145] H.C. Brookes, F.J. Graham, *S. Afr. J. Chem.*, **48**, 79 (1995).

[146] B.E. Conway, H. Angerstein-Kozlowska, M.A. Sattar, B.V. Tilak, *J. Electrochem. Soc.*, **130**, 1825 (1983).

[147] B.E. Conway, D.J. MacKinnon, *J. Electrochem. Soc.*, **116**, 1665 (1969).

[148] B.E. Conway, L. Bai, D.F. Tessier, *J. Electroanal. Chem.*, **161**, 39 (1984).

[149] P.P. Karve, S.K. Kulkarni, A.S. Nigavekar, *Solid State Communications*, **49**, 719 (1984).

[150] N. Kumagai, Y. Samata, A. Kawashima, K. Asami, K. Hashimoto, *J. Appl. Electrochem.*, **17**, 347 (1987).

[151] B.D. Cahan, S. Srinivasan, *J. Advan. Energy Conversion*, **6**, 183 (1968).

[152] N.A. Assuncao, M.J. de Giz, G. Tremiliosi-Filho, E.R. Gonzalez, *J. Electrochem. Soc.*, **144**, 2794 (1997).

[153] H. Yamashita, K. Sakai, T. Funabiki, S. Yoshida, Y. Iozumi, *J. Chem. Soc., Faraday Trans. 1*, **83**, 2895 (1987).

[154] R.K. Shervedani, A. Lasia, *J. Electrochem. Soc.*, **144**, 511 (1997).

[155] R.K. Shervedani, A. Lasia, *J. Electrochem. Soc.*, **144**, 2652 (1997).

[156] R.M. Latanision, H. Opperhause, *Met. Trans.*, **5**, 483 (1974).

[157] R.V. Nandedkar, A.K. Tyagi, *Metallic Glasses, Production, Properties and Applications*, ed. T.R. Anantharaman, Trans Tech Publications, Netherlands, p. 165 (1984).

[158] J.P. Diard, B. Le Gorrec, S. Maximovitch, *Electrochimica Acta*, **35**, 1099 (1980).

[159] L.D. Burke, P.F. Nugent, *Gold Bulletin*, **31(2)**, 39 (1998).

[160] L.M. Torres, A. F. Gil, L. Galicia, I. Gonzalez, *Journal of Chemical Education*, **73**, 808 (1996).

[161] R. Simpraga, G. Tremiliosi, S.Y, Qian, B.E. Conway, *J. Electroanal. Chem.*, **424**, 141 (1997).

APPENDIX

An excel macro was written to produce smooth cyclic voltammetric curves and to automate this process in order to analyse and draw a large number of curves. The original 4000 data points obtained from the Nicolet 3091, twin-channel digital storage oscilloscope, produced cyclic voltammograms that contained a lot of noise. The macro reduced the number of data points to about 30 by calculating an average current value (y) for each unique potential value (x) without eliminating the extreme maximum and minimum values obtained and hence produced a far smoother curve.

```
'******************************************************************
' Program: Microsoft 97 Macro.
' Author: Christine Crosby,
' Chemistry Department, University of Natal, Durban.
' Description: This macro performs the following:
' 1) Opens a number of text files and reads the data into an excel spreadsheet.
'    The text files contain results from cyclic voltammograms.
' 2) The results are then processed to extract enough data to draw a smooth graph.
' 3) A graph of the results is drawn.
' Notes: Lines starting with ' are comments.
'******************************************************************


Sub CopyFiles()
' Open all files in a sub directory and place them into an excel sheet

' Prompt the users if they are processing CV's or Tafel Plots
cyclic = MsgBox("Are you running a cyclic voltamogram?", vbYesNo)

' Directory where text files live
dir_loc = "D:\Christine\tmp\"
' Get first file name in directory
file_name = Dir(dir_loc)

firstbook = ActiveWindow.Caption

' While there are still files to process in directoy
While (file_name <> "")
 file_in = dir_loc & file_name
 ' Open the text file
 Workbooks.OpenText FileName:=file_in, Origin:= _
     xlWindows, StartRow:=1, DataType:=xlFixedWidth, FieldInfo:=Array(Array(0, _
     1), Array(10, 1))

 ' Cut all the newly opened data to the clipboard
 Windows(file_name).Activate
 ActiveSheet.Columns("A:B").Select
```

```
  Selection.Cut

  ' Add a new sheet.  Call it the name of the opened text file. Past the contents of
  ' clipboard into it
  Windows(firstbook).Activate
  Sheets.Add
  sheet_name = Mid(file_name, 1, Len(file_name) - 3)
  ActiveSheet.Name = sheet_name
  Windows(firstbook).Activate
  ActiveSheet.Columns("A:B").Select
  ActiveSheet.Paste

  Windows(file_name).Activate
  ActiveWindow.Close (False)

  If (cyclic = 6) Then
   ' Do CV part
   CyclicSort
  Else
   ' Do Tafel part
   SortCols
  End If
  ' Call the routines
  Average
  RemoveZeros
  If (cyclic = 6) Then
   CyclicChart (sheet_name)
  Else
   DrawChart (sheet_name)
  End If

  ' Get the next unprocessed file
  file_name = Dir
Wend

End Sub

'*******************************************************************

Sub RemoveZeros()
' Remove all the cells that are zero

  endr = 3999
  For y = 3999 To 1 Step -1
   tmp = Range("C" & y).Value
   If (tmp <> 0) Or (y = 1) Then
     rng = "" & endr & ":" & y + 1
     Range(rng).Select
     Selection.Delete Shift:=xlUp
     endr = y - 1
   End If
 Next y
 Range("1:1").Select
```

```
 Selection.Delete Shift:=xlUp

 Columns("B:B").Select
 Selection.Delete Shift:=xlToLeft
End Sub

Sub Average()
' Average all y values that have the same x value

 tmp1 = Range("A2").Value
 total = 0
 Count = 0
 ' Range to process cells in
 For x = 2 To 4001
  tmp = Range("A" & x).Value
  ' Compare cell to previous one
  If tmp1 <> tmp Then
   If (Count = 0) Then
    Range("C" & x - 1).Value = total
   Else
    ' Write the averaged value
    Range("C" & x - 1).Value = (total / Count)
   End If
   total = Range("B" & x).Value
   Count = 1
  Else
   Count = Count + 1
   val1 = Range("B" & x).Value
   total = total + val1
   Range("C" & x - 1).Value = 0
  End If
  tmp1 = tmp
 Next x

End Sub

'******************************************************************

Sub SortCols()
' Sort the newly read in columns.

   ' Swop the A and B columns
   Columns("A:A").Select
   Application.CutCopyMode = False
   Selection.Cut Destination:=Columns("C:C")
   Columns("B:B").Select
   Selection.Cut Destination:=Columns("A:A")
   Columns("C:C").Select
   Selection.Cut Destination:=Columns("B:B")

   ' Round all the values off to 2 decimal places
   Columns("A:A").Select
   Columns("A:A").EntireColumn.AutoFit
```

```
    Columns("A:B").Select
    Selection.NumberFormat = "0.0000"
    Range("C1").Select
    ActiveCell.FormulaR1C1 = "=ROUND(RC[-2],2)"
    Range("C1").Select
    Selection.Copy
    Range("C2:C4000").Select
    ActiveSheet.Paste
    Columns("C:C").Select
    Application.CutCopyMode = False
    Selection.Copy
    Range("D1").Select
    Selection.PasteSpecial Paste:=xlValues, Operation:=xlNone, SkipBlanks:= _
        False, Transpose:=False
    Columns("C:C").Select
    Application.CutCopyMode = False
    Selection.ClearContents
    Columns("A:A").Select
    Selection.ClearContents
    Columns("D:D").Select
    Selection.Cut Destination:=Columns("A:A")

    ' Find the log of the y values
    Range("C1").Select
    ActiveCell.FormulaR1C1 = _
        "=IF(RC[-1]=0,0,IF(RC[-1]<0,LOG(-RC[-1]),LOG(RC[-1])))"
    Range("C1").Select
    Selection.Copy
    Range("C2:C4000").Select
    ActiveSheet.Paste
    Columns("C:C").Select
    Application.CutCopyMode = False
    Selection.Copy
    Range("D1").Select
    Selection.PasteSpecial Paste:=xlValues, Operation:=xlNone, SkipBlanks:= _
        False, Transpose:=False
    Columns("B:C").Select
    Application.CutCopyMode = False
    Selection.ClearContents
    Columns("D:D").Select
    Selection.Copy
    Range("B1").Select
    ActiveSheet.Paste
    Columns("D:D").Select
    Application.CutCopyMode = False
    Selection.ClearContents
    Columns("A:B").Select
    ' Sort the values
    Selection.Sort Key1:=Range("A1"), Order1:=xlDescending, Header:=xlGuess, _
        OrderCustom:=1, MatchCase:=False, Orientation:=xlTopToBottom

End Sub
```

```
'*****************************************************************

Sub CyclicSort()
' Only round the y values

   Range("C1").Select
   ActiveCell.FormulaR1C1 = "=ROUND(RC[-1],2)"
   Range("C1").Select
   Selection.Copy
   Range("C2:C4000").Select
   ActiveSheet.Paste
   Columns("A:A").Select
   Application.CutCopyMode = False
   Selection.Cut Destination:=Columns("D:D")
   Columns("C:C").Select
   Selection.Copy
   Columns("A:A").Select
   Selection.PasteSpecial Paste:=xlValues, Operation:=xlNone, SkipBlanks:= _
      False, Transpose:=False
   Columns("B:C").Select
   Application.CutCopyMode = False
   Selection.ClearContents
   Columns("D:D").Select
   Selection.Cut Destination:=Columns("B:B")
   Columns("A:B").Select
   Selection.NumberFormat = "0.0000"

End Sub

Sub CyclicChart(sheet_name)
' Create a new chart object of the processed CV data

   s_name = ActiveSheet.Name

   ' Name the chart sheet the same as the text file appending "_chrt" on.
   chart_name = sheet_name & "_chrt"
   Columns("A:B").Select

   Charts.Add
   ActiveChart.Name = chart_name
   ActiveChart.ChartType = xlXYScatterSmoothNoMarkers
   ActiveChart.SetSourceData Source:=Sheets(s_name).Range("A1:B4000"), PlotBy _
      :=xlColumns
   ActiveChart.Location Where:=xlLocationAsNewSheet
   ActiveChart.PlotArea.Select
   With Selection.Border
      .ColorIndex = 16
      .Weight = xlThin
      .LineStyle = xlContinuous
   End With
   With Selection.Interior
      .ColorIndex = 2
      .PatternColorIndex = 1
```

```
    .Pattern = xlSolid
  End With


End Sub

'************************************************************

Sub DrawChart(sheet_name)
' Draw a tafel plot chart object

  s_name = ActiveSheet.Name

  chart_name = sheet_name & "_chrt"
  Columns("A:B").Select
  Charts.Add
  ActiveChart.Name = chart_name
  ActiveChart.ChartType = xlXYScatter
  ActiveChart.SetSourceData Source:=Sheets(s_name).Range("A1:B4000"), PlotBy _
    :=xlColumns
  ActiveChart.Location Where:=xlLocationAsNewSheet
  With ActiveChart
    .HasTitle = False
    .Axes(xlCategory, xlPrimary).HasTitle = False
    .Axes(xlValue, xlPrimary).HasTitle = False
  End With
  With ActiveChart.Axes(xlCategory)
    .HasMajorGridlines = True
    .HasMinorGridlines = False
  End With
  With ActiveChart.Axes(xlValue)
    .HasMajorGridlines = True
    .HasMinorGridlines = False
  End With
  ActiveChart.Axes(xlCategory).Select
  With ActiveChart.Axes(xlCategory)
    .MinimumScaleIsAuto = True
    .MaximumScale = -1.2
    .MinorUnitIsAuto = True
    .MajorUnitIsAuto = True
    .Crosses = xlAutomatic
    .ReversePlotOrder = False
    .ScaleType = xlLinear
  End With
End Sub

'************************************************************
```